Université Paris-Sud
Ecole Doctorale de Chimie Paris-Sud
Spécialié Chimie Physique

Laboratoire de Chimie Physique

Thèse de Doctorat

soutenue le 23/09/2013

par
Zhe PENG

Experimental and theoretical simulations of Titan's VUV photochemistry

---

Directeur de thèse : Pascal PERNOT (Directeur de recherche, LCP, Univ. Paris-Sud)

Co-encadrante : Nathalie CARRASCO (Maître de conférences, LATMOS, UVSQ)

Composition du Jury

Dr. Karine BEROFF (Directeur de recherche, ISMO, Univ. Paris-Sud)	Présidente du jury
Pr. Marie-Claire GAZEAU (Professeur, LISA, Univ. Paris-Est Créteil)	Rapporteur
Dr. Valentine WAKELAM (Chargé de recherche, LAB, Univ. Bordeaux 1)	Rapporteur
Dr. Michel DOBRIJEVIC (Maître de conférences, LAB, Univ. Bordeaux 1)	Examinateur
Dr. Roland THISSEN (Chargé de recherche, IPAG, Univ. Joseph Fourier)	Examinateur
Dr. Pascal PERNOT (Directeur de recherche, LCP, Univ. Paris-Sud)	Directeur de thèse
Dr. Nathalie CARRASCO (Maître de conférences, LATMOS, UVSQ)	Membre invité

Acknowledgements

First of all, I would express my appreciation to my committee members: Dr. Karine Beroff, Prof. Marie-Claire Gazeau, Dr. Valentine Wakelam, Dr. Michel Dobrijevic and Dr. Roland Thissen. I would like to thank them for their time in reviewing my doctoral thesis and attending my defence. Their constructive comments on my manuscript and our discussions have improved the quality of my thesis. In particular, I would like to acknowledge Dr. Michel Dobrijevic for his photochemical model of Titan and our fruitful collaboration.

Pursuing the highest degree has not made me feel more powerful, but in need for more others' valuable help. Without the support of kind people around me, completion of my thesis would have been impossible. They are so many that I can only mention in particular a small part of them here.

Above all, I would like to thank my family. I am extremely grateful to my wife Peiyu for her unique love and encouragement during the past decade. She has been making me, a school boy with nothing but video games in his mind ten years ago, grow into a man who bears responsibilities and tries to cave out his own career. Without her affecting me, I might still be a nerd playing video games every day, and will certainly neither aspire to do research nor go abroad for the furtherance of my studies. Moreover, I wish to thank her for her open mind and unconditional mental support to my pursuit of a scientific career, regardless of the fact that my meager PhD salary is often considered as an evidence of irresponsibility to family in Chinese culture. I am also grateful to my parents-in-law for their raising their daughter into such a wonderful girl. To my parents, I would express not only my gratitude for raising me and giving me their support always and throughout, but also my apology for not being with them for more than 5 years.

I am also greatly indebted to my advisors, Dr. Pascal Pernot and Dr. Nathalie Carrasco, for their valuable guidance. I appreciate Pascal's expertise, academic rigor and professionalism in conducting research and guiding me. I am grateful for his patience to cope with a large variety of problems and difficulties, not only scientific ones, of his foreign student. I am thankful for his tolerance when I made serious mistakes. I also like that he is easily reachable and has plenty of sense of humor, which I can feel, but am not always able to follow unfortunately, due to my poor French. Nathalie's dynamism and optimism are extraordinarily impressive to me. She is always positive and active. It is amazing that she always managed to guide and motivate me to face the problems that I encountered during my PhD, particularly for experimental issues which I am not familiar with. Furthermore, I appreciate her strong wish to be a real friend with her students. I was a great pleasure working with both of you, Pascal and Nathalie, thank you.

Meanwhile, I would like to appreciate essential efforts of all my collaborators to carry out our sophisticated projects successfully. I am thankful to Dr. Sylvain Plessis for the substantial work during his PhD at LCP, a foundation of my modeling study, and to Dr. Bérenger Gans and Prof. Dolorès Gauyacq for their delicate measurements of methane photolysis branching ratios, maybe the most important data in my model. I am also thankful to Jean-Jacques Correia for the design and embodiment of the APSIS reactor, to Dr. Alexandre Giuliani for his reception and support at SOLEIL, and to Thomas Gautier and Dr. Ahmed Mahjoub for sharing exhausting but wonderful experiences of all-night APSIS experiments. I wish to acknowledge Prof. Guy Cernogora, Dr. Cyril Szopa, Prof. Yves Bénilan and Dr. Arnaud Buch for their contributions to the APSIS experiments that cannot however be detailed here.

Many nice people at LCP also deserve my sincere thanks. I would like to acknowledge Prof. Mehran

Mostafavi, Director of LCP, who provided me such a good environment for my PhD work. Marie-Françoise Lecanu, general secretary of LCP, was really helpful in handling my tough administrative problems. Dr. Fabien Cailliez devoted much time to improving my papers, presentations and so on, which is not his duty. Jean-Marie Teuler demonstrated his great competences in managing the lab's computer system, which ensures that work of modelers, such as me, goes well. A thank to Drs. David Lauvergnat, Bernard Lévy, Jacqueline Ridard, Aurélien de la Lande and all other TheoSim group members that I cannot mention individually. They created a homely atmosphere all over the lab's 3rd floor, which I have enjoyed for more than 3 years. Also a thank to Aurélie, Gabriella, Sébastien, Adbel Karim, Zibin, Jun and all other current and former PhD students at LCP for spending our last post-graduate days together.

In addition, I wish to express my gratitude to my friends in Europe, Linhao, Zhaoyu, Shun, Hailing... as well as many others in China and America for our precious companionship and their help and support to my studies and my life these years.

I would like to express a special greeting to the Préfectures, which trained me to finish this thesis serenely as a "sans-papier".

Lastly, thanks in advance to the readers of this thesis, for your interest in it and your prospective comments and suggestions. Happy reading!

I dedicate this thesis to my wife, Peiyu,
for her unique love and unconditional support.
I love you.

Abstract

Titan's VUV photochemistry is studied by laboratory simulation and numerical modeling.

In the laboratory simulations, a gas flow of N_2/CH_4 (90/10) was irradiated by a continuous VUV (60-350 nm) synchrotron beam in a new reactor, named APSIS (Atmospheric Photochemistry SImulated by Synchrotron). The production of C2-C4 hydrocarbons as well as several nitriles is detected by *in situ* mass spectrometry and *ex situ* GC-MS of a cryogenic experiment.

Our modeling strategy includes the treatment of uncertain parameters. We propose separate representations of the uncertain photolysis cross-sections and branching ratios. This enables to develop a wavelength-dependent model for the branching ratios.

Owing to this separation, in the modeling of Titan's atmosphere, we observe specific altitudes where the uncertainty on the photolysis rate constants vanishes. We show that the Ly-α methane photolysis branching ratios of Wang et al. (2000) and the commonly used "100% CH_3" hypothesis for out-of-Ly-α ones should be avoided in Titan's photochemical models.

A new ion-neutral coupled model was developed for the APSIS experiments. By this model, ion chemistry and in particular dissociative recombination are found to be very important. We identified three growth families, of which the most unsaturated one, promoted by C_2H_2, is dominant. This agrees well with the unsaturated production in Titan's upper atmosphere observed by the Cassini INMS, but not with the *in situ* MS in the APSIS and Imanaka and Smith (2010)'s experiments, whose saturated productions are substantially higher and likely to originate from the catalysis by metallic walls of the reactors.

Keywords: Titan, photochemistry, laboratory simulation, modeling, uncertainty

Simulations expérimentales et théoriques de la photochimie VUV de Titan

Résumé

La photochimie de Titan amorcée par rayonnements VUV est étudiée par la simulation en laboratoire et la modélisation numérique.

Dans les simulations en laboratoire, nous avons irradié un flux de gaz de N_2/CH_4 (90/10) par un faisceau synchrotron VUV continu (60-350 nm) dans un nouveau réacteur, nommé APSIS (Atmospheric Photochemistry SImulated by Synchrotron). La production d'hydrocarbures C2-C4 ainsi que de plusieurs nitriles est détectée par la spectrométrie de masse *in situ* et GC-MS *ex situ* d'un piège cryogénique.

Notre stratégie de modélisation comprend le traitement des paramètres incertains. Nous proposons des représentations séparées des sections efficaces et des rapports de branchement incertains de photolyse. Cela permet de développer un modèle dépendant de la longueur d'onde pour les rapports de branchement.

Grâce à cette séparation, dans la modélisation de l'atmosphère de Titan, nous observons les altitudes spécifiques où l'incertitude sur les constantes de vitesse de photolyse disparaît. Nous montrons que les rapports de branchement de la photolyse du méthane de Wang et al. (2000) et l'hypothèse "100% CH_3" pour ceux hors Ly-α, couramment utilisés, doivent être évités dans les modèles photochimiques de Titan.

Nous avons dévéloppé un modèle ion-neutre couplé pour les expériences APSIS. Par ce modèle, nous trouvons que la chimie des ions et, en particulier, la recombinaison dissociative sont très importants. Nous avons identifié trois familles de croissance, dont la plus insaturée, promue par C_2H_2, est prédominante. Ceci est en bon accord avec la production des espèces insaturées dans la haute atmosphère de Titan détectée par le Cassini INMS, mais pas avec les spectres de masse *in situ* dans les expériences APSIS et celles d'Imanaka and Smith (2010), dont les productions d'espèces saturées sont nettement plus élevées et probablement dues à catalyse par les parois métalliques des réacteurs.

Mots-clés : Titan, photochimie, simulation expérimentale, modélisation, incertitude

Contents

Chapter 1

Introduction

Contents

1.1 Titan

1.1.1 From observation to pre-Cassini era

The discovery by Dutch scientist Christaan Huygens of Titan, the biggest moon of Saturn, dates back to March 25, 1655. However, its scientific interest was ignored until the beginning of the 20th century, when Spanish astronomer Josep Comas Solá (Solá, 1908) observed limb darkening of Titan and interpreted it as the presence of an atmosphere. In 1944 Gerard Kuiper confirmed the existence of Titan's atmosphere by spectroscopic techniques and found methane in its composition for the first time (Kuiper, 1944).

Since then, Titan's methane-containing atmosphere has been attracting more and more researchers. The evidences of a series of hydrocarbons and of the climatic phenomena relative to them were spectroscopically detected (Larson, 1980). This hints at a chemistry behind these minor hydrocarbons, as well as methane. Titan was visited by the crafts *Pioneer 11* and *Voyager* around 1980. The latter took pictures of its orange haze and measured the composition of the atmosphere, *i.e.* ∼98% N_2 and ∼2% CH_4, and its main physical characteristics (Tab. 1.1).

Titan exhibits a lot of similarities with Earth (size, gravity, atmospheric pressure, occurrence of a chemistry in the atmosphere, *etc.*), provoking more associations on the subject about which man is always curious: the possibility of the existence of extraterrestrial life. Although its atmospheric temperature (∼100-150 K) is likely to be too low to breed a form of life very similar to ours, Titan

Property	Earth	Titan
Radius (km)	6.4×10^3	2.6×10^3
Mass (kg)	6.0×10^{24}	1.3×10^{23}
Orbital period (d)	1	16
Surface atmospheric pressure (bar)	1.0	1.5
Atmospheric compsition	N_2 78.1% , O_2 20.9%	N_2 ~98%, CH_4 ~2%
Surface temperature (K)	298	94
Surface gravity ($m.s^{-2}$)	9.8	1.4

Table 1.1: Main physical properties of Earth and Titan.

is considered as a natural "laboratory" of prebiotic chemistry (Sagan et al., 1992), *i.e.* the chemical evolution before the origin of life:

In this "laboratory", the chemistry surprisingly complexifies the atmospheric composition from the activation of such simple main components, N_2 and CH_4, by solar UV photons and energetic particles (*e.g.* electrons from Saturn's magnetosphere) and leads to molecular growth till the formation of aerosols. These aerosols deposit towards Titan's surface and are the origin of the orange haze. They are likely to be often nitrogented ones and of prebiotic interest (Sagan and Khare, 1979). However, the bridge between N_2 and CH_4, and complex tholins, *i.e.* the minor species acting as intermediates of the molecular growth (Fig. 1.1) and the processes undertaking the molecular growth, was very poorly known. The situation had not been significantly changed until the Cassini-Huygens spacecraft arrived at Titan.

1.1.2 The Cassini-Huygens Mission

The Cassini-Huygens spacecraft was designed for the *in situ* study of the Saturnian system, including the moons, especially Titan. After a 7-year journey, it made the first flyby of Titan on July 2, 2004. Since then, it has been enriching the knowledge on Titan: the Huygens probe, detached from the Cassini orbiter, measured the column composition of Titan's atmosphere during its descent and landing on Titan's surface (Niemann et al., 2005). The Composite InfraRed Spectrometer (CIRS) measured infrared emissions from Titan's atmosphere for the determination of the composition of Titan's lower atmosphere (Coustenis et al., 2007). The CAssini Plasma Spectrometer (CAPS) measured ion density in Titan's ionosphere to probe the impact of Saturn's magnetosphere on Titan's ionosphere (Lipatov et al., 2012). However, for the purpose of the measurements of the composition of Titan's upper atmosphere, where molecular growth is initiated by solar VUV photons, none of the instruments mentioned above are more suitable than the Ion and Neutral Mass Spectrometer (INMS).

1.1.2.1 The Ion and Neutral Mass Spectrometer: a new picture of the molecular growth in Titan's atmosphere

The Cassini Ion and Neutral Mass Spectrometer (INMS), as its name implies, measures both ions and neutrals in Titan's upper atmosphere by mass spectrometry (Waite et al., 2004). To achieve this, the instrument uses two different ion sources, a closed and an open source:

- the closed source consists of an antechamber with an entrance aperture, a filament and a transfer tube between them. The high conductance of the inflow through the entrance aperture and the low conductance of the flow in the transfer tube increase the gas density in the

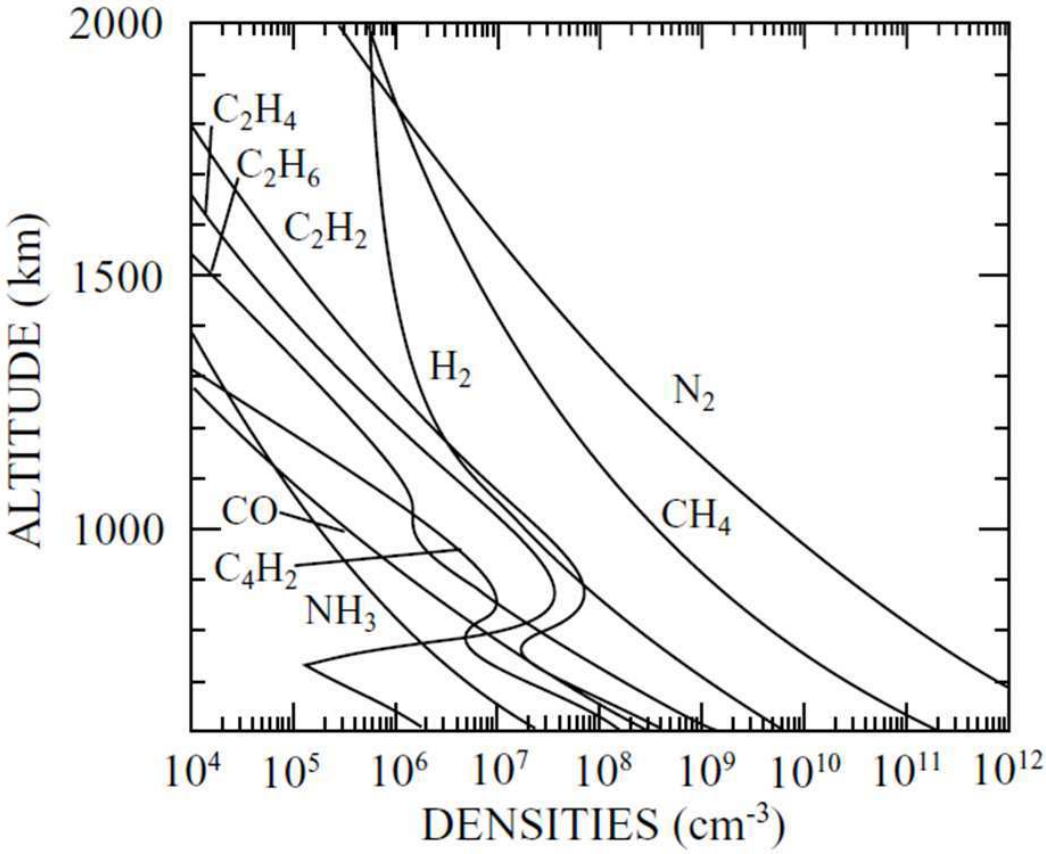

Figure 1.1: Neutral densities vs altitude in Titan's upper atmosphere (Figure from Waite et al. (2004)).

antechamber (Fig. 1.2). This results in an improvement of the detection limit, as well as collsions between the molecules gathered in the antechamber, which makes reactive molecule disappear. Therefore, the closed source is used for the detection of stable neutral species.

- the open source has no antechamber for gas accumulation. Thus, it can detect both neutral species, radicals and ions. Four ion deflectors, installed just after the entrance aperture (Fig. 1.2), realize the filtering or the concentration of positive ions. This function allows the choice of the type of species to be measured, between neutrals and ions.

From both sources, the sampled gas is finally measured by a quadrupole mass analysis and detection system, with a mass resolution of 1 u and an upper limit of 99 u. The *in situ* measurements by the INMS brought out a spectacular progress of our knowledge about the composition of Titan's upper atmosphere.

The INMS provided the first evidence of the existence of a series of minor organic components of Titan's atmosphere, including ions (Waite et al., 2005, 2007). The mass spectra revealed compounds up to its upper limit, which directly and comprehensively corroborate the complexity of the chemistry of Titan's upper atmosphere and the large variety of its components, which are not easy to confirm with spectroscopic means. In particular, the richness of the ion chemistry in Titan's atmosphere has been discovered through the block pattern in the INMS ion MS, illustrating a remarkable growth through ionic pathways. Waite et al. (2007) proposed correlations between the blocks of the same heavy atom number in the neutral and ion spectra, implying significant neutral productions by ion chemistry. (see Fig. 1.3) The INMS detected N-bearing compounds (Waite

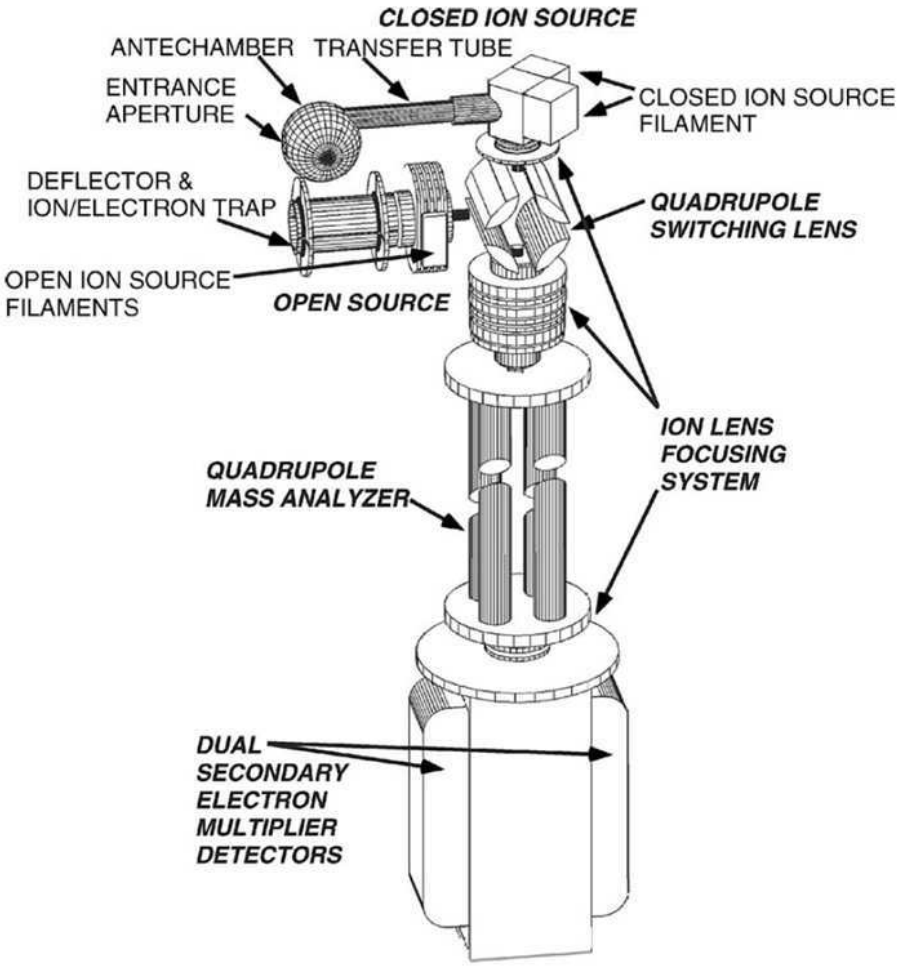

Figure 1.2: Scheme of the Cassini INMS intrument (Figure from Waite et al. (2004)).

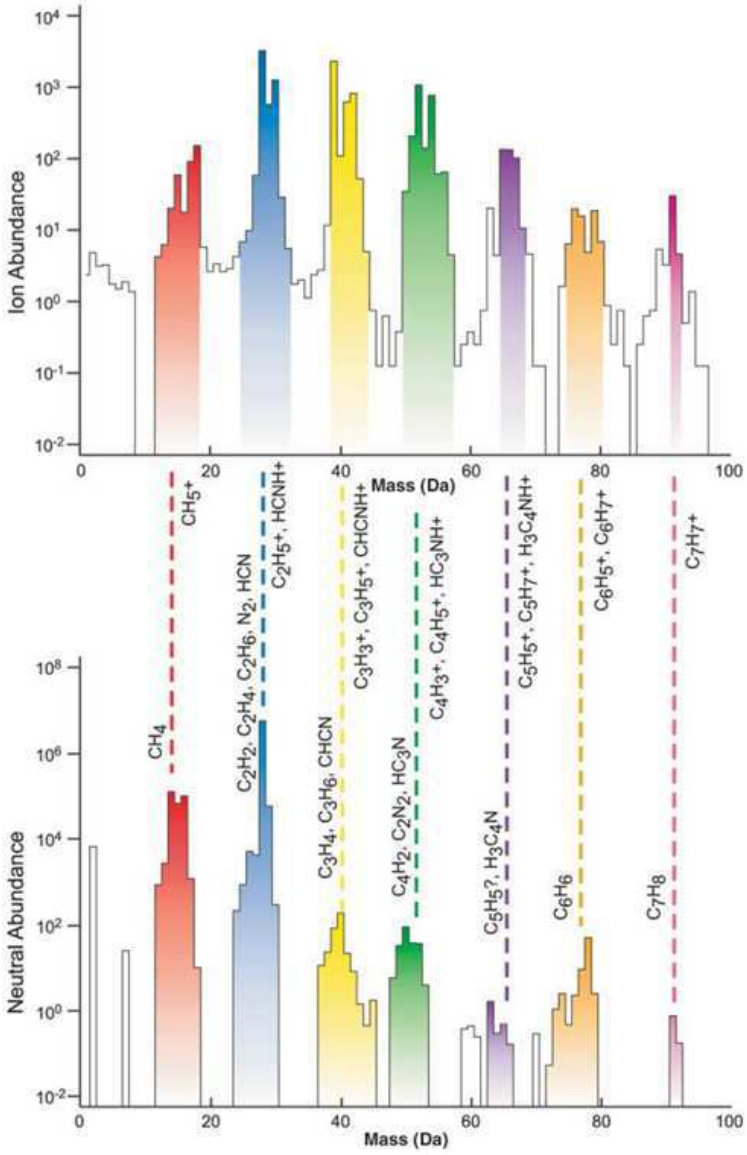

Figure 1.3: Ion (upper) and neutral (lower) mass spectra measured by the INMS during T19 flyby between 950 and 1000 km (Figure from Waite et al. (2007)).

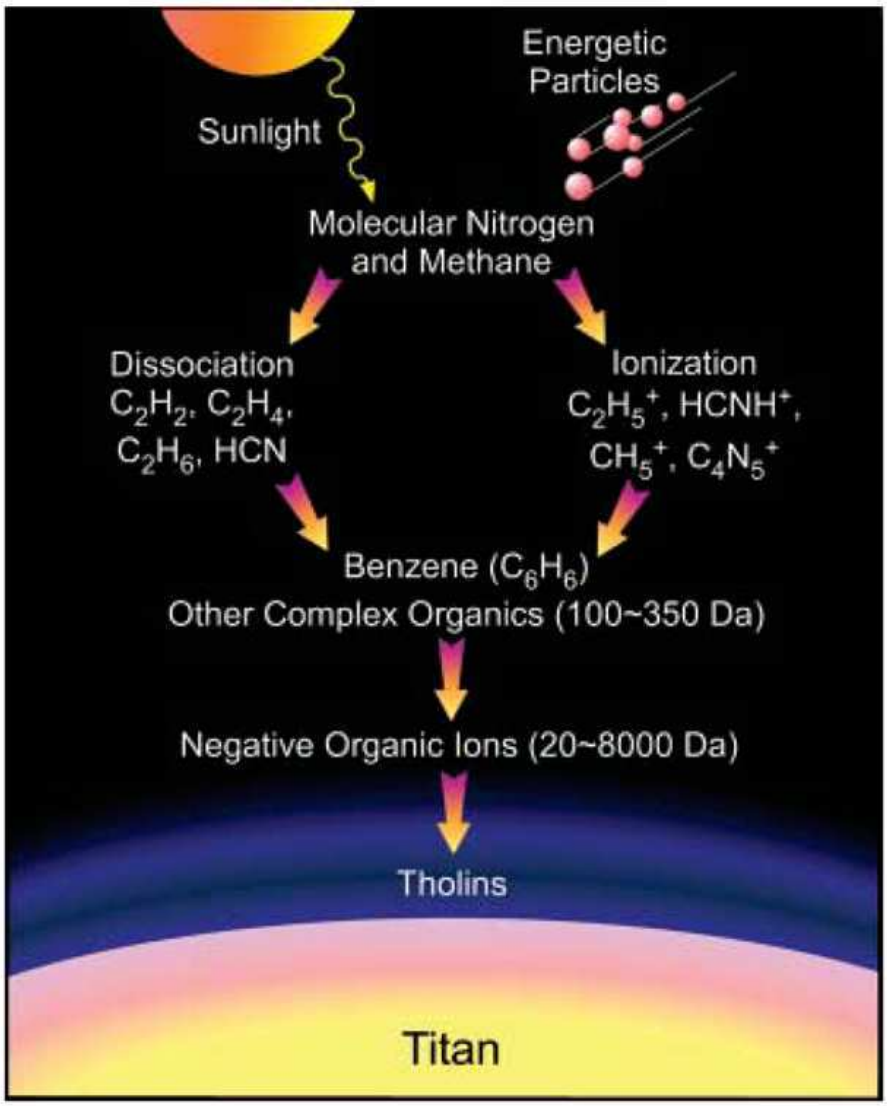

Figure 1.4: Scheme of the processes leading up to the formation of tholins in Titan's upper atmosphere (Figure from Waite et al. (2007)).

et al., 2005; Vuitton et al., 2006, 2007) and O-bearing species (Cravens et al., 2006) and some noble gas components (Waite et al., 2005). Isotopic ratios can be deduced from its data (Waite et al., 2005; Mandt et al., 2012b). As the INMS data of more and more flybys were registered, researchers could even describe the evolution of the composition of Titan's upper atmosphere to some extent (Mandt et al., 2012a).

From these observations, a broad-brush scheme of the molecular growth in Titan's upper atmosphere has been established (Waite et al., 2007)(see Fig. 1.4): solar photons and energetic particles that arrive at Titan's atmosphere react with its main components, N_2 and CH_4. This results in the dissociation or the ionization of molecular nitrogen and methane, and in the production of reactive neutral radicals and positive ions. These reactive species, along with N_2 and CH_4, realize the molecular growth through neutral and ionic pathways, which form C_2H_2, C_2H_4, HCN... and $C_2H_5^+$, $HCNH^+$, $C_4H_5^+$... respectively. The molecular growth also leads to the formation of an important species, benzene. Benzene is a critical precursor of (nitrogenated) polycyclic aromatic hydrocarbons (PAHs) (Frenklach, 2002), which are believed to be essential components of Titan's aerosols and may play an important role in the origin of life (Ehrenfreund et al., 2006).

1.1.2.2 Limitations of the INMS data

However, the INMS is still far from being able to reveal the whole chemistry in Titan's upper atmosphere. The detection of stable neutrals and positive ions are not enough to enable us to clearly know the underlying growth mechanisms between the detected species. To get information on kinetic, even mechanistic aspect, species concentrations are necessary. Ion concentrations can be directly measured by the open mode of the INMS. But ions are not sufficient to infer the whole chemistry. The INMS neutral MS data do not directly give species concentrations, but the total signals of their fragments by electron impact.

Since the first INMS neutral MS was measured, researchers have been trying to deconvolve the INMS neutral MS or fit them with concentrations obtained by photochemical models (see Section 1.2), in order to determine species concentrations (Waite et al., 2005, 2007; Vuitton et al., 2006, 2007; Cui et al., 2009; Magee et al., 2009). Nevertheless, there are several problems preventing these studies from providing quantitative results. The inherent measurement uncertainty of the instrument and the variability of Titan's atmosphere make the signals of the INMS always uncertain. This results in difficulty in the unmixing of signal peaks including both the major peak of a minor species and a fragment peak of other species with larger concentrations (Magee et al., 2009). Moreover, uncertainties of model predictions due to both uncertain kinetic parameters and incompleteness of models (see Section 1.2.2), along with observational uncertainties, make it impossible to fit precisely the INMS neutral MS by models (Bézard et al., 2013).

Aside from these data analysis issues, the INMS instrument presents several technical problems introducing artefacts into the measured MS, and lowering the reliability of the INMS data:

- the antechamber walls catalyze radicals recombination, as it has been brought out by (Vuitton et al., 2008, 2009a) for the production of benzene;
- recently, Jaramillo-Botero et al. (2012) demonstrated by molecular simulation that the relative velocity between the the Cassini orbiter and gas molecules in Titan's atmosphere during the flybys are sufficiently high to cause chemisorption of the gas molecules on the internal walls of the INMS instrument, and maybe their fragmentation.

One should therefore be cautious in the interpretation of the INMS data, and modeling is a necessary complement to the Cassini observations for the study of Titan's atmospheric chemistry.

1.2 Modeling of Titan's atmospheric chemistry

1.2.1 Nominal models

Since the arrival of Voyager I at Titan, researchers have been developing different types of models to compare with the observations (Yung et al., 1984; Yung, 1987). These studies induced progress in a lot of aspects: polyacetylene chemistry (Yung et al., 1984), nitrile chemistry (Yung, 1987), ion chemistry (Keller et al., 1998), haze formation (Wilson and Atreya, 2003), *etc.* Recently, models for the photochemistry coupled with haze formation (Lavvas et al., 2008a,b; Krasnopolsky, 2009) and 2D/3D circulation (Lebonnois et al., 2001, 2012) have also been established.

A drawback is that these models use only the nominal values of their input parameters. However, there might be several irreconcilable measurements for a parameter, and many parameters are even estimated, sometimes by several methods. The corresponding options of parameters choice result in

different model predictions. Incompleteness of models may also be a source of discrepancy: different reactions and other types of processes included in the models may lead to different results.

The criteria for choosing the processes included in the models and the kinetic data for these processes are difficult to justify, and kinetic data are often selected, sometimes even adapted, to provide results which compare better to the (maybe biased) observations. For examples, see the analysis by Plessis et al. (2010) of the scenarii for the branching ratios of dissociative recombination in Titan models.

Even if this problem was overcome, the measurement uncertainty of physico-chemical parameters still prevents nominal models from exact predictions. In fact, without uncertainty consideration, the photochemical models are not able to estimate how far they deviate from observations. This always limits the representativity of "nominal models".

1.2.2 Uncertain models

These difficulties can in a large part be avoided through models taking parametric uncertainty into account. Hébrard et al. (2006) extensively investigated the uncertain parameters of an exhaustive neutral reaction scheme of Titan's photochemical models. They recommended preferred values and uncertainty for all kinetic parameters in their scheme. Hébrard et al. (2007) reported the first results of the photochemical model based on this uncertain reaction scheme. With the uncertain parameters, especially due to their extrapolation to low temperature (Sander et al., 2006), the model gave very uncertain predictions, even bimodal distributions for several species concentrations (Dobrijevic et al., 2008). This revealed the necessity of reevaluation of the uncertain kinetic parameter to improve the precision of the model predictions.

To find the *key reactions, i.e.* the parameters contributing the most to the total uncertainties of the model, sensitivity analysis (Saltelli et al., 2005) can be applied. Hébrard et al. (2009) have shown for instance that a rate constant measurement at low temperature (for the reaction $CH + CH_4 \longrightarrow C_2H_4 + H$, one of key reactions), enables to reduce considerably the uncertainty on this rate constant, and the uncertainty on the model predictions.

On the other hand, through their sensitivity analysis, Hébrard et al. (2009) found an important role of the photolysis reactions in the key reaction list. This was confirmed by Peng et al. (2010), in a photochemical model where all rate constants are assumed to be well measured, with an optimistic relative uncertainty of 10 %. In this study, with the influence of input uncertainties attenuated, the intrinsic importance of the photolysis in the reaction network was highlighted. They also proved and interpreted the importance of the initiation steps in a reaction network by a simplified 0D model and several analytical elementary reaction schemes.

Knowing the importance of the photolysis processes, an appropriate representation of photolysis parameters in the model seems to be a priority, because:

- the model of Hébrard and coworkers used a simplified treatment of uncertain photolysis rate constants, as proposed by Sander et al. (2006), and they assumed *altitude-independent* uncertainty of photolysis rate constants;

- the most important photolysis for hydrocarbon growth, that of methane, had controversial sets of branching ratios data for many years (Romanzin et al., 2005, 2008), leading to discrepant models, as discussed in Section 1.2.1.

To pursue the photochemical modeling of Titan's atmosphere, these two problems should be solved first.

In addition to neutral models, uncertain models for ion chemistry of Titan's upper atmosphere have also been developed. Based on the model of Banaszkiewicz et al. (2000a,b), Carrasco et al. (2007a, 2008a,b) performed a sensitivity analysis for the ion-molecule reactions in Titan's ionosphere and tried to reduce the ion-molecule reaction scheme. Plessis et al. (2010) developed a new knowledge-based probabilistic representation for branching ratios of dissociative recombination, which are important in Titan's ionosphere, but usually have very complex reaction channels and few branching ratio measurements. Plessis et al. (2010, 2012) applied this representation to Titan's photochemical model and showed that the ion chemistry significantly contribute to neutral production. However, Plessis *et al.* coupled their ion chemistry model with the neutral model of Hébrard and coworkers in an indirect way, *i.e.* through iterations between the neutral model giving the species concentrations and the ion model giving the neutral production due to the ion chemistry. This model has not yet been run up to convergence.

Considering these issues, it is desirable to develop a fully ion-neutral coupled model with a consistent representation of all uncertain parameters. Thanks to the recent and reliable measurements of methane photolysis branching ratios at 118.2 nm and Ly-α by Gans et al. (2011) and the branching ratio representation of Plessis et al. (2010), we had all the elements for a revision of the representation of methane photolysis branching ratios. In this thesis, a new representation of methane photolysis branching ratios has been developed and extended to other species. This representation has been implemented in a fully coupled model, which simultaneously integrates the neutral scheme of Hébrard and coworker and the scheme of ion chemistry of Plessis and coworkers, as well as the photolysis scheme revised by us.

1.3 Laboratory simulation experiments of Titan's atmospheric chemistry

Since Miller-Urey experiments (Miller and Urey, 1959) showed the possibility of the synthesis of complex organic, even prebiotic, compounds from very simple substances with an energy deposition, laboratory simulation studies are powerful tools to investigate planetary atmospheres. There is no exception for Titan. Laboratory simulation experiments have suceeded in producing analogues of Titan's aersols (Tran et al., 2003; Szopa et al., 2006a; Imanaka and Smith, 2010), named *Tholins* by C. Sagan (Sagan and Khare, 1979). This shows that laboratory simulation studies are complementary to modeling studies, to understand the important, but uncertain effects of energy deposition (photolysis and impact of energetic particles) on the molecular growth in Titan's atmosphere.

Two kinds of laboratory studies are realized in gas-phase reactors with an energy source initiating the primary ionization and dissociation processes of N_2-CH_4 gas mixtures. With plasma discharges, such as in the PAMPRE reactor, energy is deposited through electron impact (Alcouffe et al., 2010; Carrasco et al., 2009; Szopa et al., 2006b), whereas VUV monochromatic irradiation has been used in photochemical studies (Imanaka and Smith, 2007, 2008, 2010).

On the one hand, plasma discharges are more efficient for the production of aerosols, but Titan's chemistry is mainly driven by photochemical processes. On the other hand, the photon source of the VUV irradiation study of Imanaka and Smith (2010) is monochromatic, unlike the solar spectrum. In this thesis, we propose another simulation experiment, named APSIS, using a continuous VUV-

UV (60-350 nm) irradiation, to compare with other laboratory simulation studies, as well as Titan observations (INMS).

However, there are always questions about the representativity of laboratory experiments mimicking Titan's atmospheric chemistry: for instance, the APSIS experiment in this study has an irradiation source with a continuous, but rather flat spectrum, which is still significantly different from the solar spectrum. Which effects do these spectral differences result in? This kind of questions can seldom be answered by the laboratory simulations themselves, but by photochemical models. A model of the simulation experiments has thus been developed, using the above-mentioned fully coupled code. This approach enables us, *inter alia*, to assess the representativity of the laboratory experiments.

1.4 Objectives and outline of this thesis

This thesis focuses on the photochemistry of Titan's upper atmosphere, in both experimental and theoretical aspects. The central objectives of the theoretical study is to develop an appropriate representation of important but uncertain photolysis processes and to assess its impact on Titan's photochemical model. The photolysis branching ratios, especially those of CH_4, are addressed first. In the experimental study, we present a laboratory simulation with a continuous-spectrum irradiation source, to be compared with other laboratory simulations and the Cassini INMS observations. To answer the question of representativity of these experiments, we also develop a model, to interpret the experiments and the photochemistry of Titan's upper atmosphere, as well as the relations between them, which establishes a link between the two aspects of this thesis.

In Chapter 2, we present the methods necessary to represent the uncertain parameters, to propagate them in the models and to analyze the uncertain results. A wavelength-dependent representation of photolysis branching ratios has been developed for methane, and generalized for all photolysis processes, including ionic pathways. Then, we treated explicitly the uncertain cross-sections and branching ratios, and successively investigated their effects in Titan's photochemical models (Chapter 3). As a complement of modeling studies, we performed simulation experiments, with a continuous VUV source at SOLEIL synchrotron facility, and compare our results with previous studies (Carrasco et al., 2012; Imanaka and Smith, 2010) (Chapter 4). Finally, in Chapter 5, we present the development of the fully ion-neutral coupled model, and use it to explain the observations in Chapter 4, as well as in other experiments and Titan's upper atmosphere.

1.5 Publications relative to this thesis

Peer-reviewed articles:

- **Peng Z.**, Gautier T., Carrasco N., Pernot P., Giuliani A., Mahjoub A., Correia J.-J., Buch A., Bénilan Y., Szopa C., Cernogora G. **Titan's atmosphere simulation experiment using continuum UV-VUV synchrotron radiation.** *Journal of Geophysical Research E - Planets*, **118**, 4 (2013), 778-788;

- Gans B., **Peng Z.**, Carrasco N., Gauyacq D., Lebonnois S., Pernot P. **Impact of a new wavelength-dependent representation of methane photolysis branching ratios on the modeling of Titan's atmospheric photochemistry.** *Icarus*, **223**, 1 (2013), 330-343;

- Gautier T., **Peng Z.**, Giuliani A., Carrasco N., Cernogora G., Mahjoub A., Correia J.-J., Szopa C., Pernot P., Buch A., Bénilan Y. **Photochemistry simulation of planetary atmosphere using synchrotron radiation at SOLEIL: Application to Titan's atmosphere.** *EAS Publications Series*, **58** (2012), 199-203;

- **Peng Z.**, Cailliez F., Dobrijevic M., Pernot P. **Null Variance Altitudes for the photolysis rate constants of species with barometric distribution: Illustration on Titan upper atmosphere modeling.** *Icarus*, **218**, 2 (2012), 950-955;

- **Peng Z.**, Dobrijevic M., Hébrard E., Carrasco N., Pernot P. **Photochemical modeling of Titan atmosphere at the "10 percent uncertainty horizon".** *Faraday Discussions*, **147** (2010), 137-153.

Oral communication:

- **Peng Z.**, Carrasco N., Pernot P. **Modeling of Atmospheric Photochemitry SImulated by Synchrotron setup.** *EPSC-DPS Joint Meeting 2011*, Nantes, France (Oct. 2011).

Posters:

- **Peng Z.**, Gautier T., Carrasco N., Giuliani A., Mahjoub A., Correia J.-J., Pernot P., Buch A., Bénilan Y., Szopa C., Cernogora G. **Titan's atmosphere simulation experiment using a continuous-spectrum UV-VUV synchrotron beamline.** *European Planetary Science Congress 2012*, Madrid, Spain (Sept. 2012);

- **Peng Z.**, Cailliez F., Carrasco N., Hébrard E., Dobrijevic M., Pernot P. **Effects of uncertain photolysis parameters on predictions of Titan's photochemistry models.** *EPSC-DPS Joint Meeting 2011*, Nantes, France (Oct. 2011);

- **Peng Z.**, Gautier T., Carrasco N., Giuliani A., Cernogora G., Correia J.-J., Szopa C., Pernot P., Buch A., Benilan Y. **APSIS: a Titan's atmosphere simulation experiment using a continuous-spectrum UV synchrotron beamline.** *EPSC-DPS Joint Meeting 2011*, Nantes, France (Oct. 2011);

- **Peng Z.**, Gans B., Carrasco N., Lebonnois S., Gauyacq D., Pernot P. **Impact of a new wavelength-dependent representation of methane photolysis branching ratios on the modeling of Titan's atmospheric photochemistry.** *EPSC-DPS Joint Meeting 2011*, Nantes, France (Oct. 2011).

Chapter 2

Methods

Contents

This chapter presents the photochemical models and the theoretical methods which have been used throughout this thesis. Three photochemical models are presented in Section 2.1. They have been used in different parts of this thesis: the 1D radiative transfer model, presented in Section 2.1.1, has been used for the study of the impact of the uncertain photolysis cross-sections on the photolysis rate constants in Titan's photochemistry (see Section 3.1); the 1D IPSL model, presented in Section 2.1.2, has been applied to investigate the impact of methane photolysis branching ratios on the composition of Titan's upper atmosphere (see Section 3.2); a new 0D-2D model, briefly introduced in Section 2.1.3, has been established for the study of laboratory simulation setups of Titan's photochemistry (see Chapter 5).

Uncertainty on the model outputs is obtained by uncertainty propagation (BIPM et al., 2008; BIPM et al., 2008). This requires appropriate probabilistic representations of the inputs, which are detailed in Section 2.2. In addition to the distributions already used in previous studies of Titan's photochemistry (Hébrard et al., 2006; Carrasco et al., 2007a, 2008a; Dobrijevic et al., 2008;

Peng et al., 2010; Plessis et al., 2010, 2012), a new form of generalized Dirichlet distribution and a wavelength-dependent model are introduced for the representation of methane photolysis branching ratios. Then, two common methods for uncertainty propagation are presented in Section 2.3. Sensitivity analysis is used to gain insight into the relation between the uncertain inputs and outputs. It is presented in Section 2.4. At last, we explain how we generate theoretical mass spectra from species concentrations.

2.1 Photochemical models

For historical reason, throughout this study, we have used several photochemical models, among which a 1D radiative transfer model 2.1.1 and 1D IPSL photochemical model 2.1.2 to investigate Titan's upper atmosphere (see Chapter 3). The original contribution of this thesis is a new 0D-2D ion-neutral coupled model for the APSIS reactor, presented in Section 2.1.3.

2.1.1 1D radiative transfer model

The 1D radiative transfer model is adapted from Dobrijevic et al. (2003), where the incident solar flux at every wavelength λ and at every level z in the atmosphere $I_\lambda(z)$ is calculated as a function of the diurnally averaged unattenuated solar flux at the top of the atmosphere I_λ^∞.

Beer-Lambert molecular absorption of N_2, CH_4 and 33 minor species, and N_2 Rayleigh scattering are considered in these calculations. Aerosols absorption and multiple scattering are not included at this stage, which is reasonable for the upper atmosphere of Titan. The density profiles for all species are taken from Hébrard et al. (2009), with the upper boundary of the atmosphere at $z_u = 1300\,\mathrm{km}$.

This model is only used for radiative transfer study, but *not* for species density calculation. No reaction is thus considered in the model.

2.1.2 1D IPSL model

The IPSL05 1-dimensional model has been first developed by Toublanc et al. (1995). It was built to go from the surface up to 1300 km altitude. It computes neutral photochemical sources and sinks (∼500 reactions) for hydrocarbons and nitriles (∼50 species). It includes molecular diffusion in N_2, as well as eddy diffusion. CH_4 and N_2 abundances are fixed at the surface, while for all other compounds, no surface exchanges are allowed. Condensation is taken into account. At the upper boundary, Jeans escape is computed for atomic and molecular hydrogen (see also the specific study on hydrogen budget: Lebonnois et al. (2003)). A flux of nitrogen atoms is also included, to take into account the dissociation of N_2 occurring above the upper limit of the model. An additional flux of atomic nitrogen may also be taken into account due to dissociation of N_2 by galactic cosmic rays, following the dissociation profile used by Lara et al. (1996). Photochemistry of benzene was also added after a specific study, including comparison with Jupiter's photochemistry (Lebonnois, 2005).

2.1.3 A new 0D-2D ion-neutral coupled model

This model has been designed to interpret the experimental results of a laboratory simulation setup of Titan's photochemistry, named APSIS (see Chapter 4). In consideration of nearly uniform gas in the APSIS reactor, a 0D (1-cell) model has been established (see Chapter 5). It can easily be

extended to 2D by including the internal gas diffusion of the reactor, if a more extensive study is needed. Indeed, a preliminary 2D study with a simplified chemical model has been performed (see (Peng et al., 2011) and A).

This model is an ion-neutral coupled one: its chemical scheme includes all reactions in the neutral model of Dobrijevic *et al.* (Hébrard, 2006; Hébrard et al., 2007) and the scheme of ion chemistry from S. Plessis (Plessis et al., 2010, 2012). Moreover, it integrates in a single code all steps previously treated in separate codes, *i.e.* radiative transfer, neutral chemistry and ion chemistry for 244 C-, H- and N-bearing species (125 neutrals and 119 ions), totaling 1708 reactions (33 photolysis reactions, 415 bimolecular reactions, 82 trimolecular reactions 574 dissociative recombinations and 604 ion-molecule reactions). This realizes a direct coupling between neutral and ion chemistries and allows us to study the time-evolution of ion chemistry, which is an important upgrade from the work of S. Plessis.

2.2 Probabilistic representation of the uncertain kinetic parameters of photochemical models

There are a large variety of kinetic parameters in the photochemical models. Moreover, we have different levels of knowledge of parameters of the same type. Therefore, it is important to use adapted representation for various uncertain parameters to express all information on them properly:

- log-uniform or log-normal distributions (see Section 2.2.1) for total rate constants of neutral reactions and cross-sections of photolysis and ionic reactions;
- uniform or normal distributions, or truncated variants of normal distribution (see Section 2.2.1) for unitless powers in rate constant expressions (*e.g.* temperature dependency expression of dissociative recombination rate constant. See Chapter 5 for details);
- Branching ratios are handled by representation based on Dirichlet-type distributions: nested Dirichlet-type distributions (see Section 2.2.2) for most branching ratios, extended to wavelength-dependent representation (see Section 2.2.3) for methane photolysis branching ratios.

2.2.1 Basic distributions

Uniform distribution: $\mathcal{U}(a,b)$. It is often used when only the lower and upper limits of a random variable X are known. If $X \sim \mathcal{U}(a,b)$, its probability density function $f_X(x;a,b)$ is

$$f_X(x;a,b) = \begin{cases} \frac{1}{b-a} & , \quad x \in [a,b] \\ 0 & , \quad \text{elsewhere} \end{cases} \tag{2.1}$$

Normal distribution: $\mathcal{N}(\mu,\sigma^2)$. It is used to describe ordinary random variable X without specific constraint and whose mean value μ and standard deviation σ are known. If $X \sim \mathcal{N}(\mu,\sigma^2)$, its probability density function $f_X(x;\mu,\sigma)$ is

$$f_X(x;\mu,\sigma^2) = \frac{1}{\sigma\sqrt{2\pi}} \exp\left(-\frac{(x-\mu)^2}{2\sigma^2}\right) \tag{2.2}$$

Truncated normal distribution: $\mathcal{N}_t\left(\mu, \sigma^2, a, b\right)$**.** It is used to describe a normally-distributed random variable X with a mean value μ and a standard deviation σ and restrained in the interval $[a, b]$. If $X \sim \mathcal{N}_t\left(\mu, \sigma^2, a, b\right)$, its probability density function $f_X\left(x; \mu, \sigma, a, b\right)$ is

$$f_X\left(x; \mu, \sigma, a, b\right) = \begin{cases} \dfrac{\dfrac{1}{\sigma\sqrt{2\pi}} \exp\left(-\frac{(x-\mu)^2}{2\sigma^2}\right)}{\Phi\left(\frac{b-\mu}{\sigma}\right) - \Phi\left(\frac{a-\mu}{\sigma}\right)} & , \quad x \in [a, b] \\ 0 & , \quad \text{elsewhere} \end{cases} \tag{2.3}$$

where $\Phi\left(x\right)$ is the cumulative distribution function of the standard normal distribution ($\mu = 0$, $\sigma = 1$).

According to Plessis et al. (2010), these three distributions, *i.e.* uniform, normal and truncated normal, are adapted to represent unitless powers in dissociative recombination rate constant expression in the following cases, respectively:

1. Uniform: no information on the parameter (typical values of its minimal and maximal values in the literature as lower and upper limits), or with contradictory information (minimal and maximal values in different measurements as lower and upper limits);

2. Normal: a nominal value, and associated uncertainty;

3. Truncated normal: only a nominal value, but no uncertainty (nominal value as mean, 100% relative uncertainty assigned for standard deviation, and general figures of its minimal and maximal values in the literature as the limits of the restrictive interval).

Log-normal distribution: $\ln\mathcal{N}\left(\mu, \sigma^2\right)$**.** It describes a random variable X whose logarithm follows a normal distribution $\mathcal{N}\left(\mu, \sigma^2\right)$. If $X \sim \ln\mathcal{N}\left(\mu, \sigma^2\right)$, its probability density function $f_X\left(x; \mu, \sigma\right)$ is

$$f_X\left(x; \mu, \sigma\right) = \frac{1}{x\sigma\sqrt{2\pi}} \exp\left(-\frac{\left(\ln x - \mu\right)^2}{2\sigma^2}\right), \quad x > 0 \tag{2.4}$$

Consequently, the random variable's geometric mean and geometric standard deviation are respectively e^{μ} and e^{σ}. The latter is more commonly called uncertainty factor F. If the relative uncertainty $\frac{u}{\bar{x}}$ of a log-normal distribution is small, it has an approximate and simple relation to the uncertainty factor F

$$F \simeq 1 + \frac{u}{\bar{x}} \tag{2.5}$$

Note that a log-normally distributed random variable must be *positive* to ensure its logarithm's meaning. This property provides a wide application to the representation of various non-negative physical quantities in photochemical models, including reaction rate constants (Thompson and Stewart, 1991; Hébrard, 2006), photolysis cross-sections (see Chapter 3) and concentrations. In addition, this distribution gives a satisfactory representation of these quantities, even in the case of associated uncertainties up to several orders of magnitude.

Log-uniform distribution: $\ln\mathcal{U}\left(a, b\right)$**.** By analogy, the log-uniform distribution describes a random variable X whose logarithm follows a uniform distribution $\mathcal{U}\left(a, b\right)$. If $X \sim \ln\mathcal{U}\left(a, b\right)$, its

probability density function $f_X(x;a,b)$ is

$$f_X(x;a,b) = \begin{cases} \frac{1}{(b-a)x} & , \quad \ln x \in [a,b] \\ 0 & , \quad \text{elsewhere} \end{cases} \tag{2.6}$$

and it varies between e^a and e^b. As log-normal distribution, log-uniform distribution also maintains the random variable's positivity, and hence are suitable to represent the quantities mentioned above, especially in the cases when no measurements or theoretical estimations are available.

2.2.2 Knowledge-based nested Dirichlet-type distributions for branching ratios

Among the photochemical kinetic parameters, branching ratios are compositional data, whose sum is equal to 1. Compositional data are quantitative descriptions of parts in an entirety, in another word, relative values with respect to the total quantity. The sum of the relative values is thus implicitly constant. An n-variable random vector $X = (X_1, X_2, \cdots, X_n)$ for such sum-to-one compositional data, *i.e.*

$$\sum_{i=1}^{n} X_i = 1, \tag{2.7}$$

has only $n-1$ independent variables and are often regarded as a distribution in a $(n-1)$-dimensional simplex of the unit hypercube (generalization of the triangle simplex of the unit cube) in the n-dimensional Euclidean space $\mathbb{R}^n$.

Carrasco and Pernot (2007) proposed to use Dirichlet distributions (Aitchison, 1986) to express branching ratios in the chemical networks. These distributions preserve the positivity and the sum-to-one property of branching ratios. Hence, they avoid undesirable propagation of uncorrelated representation of branching ratios in the chemical network (Carrasco et al., 2008a). Thanks to the efforts of Plessis et al. (2010), different variants of the Dirichlet distribution were designed for branching ratios on which we have different levels of knowledge.

2.2.2.1 The Dirichlet distribution and its variants

Dirichlet distribution: $Diri(\alpha_1, \alpha_2, \cdots, \alpha_n)$**.** The Dirichlet distribution of a random vector of n sum-to-one variables $X = (X_1, X_2, \cdots, X_n)$ with parameters $\alpha_1, \alpha_2, \cdots, \alpha_n > 0$ is denoted as $X \sim Diri(\alpha_1, \alpha_2, \cdots, \alpha_n)$, and has a probability density function

$$f_X(x_1, x_2, \cdots, x_{n-1}; \alpha_1, \alpha_2, \cdots, \alpha_n) = \frac{\Gamma\left(\sum_{i=1}^{n} \alpha_i\right) \prod_{i=1}^{n} x_i^{\alpha_i - 1}}{\prod_{i=1}^{n} \Gamma(\alpha_i)} \tag{2.8}$$

where $\Gamma(x)$ is the gamma function. The random vector's mean value $(\mu_1, \mu_2, \cdots, \mu_n)$ is given by

$$\mu_i = \frac{\alpha_i}{\gamma}, \quad i = 1, 2, \cdots, n \tag{2.9}$$

where $\gamma = \sum_{i=1}^{n} \alpha_i$ is a global precision factor. Carrasco et al. (2007a) proposed that γ can be obtained by a least-squares optimization over the standard uncertainties σ_i as a function of their relative uncertainty r,

i.e. $\sigma_i = r\mu_i/2$,

$$\gamma = \arg\min_\gamma \sum_i \left(\sigma_i - \left(\frac{\mu_i (1-\mu_i)}{\gamma + 1} \right)^{1/2} \right)^2 \tag{2.10}$$

$$= \frac{4}{\gamma^2} \left(\frac{\sum_i \mu_i (1-\mu_i)}{\sum_i \mu_i \sqrt{\mu_i (1-\mu_i)}} \right)^2 - 1 \tag{2.11}$$

In order to ensure the unimodality of the distribution, another constraint

$$\gamma \geq \left\{ \min \left(\max (\mu_1, 1-\mu_1), \max (\mu_2, 1-\mu_2), \cdots, \max (\mu_n, 1-\mu_n) \right) \right\}^{-1} \tag{2.12}$$

was introduced. Note that the relative uncertainty γ is uniformly assigned to all components, which may not be suitable for all types of branching ratios. This description is not able to cope properly with large differences in branching ratios. Therefore, more sophisticated representations have been used since.

Generalized Dirichlet distribution: The generalization of Dirichlet distribution, with a more general covariance structure, *i.e.* no longer a single relative uncertainty for all variables, can be realized in different manners.

Dirg: In Plessis et al. (2010) study, a technique decribed in Lingwall et al. (2008) was used to perform the sampling of this distribution numerically. However, this technique is not theoretically rigorous. This approximate generalized Dirichlet distribution (*Dirg*) includes simultaneously the independent information (nominal values $(\mu_1, \mu_2, \cdots, \mu_n)$ and uncertainties $(\sigma_1, \sigma_2, \cdots, \sigma_n)$, often extracted from independent measurements) of all variables in the n-dimensional random vector $X = (X_1, X_2, \cdots, X_n)$, *i.e.*

$$X \sim Dirg (\mu_1, \mu_2, \cdots, \mu_n; \sigma_1, \sigma_2, \cdots, \sigma_n) \tag{2.13}$$

If the sum-to-one constraint is preserved, the n variables, along with their uncertainties, cannot be all independent. The technique of Lingwall et al. (2008) makes the variables, all generated independently at first, compromise with each other through a renormalization to ensure their sum equal to 1. In fact, after the renormalization, all variables are correlated, but their marginal distributions are more or less different from the original ones. Nevertheless, as long as the independent information do not evidently contradict one another and their sum do not substantially violate the constraint, the samples generated by this technique are satisfyingly representative.

An important advantage of *Dirg* is its ability to reconcile and synthesize different independent sources of information within a random vector whose variables are sum-constrained. *Dirg* is suitable to make use of as much information as possible to represent branching ratios that do not need to be highly accurately reproduced.

Dirw: During this thesis, we introduce another strategy to establish a generalized Dirichlet distribution (*Dirw*), proposed by Connor and Mosimann (1969); Wong (1998, 2010). This method is theoretically rigorous, but not very practical unless a consistent dataset of all variables of an n-part unit-sum compositional random vector $X = (X_1, X_2, \cdots, X_n)$ is provided for parameter

estimation.

For an $X = (X_1, X_2, \cdots, X_n)$ following $Dirw$ distribution, only $2\,(n-1)$ parameters

$$(\alpha_1, \ldots, \alpha_{n-1}, \beta_1, \ldots, \beta_{n-1})$$

corresponding to nominal values and uncertainties of the first $n-1$ variables, are necessary to define its probability density function, since the last variable is determined by $X_n = 1-(X_1 + X_2 + \ldots + X_{n-1})$. If $X = (X_1, \cdots, X_n) \sim Dirw(\alpha_1, \ldots, \alpha_{n-1}; \beta_1, \ldots, \beta_{n-1})$, its probability density function is

$$f_X\left(x_1, \cdots, x_{n-1}; \alpha_1, \cdots, \alpha_{n-1}, \beta_1, \cdots, \beta_{n-1}\right) = \prod_{i=1}^{n-1} \frac{\Gamma(\alpha_i + \beta_i)}{\Gamma(\alpha_i)\Gamma(\beta_i)} x_i^{\alpha_i - 1}(1 - x_1 - \ldots - x_i)^{\gamma_i} \quad (2.14)$$

where $\gamma_i = \beta_i - \alpha_{i+1} - \beta_{i+1}$ for $i = 1, 2, \ldots, n-2$, and $\gamma_k = \beta_k - 1$.

The parameters $(\alpha_1, \ldots, \alpha_{n-1}, \beta_1, \ldots, \beta_{n-1})$ of the $Dirw$ distribution can be identified from a consistent (sum-to-one) compositional dataset with different methods: Bayesian inference (maximum a posteriori estimation) (Gregory, 2005) and the method of moments (Wong, 2010). We checked that both methods provide similar results. The faster method of moments is presented here.

By transforming the original variables $X_1, \ldots, X_k$ to a new set of variables $Z_1, \ldots, Z_k$ by

$$Z_1 = X_1 \quad (2.15)$$

$$Z_i = X_i/(1 - X_1 - \cdots - X_{i-1}) \quad (2.16)$$

one obtains independent variables with Beta distribution $Z_i \sim Beta(\alpha_i, \beta_i)$ (Evans et al., 2000). The values of the parameters can be directly obtained from samples of the transformed data by inversion of the formulae for the mean and variance (corresponding to the first and second order moments, respectively)

$$\mathrm{E}(Z_i) = \frac{\alpha_i}{\alpha_i + \beta_i} \quad (2.17)$$

$$\mathrm{Var}(Z_i) = \frac{\alpha_i \beta_i}{(\alpha_i + \beta_i)^2(1 + \alpha_i + \beta_i)} \quad (2.18)$$

i.e.

$$\alpha_i = \mathrm{E}(Z_i)^2(1 - \mathrm{E}(Z_i))/\mathrm{Var}(Z_i) - 1 \quad (2.19)$$

$$\beta_i = \mathrm{E}(Z_i)(1 - \mathrm{E}(Z_i))^2/\mathrm{Var}(Z_i) - 1. \quad (2.20)$$

The $Dirw$ distribution is well adapted to represent the branching ratios with consistent datasets or samples. This description is crucial in the model. It has been used for the methane photolysis branching ratios at 118.2 nm and 121.6 nm with the measurement data provided by Gans et al. (2011) (as detailed in Section 2.2.3).

Uniform Dirichlet distribution: $Diun\,(n)$ It can be considered as a special case of Dirichlet distribution with a uniform distribution in the simplex. A n-dimensional random vector $X = (X_1, X_2, \cdots, X_n)$ following Dirichlet distribution with the parameters $(\alpha_1, \alpha_2, \cdots, \alpha_n) = (1, 1, \cdots, 1)$

is equivalent to that following a uniform Dirichlet distribution $Diun\,(n)$, *i.e.*

$$X \sim Diun\,(n) \equiv Diri\,(1, 1, \cdots, 1) \tag{2.21}$$

It is an appropriate representation of the branching ratios of a single reaction with no available information.

Truncated uniform Dirichlet distribution: $Diut\,(a_1, a_2, \cdots, a_n; b_1, b_2, \cdots, b_n)$ The sample space of an n-variate truncated Dirichlet distribution $Diut\,(a_1, a_2, \cdots, a_n; b_1, b_2, \cdots, b_n)$ is a subset of the simplex of an n-variate uniform Dirichlet distribution, with samples confined within the intervals $[a_1, b_1]$, $[a_2, b_2]$,$\cdots$, and $[a_n, b_n]$ in the 1st, 2nd, $\cdots$, and nth dimension, respectively. Fang and Yang (2000) algorithm based on conditional distributions is used for the sampling of this distribution.

Ordered Dirichlet distribution: $Dior\,(n)$ As truncated uniform Dirichlet distribution, an n-variate ordered Dirichlet distribution $Dior\,(n)$ also has a sample space which is a subset of the corresponding uniform Dirichlet distribution, nevertheless no longer confined by the limits of variables, but with an order constraint (*e.g.* $X_1 \geq X_2 \geq \cdots \geq X_n$ for a random vector $X = (X_1, X_2, \cdots, X_n)$). The *Dior* distribution can be easily sampled by reordering the samples of the corresponding *Diun* distribution to conform with the constraint, *i.e.*

$$X \sim Dior\,(n) = \mathrm{sort}\,(Diun\,(n)) \tag{2.22}$$

Diut and *Dior* distributions are able to utilize some very limited information that may usually not be straightforwardly useful to the probabilistic representation of branching ratios. For example, to constraint the branching ratios with no direct measurements, the general figures of the limits in the literature can be used by *Diut* distribution, and the qualitative orders of favorable channels given by thermodynamical considerations can be used by *Dior* distribution.

2.2.2.2 Knowledge-based probabilistic trees

For a reaction with many possible channels (*e.g.* dissociative recombination of large ions), there are rarely measurements consistently reporting the branching ratios of all channels: either the branching ratios of different channels of a single reaction are measured in different experiments, or, more commonly, there are still some channels of a reaction that have not been measured so far, despite the contributions of different experimentalist groups. None of the Dirichlet-type distributions mentioned above is able to cope with such complex cases. To preserve all kinds of information on the branching ratios of a reaction, *i.e.* the ones that have already been measured, the ones on which we have only limited qualitative knowledge, and even the ones that we know *nothing* about, a nesting for the Dirichlet-type distributions (Null, 2008; Tian et al., 2010) was introduced by Plessis et al. (2010), to build probabilistic trees.

The nesting strategy is explained here, with the aid of the following example:

$$\mathrm{I}^+ + \mathrm{e}^- \text{ or } \mathrm{R}{+}h\nu \longrightarrow \begin{cases} \xrightarrow{B_1 \pm \Delta B_1} \begin{cases} \xrightarrow{B_{11} \pm \Delta B_{11}} \mathrm{M}_1 \\ \xrightarrow{B_{12} \pm \Delta B_{12}} \mathrm{M}_2 \end{cases} \\ \xrightarrow{B_3 \pm \Delta B_3} \mathrm{M}_3 \end{cases} \tag{2.23}$$

where the branching ratio data are extracted from two independent experiments. One measured the relative efficiencies of the productions of $M_1 + M_2$ (B_1) and M_3 ($B_3 = 1 - B_1$). Another experiment measured the branching ratios between M_1 (B_{11}) and M_2 ($B_{12} = 1 - B_{11}$). Each experiment comes with it's own set of uncertainty, *i.e.* ($\Delta B_1, \Delta B_3$) and ($\Delta B_{11}, \Delta B_{12}$). The nominal values ($\mu_1, \mu_2, \mu_3$) of the final branching ratios for M_1, M_2 and M_3 (b_1, b_2, b_3) can be computed from both data sets

$$\begin{aligned} \mu_1 &= B_1 \times B_{11}, \\ \mu_2 &= B_1 \times B_{12}, \\ \mu_3 &= B_3. \end{aligned} \tag{2.24}$$

Assuming that both sets of branching ratios follow *Dirg* distribution, *i.e.* $Dirg\,(B_1, B_3; \Delta B_1, \Delta B_3)$ and $Dirg(B_{11}, B_{12}; \Delta B_{11}, \Delta B_{12})$, respectively, the nested form of the overall distribution can be noted as

$$(b_1, b_2, b_3) \sim Dirg\,(B_1 \otimes Dirg(B_{11}, B_{12}; \Delta B_{11}, \Delta B_{12}), B_3; \Delta B_1, \Delta B_3) \tag{2.25}$$

where the $\otimes$ symbol is used to emphasize that the values sampled from the external *Dirg* distribution $Dirg\,(B_1, B_3; \Delta B_1, \Delta B_3)$ *do not* depend on the values sampled from the internal distribution $Dirg(B_{11}, B_{12}; \Delta B_{11}, \Delta B_{12})$. Practically, both sets of random numbers are sampled independently, and similar products to Eqs. 2.24 are performed to get the values of the final samples.

Plessis et al. (2010) showed that while involving large uncertainties, as is often the case for photolysis and dissociative recombination branching ratios, this nested distribution is remarkably different from

$$(b_1, b_2, b_3) \sim Dirg\,(\mu_1, \mu_2, \mu_3; u_1, u_2, u_3)\,, \tag{2.26}$$

i.e. the distribution of the branching ratios of a "one-level" scheme

$$\mathrm{I}^+ + \mathrm{e}^- \text{ or } \mathrm{R}{+}h\nu \longrightarrow \begin{cases} \xrightarrow{\mu_1 \pm u_1} \mathrm{M}_1 \\ \xrightarrow{\mu_2 \pm u_2} \mathrm{M}_2 \\ \xrightarrow{\mu_3 \pm u_3} \mathrm{M}_3 \end{cases} \tag{2.27}$$

with the same nominal values (μ_1, μ_2, μ_3) and the uncertainties (u_1, u_2, u_3) calculated from the two independent uncertainty sets ($\Delta B_1, \Delta B_3$) and ($\Delta B_{11}, \Delta B_{12}$) by combination of variances (see Section 2.3.1). This highlights the necessity of nesting, when we have different sources of information.

In the cases of incomplete measurements for branching ratios, the nested Dirichlet distributions can also implement partial knowledge into kinetic modeling: for instance, if no experimental data are available for (B_{11}, B_{12}) in Eq. 2.23, a *Diun* (2) can easily be used instead. This clearly illustrates the large flexibility of the nested Dirichlet distributions.

2.2.3 Wavelength-dependent representation for the photolysis branching ratios of CH_4

2.2.3.1 Probabilistic tree representation of the photolysis branching ratios of CH_4

As discussed in Chapter 1, CH_4 photolysis has a unique importance in Titan's photochemical models. However, up to now, reliable branching ratios of all major channels of CH_4 photolysis have been provided at only two wavelengths, *i.e.* 118.2 nm and 121.6 nm (Gans et al., 2011). To construct the representation of the branching ratios of all CH_4 photolysis channels and at all wavelengths

	Dissociation channel	Notation in models	Branching ratio at 121.6 nm	Branching ratio at 118.2 nm
(1)	$CH_3(X^2A_2'') + H$	CH_3	$\Phi(1) = 0.42 \pm 0.05$	$\Phi(1) = 0.26 \pm 0.04$
(2)	$CH_2(a^1A_1) + H_2$	$^1CH_2$	$\Phi(2) = 0.48 \pm 0.05$	$\Phi(2) + \Phi(3) = 0.17 \pm 0.05$
(3)	$CH_2(a^1A_1) + 2H$		$\Phi(3) \approx 0$	
(4)	$CH_2(b^1B_1) + H_2$	-	$\Phi(4) \approx 0$*	$\Phi(4) \approx 0$*
(5)	$CH_2(X^3B_1) + 2H$	$^3CH_2$	$\Phi(5) = 0.03 \pm 0.08$	$\Phi(5) = 0.48 \pm 0.06$
(6)	$CH(X^2\Pi) + H + H_2$	CH	$\Phi(6) = 0.071$**	$\Phi(6) = 0.097$**
(7)	$C(^1D) + 2H_2$	-	$\Phi(7) = 0 \pm 0.006$	$\Phi(7) = 0 \pm 0.006$

Table 2.1: New branching ratios for methane photolysis channels at 121.6 nm and 118.2 nm with $1\,\sigma$ standard uncertainties (Gans et al., 2011): * from Lee and Chiang (1983) and ** interpolated from Rebbert and Ausloos (1972/73).

where it occurs, we start with an analysis of Gans et al. (2011) branching ratio determination: only the relative productions among CH_3, $^1CH_2$ and $^3CH_2$ were measured in their experiments. An interpolation of the branching ratio of CH channel measured at ∼106 and 123.6 nm (Rebbert and Ausloos, 1972/73) was performed to estimate the branching ratio of CH $B_2(\lambda)$. The contribution of the other channels was shown to be negligible (see Tab. 2.1).

By analogy with the example scheme (Eq. 2.23) introduced in Section 2.2.2, the methane photolysis branching ratios, whose data stem from two independent measurements, should be represented at two levels, *i.e.*

$$CH_4 + h\nu(\lambda) \longrightarrow \begin{cases} \xrightarrow{B_1(\lambda)=1-B_2(\lambda)} \begin{cases} \xrightarrow{B_{11}(\lambda)} CH_3 + H \\ \xrightarrow{B_{12}(\lambda)} {}^1CH_2 + H_2 \\ \xrightarrow{B_{13}(\lambda)} {}^3CH_2 + 2H \end{cases} \\ \xrightarrow{B_2(\lambda)} CH + H_2 + H \end{cases} \tag{2.28}$$

where $B_i(\lambda)$ and $B_{ii}(\lambda)$ are uncertain wavelength-dependent probabilities such that

$$\begin{aligned} B_1(\lambda) \times B_{11}(\lambda) &= \Phi_\lambda(1) \\ B_1(\lambda) \times B_{12}(\lambda) &= \Phi_\lambda(2) + \Phi_\lambda(3) \\ B_1(\lambda) \times B_{13}(\lambda) &= \Phi_\lambda(5) \\ B_2(\lambda) &= \Phi_\lambda(6) \\ B_1(\lambda) + B_2(\lambda) &= 1 \\ B_{11}(\lambda) + B_{12}(\lambda) + B_{13}(\lambda) &= 1 \end{aligned} \tag{2.29}$$

where $\Phi_\lambda(1)$, $\Phi_\lambda(2)$, $\Phi_\lambda(3)$, $\Phi_\lambda(5)$ and $\Phi_\lambda(6)$ are respectively the measured branching ratios of the channels $CH_3(X^2A_2'') + H$, $CH_2(a^1A_1) + H_2$, $CH_2(a^1A_1) + 2H$, $CH_2(X^3B_1) + 2H$ and $CH(X^2\Pi) + H + H_2$ (see Tab. 2.1).

Note that Mebel et al. (1997) report that the $^1CH_2 + 2H$ channel is open below 121.3 nm. This channel was neglected in this wavelength-dependent scheme, because Mebel et al. (1997) find a significant energy barrier (∼30 kcal/mol) in the channel $CH_4\left(^1T_2\right) \longrightarrow {}^1CH_2 + 2H$ and consider it as the slowest channel of methane photolysis around Ly-α. However, the $^1CH_2 + 2H$ channel

λ / nm	Constraints on the branching ratios	Origin
100.0	$(B_{11}, B_{12}, B_{13}) \sim Diun(3)$	No data
106.0	$B_2 \sim \mathcal{N}\left(0.23, 0.03^2\right)$	Exp. data
118.2	$(B_{11}, B_{12}, B_{13}) \sim Dirw\left(48.80, 7.76; 118.76, 19.21\right)$	Exp. data
121.6	$(B_{11}, B_{12}, B_{13}) \sim Dirw\left(66.26, 13.05; 84.39, 1.89\right)$	Exp. data
123.6	$B_2 \sim \mathcal{N}\left(0.059, 0.005^2\right)$	Exp. data
135.6	$B_{13} = 0$	Thermo. threshold
136.9	$B_2 = 0$	Thermo. threshold
140.0	$(B_{11}, B_{12}) \sim Diun\left(2\right)$	No data

Table 2.2: Constraints on the wavelength-dependent probabilistic tree model of CH_4 photolysis branching ratios. $Diun\left(n\right)$ is the uniform Dirichlet distribution over the n-simplex; $Dirw(\alpha_1, \alpha_2; \beta_1, \beta_2)$ is the rigorous generalized Dirichlet distribution for three branching ratios and $\mathcal{N}\left(\mu, \sigma^2\right)$ is the normal distribution with mean μ and standard deviation σ.

should be taken into account in shorter-wavelength range, since this channel may start with a different excited state of CH_4. Also, for wavelengths below the ionization threshold of methane ($\lambda \simeq 80$ nm), this tree should be nested inside a tree accounting for the branching between ions and neutral products, derived from separate measurements of the total absorption cross section and the ionization cross-section. This extension of the probabilistic tree of CH_4 photolysis branching ratios will be detailed in Section 2.2.4.

2.2.3.2 A wavelength-dependent model of branching ratios

As mentioned in Chapter 1, the branching ratios of CH_3, $^1CH_2$ and $^3CH_2$ strongly differ at 121.6 nm and 118.2 nm. Unfortunately, with the lack of reliable measurements at other wavelengths, we can only extrapolate the evolution of these branching ratios between 100 nm (where N_2 starts to be the major absorbing species) and 140 nm (the absorption threshold of methane).

Previous studies (Zhang et al., 2010; Van Harrevelt, 2006) have shown that a conical intersection between two potential energy surfaces in the molecule could be responsible of dramatic changes in the photodissociation dynamics. In this case, the evolution of the branching ratios could exhibit some local drastic changes in such a way that extrapolation from the available sets of branching ratios at 121.6 nm and 118.2 nm is questionable. On the other hand, Lee and Chiang (1983) have measured the fluorescence yield of CH_2(b) produced by methane photolysis in the wavelength range between 106 nm and 142 nm. This measurement allowed them to deduce the branching ratio of the corresponding channel (Channel (4), $CH_2(b^1B_1) + H_2$, see Tab. 2.1). Their study presents a smooth increase of the branching ratio when the wavelength decreases from 142 nm to 102 nm. Although this channel is negligible when compared to the others, one assumes that a same kind of "smooth variation" can be expected for the other photodissociation channels.

These considerations were used to design an interpolation model of the branching ratios outside of the experimental measurements at 118.2 and 121.6 nm, by incorporating as many other constraints as possible.

Available data/constraints We present here all the data and constraints which were used in the design of the wavelength-dependent branching ratios model. A summary is provided in Tab. 2.2.

- The values and uncertainty for b_{CH} at $\sim$ 106 and 123.6 nm are obtained from Rebbert and

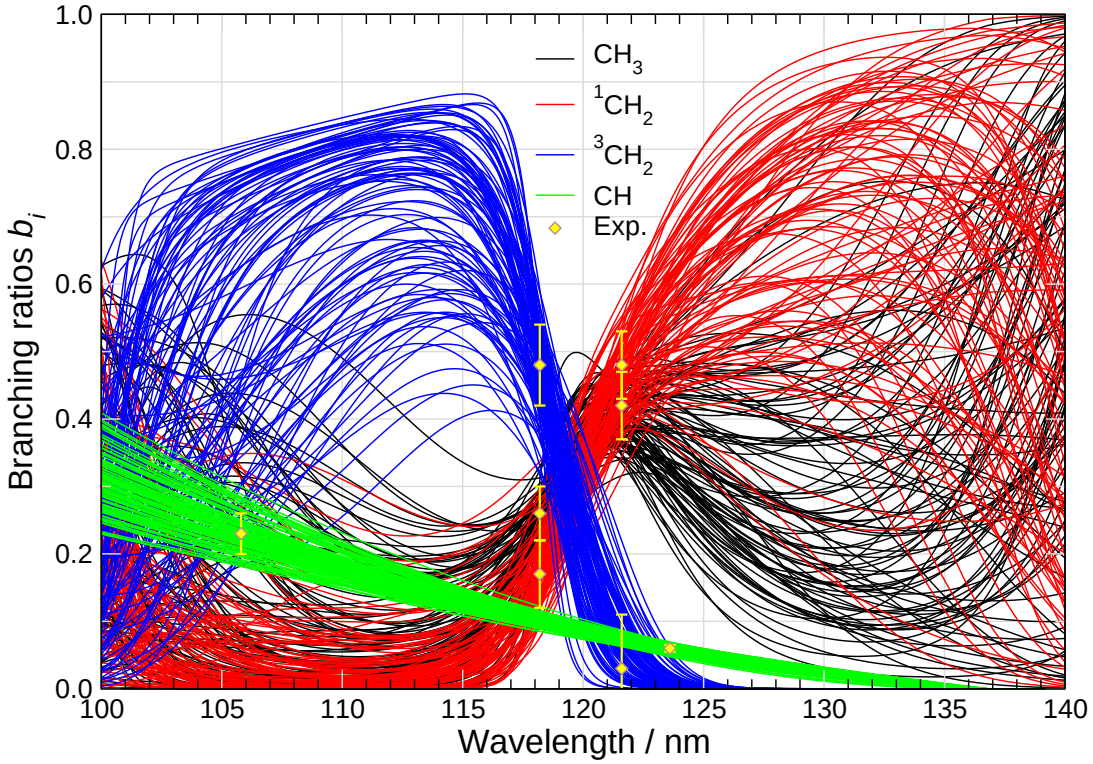

Figure 2.1: Sample of simulated wavelength-dependent branching ratios: (black) b_{CH_3}; (red) $b_{^1CH_2}$; (blue) $b_{^3CH_2}$; (green) b_{CH}. The experimental data are represented as yellow bullets with 1σ uncertainty bars.

Ausloos (1972/73), which report $b_{CH} = 0.059 \pm 0.005$ at $\lambda = 123.6$ nm and $b_{CH} = 0.23 \pm 0.03$ at $\lambda = 104.8 - 106.7$ nm. These data are used to build the normal distributions reported in Tab. 2.2.

- The thermodynamic threshold of the CH pathway is 136.9 nm (Mebel et al., 1997), where we assume that b_{CH} is null. Similarly, the threshold for $^3CH_2$ is 135.6 nm, from which upwards we impose $B_{13} = 0$. In practice, this branching ratio vanishes above 128 nm, and we do not have to use the constraint in the algorithm.

- The distributions for (B_{11}, B_{12}, B_{13}) at 121.6 and 118.2 nm have been designed from the experimental data of Gans et al. (2011), by the method of moments as described in Section 2.2.2.1.

- To account for the absence of knowledge for (B_{11}, B_{12}, B_{13}), we impose random constraints at the limits of the wavelength grid of interest through uniform Dirichlet distributions ($Diun$):

  - for $^1CH_2$ and CH_3 at 140 nm (below the thermodynamic threshold of $^3CH_2$): $(B_{11}, B_{12}) \sim Diun\,(2)$;
  - for $^1CH_2$, $^3CH_2$ and CH_3 at 100 nm: $(B_{11}, B_{12}, B_{13}) \sim Diun\,(3)$.

2.2.3.3 The interpolation model

In order to get a smooth model respecting the above constraints, we chose to use polynomial functions, designed in order to respect the structure/independence of the data sets. For the probabilistic tree (Eq. 2.28), the branching ratios at the two levels, (B_i) and (B_{1i}) are treated separately and finally combined using Eq. 2.29. For each level, one performs a five-stages process:

1. generate random sets of data by sampling the stochastic constraints in Tab. 2.2;
2. transform these to *logratios* (see below);
3. perform a polynomial interpolation (degree depending on number of data);
4. generate the values of the polynomial regression on the target wavelength grid;
5. back-transform the results from logratios to branching ratios.

Logratio transform for the generation of wavelength-dependent branching ratios. Any composition $(x_1, \cdots, x_n)$ with constraint $\sum_{i=1}^{n} x_i = 1$ can be transformed to $\mathbb{R}^n$ by using logratios. For instance, the centered logratio (clr) transform $(z_1, \cdots, z_n) = \mathrm{clr}\,(x_1, \cdots, x_n)$ is defined by $z_i = \ln(x_i/c)$, where $c = (\Pi_{i=1}^{n} x_i)^{1/n}$ is the geometric mean of the composition. The inverse transform (clrinv) is $x_i = \exp(z_i)/\sum_{j=1}^{n} \exp(z_j)$.

We present here the algorithm used to sample from the probabilistic tree model (Eq. 2.28).

1. Define the target wavelength grid $\{\lambda_j;\, j = 1, N_\lambda\}$.
2. To generate a sample of branching ratios curves on this grid, repeat the following sequence:
   (a) Generate a random curve $\{B_2(\lambda_j)\}$
      i. generate a triplet of values $\left(x^{(1)}, x^{(2)}, x^{(3)}\right)$ at the three reference wavelengths $\{105.8, 123.6, 136.9\}$ by sampling the corresponding distributions in Tab. 2.2
      ii. transform these values to logratios $\left(z^{(1)}, z^{(2)}, z^{(3)}\right)$ by clr
      iii. generate the quadratic interpolation of $\left(z^{(1)}, z^{(2)}, z^{(3)}\right)$ over the wavelength grid of interest $\{z(\lambda_j)\}$
      iv. for each point of the wavelength grid, back transform $\{z(\lambda_j)\}$ to get $B_2(\lambda_j)$.
   (b) Generate random curves for $(B_{11}(\lambda), B_{12}(\lambda), B_{13}(\lambda))$
      i. generate a quadruplet of compositions $\left\{\left(x_1^{(i)}, x_2^{(i)}, x_3^{(i)}\right);\, i = 1, 4\right\}$ at the reference wavelengths $\{110, 118.3, 121.6, 140\}$
      ii. for each reference wavelength i transform the composition values to logratios $\left(z_1^{(i)}, z_2^{(i)}, z_3^{(i)}\right) = \mathrm{clr}\left(x_1^{(i)}, x_2^{(i)}, x_3^{(i)}\right)$
      iii. for each pathway k, generate the cubic interpolation of $\left\{z_k^{(1)}, z_k^{(2)}, z_k^{(3)}, z_k^{(4)}\right\}$ over the wavelength grid of interest $\{z_k(\lambda_j)\}$
      iv. at each point of the target wavelength grid, back transform the logratios $(B_{11}(\lambda_j), B_{12}(\lambda_j), B_{13}(\lambda_j)) = \mathrm{clrinv}\,(z_1(\lambda_j), z_2(\lambda_j), z_3(\lambda_j))$

(c) For each point of the wavelength grid, combine the values of both levels of the tree

$$
\begin{aligned}
b_{\mathrm{CH_3}}(\lambda_j) &= B_{11}(\lambda_j) \times (1 - B_2(\lambda_j)) \\
b_{\mathrm{CH_{2(a)}}}(\lambda_j) &= B_{12}(\lambda_j) \times (1 - B_2(\lambda_j)) \\
b_{\mathrm{CH_{2(X)}}}(\lambda_j) &= B_{13}(\lambda_j) \times (1 - B_2(\lambda_j)) \\
b_{\mathrm{CH}}(\lambda_j) &= B_2(\lambda_j)
\end{aligned}
$$

This model assumes that the representative samples of the experimental data are uncorrelated. A set of curves generated from this model is displayed in Fig. 2.1. One can see that the specified constraints (experimental data, thresholds and boundary conditions) are properly accounted for by our construction method. Although it is not visible in this representation, for each element of the sample, the branching ratio curves form quadruplets with unit sum at all wavelengths.

This representation has been used for a neutral photochemical model (see Chapter 3).

2.2.4 Representation of photolysis branching ratios, including ionic channels

In Section 2.2.3, a neutral model for methane photolysis branching ratios was established. For the photochemical model of the APSIS experiments with ionizing photons as an energy source (see Chapter 5), we can no longer restrict to the database of neutral branching ratios, such as in Hébrard (2006); Gans et al. (2013). The construction of the representation of branching ratios of photolytic processes has to include ionic channels. This is true for all species involved in photolysis, not only methane.

A problem is the intricate source of the branching ratio data. The available data are composed of the nominal data and the corresponding uncertainties for neutral channels in Dobrijevic *et al.*'s neutral model (Hébrard, 2006), the SWRI nominal data for both neutral and ionic channels (Huebner and Link, 2011), and the novel probabilistic representation for the neutral channels of methane (see Section 2.2.3). There are overlaps between these data, and some contradictions as well. The representation for methane is the most appropriate among the 3 sources for the neutral channels of methane, but it includes no data for the ionic channels of methane photolysis. The SWRI data, only available for several intuitively important species, *i.e.* CH_4, N_2, H_2, C_2H_2, C_2H_4, C_2H_6 and HCN, are however convenient for use, especiallly for the ionic channels. Dobrijevic *et al.*'s data, available for a large variety of species and to which uncertainties were assigned, include no ionic pathways. The available data have been considered as follows:

- for the species without photoionization channel, nominal data in Dobrijevic *et al.*'s neutral model are applied, while corresponding uncertainties are taken from Hébrard (2006);

- for N_2, H_2, C_2H_2, C_2H_4, C_2H_6 and HCN, nominal data in the SWRI database are used, and uncertainties for neutral channels are also taken from Hébrard (2006), since there is no other recent and reliable recommendation up to now. However, ionic channels have no recommended uncertainty. Considering that there is generally a much higher precision for ion detection techniques than for neutrals or radicals, we express the channels in a nested scheme

to preserve as much uncertainty information as possible:

$$\mathrm{A} + \mathrm{h}\nu \longrightarrow \begin{cases} \xrightarrow{B_{neu}\left(1\pm\Delta B_{n/i}\right)} \begin{cases} \xrightarrow{B_{n1}(1\pm\Delta B_{n1})} \text{Neutral Channel 1} \\ \xrightarrow{B_{n2}(1\pm\Delta B_{n2})} \text{Neutral Channel 2} \\ \ldots\ldots \end{cases} \\ \xrightarrow{B_{ion}\left(1\pm\Delta B_{n/i}\right)} \begin{cases} \xrightarrow{B_{i1}(1\pm\Delta B_{i1})} \text{Ionic Channel 1} \\ \xrightarrow{B_{i2}(1\pm\Delta B_{i2})} \text{Ionic Channel 2} \\ \ldots\ldots \end{cases} \end{cases}$$

where A represent the species, B_{neu} and B_{ion} are respectively the total neutral and ionic contributions and both have a relative uncertainty of $\Delta B_{n/i}$. B_{n1}, B_{n2}... and B_{i1}, B_{i2}... are the branching ratios of the neutral channels and the ionic channels, respectively, and $\triangle B_{n1}$, $\triangle B_{n2}$... and $\triangle B_{i1}$, $\triangle B_{i2}$... are their corresponding relative uncertainties. For lack of data, we assume that the branching ratios of all ionic channels and their total contribution have a relative uncertainty of 20% and 3%, respectively, according to their typical values in the literature (Anicich, 1993).

- the representation of CH_4 is based on the same scheme. We apply the representation describes in Section 2.2.3 to its neutral part, nevertheless, in a form whose lower wavelength limit is extended to 80 nm, where the neutral channels become negligible according to their total contribution in the SWRI data, though the neutral channels in the SWRI database (Huebner and Link, 2011) and in the representation in Section 2.2.3 are not identical. The remaining part of this representation is the same as the previous case (see Fig. 2.2).

Additionally, we should preserve the correlation between wavelengths in a branching ratio sample, to ensure the continuity due to the interpolation and extrapolation (see Section 2.2.3) or of the branching ratio data for wavelength intervals (*e.g.* branching ratios provided in SWRI (Huebner and Link, 2011) or recommended in Hébrard (2006)).

However, the preservation of the correlation is difficult to achieve, since branching ratios are compositional data. Furthermore, we cannot perform the sampling by interpolation and extrapolation once again, because the available data for wavelength intervals are themselves continuous. We use then the generalized Dirichlet distribution (*Dirg*), which can be easily expressed by nominal values and uncertainties (see Section 2.2.2.1). To handle the problem of correlation in a wavelength interval during the sampling of a *Dirg* distribution, we adopt an *adhoc* technique: while generating the values at different wavelengths in the same sample, we always retain the same random seed, hence ensuring a full correlation (see examples in Fig. 2.2).

2.3 Uncertainty propagation

Uncertainty propagation enables to assess the effect of the uncertainty of input parameters on the predictions of a model. It has been long used in science and engineering and standardized by the "Bureau International des Poids et Mesures" (BIPM) in 2008 (BIPM et al., 2008; BIPM et al., 2008). Two categories of uncertainty propagation methods are defined: combination of variances and propagation of distributions.

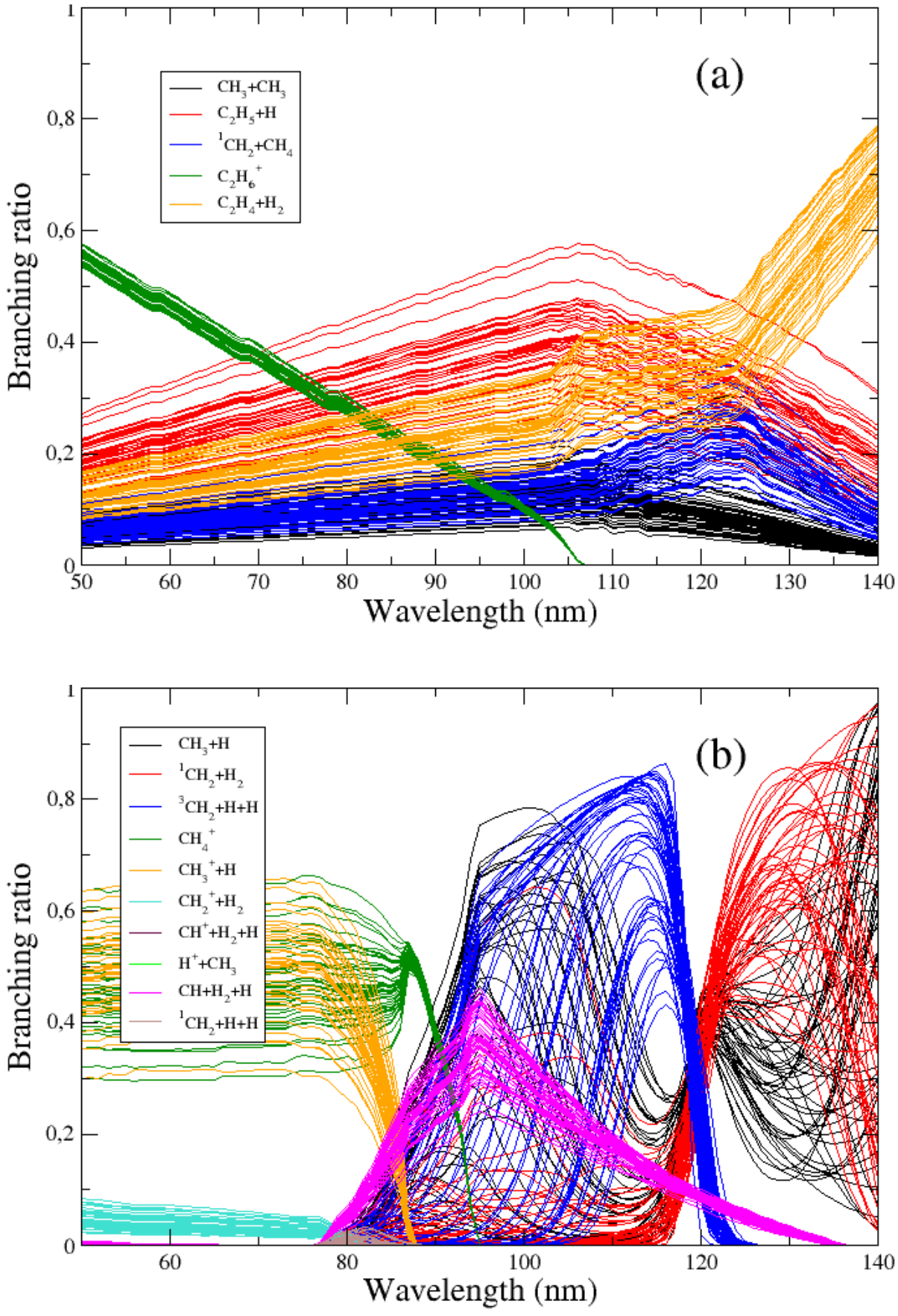

Figure 2.2: Subset (50 draws) of the samples of the photolysis branching ratios of (a) C_2H_6 and (b) CH_4.

2.3.1 Combination of variances

For linear models, the variance of an output Y, as a function of the inputs $(X_1, X_2, \cdots, X_n)$, *i.e.* $Y = f(X_1, X_2, \cdots, X_n)$, can be expressed by the formula of a linear combination of covariances (BIPM et al., 2008)

$$u_Y^2 = \sum_{i=1}^{n} \sum_{j=1}^{n} \left(\frac{\partial f}{\partial X_i} \right)_{\bar{X}_i} \left(\frac{\partial f}{\partial X_j} \right)_{\bar{X}_j} \operatorname{cov}(X_i, X_j) \tag{2.30}$$

where $\bar{X}_i$ is the mean of the ith input parameter X_i. The covariance between X_i and X_j, $\operatorname{cov}(X_i, X_j)$, measures either an input parameter's uncertainty (variance) $(i = j)$, or the uncertainties of two parameters as well as their correlation $(i \neq j)$.

$\left(\frac{\partial f}{\partial X_i} \right)_{\bar{X}_i}$, called the sensitivity coefficient, may be regarded as a scaling factor for the translation of the uncertainty on the input parameter X_i into the output.

In the case of independent input parameter, only the variances, $\operatorname{cov}(X_i, X_i), i = 1, 2, \cdots, n$, are non-zero, and Eq. 2.30 is simplified to

$$u_Y^2 = \sum_{i=1}^{n} \left(\frac{\partial f}{\partial X_i} \right)_{\bar{X}_i}^2 \operatorname{Var}(X_i) \tag{2.31}$$

where each input parameter's contribution to the output uncertainty, $\left(\frac{\partial f}{\partial X_i} \right)_{\bar{X}_i}^2 \operatorname{Var}(X_i)$, is more clearly revealed.

The formula of a linear combination of covariances (Eq. 2.30) is actually a first-order cut-off of the Taylor expansion of the variance of functions of random variables. This first-order (linear) approximation is valid only if the relative uncertainties of random variables are small (typically less than 30%). However, in photochemical models, relative uncertainties on the kinetic parameters are often larger than 100%, which enables the parameters to explore the non-linear behavior of the kinetic model. In these cases, we use the propagation of distributions more commonly, to evaluate the output uncertainty.

2.3.2 Propagation of distributions: the Monte Carlo method

The formula of the propagation of distributions (BIPM et al., 2008)

$$p(Y = y) = \int \mathrm{d}X_1 \mathrm{d}X_2 \cdots \mathrm{d}X_n p(X_1, X_2, \cdots, X_n) \, \delta(y - f(X_1, X_2, \cdots, X_n)) \tag{2.32}$$

provides a transformation from the joint probability density function of all input parameters to that of the output $Y = f(X_1, X_2, \cdots, X_n)$. With the probability density function known, we can compute various quantities relative to the output, including the uncertainty.

It is rarely possible to perform the integration above analytically. Instead, the BIPM recommends the use of Monte Carlo Uncertainty Propagation (MCUP) methods, through which we propagate representative samples of the inputs distributions, rather than the analytic distributions themselves. We generate a large number of random sets of input parameters according to their probability density function, and then, for each set, evaluate the corresponding output samples in the model. All evaluated output samples form, as a whole, a representation of the output distributions.

The MCUP methods are convenient to treat models with many inputs and outputs. Their sample size does not depend on the number of input parameters. Moreover, they are directly applicable

to multi-output models, through a single set of samples. As a result, the correlation between the outputs is preserved.

However, the MCUP methods are usually expensive in computer time, due to the repeated running of the model over a large number of samples, necessary for a significant statistics.

2.4 Sensitivity analysis

Sensitivity analysis is commonly defined as *the apportionment of output variance between the uncertain inputs* (Saltelli et al., 2000, 2004).

In a linear model with independent inputs, the output variance is a simple combination of the input variances (Eq. 2.31), which directly shows the contribution of each input to the output variance. Although, in Titan photochemical model, large uncertainties on the kinetic parameters bring about the non-linear behavior of the output samples (Dobrijevic et al., 2008), a sensitivity analysis based on Eq. 2.31 provides a first glance at the composition of the uncertainty of the output, neglecting the complicated interactions between the inputs (see Chapter 5).

For the sensitivity analysis of very complex models, it is convenient to calculate the correlation coefficients between the inputs and the outputs. Calculation of the correlation coefficients recycles the samples used for the Monte Carlo uncertainty propagation.

Pearson's correlation coefficient between one of the inputs, X_i, and the output $Y = f(X_1, X_2, \cdots, X_n)$ is

$$r_{X_i,Y} = \frac{\operatorname{cov}(X_i, Y)}{\sqrt{\operatorname{Var}(X_i)\operatorname{Var}(Y)}} \tag{2.33}$$

It is demonstrated that in a linear model with independent inputs, the square of the correlation coefficient is approximately X_i's relative contribution to the variance of the output Y (Saltelli et al., 2005), *i.e.*

$$r^2_{X_i,Y} \simeq \frac{\left(\frac{\partial f}{\partial X_i}\right)^2_{\bar{X}_i} \operatorname{Var}(X_i)}{\operatorname{Var}(Y)} \tag{2.34}$$

This relation shows the interest of correlation coefficients in sensitivity analysis and will be used in Chapter 5.

It has been recommended to use Spearman's rank correlation coefficients instead of Pearson's linear correlation coefficients for non-linear models (Helton et al., 2006). Although, practically, only minor differences between the two types of correlation coefficients have been observed in the sensitivity analysis of chemical networks (Wakelam et al., 2010), we use Spearman's rank correlation coefficients. The above formulae are then transposed to the ranks of the variables.

Not all types of samples can be well treated by correlation coefficients in sensitivity analysis. For example, variables of a non-linear relation are often little correlated around an extremum, and correlation coefficients can hardly analyze multimodal samples properly, *etc.* Nevertheless, we check that in general, these cases are not common in the photochemical model of Titan. It is safe to use correlation coefficients for sensitivity analysis in this study.

Other estimators of sensitivity, for instance Sobol' sensitivity index (Sobol, 1990), are not applied, due to too expensive calculation time for Titan's photochemical model.

In this study, we perform sensitivity analysis essentially for the identification of *key reactions*. Wakelam et al. (2010) defined key reactions as the reactions that contribute significantly to the model output uncertainty. In view of the importance of both sensivity coefficients $\left(\frac{\partial f}{\partial X_i}\right)_{\bar{X}_i}$ and

input uncertainties in sensivity analysis, as revealed by Eq. 2.31, key reactions can be regarded as the following ones:

- reactions that have a strong effect on the mass flux in a reaction network;
- or reactions with a rate constant in need of further study to improve the prediction precision of model outputs;
- or both.

2.5 Generation of theoretical mass spectra from species concentrations

The mass spectra measured by Cassini INMS are of great importance in the analysis of the composition of Titan's upper atmosphere. In the modeling study, we want to compare the INMS mass spectra with those that we simulate.

The intensity, I_j, of a mass peak at m/z j is modeled by (Puccio and Miller, 2010)

$$I_j = \sum_i \sigma_i c_i f_{ij}, \quad j = 1, 2, \cdots, n \tag{2.35}$$

where σ_i and c_i are respectively the electron impact cross-section and the concentration of the ith species. f_{ij} is the fragmentation pattern of the ith species at m/z j. j can be any integer mass between 1 and n, the maximal mass, with the same mass resolution as the INMS mass spectra, *i.e.* 1 u.

Since the simulated mass spectra are functions of the species concentration, they are generated by Monte Carlo uncertainty propagation using concentration samples. In detail, the generation of the neutral MS is performed according to the following steps:

1. Estimate the electron impact cross-section of each species by the formula proposed by Puccio and Miller (2010)

   $$\sigma_i = 2.019w + 0.460x + 1.086y + 1.348z \tag{2.36}$$

   where the cross-section of the ith species σ_i is in Å^2, and x, y, z and w are respectively the C, H, N and O atom number of the species.

2. Extract and normalize the fragmentation patterns of the species from the NIST Chemistry Webbook (`http://webbook.nist.gov/chemistry/`). The fragmentation pattern of the ith species is denoted as $(f_{i1}, f_{i2}, \cdots, f_{in})$, with the constraint $\sum_{j=1}^{n} f_{ij} = 1$. The NIST database provides the fragmentation data of almost all stable species up to 6 heavy (C, N or O) atoms and some heavier species, well covering the stable species of interest in this study. However, it provides no radical fragmentation data and there are very few data of this type in the literature. Thus, we chose to exclude completely the radicals from the MS, *i.e.*

   $$(f_{i1}, f_{i2}, \cdots, f_{in}) = (0, 0, \cdots, 0), \quad i = \text{radical} \tag{2.37}$$

3. Average the fragmentation patterns of isomers, if the isomers are not distinguished in the model. For example, C_3H_6 represents both propene and cyclopropane. Thus, their fragmentation patterns are averaged with equal weights.

4. Perform the Monte Carlo loop by calculating the kth *sample* of the intensities $I_j^{(k)}$, (j = 1,2,$\cdots, n$; $k = 1, 2, \cdots, m$) at different m/z from the kth of m *samples* of the species concentrations $c_i^{(k)}$ by

$$I_j^{(k)} = \sum_i \sigma_i c_i^{(k)} f_{ij}, \quad j = 1, 2, \cdots, n;\ k = 1, 2, \cdots, m \tag{2.38}$$

5. Normalize, within *each set of samples*, the intensities with respect to that at m/z 28 (molecular ion signal of N_2, the most abundant species), for comparison with the INMS (or other experimental) mass spectra.

6. Generate statistics on the samples of the normalized intensities to obtain the distributions and relative quantities of the simulated MS.

Note that the estimated electron impact cross-sections and the NIST fragmentation patterns are actually uncertain. However, compared to the relative uncertainties on the kinetic parameters and the concentrations (often larger than 100%), their relative uncertainties (∼10% (Puccio and Miller, 2010)) are negligible. Therefore, they are considered as constants in the procedure above.

There are some sources of bias: for instance, the INMS and the NIST standard MS were measured at very different pressures, which may significantly influence the fragmentation patterns (see discussion in Chapter 4); different instruments may overlap the major peaks (*e.g.* m/z 28) with neighboring peaks in different ways, interfering in the determination of the intensities of neighboring minor peaks. These are difficult to quantify, thus not included in the generation of the simulated MS. Nevertheless, they will still be taken into account in the discussions (see Chapters 4 and 5).

Chapter 3

Impact of the uncertain photolysis parameters on Titan's photochemical modeling

Contents

As discussed in Chapter 1, photolysis has been shown to be responsible for an important part of the uncertainty on the predicted densities of numerous compounds in Titan's upper atmosphere (Hébrard et al., 2009; Peng et al., 2010). The calculation of the photolysis rate of a compound i is based on the absorption cross-section $\sigma_i^a(\lambda)$ and the incident light flux at every level in the atmosphere, $I_\lambda(z)$. For a solar zenith angle of 0°, the photolysis rate constant $J_i(z)$ of an absorbing species is modeled in the parallel plane approximation by

$$J_i(z) = \int_0^\infty \mathrm{d}\lambda \, I_\lambda(z) \sigma_i^a(\lambda) \tag{3.1}$$

$$I_\lambda(z) = I_\lambda^\infty \exp\left[-\tau(\lambda, z)\right] \tag{3.2}$$

$$\tau(\lambda, z) = \sum_i \sigma_i^a(\lambda) \int_z^{z_{top}} \mathrm{d}z' \, c_i(z') \tag{3.3}$$

where $c_i(z)$ is the density profile of species i, $\tau(\lambda, z)$ is the optical depth, and I_λ^∞ is the photon flux at the top of the atmosphere (altitude z_{top}).

In this model, the sources of uncertainty for $J_i(z)$ are the values of the absorption cross section $\sigma_i^a(\lambda)$, the photon flux at the top of the atmosphere I_λ^∞ , and the absorbing species density profile $c_i(z)$. As the latter depends itself on the photolysis rate constant, it is difficult to assess its impact without an extensive investigation. This work had been postponed in previous studies on the effects of chemical uncertainties in Titan's photochemistry (Hébrard et al., 2007; Dobrijevic et al., 2008; Hébrard et al., 2009; Peng et al., 2010), which used an approximate treatment of photolysis rate constants uncertainty: a constant uncertainty factor was assigned to each photolysis pathway, corresponding to the uncertainty at the top of the atmosphere. This treatment assumes that the uncertainty factor does not depend on the altitude and that all channels are independent. However, the photolysis channels of the same species should be correlated and have sum-to-one branching ratios (Carrasco and Pernot, 2007).

In this chapter, we revisit this approximation through a separate representation of uncertain photolysis cross-sections and branching ratios. These two types of parameters are investigated *successively*:

- In Part 1 (Section 3.1), we model explicitly the uncertainty of the photolysis rate, as a function of altitude, due to the uncertainty on the photolysis cross-sections. This study has been published in Peng, Cailliez, Dobrijevic, and Pernot (2012).

- In Part 2 (Section 3.2), we consider the impact of the new representation of methane photolysis branching ratios (see Section 2.2.3), including new data obtained by (Gans et al., 2011). This study has been published in Gans, Peng, Carrasco, Gauyacq, Lebonnois, and Pernot (2013).

In Titan's photochemical models, large uncertainties on other kinetic parameters (rate constants of neutral bimolecular and trimolecular reactions, cross-sections and branching ratios of ionic reactions *etc.*) may complicate the studies by blurring the effects of the uncertain photolysis parameters. To highlight their impacts, we studied these two cases with only uncertain photolysis cross-sections (Part 1) and uncertain photolysis branching ratios (Part 2), respectively. The possible interactions between these two types of parameters are also discussed.

3.1 Photoabsorption cross-sections

We first focus on the effects of uncertain photoabsorption cross-sections by explicitly computing photolysis rates, $J_i(z)$, and their altitude-dependent uncertainty factors, $F_{J_i}(z)$, in a 1D radiative transfer model (see Section 2.1.1). The uncertainty propagation is realized by Monte Carlo sampling of uncertain cross-sections, but not that of stationary species concentrations, since the present model is only a radiative transfer model, but not a reaction-transport model. The results for the main species N_2 and CH_4 are presented and discussed in Section 3.1.2. We provide an analytic model to interpret these results in Section 3.1.3.

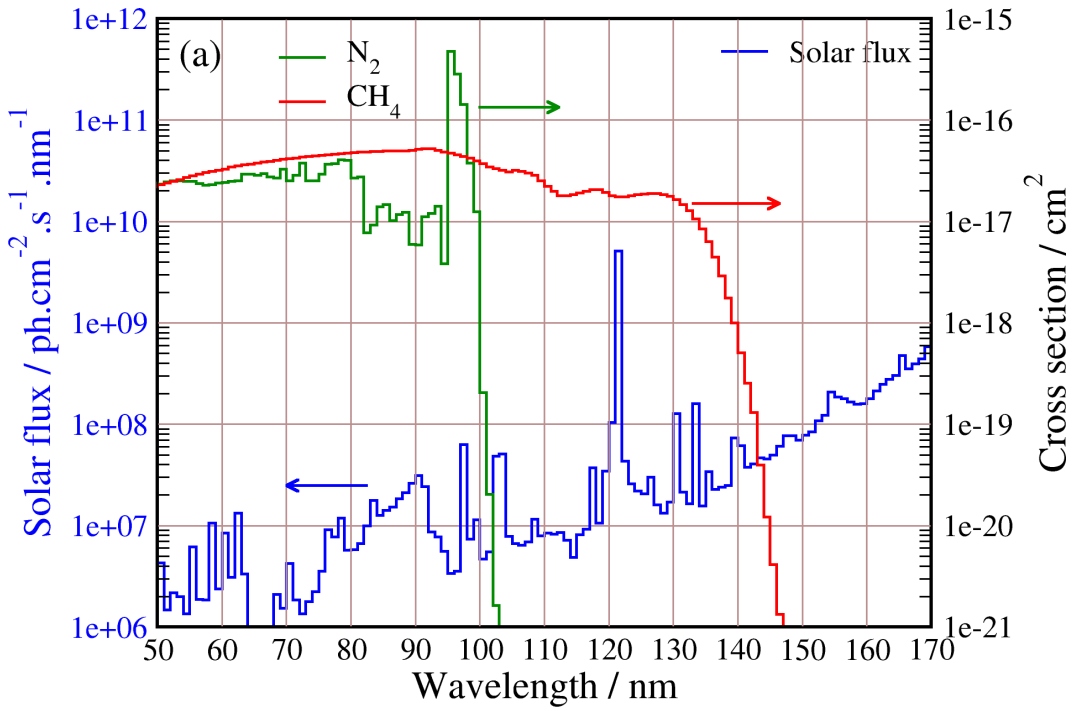

Figure 3.1: Cross-sections for N_2 (green line) and CH_4 (red line) (right scale) and the incident solar flux I_λ^∞ (blue line; left scale).

3.1.1 Uncertainties on photolysis cross-sections

For the species considered here, the uncertainty in cross-section values at a given wavelength results mainly from the discrepancy between different datasets and from temperature effects (Chen and Wu, 2004; Hébrard, 2006). In comparison, the random errors within each dataset are marginal. Thus, for a given species, only the strongly correlated (systematic) uncertainties of the cross-section at different wavelengths are taken into account.

Considering that there is typically not enough information in the literature to define a wavelength-dependent uncertainty factor, we adopt here a representation with full inter-wavelength correlation, by using a wavelength-independent uncertainty factor F_{σ_i} for the species i, to account for this dominant systematic error. In the Monte Carlo Uncertainty Propagation (see Section 2.3.2), random samples of the cross-section are obtained through

$$\ln \sigma_i(\lambda) = \ln \sigma_i^0(\lambda) + \epsilon_i, \tag{3.4}$$

where we use for all wavelengths the same random number ϵ_i, sampled from a normal distribution with mean zero and standard deviation $\ln F_{\sigma_i}$. The photolysis rate constants are calculated for each point in the sample and stored for statistical analysis.

The reference cross-sections for N_2 and CH_4 are plotted in Fig. 3.1(a). The values were respectively extracted from the SWRI database (Huebner and Link, 2011) and updated from Hébrard (2006), using references Clark (1952); Huffman et al. (1963); Huffman (1969); Cook and Metzger (1964); Samson and Cairns (1964); Huber et al. (1993); Chan et al. (1993). Interpolation and integration were performed to adapt the data to the spectral resolution of 1 nm.

For all the cross-sections (35 species), we used the uncertainty factors recommended by Hébrard (2006), notably $F_{\sigma_{N_2}} = 1.2$ and $F_{\sigma_{CH_4}} = 1.15$.

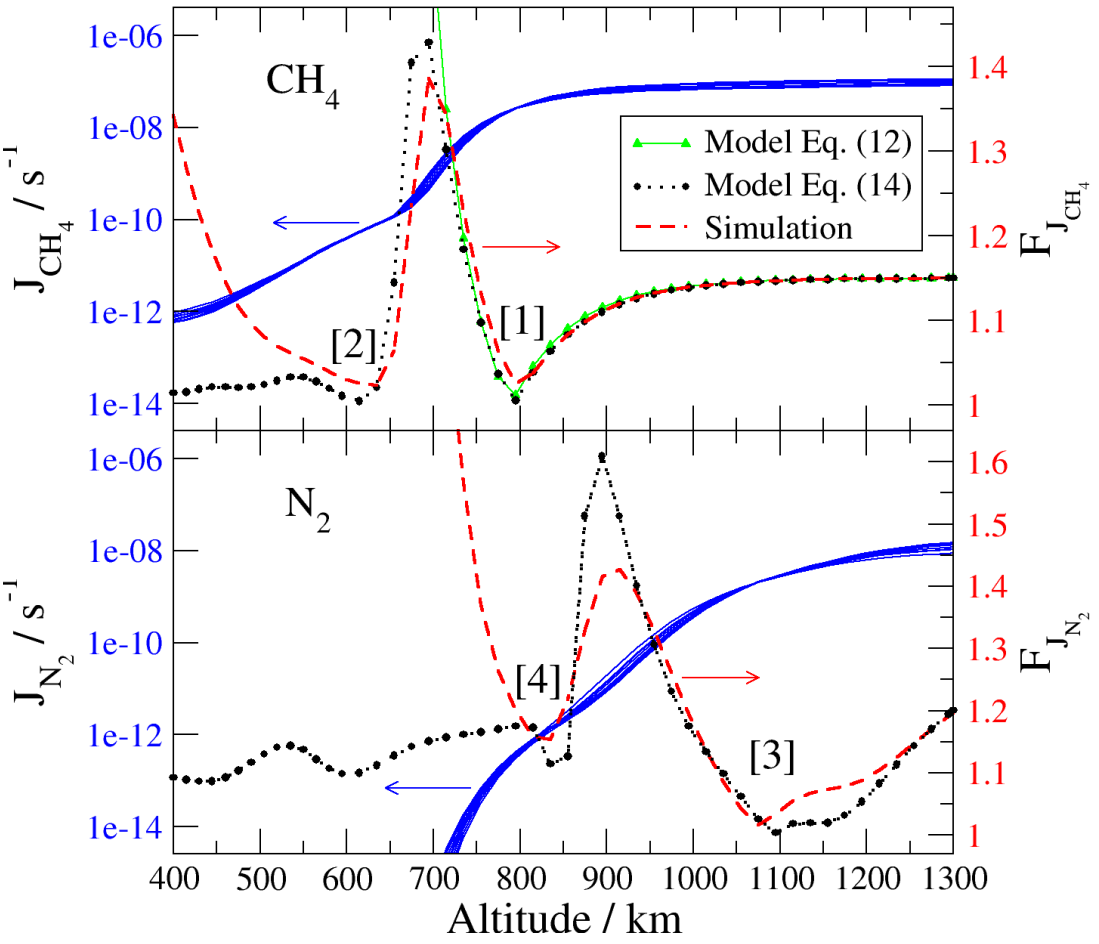

Figure 3.2: Samples of altitude-dependent photolysis rate coefficients for N_2 and CH_4 (blue full lines; left scale) and the corresponding uncertainty factors (dashed red line; right scale). Analytical uncertainty factors calculated by Eq. 3.13 (green curve and triangles) and Eq. 3.14 (black dotted line and circles) are reported for comparison with the simulation results. The main features of interest (Null Variance Altitudes) are numbered in square brackets.

3.1.2 Altitude variation of photolysis rate uncertainty coefficient

Using the Monte Carlo Uncertainty Propagation, we generated an output sample of 1000 photolysis rate coefficients $J_i(z)$ for all absorbing species in the model, from which we evaluated the corresponding $F_{J_i}(z)$. We focus in the following on $F_{J_{N_2}}(z)$ and $F_{J_{CH_4}}(z)$, which present marked structures, which is not the case for the minor species.

A subset of photolysis rate constant profiles is shown in Fig. 3.2 (blue lines), along with the uncertainty factors resulting from the full sample (red-dashed line). In the present study, we focus on the dispersion of the rate coefficient curves, and its variation with altitude. This dispersion is not uniform: for N_2, we observe neatly localized curve crossings, slightly below 1100 km [3] and above 800 km [4]; and for CH_4, a similar curve crossing occurs around 800 km [1], and a less localized one occurs between 550 and 650 km [2]. Code numbers in square brackets have been attributed to these four features (Fig. 3.2) for reference in the following discussions.

These features are reflected in the dips observed in the altitude-dependent uncertainty factors (Fig. 3.2). For N_2, starting at the top of the atmosphere, the uncertainty factor decreases from its asymptotic value $F_{J_{N_2}}(z_u) = 1.2$, to a very small value $F_{J_{N_2}}(1070) \simeq 1.02$, then increases to peak value $F_{J_{N_2}}(930) \simeq 1.44$, and decreases again to a value slightly smaller than the asymptotic

uncertainty $F_{J_{N_2}}(825) \simeq 1.16$. At lower altitudes, the uncertainty factor diverges because of the vanishing photon flux at the wavelengths absorbed by N_2. A similar scenario, albeit shifted to lower altitudes, is observed for CH_4.

To our knowledge, the existence of specific altitudes with vanishing uncertainty on the photolysis rate constants has not been reported before. As this concerns the major absorbers in the atmosphere and might be of interest for the uncertainty budget of photochemical models, we focused on these features in the next section.

3.1.3 The origins of null/low variance altitudes

To understand the origins of these features, we build analytical models of $F_J(z)$ for the main species N_2 and CH_4, which can be considered to be barometrically distributed.

3.1.3.1 Single-species/monochromatic case

Let us consider a chemical species with barometric distribution of concentration

$$c(z) = c_0 \exp\left(-\frac{z}{H}\right) \tag{3.5}$$

where c_0 is the concentration at the surface, $H = k_B T/mg$ is the scale height, m is the molecular mass of the species (in kg), g is the (constant) gravitational acceleration (in m.s^{-2}), k_B is the Boltzmann constant (in J.K^{-1}) and T is the temperature (in K).

Considering a monochromatic illumination and assuming the absence of additional extinction processes, the photolysis rate constant can be expressed as a function of the optical depth as

$$J(z;\sigma) = \sigma I^{\infty} \exp\left(-\tau(z;\sigma)\right), \tag{3.6}$$

where

$$\tau(z;\sigma) = \sigma c_0 H \exp\left(-\frac{z}{H}\right). \tag{3.7}$$

The uncertainty on the photolysis rate constant due to an uncertain absorption cross-section can be estimated by standard variance propagation (see Section 2.3)

$$u_J(z) = \sqrt{\left(\frac{\partial J}{\partial \sigma}\right)^2_{\sigma=\bar{\sigma}} u_\sigma^2} \tag{3.8}$$

$$= u_\sigma I^{\infty} \exp\left(-\tau(z;\overline{\sigma})\right) \left|1 - \tau(z;\overline{\sigma})\right| \tag{3.9}$$

where $\overline{\sigma}$ is the mean value of the cross-section and u_σ its standard uncertainty. We see that the uncertainty/variance of the photolysis rate constant can be null when $\tau(z;\overline{\sigma}) = 1$, *i.e.* at a specific altitude defined by

$$z_0 = H \ln(\overline{\sigma} c_0 H). \tag{3.10}$$

This altitude is referred to as Null Variance Altitude (NVA) throughout the text. The NVA, z_0, is also the altitude where the photolysis rate

$$v(z;\sigma) = \sigma I^{\infty} c_0 \exp\left(-\tau(z;\sigma) - \frac{z}{H}\right) \tag{3.11}$$

reaches its maximum. We can thus expect it to contribute significantly to a reduction of uncertainty in the predictions of the photochemical model.

The expression of the uncertainty factor for the photolysis rate constant as a function of altitude is obtained in compact form

$$F_J(z) = \exp\left[u_{\log J}(z)\right] \tag{3.12}$$

$$= F_\sigma{}^{|1-\tau(z;\overline{\sigma})|}. \tag{3.13}$$

Remarks

- as $\tau(z;\overline{\sigma})$ increases monotonically from the top of the atmosphere to values eventually larger than one at lower altitudes, one can expect a barometrically distributed species to present a single NVA in the case of monochromatic photolysis.
- the presence of a NVA derive from the barometric law. No such feature could occur, for instance, in an experimental photoreactor with a uniform (nearly uniform) concentration of the absorbing species: a uniform concentration, equivalent to a barometrically distributed one with an infinitely large scale height H, makes the NVA meaningless. However, a barometric distribution is not strictly necessary for the existence of a NVA. In theory, it occurs just at the altitude where the optical depth is equal to 1. At this altitude, there is always a "local" scale height that is not extremely large, as long as the distribution is not greatly different from a barometric one. The density distribution above the NVA can only affect its position, but not its existence.
- the NVA feature is preserved for solar zenith angles χ smaller than 75° (see *e.g. Kostov and Velinov (2001)*): in that case, we can replace σ by $\sigma \sec\chi$ in the formulae, which would affect only the actual location of the NVA. For larger values of solar zenith angles, the present radiative transfer model, based on the parallel-planes approximation becomes inadequate.

The present model applies also directly to the case of *polychromatic irradiation of a species with a wavelength-independent cross-section*, the only difference being that I^∞ becomes the integrated photon flux at the top of the atmosphere, *i.e.* $I^\infty = \int_0^\infty I_\lambda^\infty \mathrm{d}\lambda$. This approximation represents well CH_4, which has a rather flat absorption band in the Ly-α region (Fig. 3.1), explaining NVA [1] (Feature [1] in Fig. 3.2) at $z \simeq 800\,\mathrm{km}$. The values of $F_{J_{CH_4}}(z)$ obtained by the analytical model (Eq. 3.13) are reported in Fig. 3.2 and compared with simulation results. For NVA [1], and despite major approximations, the model is in quantitative agreement with the Monte Carlo simulation uncertainty factors. However, this model is unable to explain the features observed for CH_4 below 700 km.

If one plots the wavelength-dependent unity optical depth ($\tau(z;\overline{\sigma}(\lambda)) = 1$) for N_2 and CH_4 (Fig. 3.3), one sees that it covers a wide range of altitudes with marked flat regions as a function of wavelength. Except for the highest CH_4 NVA [1], as shown above, it is therefore not straightforward to use the previous model, developped for a single species in the monochromatic case, to interpret all the features in the $F_{J_i}(z)$ curves. In consequence, we consider now more complete models.

3.1.3.2 Single-species/polychromatic case

If we remain in the context of the barometric distribution, a major approximation in the previous model is the monochromatic illumination hypothesis. It can be generalized to the polychromatic

case (see details in Algorithm 3.2), where the uncertainty factor of the photolysis rate constant is found to be

$$F_J(z) \quad = \quad F_\sigma^{\left|1-\int_0^\infty \left[J_\lambda(z;\bar{\sigma})/\bar{J}(z)\right]\tau(z;\bar{\sigma}(\lambda))\mathrm{d}\lambda\right|}, \tag{3.14}$$

where $J_\lambda(z;\bar{\sigma}(\lambda))$ is the photolysis rate constant at wavelength λ. The integral term can be seen as a weighted average optical depth with weights being the relative photolysis rate constant. In the monochromatic case, one recovers the optical depth. For the considered species, the optical depth at all wavelengths below 140 nm goes from 0 to values larger than 1 as the altitude decreases to 500 km (Fig. 3.3). The integral in Eq. 3.14 must therefore be equal to 1 somewhere within this range. NVAs should therefore also be observed in the polychromatic case.

Results of Eq. 3.14 for CH_4 and N_2 are shown in Fig. 3.2. For both species this model recovers the main features of the uncertainty factor curves, notably two NVAs at different altitudes, separated by a marked maximum with an uncertainty factor exceeding the value at the top of the atmosphere. Below the second minimum, the model and simulation results diverge. This is due to the fact that the simulation involves minor species absorbing at the lower altitudes, which causes the photolysis rates of CH_4 and N_2 to drop rapidly and therefore their relative uncertainty to increase also rapidly. These minor species are not accounted for in Eq. 3.14 and the major species remain major absorbers at low altitudes, despite their very small cross-sections at the wavelengths which are still available at these altitudes.

3.1.3.3 Multiple-species/monochromatic case

At the deeper minimal variance altitude for N_2, NVA [4], the uncertainty factor of the photolysis rate constant is significantly larger than 1, in contradiction with the monospecies models. Indeed N_2, as its cross-section drops rapidly around 100 nm, loses its predominance as an absorber in this wavelength range. In order to find the uncertainty source at this location, it is necessary to introduce a n-species system (Algorithm 3.2), in which the uncertainty factor of a species photolysis rate constant is

$$F_{J_i}(z) \quad \simeq \quad 1 + \sqrt{\left(1-\tau(z;\sigma_i)\right)^2 \left(F_{\sigma_i}-1\right)^2 + \sum_{j=1,j\neq i}^{n} \tau(z;\sigma_j)^2 \left(F_{\sigma_j}-1\right)^2}. \tag{3.27}$$

Note that under the radical sign, only the first term (also present in the monospecies models) could vanish, while the second term always increases with the optical depth. We can thus expect that competition of absorbers in a wavelength range prevents the existence of a "perfect" NVA. For notation simplicity, this structure will improperly be referred to as a NVA in the following.

3.1.4 Interpretation of the simulation results with the analytical models

The structure of the $F_{J_i}(z)$ curves in Fig. 3.2 has been related to the location of unity optical depth for N_2 and CH_4. The results of the analytical models derived in the previous section are compared with the Monte Carlo results in (Fig. 3.2). They are mostly in quantitative agreement, notably for the location of NVAs, although some discrepancies are observed for the most spectrally complex regions, such as for NVA [3].

We propose here to summarize these observations and their interpretation on the basis of the

Algorithm 3.1 Derivation of the uncertainty factor of polychromatic photolysis rate constant.

Let us consider photolysis rate constant $J(z)$ of a species under a polychromatic illumination

$$J(z) = \int_0^\infty \sigma(\lambda) I_\lambda^\infty \exp\left(-\tau(z;\sigma(\lambda))\right) \mathrm{d}\lambda \tag{3.15}$$

$$= \int_0^\infty J_\lambda(z;\sigma) \mathrm{d}\lambda \tag{3.16}$$

where $J_\lambda(z;\sigma) = \sigma(\lambda) I_\lambda^\infty \exp\left(-\tau(z;\sigma(\lambda))\right)$ is the photolysis rate constant at the wavelength λ. The polychromatic photolysis rate constant can be easily reexpressed as a discrete sum

$$J(z) = \lim_{n\to\infty} \sum_{i=1}^{n_\lambda} J_\lambda(z;\sigma(\lambda_i)) \Delta\lambda_i, \tag{3.17}$$

where $\lambda_1 = 0$, $\lambda_n = \infty$ and $\Delta\lambda_i = \lambda_{i+1} - \lambda_i$. Then, one can estimate the uncertainty on the photolysis rate constant $u_J(z)$ by the following variance combination expression

$$u_J(z)^2 = \lim_{n\to\infty} \sum_{i=1}^{n_\lambda} \sum_{j=1}^{n_\lambda} \left(\frac{\partial J(z)}{\partial \sigma(\lambda_i)} \frac{\partial J(z)}{\partial \sigma(\lambda_j)} \right)_{\sigma=\overline{\sigma}} \mathrm{cov}\left(\sigma(\lambda_\mathrm{i}), \sigma(\lambda_\mathrm{j})\right), \tag{3.18}$$

where $\bar{\sigma}(\lambda_i)\,(i = 1, 2, \ldots, n)$ is the mean value of the cross-section at λ_i. Note that we use the same multiplicative error for all cross-section, which are thus fully linearly correlated, *i.e.*

$$\mathrm{cov}\left(\sigma(\lambda_i), \sigma(\lambda_j)\right) = u_\sigma(\lambda_i) u_\sigma(\lambda_j) \tag{3.19}$$

$$\simeq \bar{\sigma}(\lambda_i) \bar{\sigma}(\lambda_j) r_\sigma^2, \tag{3.20}$$

where $u_\sigma(\lambda_i)$ is the uncertainty on the cross-section at λ_i and r_σ is the unique relative uncertainty. With the aid of the relation above, one can simplify the expression of $u_J(z)^2$

$$u_J(z)^2 = r_\sigma^2 \lim_{n\to\infty} \sum_{i=1}^{n} \frac{\bar{\sigma}(\lambda_i) \partial J(z)}{\partial \sigma(\lambda_i)} \sum_{j=1}^{n} \frac{\bar{\sigma}(\lambda_j) \partial J(z)}{\partial \sigma(\lambda_j)} \tag{3.21}$$

$$= r_\sigma^2 \lim_{n\to\infty} \left[\sum_{i=1}^{n} \frac{\bar{\sigma}(\lambda_i) \partial J(z)}{\partial \sigma(\lambda_i)} \right]^2 \tag{3.22}$$

$$= r_\sigma^2 \lim_{n\to\infty} \left[\sum_{i=1}^{n} \bar{\sigma}(\lambda_i) I_\lambda^\infty \exp\left(-\tau(z;\bar{\sigma}(\lambda_i))\right) \left(1 - \tau(z;\bar{\sigma}(\lambda_i))\right) \Delta\lambda_i \right]^2 \tag{3.23}$$

$$= r_\sigma^2 \left[\int_0^\infty J_\lambda(z;\bar{\sigma}) \left(1 - \tau(z;\bar{\sigma}(\lambda))\right) \mathrm{d}\lambda \right]^2. \tag{3.24}$$

Finally, one gets the uncertainty factor of the photolysis rate constant

$$F_J(z) = F_\sigma^{\left|1 - \int_0^\infty \left[J_\lambda(z;\bar{\sigma})/\bar{J}(z)\right] \tau(z;\overline{\sigma}(\lambda)) \mathrm{d}\lambda\right|} \tag{3.25}$$

where

$$\overline{J}(z) = \int_0^\infty J_\lambda(z;\bar{\sigma}) \mathrm{d}\lambda. \tag{3.26}$$

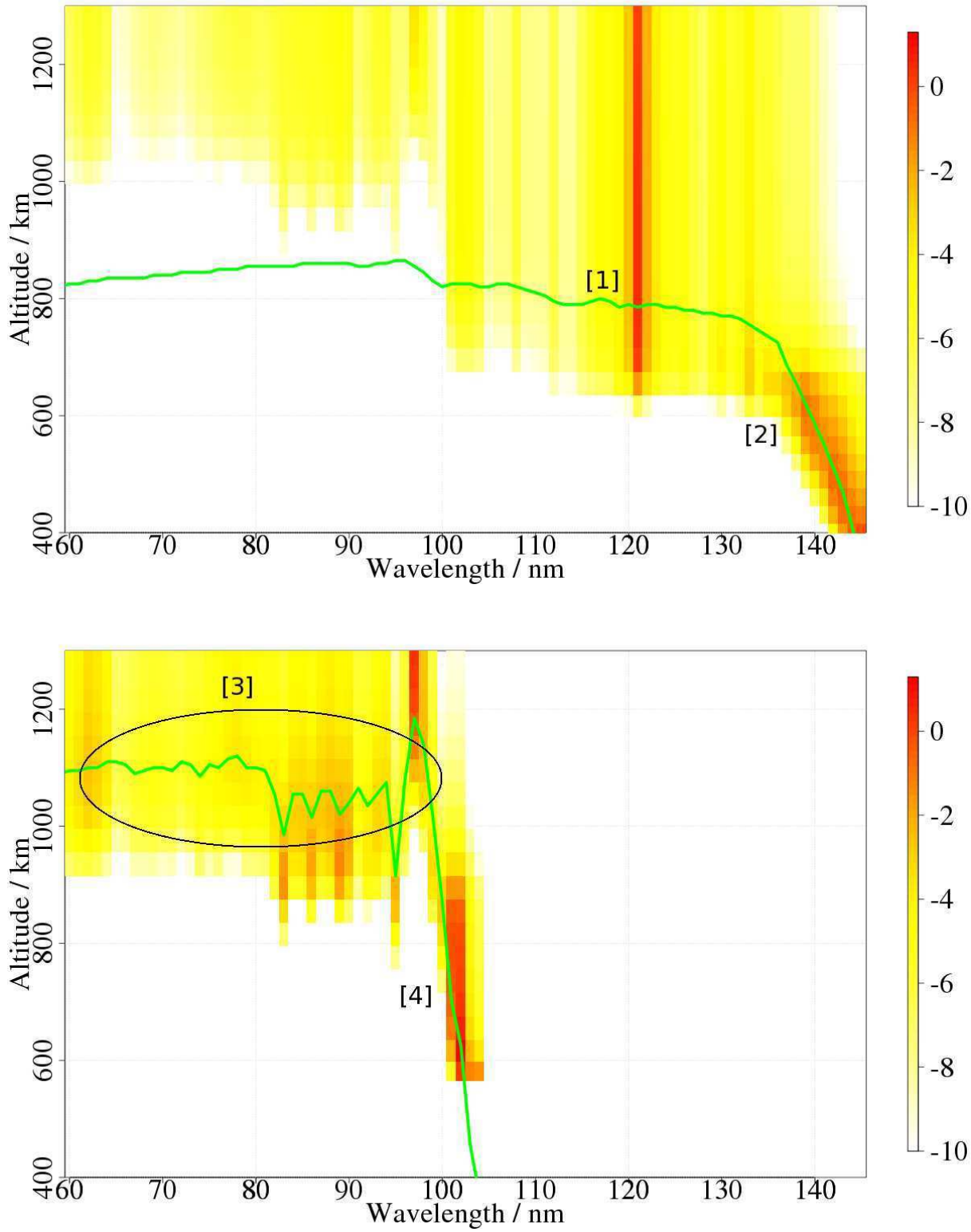

Figure 3.3: Weighted photolysis rates $W_\lambda(z) = J_\lambda(z;\bar{\sigma})/\bar{J}(z)$ for CH_4 (top) and N_2 (bottom), showing the relative contributions of different wavelength groups to altitude structures. The colors correspond to the values of $-\ln(1/W_\lambda(z) - 1)$, as reported in the colorscales. The (green) lines represent the unity optical depth for each species. The number in square brackets correspond to the numbered features in Fig. 3.2.

Algorithm 3.2 Derivation of the uncertainty factor of monochromatic photolysis rate constants in a multispecies model.

Based on Eq. 3.6, one can obtain the photolysis rate constant of the ith species in an n-species system by simply using the sum of the optical depth of all species instead of the optical depth of a single species, *i.e.*

$$J_i(z;\sigma_i) = \sigma_i I^\infty \exp\left(-\sum_{j=1}^{n}\tau(z;\sigma_j)\right) \tag{3.28}$$

where σ_i is the cross-section of the ith species. Therefore, the uncertainty factor corresponding to this rate constant is estimated by

$$\begin{aligned} F_{J_i}(z) &\simeq 1 + u_{J_i}(z)/\bar{J}_i(z) && (3.29)\\ &= 1 + \frac{1}{\bar{J}_i(z)}\sqrt{\sum_{j=1}^{n}\left(\frac{\partial J_i(z)}{\partial\sigma_j}\right)^2_{\sigma_j=\bar{\sigma}_j} u^2_{\sigma_j}} && (3.30)\\ &= 1 + \sqrt{\left(1-\tau(z;\sigma_i)\right)^2\left(F_{\sigma_i}-1\right)^2 + \sum_{j=1,j\neq i}^{n}\tau(z;\sigma_j)^2\left(F_{\sigma_j}-1\right)^2} && (3.31) \end{aligned}$$

NVA models, with the aid of Fig. 3.3 which overlaps the unity optical depth for each species with the $W_\lambda(z) = J_\lambda(z;\bar{\sigma})/\bar{J}(z)$ term of Eq. 3.14.

- CH_4
  - NVA [1] ($100 < \lambda < 130$ nm): in this range, the Ly-α band is the dominant contribution to the average unity optical depth, and the corresponding altitude (800 km) is a NVA. This could also be interpreted as a monochromatic NVA (Eq. 3.13).
  - NVA [2] ($\lambda > 130$ nm): CH_4 has a dropping cross-section which contributes to its absorption at lower altitudes (below 700 km), where all photons at shorter wavelengths have been already absorbed. This region appears as an absorbing feature decoupled from the one at shorter wavelengths, and a NVA appears at the averaged unity optical depth (Eq. 3.14).
- N_2
  - NVA [3] ($\lambda < 100$ nm): N_2 absorption is dominant in this wavelength range. The peaks in $W_\lambda(z)$ (red regions in Fig. 3.3) in this wavelength range overlap in altitude and contribute to the definition of an average unit optical depth around 1100 km. Here again, the single-species/polychromatic case (Eq. 3.14) provides a rather good representation.
  - NVA [4] ($\lambda \sim 100$ nm): N_2 has a dropping cross-section which contributes to its absorption at lower altitudes (below 900 km). If the atmosphere were of pure N_2, one should observe a "perfect" NVA somewhere in this altitude range. However, CH_4 has a partial optical depth comparable to the one of N_2 in this wavelength range, and it becomes impossible for N_2 to present a "perfect" NVA (Eq. 3.27).

3.1.5 Effect of the resolution of cross-sections

Lavvas et al. (2011) have shown that the highly structured absorption cross-section of N_2 can lead

to different results depending on the spectral resolution adopted for radiative transfer calculations. In their article, they gave the photolysis rate profiles at high altitudes for different resolutions of the cross-sections. When compared with these curves, the photolysis rate constants obtained by our photochemical model (with a spectral resolution of 1 nm) are more consistent with their results at high resolution. This is probably the case not only because the cross-sections of N_2 in our model are well selected, but also because the contribution of the wavelength range in which the N_2 cross-section is highly structured plays a minor part in the photolysis rate constant of N_2.

Which impact could the details of cross-section structure have on NVAs? For the higher NVAs of N_2 [3] and CH_4 [1], the uncertainty on the photolysis rate constants and the NVA characteristics could only weakly be affected by the resolution of the cross-section of N_2: for CH_4, the contribution of Ly-α is strongly dominant and for N_2, the frequency of the peaks in the high resolution cross-section would not substantially change the *average* optical depth as defined in Eq. 3.14.

For the NVA [4], the interaction between N_2 and CH_4, depending on their relative contribution to the total absorption, becomes inevitable. The baseline in the peaked region ($\sim$80-95 nm in Fig. 1 of Lavvas et al. (2011)) of the high resolution absorption cross-section of N_2 ($\sim 10^{-20}$-$10^{-18}\,cm^2$) results in an optical depth comparable to, or lower than, the one of CH_4. All wavelengths where the unity optical depths of N_2 and CH_4 have similar altitudes contribute to the deeper NVA of N_2, in the same way as explained in the section above. The photons at the wavelengths where the unity optical depth of N_2 is lower in altitude than the one of CH_4 would be absorbed by the flat band of CH_4 ($\sim$50-130 nm) and could not raise a third NVA for N_2. In this altitude zone, the NVA [1] of CH_4 is very stable due to the dominant contribution of Ly-α.

3.2 Photolysis branching ratios of CH_4

We turn now to the effects of branching ratios, in particular, of methane photolysis, one of the central primary processes initiating the unique radical and ion chemistry network of "Titan's organic factory" (Atreya, 2007). Its influence on Titan's atmospheric chemical species has been quantified in the global sensitivity study led in Hébrard et al. (2009). This work shows that methane photolysis is a key process at altitudes as low as 600 km, with an increasing weight in the upper atmosphere.

Methane photolysis in the upper layers of the atmosphere is mainly driven by the Ly-α wavelength (121.6 nm), for which experimental fragmentation probabilities are available. However, this predominance disappears below $\sim$700 km (see Fig. 3.3), and the evolution of the methane fragmentation pattern with wavelength can affect the photochemistry occurring at various altitudes in Titan's atmosphere. The variation of the branching ratios among the products of methane photolysis at other wavelengths than Ly-α is mostly unexplored, and recent results by Gans et al. (2011) shed a new light on this topic (Tab. 2.1).

To assess the influence of the values of these branching ratios in a photochemical model of Titan's atmosphere, a local sensitivity study was performed by Wilson and Atreya (2000) for hydrocarbon species. Varying methane photodissociation branching ratios sequentially at Ly-α and in the rest of the spectral range, they found a significant effect of the Ly-α branching ratios for heavier species (containing more than two carbon atoms). But, the effect of non-Ly-α branching ratios was found to be small, modifying at most C_2H_6 density by 65 %. In this study however, Ly-α remains the main contribution to methane photolysis down to 600 km.

The aim of this section is to quantify the impact of the new measurements of methane photolysis

branching ratios by Gans et al. (2011) on the predictions of a photochemical model of Titan's atmosphere, and on their precision. We implement the wavelength-dependent representation of methane photolysis branching ratios developed in Section 2.2.3 in the 1D IPSL photochemical model (see Section 2.1.2) of Titan's atmosphere and used for a comparison of the predicted stationary densities of minor chemicals with those produced by the dichotomous Ly-α/non-Ly-α representation. The results are presented an discussed in Sections 3.2.3 and 3.2.4.

3.2.1 Photochemical model

The present model is based on the IPSL model (see Section 2.1.2), with minor modifications, in order to deal with wavelength-dependent branching ratios for methane and to implement the Monte Carlo procedure. The photochemical dataset is based on the work of Hébrard et al. (2009). It contains 543 reactions involving 56 chemical species (hydrocarbons and N-bearing species).

3.2.2 Wavelength-dependent representation of methane photolysis branching ratios

The wavelength-dependent model presented in Section 2.2.3 encompasses the large uncertainty on methane photolysis branching ratios in most wavelength regions. It is inherently stochastic and has to be treated accordingly. We use a Monte Carlo procedure to implement the branching ratios model, in which we generate a representative sample of the $b_i(\lambda)$ curves (Fig. 2.1) and perform one run of the photochemical model for each element of this sample. The density profiles of all species (the outputs of the photochemical model) for each run are stored and used for statistical analysis. The whole procedure is similar to the one used for uncertainty propagation and sensitivity analysis by Carrasco and Pernot (2007); Carrasco et al. (2008a); Plessis et al. (2010, 2012) to deal with non-wavelength-dependent branching ratios, or by other authors to deal with uncertain rate constants in atmospheric chemistry (Dobrijevic and Parisot, 1998; Thompson and Stewart, 1991; Dobrijevic et al., 2003; Hébrard, 2006; Hébrard et al., 2007; Dobrijevic et al., 2008; Hébrard et al., 2009; Dobrijevic et al., 2010; Peng et al., 2010, 2012).

A sample of 60 random values of the branching ratios was generated from the above described model and used to run the photochemistry code, which represents one day of computer time per model on a tabletop computer. This sample size was deemed sufficient to display the effects of interest in this study.

3.2.3 Branching ratios scenarii

Three scenarii were considered in order to estimate the effects of non-Ly-α branching ratios on the predictions of the photochemical model:

- Scenario 1 implements the dichotomous model commonly found in Titan's photochemical models, *i.e.* the values of the branching ratios at Ly-α are taken from our reference sample, and the values of the branching ratios for the other wavelengths are fixed at $(b_{CH_3}, b_{^3CH_2}, b_{^1CH_2}, b_{CH})_{\lambda \neq 121.6} = (1, 0, 0, 0)$;
- Scenario 2 uses the full wavelength-dependent branching ratio curves (Fig. 2.1);
- Scenario 3 is based on Scenario 2, but aggregates the two electronic states of CH_2 and considers only the production of the excited state, *i.e.* $b_{^1CH_2}$ (Scenario 3) $= b_{^3CH_2} + b_{^1CH_2}$ (Scenario 2).

Source	Ly-α			
	b_{CH_3}	$b_{^1CH_2}$	$b_{^3CH_2}$	b_{CH}
Mordaunt et al. (1993) (2 scenarii)	0.49	0.00	0.00	0.51
	0.51	0.49		0.00
Romani (1996)	0.41	0.28	0.21	0.10
Wang et al. (2000)	0.29	0.64	0.00	0.07
Gans et al. (2011)	0.42	0.48	0.03	0.07

Table 3.1: Methane neutral photodissociation branching ratios, as implemented in various 1D models of Titan's atmospheric chemistry. We consider only the wavelength range above methane ionization threshold at 95 nm.

The comparison of Scenarii 1 and 2, differing only in the representation of the branching ratios at non-Ly-α wavelengths, should enable to estimate the impact of the non-Ly-α photolysis on the production of minor species and on the corresponding prediction uncertainty. The comparison of Scenarii 2 and 3 is designed to evaluate the importance of discriminating the production pathways of the CH_2 singlet and triplet states in Titan's atmosphere, knowing that the singlet state should be efficiently quenched by N_2 (Wilson and Atreya, 2000).

For each Monte Carlo run, the mixing ratios of all species in the model were stored, and analyzed *a posteriori* to get, for each species, the mean value ($\overline{y}$) and standard uncertainty factor ($F_y = 10^{\sigma(\log y)}$), where $\sigma(\log y)$ is the standard deviation of the log of the mixing ratio y (Tab. 3.2). Note that the relative uncertainty is related to the uncertainty factor by $\sigma(y)/\overline{y} \simeq F_y - 1$.

Fig. 3.4 presents, for the three scenarii, the mean values and 95% confidence intervals $[\overline{y}/F_y^2, \overline{y} \times F_y^2]$ for a set of representative species.

If one considers Scenario 1, most species display a very weak sensitivity to the uncertainty in the Ly-α branching ratios. If one estimates the relative uncertainty on the branching ratios to be about 10%, many mixing ratios appear to have a lower relative uncertainty. For CH_3, the maximal uncertainty occurs at 960 km with $F \simeq 1.1$, *i.e.* a 10% relative uncertainty. For all other hydrocarbons, the uncertainty factor remains below 1.04. On the other hand, N-bearing species are more sensitive, although mostly at altitudes where their mixing ratio decays rapidly. For instance, the uncertainty on $N(^4S)$ mixing ratio reaches $F = 1.4$ at 800 km, where the value is more than 100 times smaller than its maximal mixing ratio (not shown). An exception is C_2N which uncertainty reaches $F \simeq 1.1$ around its maximal mixing ratio at 900 km.

When relaxing the strong constraint on non-Ly-α branching ratios, from Scenario 1 to Scenario 2, uncertainty factors get larger for most species, with a notable increase for CH_3 and C_2N. In most cases however, the uncertainty factor remains rather small, on the order of a few percents (Tab. 3.2). More notably, the mean values of some species are significantly changed, in the sense that the confidence intervals issued from both scenarii do not overlap: CH_2, CH_3, C_2H_6, C_3H_8, C_4H_8, C_4H_{10}, HCN, HC_2N_2, C_2N...

The results of Scenario 3 differ only slightly from those of Scenario 2, with a notable difference in the mixing ratios of some of the heavier hydrocarbons like C_3H_8, C_4H_8 or C_6H_6, which become more abundant for an increased production of $^1CH_2$ (Fig. 3.4). A correlation analysis between the inputs and outputs samples points to a pathway implying C_2H_5 and C_3H_7 radicals.

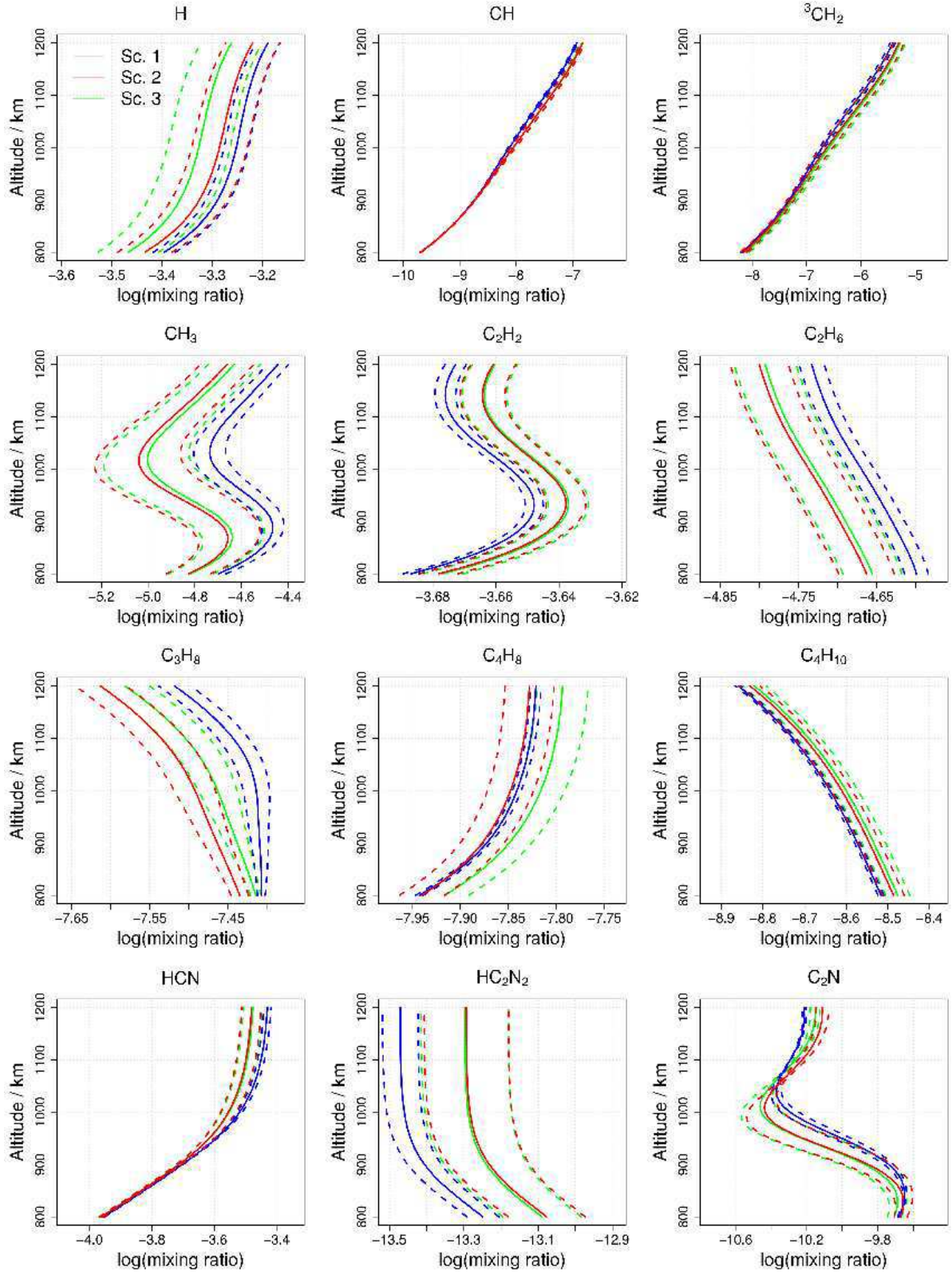

Figure 3.4: Mean (full) and 95% confidence intervals (dashes) of altitude-dependent mixing ratios for a set of representative minor species in the upper atmosphere (800-1200 km): (blue) Scenario 1, implementing a fixed value of the branching ratios at non-Ly-α wavelengths ($b_{CH_3} = 1$) ; (red) Scenario 2, implementing the new wavelength-dependent branching ratios model; (green) Scenario 3, with b_{1CH_2} (Scenario 3) $= b_{3CH_2} + b_{1CH_2}$ (Scenario 2).

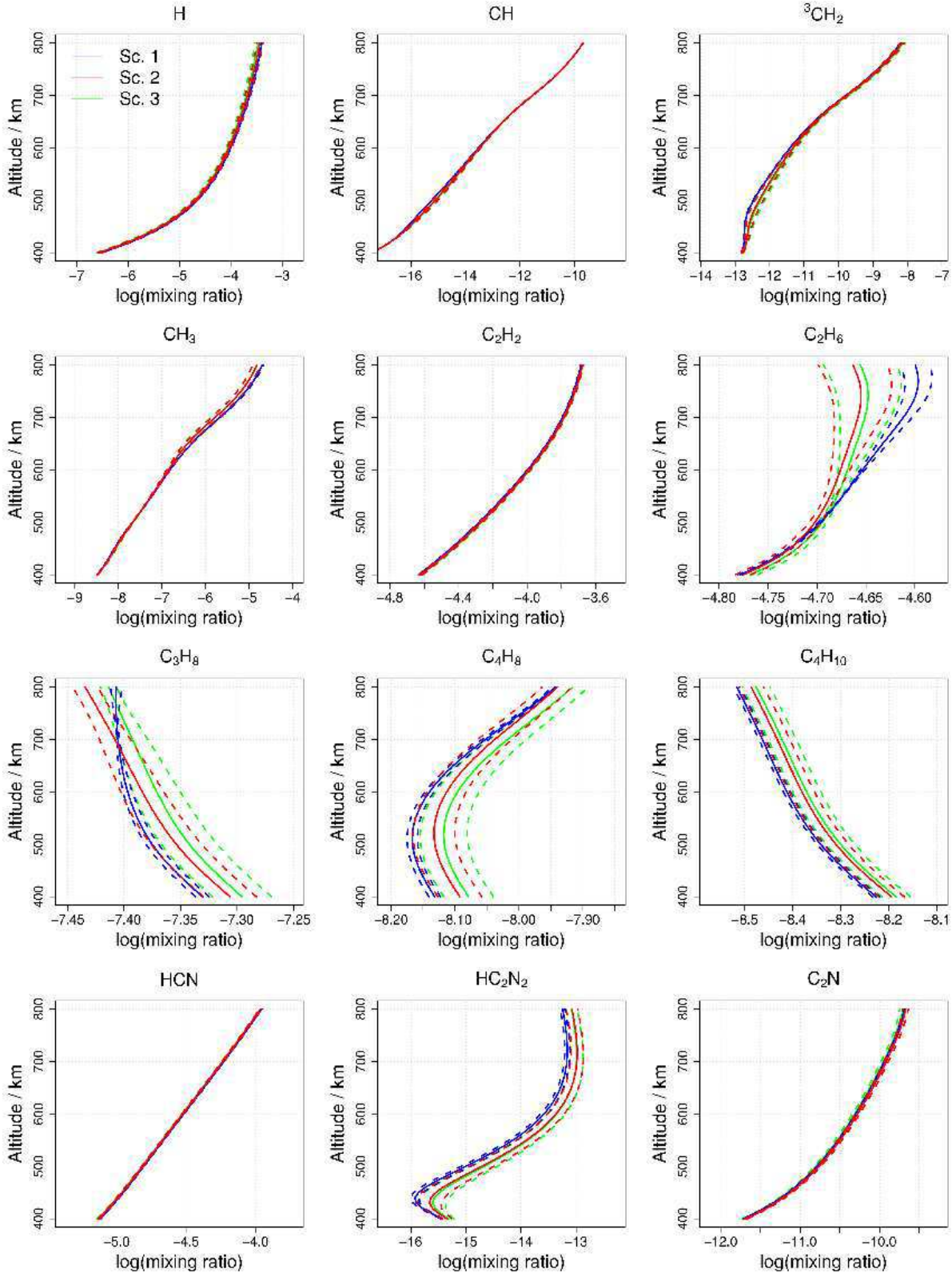

Figure 3.5: Same as Fig. 3.4, with the focus on the 400-800 km range.

	Scenario 1		Scenario 2		Scenario 3	
Species	$\overline{y}$	F_y	$\overline{y}$	F_y	$\overline{y}$	F_y
H	5.45e-04	1.03	5.04e-04	1.07	4.50e-04	1.09
$^3CH_2$	1.11e-07	1.04	1.27e-07	1.11	1.47e-07	1.15
CH_3	2.50e-05	1.09	1.18e-05	1.28	1.20e-05	1.37
C_2H_2	2.24e-04	1.00	2.30e-04	1.01	2.30e-04	1.01
C_2H_4	3.21e-04	1.01	3.37e-04	1.02	3.40e-04	1.02
C_2H_6	2.22e-05	1.02	1.90e-05	1.04	1.96e-05	1.05
C_3H_4	3.22e-05	1.01	3.36e-05	1.02	3.39e-05	1.02
C_3H_8	3.88e-08	1.02	3.31e-08	1.03	3.50e-08	1.04
C_4H_8	1.41e-08	1.00	1.39e-08	1.03	1.49e-08	1.03
C_4H_{10}	2.45e-09	1.01	2.62e-09	1.03	2.65e-09	1.04
C_6H_6	5.57e-07	1.02	6.22e-07	1.06	6.59e-07	1.08
HCN	2.65e-04	1.01	2.51e-04	1.02	2.50e-04	1.03
C_2N_2	1.05e-06	1.05	1.52e-06	1.11	1.50e-06	1.14
HC_2N_2	3.57e-14	1.06	5.35e-14	1.14	5.46e-14	1.18
C_2N	8.53e-11	1.07	5.15e-11	1.23	4.77e-11	1.30

Table 3.2: Mean mixing ratio $\overline{y}$ and uncertainty factor F_y of selected species for the three scenarii. All values are estimated at 960 km, where CH_3 has its maximal uncertainty factor in Scenario 2.

3.2.4 Discussion

In their local sensitivity study, Wilson and Atreya (2000) tested four deterministic scenarii at Ly-α, based on propositions of Mordaunt et al. (1993) (2 scenarii), Romani (1996) and Smith and Raulin (1999). They observed only minor effects for the smaller hydrocarbons, but major variations for the C_3 species present in their model (C_3H_4 and C_3H_6). In consequence, they retained the nominal scheme of Romani (1996) which provides intermediate results. Note that this scheme is very close at Ly-α to the branching ratios of Gans et al. (2011) implemented in our study, except for the partition between $^1CH_2$ and $^3CH_2$. They complemented their exploration by comparing three schemes out of Ly-α, with a varying balance between CH_3 and $^1CH_2$, from which they observed only minor effects, the largest being a 65% variation in C_2H_6 abundance.

The present study differs from this previous works on a few main points: (i) the chemical model of Hébrard et al. (2009) includes larger hydrocarbons and N-bearing species; (ii) we adopt a probabilistic method in which many schemes are covered by uncertainty modeling; and (iii) we adopt a continuous, wavelength-dependent model of branching ratios accounting for all recent measurements (Scenario 2) and compare it to the commonly used "100% CH_3" out-of-Ly-α scheme (Scenario 1).

We observe for each scenario that the uncertainty in the branching ratios accounted for by our model (about 10%, see Tab. 2.1) results in very small prediction uncertainties for most stable hydrocarbons (about 1 to 4%, see Tab. 3.2). Therefore, in agreement with Wilson and Atreya (2000), we observe only weak effects of branching ratios on the smaller hydrocarbons, but also on the heavier ones. By contrast, more notable uncertainties are obtained for N-bearing species, of same order as those of CH_3 or CH_2. This sensitivity might be explained by the present sparsity of the chemical scheme for these species. A similar effect was observed for the C3 species by Wilson and Atreya (2000), as they were terminal species (sinks) in their chemical scheme. The more complete hydrocarbons model of Hébrard et al. (2009) partially annihilates this effect on the C3 species.

3.2.4.1 Effect of CH_2 singlet/triplet partition

A notable difference between the branching ratios at Ly-α of Romani (1996) and Gans et al. (2011) is the proportion between the electronic states of CH_2. Considering the small difference between Scenario 2 ($^1CH_2$:$^3CH_2$=0.48:0.03) and Scenario 3 (0.51:0.00), the observed variations for some species, such as C_3H_8 or C_4H_8, reveal a marked sensitivity of those species. Nevertheless, this remains a second order effect in comparison with the CH_2:CH_3 partition.

3.2.4.2 Effect of the CH_2:CH_3 partition

To evaluate the importance of the CH_4 photofragments for the subsequent chemistry, we calculated the linear correlation coefficients between the inputs (branching ratios) and outputs (mole fractions) and summarized them as histograms (Fig. 3.6). The more influential branching ratios are expected to display larger values of the correlation coefficients, independently of their magnitude (Plessis et al., 2012). This was done for two altitudes: 960 km, and a lower altitude (600 km) where Ly-α has been fully absorbed.

At both altitudes, the branching ratios for $^1CH_2$ and CH_3 have markedly large correlation coefficients with most species (typically above 0.5 in absolute value), which is not the case for the other branching ratios. As stated above, the partition amongst electronic states of CH_2 is secondary. Similarly, considering the histogram of input/outputs correlation coefficients in Fig. 3.6, b_{CH} does not have a notable influence on any specific species (all correlation coefficients close to 0). This points out the importance of the accuracy of the CH_2:CH_3 partition in the photolysis of CH_4 for the precision of model predictions.

3.2.4.3 Comparison with the global chemical uncertainty

The previous simulations have shown the impact of various representations of the methane photolysis branching ratios on the mixing ratios of minor species, notably that wavelength-dependent representations of branching ratios out-of-Ly-α (Scenarii 2 and 3) predict mixing ratio profiles that differ significantly from the "100% CH_3" out-of-Ly-α scheme (Scenario 1).

For a better legibility, we had fixed all other chemical parameters to their nominal value. It is important to recast this study in the more global context, where the uncertainty of all chemical parameters is accounted for. To do this we compared the 95% confidence intervals (CI) obtained in the present study to those predicted by Hébrard et al. (2009). The latter CIs were obtained by applying the altitude-dependent uncertainty factors of Hébrard et al. (2009) to the mean curves of the present study. As shown in Fig. 3.7, the effect is large enough to justify this approximate CI evaluation: for all species, the inter-scenarii difference is much smaller than the overall uncertainty. Even for CH_3, the present level of accuracy on the branching ratios is sufficient to conclude that other chemical parameters are responsible for its mixing ratio uncertainty in Titan's atmosphere.

There remains the possibility of interactions between uncertain branching ratios and uncertain rate constants. The study of Hébrard et al. (2009) makes use of the Scenario 1 and therefore includes such interactions, albeit restricted to the Ly-α wavelength. Considering the very large prediction uncertainty of the model accounting for all chemical uncertainty sources in Titan atmospheric chemistry, it is unlikely that the small contribution of out-of-Ly-α branching ratios evidenced here could contribute significantly to major modifications of the mean mixing ratios, nor to an overall increase of the prediction uncertainty. Nevertheless, this might become a key factor when other

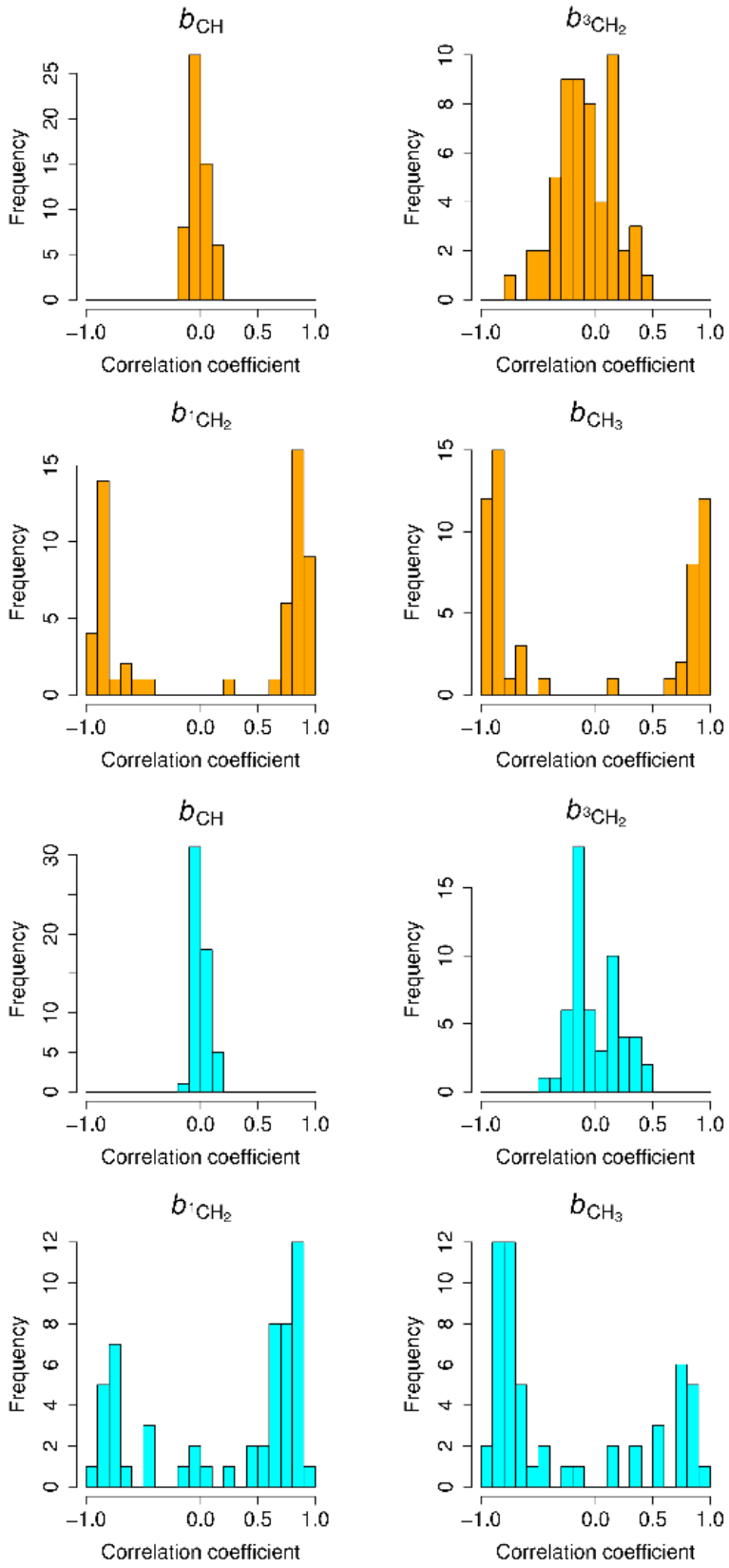

Figure 3.6: Sensitivity analysis of the CH_4 branching ratios. (Top/orange) histograms of the linear input/output correlation coefficients, where the inputs are the branching ratios of the Scenario 2 sample at Ly-α, and the outputs are the log mole fractions of all 56 neutral species at 960 km. (Bottom/cyan) same as above, but for a wavelength of 140 nm and mole fractions at 600 km.

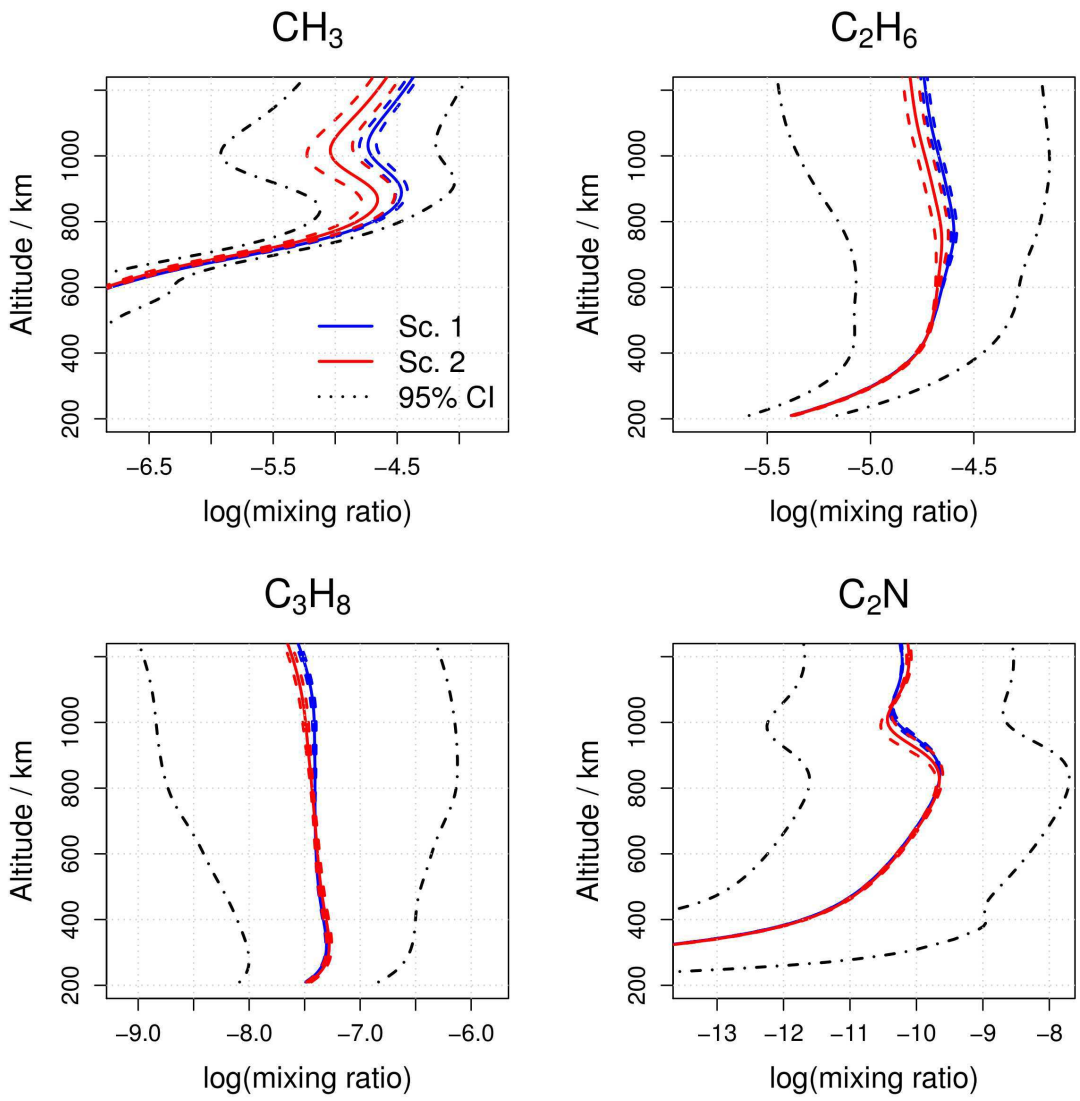

Figure 3.7: Same as Fig. 3.4 for a subset of the species, with (dash-dot) limit profiles of 95% (2σ) confidence interval (CI), obtained when considering all uncertain chemical and photochemical rate constants (Hébrard et al., 2009) .

uncertainty sources (the key reactions identified by Hébrard et al. (2009)) will have been better constrained.

At this date, we consider that there is very little to be gained in overall precision for Titan models by refining the present CH_4 branching ratios data. One has however to keep in mind that the situation might be completely different in other irradiation conditions, such as in synchrotron-coupled reactors (see Chapters 4 and 5), where Ly-α is not necessarily so dominant. In this perspective, additional measurements at wavelengths between 121.6 and 140 nm would be most welcomed.

3.3 Conclusion

In this chapter, the impacts of the uncertain photolysis cross-sections and branching ratios on Titan's photochemical models have been studied separately.

The uncertainties on the cross-sections of photolytic processes in the modeling of Titan's atmosphere have been treated explicitly in a radiative transfer model, revealing strong altitude variations

of the uncertainty on the resulting photolysis rate constants. The former use of altitude-independent uncertainty factors in this type of analysis (Hébrard, 2006; Hébrard et al., 2007, 2009) has thus to be reevaluated.

A striking and original observation for the major absorbing species is the presence of *Null Variance Altitudes* (NVAs), *i.e.* specific altitudes where the uncertainty on the photolysis rate constants vanishes. The origin of NVAs has been demonstrated analytically in the present study and related to the location of the unity optical depth, modulated by the energy distribution of the incoming photon flux, through the relative weight of different wavelengths in Eq. 3.14. According to our model, only major absorbing species with a barometric, or nearly barometric, distribution are expected to present NVAs.

In a photochemical model with full treatment of uncertainty sources, a possible limitation to the presence of NVAs might be the uncertainty on the densities of the absorbing species. This is not an issue here for N_2, but possibly for CH_4, whose density depends on uncertain parameters, such as the eddy coefficient (Lara et al., 2002; Wilson and Atreya, 2004; Carrasco et al., 2007b) and the atmospheric escape rate (Yelle et al., 2008; Strobel, 2009; Schaufelberger et al., 2012). In any case, the values of the uncertainty factors presented here should not be transferred blindly to other photochemical models of Titan's atmosphere. They have to be derived self-consistently in each case.

Besides, we applied a wavelength-dependent branching ratios description for the photolysis of CH_4 (see Chapter 2) to a photochemical model of Titan. It was shown that the model is mainly sensitive to the CH_2/CH_3 ratio, and that a slight bias is introduced in the models when neglecting the electronic state description of CH_2.

Methane photolysis is mainly driven by Lyman-α wavelength, and the corresponding branching ratios have been updated in detail in the study of Gans et al. (2011). They found values in agreement with the previous experimental based determinations of Romani (1996) and Brownsword et al. (1997), *i.e.* a balanced production of CH_3 and CH_2 radicals. Those ratios were implemented in the Titan's photochemical models of Wilson and Atreya (2004), De La Haye et al. (2008) and Bell et al. (2010). On the other hand, several models used the experimental values of Wang et al. (2000) to describe methane photolysis branching ratios at Ly-α: those should be updated, because the production of CH_2 radicals is significantly higher in the determination of Wang and coworkers, which could lead to an overestimation of the CH_2 chemistry chain.

We have also shown some significant contributions of non-Ly-α wavelengths (in particular in the 130-140 nm range) to the methane photolysis budget at altitudes between 400 and 700 km. This highlights a need of accurate *ab initio* calculations and/or extended non-Ly-α branching ratios measurements in the 130-140 nm wavelength range. Moreover, the 500-700 km altitude range corresponds to an unprobed atmospheric layer, either by the Cassini instruments or by remote sensing. Indeed the *in situ* instruments explore Titan's atmosphere down to 900 km, whereas remote sensing instruments probe the atmosphere up to 500 km (Brown et al., 2009). The so-called "nodatasphere" between 500 and 900 km can presently only be studied by photochemical models, except for a single measurement during the descent of the Huygens probe in 2005. This change of photolysis regime around 650 km shows the necessity of models to understand the photochemistry in this region. Without any study yet on the branching ratios at 130-140 nm wavelength range, those have to be extrapolated in the models. Two simple extrapolation patterns were found in the literature: a "100% CH_3" scenario, and a Ly-α-like scenario. These arbitrary scenarii were compared to our wavelength-

dependent one. The "100% CH_3" scenario positively bias the major saturated hydrocarbons density profiles (such as ethane C_2H_6 and propane C_3H_8) and should be avoided.

Because of the simultaneous but independent contribution of the cross-sections and the branching ratios to the uncertainties on the photolysis rate constants, their total effects on the photochemical model could be estimated based on the two cases of this chapter. The existence of NVAs might be of interest for the uncertainty budget and uncertainty analysis of photochemical models. As the photolysis rates of the major absorbing species have been shown to be key parameters (Hébrard et al., 2009; Peng et al., 2010), the NVAs provide reference altitudes for sensitivity analysis where the cross-sections should not contribute to prediction uncertainty, *i.e.* the branching ratios contribute alone to the photolysis uncertainty. The photolysis rate being maximal at a NVA, one can expect an improvement in the prediction precision of photochemical models. However, this improvement may be very limited, because Fig. 3.7 illustrates that thermal reactions are the dominant uncertainty source of the model, even compared to the uncertainties on the branching ratios, usually larger than those on the cross-sections. At the altitudes of the uncertainty peaks between NVAs (uncertainty factors around 1.4), the uncertainties on the total photolysis rates, *i.e.* originating from the cross-sections, are comparable to, even higher than those on the branching ratios. As a result, the prediction uncertainty of the model might be increased significantly at these altitudes.

Finally, considering the existence of NVAs for any barometrically distributed compounds and the high usability of wavelength-dependent description of methane photolysis branching ratios, we expect that the two cases investigated in this chapter may be of interest in other conditions: for example, NVAs for the photochemical modeling of other planetary atmospheres and novel representation of methane photolysis branching ratios for the interpretation of methane photochemistry induced in lab simulations with VUV sources different from the solar spectrum (see Chapter 5).

Chapter 4

Atmospheric Photochemistry SImulated by Synchrotron experiments

Contents

To understand the important, but uncertain effects of energy deposition on the molecular growth in Titan's atmosphere, laboratory simulation studies are complementary to modeling studies, such as the ones in the previous chapter.

Two kinds of laboratory studies are realized in gas-phase reactors with an energy source initiating the primary ionization and dissociation processes of N_2-CH_4 gas mixtures. With plasma discharges, such as in the PAMPRE reactor, energy is deposited through electron impact (Alcouffe et al., 2010; Carrasco et al., 2009; Szopa et al., 2006b), whereas VUV monochromatic irradiation has been used in photochemical studies (Imanaka and Smith, 2010).

Plasma discharges are more efficient for the production of aerosols, but Titan's chemistry is mainly driven by photochemical processes. In order to address the issue of the sensitivity of the global chemistry to the energy source, a new photochemical reactor, APSIS - Atmospheric Photochemistry SImulated by Synchrotron - was designed to be coupled with a VUV photon source. The

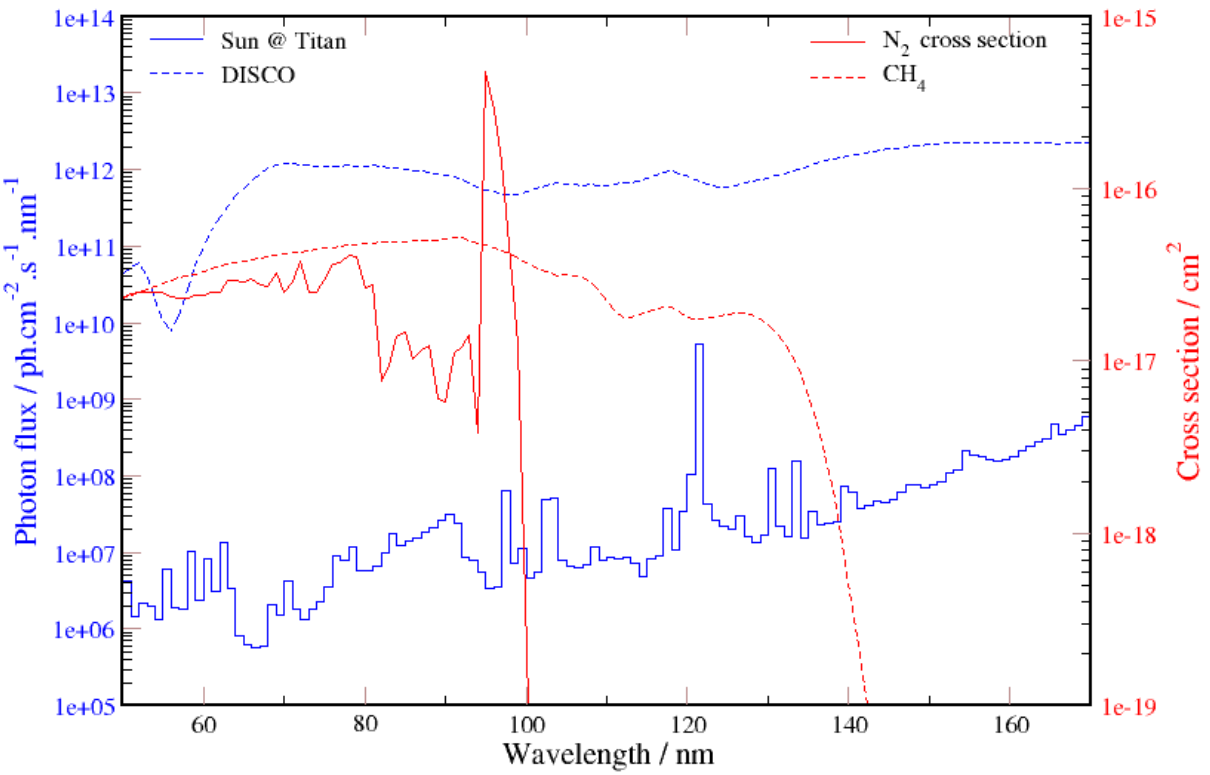

Figure 4.1: Energy spectra of APSIS and solar spectrum at the top of Titan's atmosphere and cross-sections of N_2 and CH_4.

experiment has been mounted on DISCO, a VUV beamline at the SOLEIL synchrotron radiation facility.

Activation of N_2 requires VUV wavelengths below 100 nm (Fig. 4.1). Typical leak-tight windows made of LiF, CaF_2 or MgF_2 are capable of handling the pressure difference between the ultra high vacuum of the beamline and the pressure of the reactor, but are opaque below 110 nm (11.3 eV), preventing the activation of molecular nitrogen. Photochemical reactors operating at Ly-α and above therefore focus on methane chemistry (Adamkovics and Boering, 2003; Romanzin et al., 2008; Trainer et al., 2004). Although it is relatively easy to irradiate any media with UV photons through windows, it is much more difficult to deliver to a gas sample VUV photons with energy above the transparency limit of the windows. Therefore, the APSIS chamber is coupled *windowless* to the DISCO beamline, using a differential pumping system. A non-reactive carrier gas, helium, is continuously injected between the beam line and the APSIS chamber in order to prevent the reactive mixture to be pumped out of the reactor into the differential pumping system. The spectrum of the DISCO beamline is generally 10^4 - 10^6 times more intense than the solar spectrum at Titan but much more uniform and has no peak at Ly-α, 121.6 nm (see Fig. 4.1).

This experiment differs significantly from the single previous synchrotron study of Titan's atmosphere (Imanaka and Smith, 2007, 2010), working at 0.066 or 0.13 mbar and using a narrowband synchrotron radiation source. The experiments presented here were done in the same experimental conditions (room temperature and pressure in the mbar range) as in the PAMPRE plasma reactor in order to compare the chemistries generated with photons and electrons. I have participated in

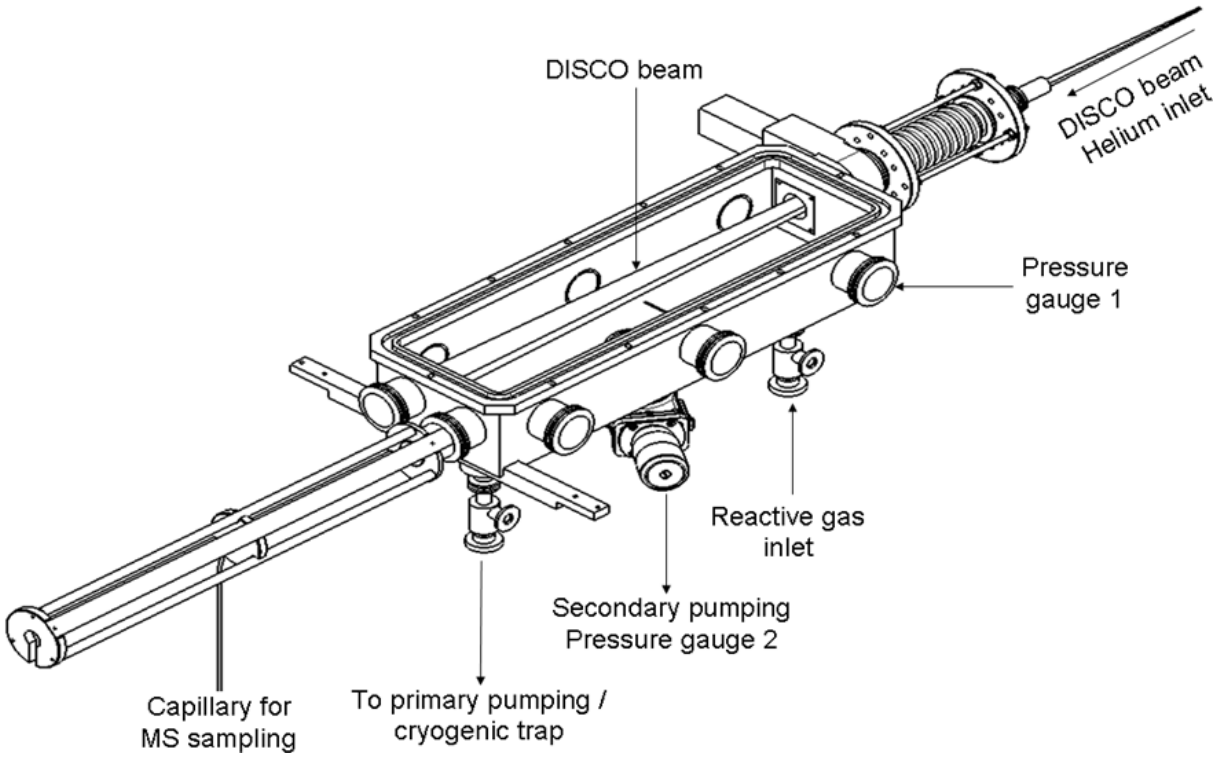

Figure 4.2: Schematic diagram of the APSIS setup.

them. In detail, I have conducted the experiments, performed the *in situ* MS measurement and treated the measurement data. This work has been published in Peng, Gautier, Carrasco, Pernot, Giuliani, Mahjoub, Correia, Buch, Bénilan, Szopa, and Cernogora (2013).

The experimental setup is detailed in Section 4.1. Specific analytical techniques involving *in situ* mass spectrometry and *ex situ* cryogenic trap and its GC-MS analysis are presented in Section 4.2. The main results addressed in Section 4.3 include the time-scale of the experiments in various pressure conditions, GC-MS product identification, and *in situ* MS product quantification. A comparison with the PAMPRE plasma results, the synchrotron results of (Imanaka and Smith, 2010), and the Cassini INMS measurements is discussed in Section 4.4.

4.1 The experimental setup

4.1.1 The APSIS reactor

The reactor, presented in Fig. 4.2, was designed by J.-J. Correia at Laboratoire Atmosphères, Milieux, Observations Spatiales (LATMOS, Guyancourt). It is made of stainless-steel for the safety reasons of its coupling with the DISCO beamline. It is a parallelepiped with internal dimensions (length × width × height) of 500 mm × l14 mm × 92 mm. The geometry is elongated to accommodate the optical depth of CH_4 in the experimental conditions described below. A reactive gas mixture is flowed into the reactor using a $0-10$ sccm (standard cubic centimeter per minute, mesuring flows equivalent to those at 0 ^{o}C and 1 atm) range MKS mass flow controller. A primary pumping unit ensures a stationary flow of reactive gas whose partial pressure reaches a few millibars and a residence time of the gas mixture of a few minutes. The pressure is measured with an absolute capacitance gauge (Ceravac from Oerlikron). Before each experiment, the reactor is pumped down to $\sim 10^{-5}$ mbar by a turbo molecular pump to clean out the chamber from residual gas traces.

Reactive $N_2 + CH_4$ gas flow (sccm)	Partial pressure of $N_2 + CH_4$ (mbar)	Total pressure with He (mbar)	Residence time of gas mixture (min)
0.6	1.3	2.1	∼11
2	1.5	2.5	∼4
7	4.5	7.0	∼3
10	6.5	8.7	∼3

Table 4.1: Experimental conditions. Pressure conditions and residence times of gas mixture in the experiments. Total pressure is measured after the addition of helium.

4.1.2 The DISCO beamline

Photon sources covering the VUV nitrogen dissociation energy domain may be found on synchrotron radiation facilities. An important property of synchrotron radiation is its spectrum, covering a wide range of photon energies, from terahertz to hard X-rays. DISCO, a bending magnet based beamline, has been described in more details elsewhere (Giuliani et al., 2009, 2011). It possesses three end-stations. One of those, referred to as APEX (for Atmospheric Pressure Experiment), is fitted with a pressure differential pumping system, which allows delivering monochromatic VUV photons down to 60 nm up to a rare gas pressure of 1 bar. The reactor was mounted on that particular port.

4.1.3 Experimental parameters

A gas mixture of $N_2/CH_4 = 90/10$ (purity $> 99.999\%$, Air Liquide) is injected at different flows, resulting in different partial pressures. Partial pressures of N_2 and CH_4, total pressures with helium and the corresponding residence times of the gas mixture at the studied gas flows are shown in Tab. 4.1. The experiments are conducted at room temperature.

4.2 Analytical techniques

4.2.1 *In situ* mass spectrometry

In situ measurement of the gas phase composition is achieved using a Pfeiffer QME 200 quadrupole mass spectrometer (MS), described in detail previously (Carrasco et al., 2012). In the MS, neutral molecules are ionized by electron impact at a standard 70 eV electron energy. Gas sampling is done through a capillary tube (0.8 mm internal diameter), mobile along the reactor length dimension and radially close to the irradiated column (Fig. 4.2). The capillary tube is long enough to reduce the conductance between the reactor chamber and the MS, which is ideally kept at an operating pressure P_{MS} below 10^{-5} mbar (Sciamma-O'Brien et al., 2010). As a consequence, only stable molecules can be measured with this setup. The MS detector has a resolution of 1 u and covers the 1 to 100 u mass range.

The DISCO photon flux, (a few 10^{11} ph.s^{-1} for 0.1 nm bandwidth) leads to a nitrogen dissociation ratio of less than 10^{-4}. The signal at m/z 28 of N_2 should therefore be constant enough throughout the experiments to be considered as a fixed reference. A slight electronic drift is often observed during the experiments lasting several hours. It affects proportionally all the ion signals, confirmed by a similar drift of the total pressure measurement in the ion source of the mass spectrometer. The intensity of the mass peak at m/z 28 is therefore used to normalize the mass spectra.

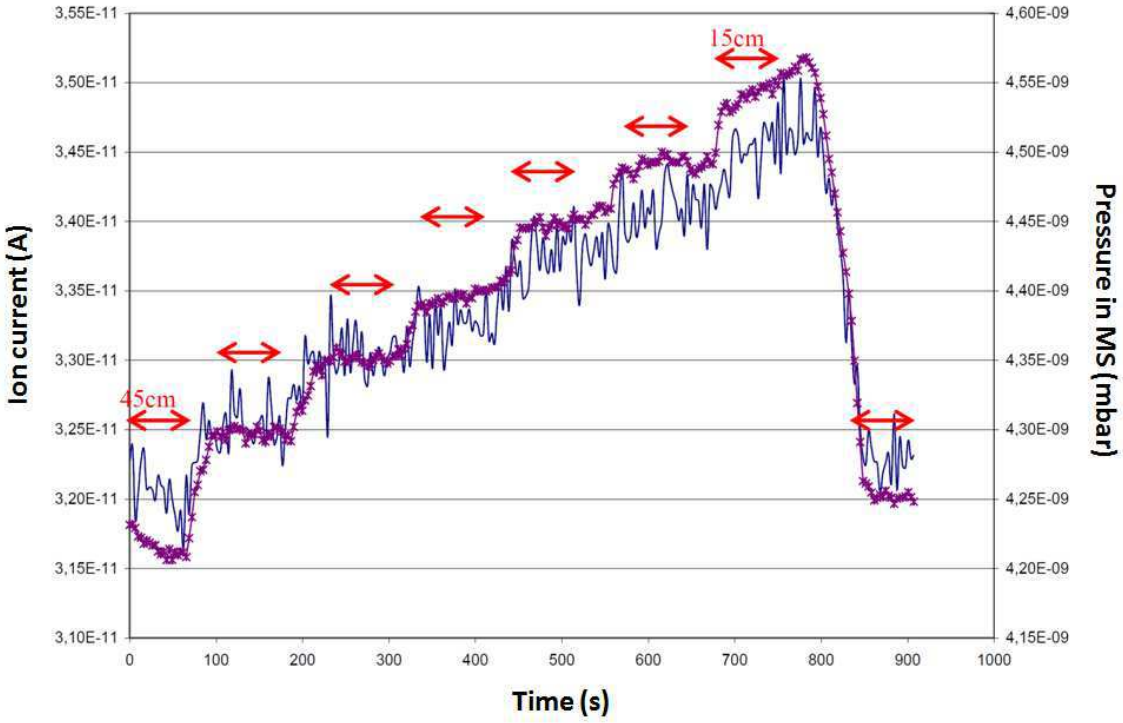

Figure 4.3: MID evolution of the pressure in MS (blue line) and the N_2 signal (at m/z 28, violet line and crosses) with the position of the MS sampling probe. Time is correlated to the sampling probe's successive shifts of 5 cm, from the position 45 cm from the reactor entrance to that 15 cm from the entrance.

We made two types of experiments in order (i) to monitor the time-dependent evolution of a series of mass peaks during the irradiation (Multiple Ion Detection (MID) measurements), and (ii) to characterize the stationary states before (DISCO OFF) and after (DISCO ON) irradiation on a continuous mass range (scan analogs). Studying the stationary state allows to increase the signal to noise ratio by long acquisition time-scales: a 10 seconds shift is chosen for each mass between m/z 2 to 80.

We measured the pressure in the MS and the N_2 intensity at different positions along the reactor length, using the mobile MS sampling probe (Fig. 4.3). They vary by only $\sim 10\%$, implying only a slight pressure variation along the reactor length. Therefore, we studied no longer the effect of the sampling probe's position, and the sampling in all *in situ* MS measurements below was performed near the reactor entrance.

We monitored the temporal evolution of the gas mixture composition recording the intensity of the maximum of mass peaks of interest in Multiple Ion Detection (MID) mode: m/z = 15, 26, 27, 28, 38, 39, 41, and 52. The signal at each of these masses was accumulated during 1 s, leading to a total time-resolution of 15 s.

As described in Sciamma-O'Brien et al. (2010), the peak at m/z 15 is representative of methane. A possible contribution of $^{15}N^+$ also occurs for N_2-CH_4 gas mixtures, but for a gas mixture with 10% of methane, this contribution is found to be negligible ($<1\,\%$).

Except for m/z 28 dominated by N_2 signature, the ion masses chosen in the MID method correspond to product formation in mass regions C2, C3 and C4, with 2, 3 or 4 heavy (C or N) atoms bearing species respectively.

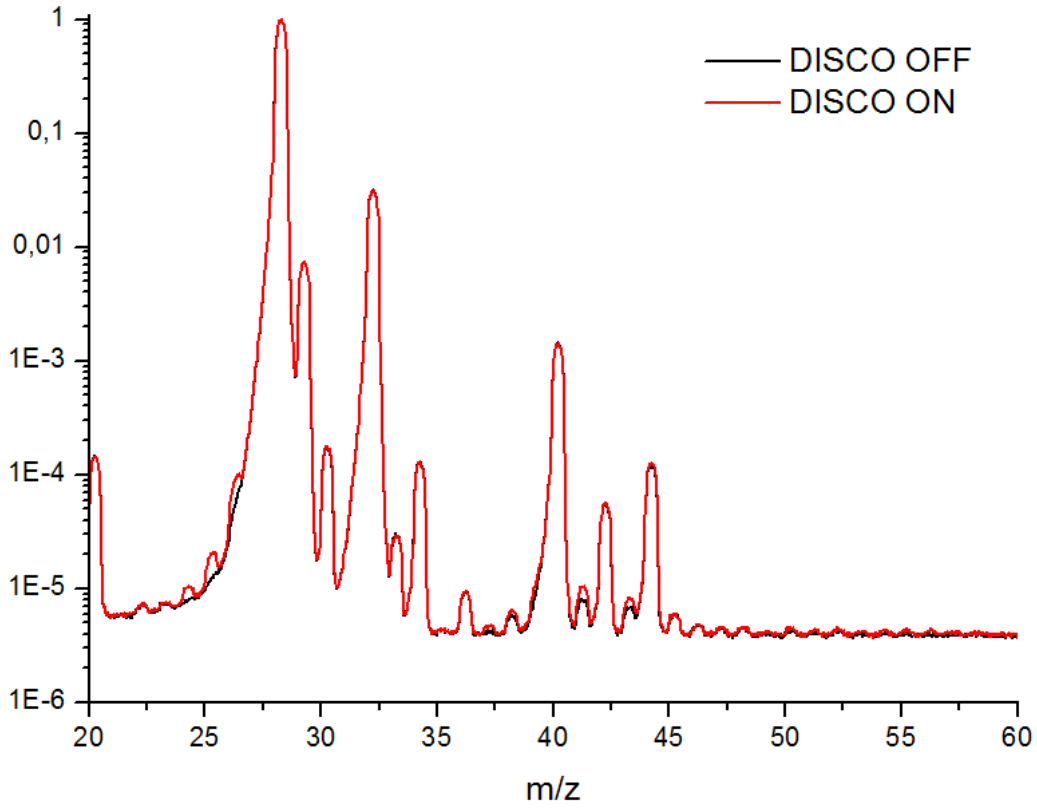

Figure 4.4: Effect of ∼1 h DISCO irradiation on the *in situ* MS relative intensities (with respect to the maximum around m/z 28) of a 10 sccm reactive gas mixture, with HP in the MS.

4.2.2 Data treatment of scan analogs

As can be seen on the scan analogs obtained at 10 sccm with the DISCO ON and DISCO OFF conditions (Fig. 4.4), productions are not obvious for masses higher than m/z 50. In order to improve the signal-to-noise ratio for these larger masses, we use two integration methods described below.

4.2.2.1 Estimation of the relative concentration of the major products versus N_2

In order to determine the intensities of the peaks in the mass spectra, signal integration for each integer m/z is applied. Effective signals are obtained by excluding the additive contribution of the baseline (Listgarten and Emili, 2005), assumed constant in a spectrum and estimated by averaging the signals above m/z 70 (called the "asymptotic zone" thereafter). Taking into account a peak center shift from integer m/z to the right by 0.2 – 0.3 u, we integrate the baseline-corrected signals in the m/z interval [i-0.25, i+0.75] and affect the result to the intensity at m/z i. Then, all intensities are normalized with respect to m/z 28, yielding relative intensities. Difference spectra (DISCO ON – DISCO OFF), calculated from the integrated signals, provide an estimation of the product relative concentrations.

4.2.2.2 Treatment for heavy species ($m/z > 45$)

In the present operational conditions, the intensities in the difference spectra (*i.e.* the productions) of the heavy species are often close to the noise level of the mass spectrometer. To detect any

significant production, the occurrence of significant peaks at masses above m/z 45 has been tested against pure noise. We checked that the signal in the asymptotic zone ($m/z > 70$) can be assimilated to white noise (Gaussian distribution, no autocorrelation) in all experiments. The spectra are baseline corrected as described above, and normalized to the maximal intensity of the m/z 28 peak. The cumulated sum (CS) of the MS DISCO ON – DISCO OFF difference is calculated, starting the summation from the higher mass limit ($m/z = 80$). Thereafter, the resulting data are named Difference Mass Spectra Cumulated Sum (DMS-CS).

Using this procedure, significant deviations of the DMS-CS trace from pure noise are easier to detect than by inspecting the raw or even unit-integrated difference MS. Significant deviations are identified against the 3-sigma (99%) confidence interval (CI) DMS-CS for pure white noise signals with mean 0 and variances equal to the asymptotic variance of each DISCO OFF and DISCO ON signals. The 99% CI is defined by $\mathrm{CI99}(k) = [-3 * U(k), 3 * U(k)]$, where $U(k) = \left\{(k - k_{\max} + 1) * \left(u_{\mathrm{On}}^2 + u_{\mathrm{Off}}^2\right)\right\}^{1/2}$ where k is the index of the current MS point, u_{ON} and u_{OFF} are the standard deviations of the signals in the asymptotic zone.

4.2.3 Cryogenic trap and GC-MS analysis

In order to detect and identify low concentration products, we installed a cryogenic trap on the outlet of the APSIS reactor, upstream of the vacuum pump. The trap, immersed in liquid nitrogen, is a cylindrical glass coil of 1.3 cm diameter with a total volume of 133 cm^3, described in Gautier et al. (2011). The gas mixture is pumped from the reactor through the cryogenic trap by the primary pump (Fig. 4.2). Products resulting from the reaction inside the reactor condense in the trap according to their phase diagrams. It has been checked that neither nitrogen nor methane condenses in the trap.

The trap is settled on the experiment for 8 hours, after which it is isolated and heated up to room temperature. Once evaporated, the trapped products are injected in a Gas Chromatograph coupled to a Mass Spectrometer (GC-MS) through a six-port valve to perform direct gas injection. The GC-MS device used is a ThermoScientific GC-Trace with a ThermoScientific DSQ II mass spectrometer in quadrupole detection mode. The column is a MXT-QPlot (Restek) of 30 m length, 0.25 mm internal diameter, and 10 µm stationary phase thickness. The stationary phase in this column is a porous polymer optimized to separate light organic molecules, bearing typically 1 to 5 carbon atoms. A temperature programming was used for the analysis, starting with an isotherm at 30 °C for five minutes, followed by a gradient of 5 $°\mathrm{C.min}^{-1}$ from 30 °C to 190 °C, and ending with a second isotherm at 190 °C for 5 min. The carrier gas is helium (99.999%) with a constant flow rate of 1 $\mathrm{mL.min}^{-1}$. Helium flow is injected through the trap in order to ensure a better introduction of products into the GC. Injector is heated up to 250 °C and operates in the splitless mode. Temperature of the ion source is set at 200 °C. A blank run is performed before each injection, to ensure that there is no contamination from the previous run.

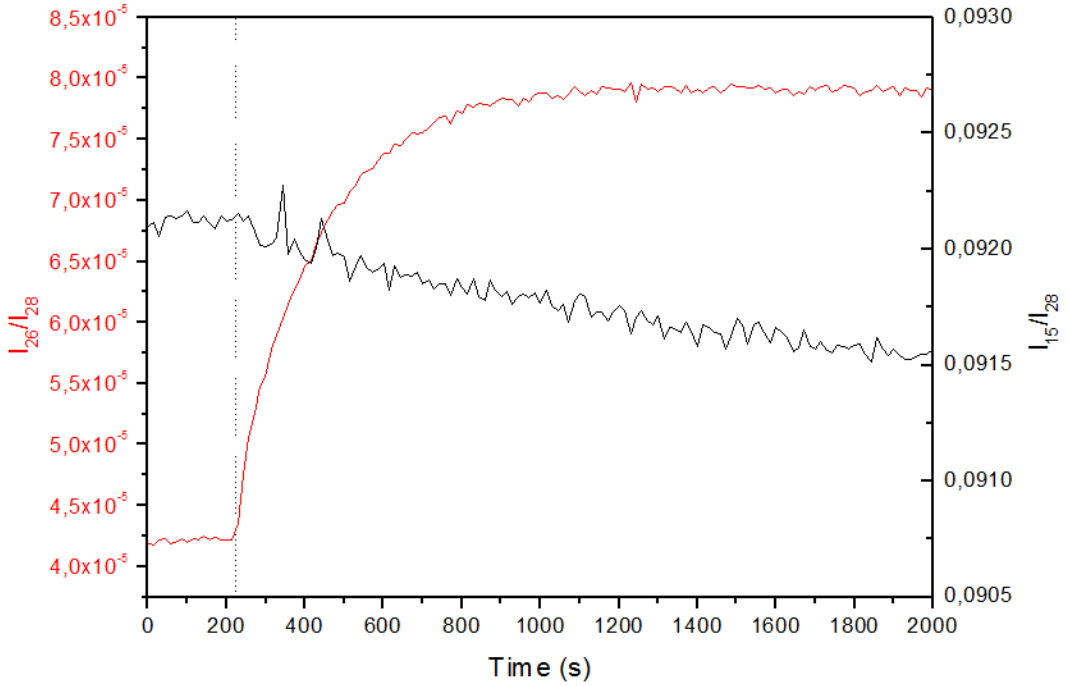

Figure 4.5: Monitoring of methane consumption (I_{15}/I_{28}) (black, right axis) and acetylene production (I_{26}/I_{28}) (grey, left axis) for 7 sccm of injected 90-10 N_2-CH_4 gas mixture. The irradiation start is depicted by the vertical dashed line at 200 s.

4.3 Results

4.3.1 MS time-dependent measurements

4.3.1.1 Methane consumption

The time evolution of the ratio of MID signals for an experiment performed at 0.6 sccm is given in Fig. 4.5, where I_{15} and I_{28} are respectively the simultaneously measured intensities of the mass peaks at m/z 15 and 28. It represents the evolution of the methane over nitrogen ratio during the experiment. The starting time of the photolysis by the DISCO beamline can be easily located by the instantaneous increase of acetylene production detected at m/z 26 (Fig. 4.5).

Methane relative consumption may be calculated by:

$$\frac{\Delta\,[CH_4]}{[CH_4]_0} = \frac{(I_{15}/I_{28})_0 - (I_{15}/I_{28})_{SS}}{(I_{15}/I_{28})_0} \tag{4.1}$$

The subscript 0 refers to the initial conditions (before the irradiation by the synchrotron beam) and the subscript SS refers to the steady state conditions when MS signal reaches an asymptotic value.

The methane relative consumption obtained for different gas flow conditions is reported in Tab. 4.2. The methane relative consumption at SS slightly increases when the gas flow decreases, from a few 10^{-3} for 10 sccm up to 1% for 0.6 sccm. This evolution is consistent with a dilution effect of the photons: at 0.6 sccm, the photons absorbed by methane (in the 100-130 nm wavelength range) penetrate in the reactor for about 15 cm, and only about 3 cm at 10 sccm.

$N_2 + CH_4$ gas flow (sccm)	$\frac{\Delta[CH_4]}{[CH_4]_0}$	$\sigma\left(\frac{\Delta[CH_4]}{[CH_4]_0}\right)$
0.6	1.7×10^{-2}	0.3×10^{-2}
2	4.6×10^{-3}	1.0×10^{-3}
7	3.4×10^{-3}	0.6×10^{-3}
7	3.0×10^{-3}	0.6×10^{-3}
7	3.7×10^{-3}	1.7×10^{-3}
10	3.2×10^{-3}	0.2×10^{-3}

Table 4.2: Methane relative consumption obtained for gas flows increasing from 0.6 to 10 sccm.

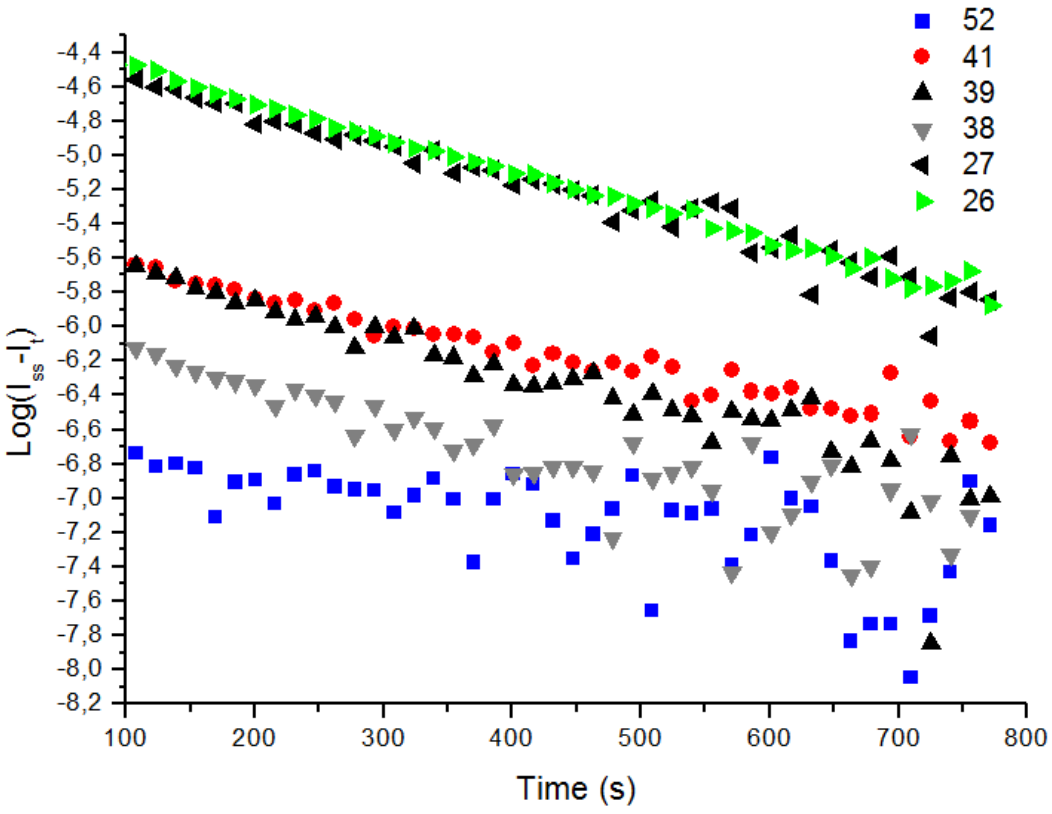

Figure 4.6: Time dependent evolution of the parameter $\log\left(I_{SS} - I\left(t\right)\right)$ for an experiment led at 10 sccm, for m/z 26, 27, 38, 39, 41 and 52.

4.3.1.2 Time-scale of the experiments

The timescale τ of the experiments is deduced from the time dependence of the m/z 26 ion abundance. As seen on Fig. 4.6, this species follows a simple exponential law:

$$I_{26}\left(t\right) = I_{26_{SS}} - \left(I_{26_{SS}} - I_{26_0}\right) \times \exp\left(-\frac{t}{\tau}\right) \tag{4.2}$$

where $I_{26_{SS}}$ is the stationary intensity, I_{26_0} the initial intensity (before irradiation), and τ the timescale of the observed evolution.

The timescale τ is obtained by a linear fit of $\log\left(I_{26_{SS}} - I_{26}\left(t\right)\right) = -t/\tau + \log\left(I_{26_{SS}} - I_{26_0}\right)$ (Fig. 4.6). The timescale is of about 5-8 minutes in all the gas flow conditions studied: from 320 s at 0.6 sccm and up to 500 s at 10 sccm, comparable to the residence time of the gas in the reactor, of a few minutes.

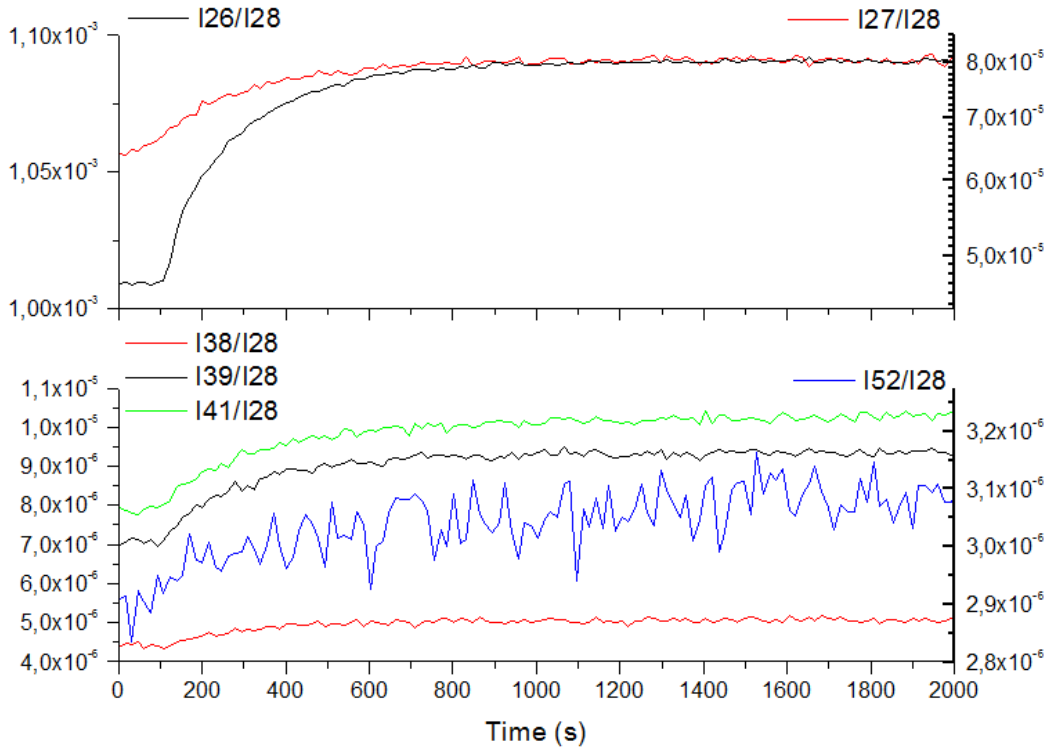

Figure 4.7: Time monitoring of products for a 10 sccm experiment.

m/z	**26**	**27**	**38**	**39**	**41**	**52**
10 sccm	500±10 s	515±30 s	645±120 s	490±60 s	705±50 s	990±360 s
0.6 sccm	320±20 s					

Table 4.3: Production time-scales for the peaks at m/z 26, 27, 38, 39, 41 and 52.

4.3.1.3 Product formation kinetics

Species with mass signatures at m/z 26, 27, 38, 39, 41 and 52 are produced simultaneously with methane consumption (see Fig. 4.6), showing a production of C2, C3 and C4 species. Even if the MS peak intensities are not directly representative of the corresponding neutral concentrations due to the different ionization thresholds and fragmentation patterns of the products, the ratio of the main peaks intensities against the one at m/z 28, provides a rough estimation of the mole fraction of the products diluted in N_2. Fig. 4.7 informs us that the products mole fractions are about 10^{-5} for C2 compounds and around the ppm for C3 and C4 species.

The calculated timescales for the above-mentioned masses in the 10 sccm experiments are reported in Tab. 4.3. A slight increase of the timescale is observed with the size of the products: from about 500 s for C2 compounds, up to 600-700 s for C3, and up to 1000 s for C4 compounds, in agreement with a sequential growth process.

The overlap of the fragments in the MS does not allow to explicitly identify those products. For example the mass peak at m/z 27 could be given by HCN^+ or the fragment ion $C_2H_3^+$ of C_2H_4. In order to rectify this ambiguity, we accumulated the products in a cryogenic trap and analyzed the content by GC-MS.

4.3.2 Products identification with the Cryogenic Trapping - GC-MS analysis

This part was performed in collaboration with A. Buch at the Laboratoire de Génie des Procédés et Matériaux.

The GC-MS analysis of products accumulated during 8 running hours of a 7 sccm experiment is shown on Fig. 4.8. It confirms the detection of C2, C3 and C4 compounds by in situ mass spectrometry MID analysis. If we assume that the GC-MS response is the same for C2 to C4 compounds we can also assume that the concentration of C2 compound is larger than C3 and C4 compounds. More interestingly, GC-MS enables the unambiguous identification of the major C2 species, such as ethane (C_2H_6), ethylene (C_2H_4) and acetylene (C_2H_2), the major C3 compounds (acetonitrile CH_3CN, propane C_3H_8 and propene C_3H_6), and C4 compounds (2-butene C_4H_8 and ethane dinitrile C_2N_2 (cyanogen)). Hydrogen cyanide, HCN, is not clearly detected in the cold trap, but it could be co-eluted with water, leading to the large peak at 17 – 18 min in the chromatogram.

4.3.3 Effect of enhancing the pressure in the mass spectrometer

The low mole fractions of about 10^{-5} observed by MID for the major products in C2 and C3 are near the detection limit of the MS. The use of this instrument in standard conditions prevents therefore any detection of products with lower concentrations, in particular for heavier compounds.

In order to enhance the dynamic range and consequently the sensitivity of the MS detection, we performed a second series of experiments in the same conditions as described in Tab. 4.1, with a shortened sampling capillary length between the APSIS reactor and the MS. The pressure reached in the ionization chamber of the MS increased from $P_{MS} = 10^{-6}$ mbar (LP Low Pressure) in the first set of experiments, up to $P_{MS} = 10^{-4}$ mbar (HP High Pressure) in the second case. The effects are illustrated on Fig. 4.9, on the example of a 10 sccm experiment. The baseline intensity is actually efficiently decreased from about 2×10^{-5} down to 4×10^{-6}, enabling to detect previously invisible products.

However, this pressure increase in the MS is not without undesirable consequences. A secondary effect is observed at high pressure in the MS on Fig. 4.9: the ratio I_{14}/I_{28} reflecting the fragmentation pattern of N_2 is lower than at low pressure. The ratio between these two mass peaks should ideally be pressure-independent, fragmentation patterns being defined by the direct and the dissociative ionization pathways of the reaction between molecular nitrogen and electrons at 70 eV in the ionization chamber.

In order to further study this unsuitable effect, we introduced only molecular nitrogen in the MS, at various pressures. Results are given in Fig. 4.10. A constant I_{14}/I_{28} ratio is obtained for P_{MS} between 2×10^{-7} to 6×10^{-6} mbar, but a strong non-linear behavior is observed above $P_{MS} = 6 \times 10^{-6}$ mbar.

The operating instructions of the instrument recommends to work with pressures no larger than $P_{MS} = 10^{-5}$ mbar in the ion source with the Secondary Electron Multiplier as a detector, in spite of the possibility to use the filament up to a pressure of $P_{MS} = 10^{-4}$ mbar. Mao and Leck (1987); Tilford (1994) reported that non-linear sensitivities can actually be observed at pressures in the range $10^{-5} - 10^{-4}$ mbar, possibly due to ion space charge effects. Some variations of fragmentation patterns of H_2 and H_2O have also been reported at high pressure by Breth et al. (1983a,b). We show that an evolution of the fragmentation pattern of N_2 can also be observed at pressures below $P_{MS} = 10^{-5}$ mbar. We have checked that this effect does not depend on the gas temperature

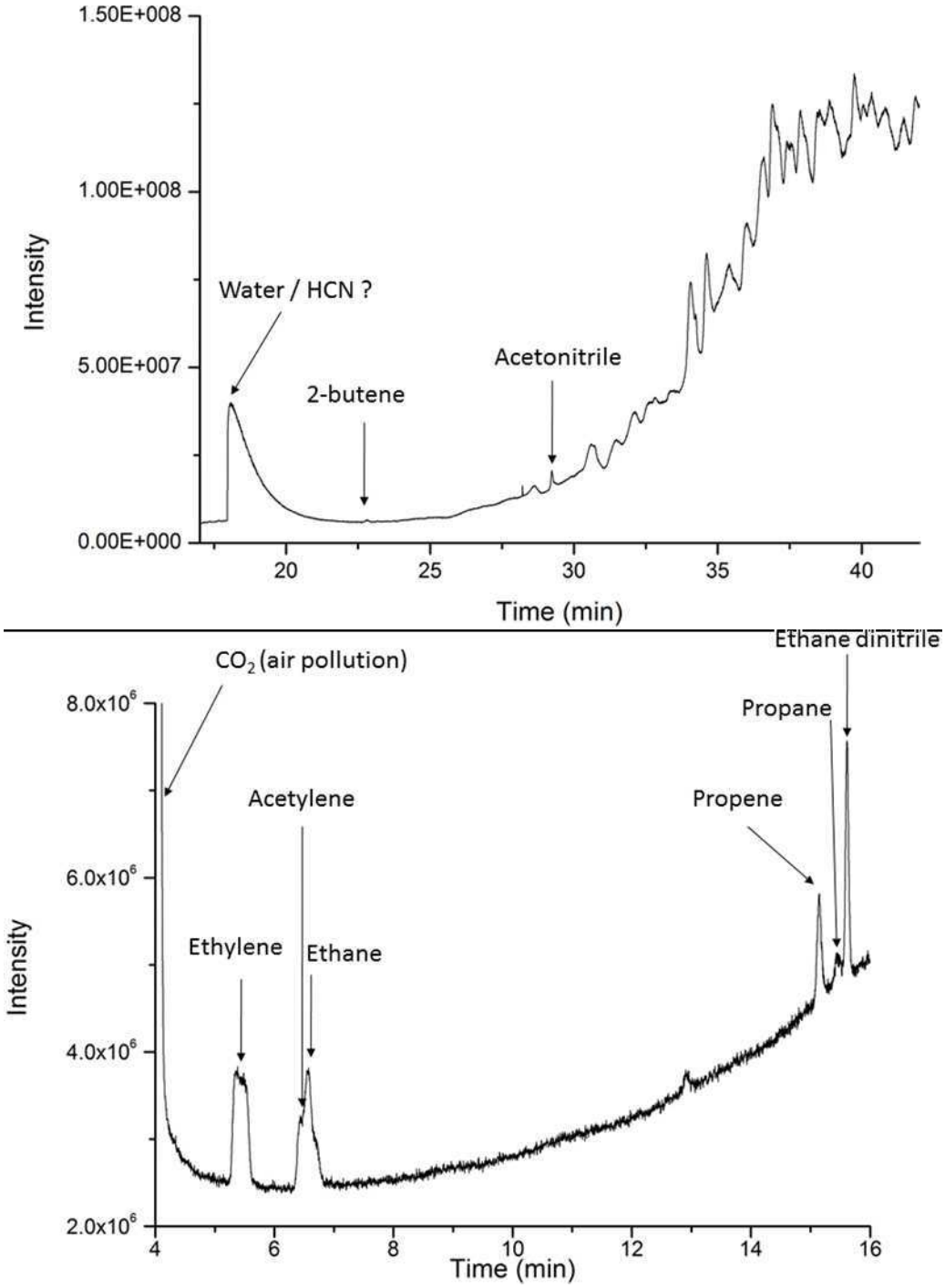

Figure 4.8: Chromatograms of the sample evaporated from the cryogenic trap.

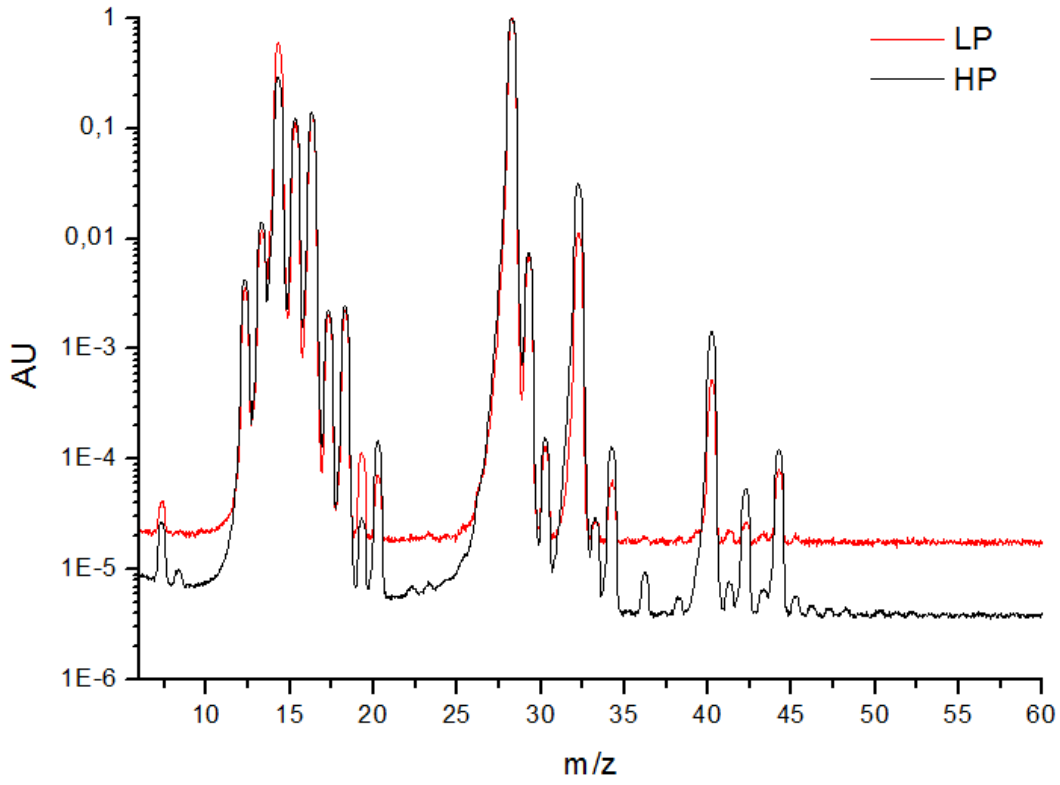

Figure 4.9: Comparison of the scan analog initial mass spectra obtained for a similar 10 sccm experimental conditions in the cases of (in grey) a low 10^{-6} mbar pressure condition in the MS; and (in black) a high 10^{-4} mbar pressure condition in the MS.

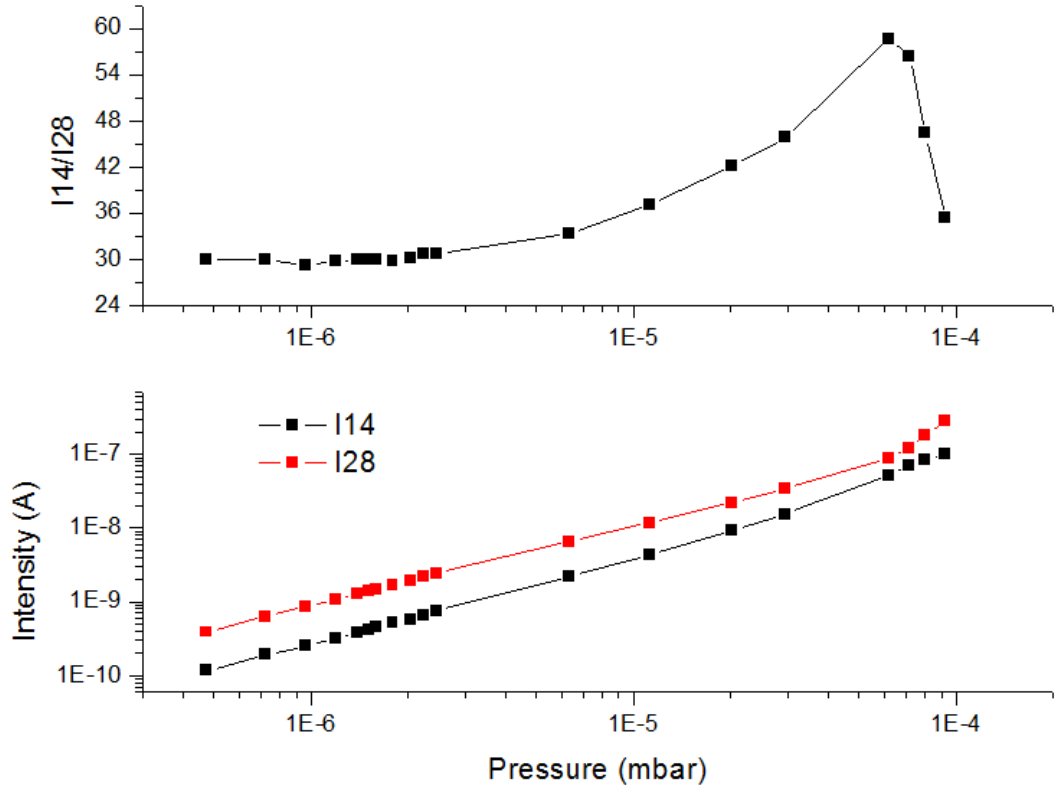

Figure 4.10: (Lower panel) Evolution of I_{14} and I_{28} for a pure nitrogen influx in the MS, at various pressure conditions; (upper panel) Pressure dependence of the ratio I_{14}/I_{28}.

(temperature lowered from room temperature down to about 200 K), and that no cross-sensitivity is observed by mixing nitrogen with a second gas like argon, helium or hydrogen.

The non-linear effects, detected at high P_{MS} pressures on the I_{14}/I_{28} signature, are certainly affecting the fragmentation patterns of other species and prevent us from any quantitative analysis. Nevertheless, in order to detect products with smaller concentrations in the scan analog MS configuration (see Analytical techniques section), we favored a high P_{MS} pressure condition in the mass spectrometer for the rest of the study (P_{MS} = a few 10^{-5} mbar), as done also by Imanaka and Smith (2007, 2010).

4.3.4 Products detection by mass spectrometry

The difference spectra, generated as described in the data treatment section, are calculated at all working flow rates: 0.6, 2, 7 and 10 sccm (Fig. 4.11). We observe that photochemical products appear at all flow rates in the C2 (m/z 25 – 30), C3 (m/z 38 – 44) and C4 (m/z 49 – 57) regions. However, only the production of C2 compounds is seen unambiguously for all conditions. The productions of C3 and C4 species become significant only at higher flow rates (7 sccm and 10 sccm), except for C_3H_8 at m/z 44.

For experiments which have been repeated at the same gas flow, some differences are noticeable, but they decrease with increasing gas flow, as expected from the signal to noise ratio improvement. However a few masses with densities above the noise level at m/z 27, 29, 31, 33 display repeatability issue. These mass peaks are located in the wings of the peaks of intense species (visible on Fig. 4.4), N_2 and O_2 (O_2 from the residual air in the MS, as described in Carrasco et al. (2012)). A slight variation in the peak shape between two scan analogs is sufficient to perturb the integrated mass spectra difference for these species.

As a result of low influx, the pressure in the reactor is low, hence that in the MS is also low: P_{MS} increases from 2.7×10^{-5} mbar for the experiment at 0.6 sccm up to 2.0×10^{-4} mbar for the experiments at 10 sccm. Working at low pressure elevates the baseline level and leads to a smaller dynamic range of the spectrum (see Fig. 4.9). The product signals seem not high enough to be significantly detected considering the low signal to noise ratio in these conditions. As, in the higher mass range (m/z 45 – 80) of our experiments, the abundances are low, the DMS-CS (see Section 4.2.2) are plotted in Fig. 4.11 for all the experiments. One sees that at 0.6 and 2 sccm, the experimental signals do not depart from the pure noise limits. It is therefore illusory to detect any product in this mass range. At 7 sccm, both experiments rise above pure noise at masses below m/z 56, revealing the presence of C4 compounds, albeit in barely detectable densities. The situation is improved at 10 sccm, where the C4 group is significantly rising above pure noise. The systematic departure from the null axis of both experiments hints to some signal emerging in the C5 range, below m/z 70, but still below the significance limit.

We therefore focus on the higher gas flow conditions, 7 and 10 sccm. When the flow rate increases from 7 sccm to 10 sccm, the relative intensities are globally preserved. The C2, C3 and C4 relative concentrations can be calculated from the spectra on Fig. 4.11: C2 are around 10^{-5}, C3 around 10^{-6} and C4 slightly higher than 10^{-7}. This expected trend of decreasing relative concentrations with the heavy atom number is predicted in Dobrijevic and Dutour (2006), and observed by Gautier et al. (2011); Thejaswini et al. (2011).

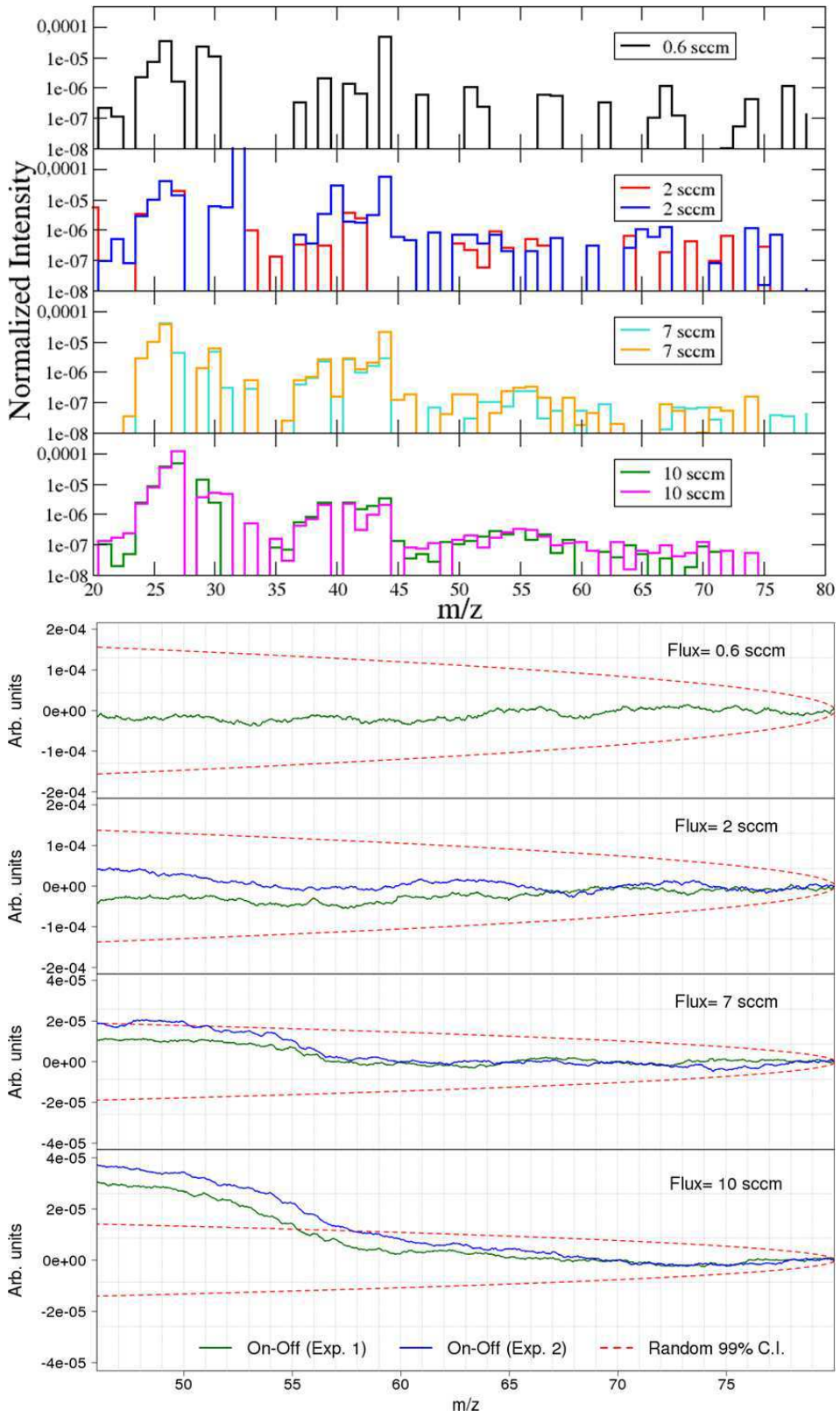

Figure 4.11: *Top*: difference between the MS of the initial state and the state after 1 h irradiation obtained for various gas flows in the APSIS reactor (and HP conditions in the MS).
Bottom: cumulative sum of "ON - OFF" MS differences (DMS-CS) for the different available pressure conditions (black and gray curves). The DMS-CS is computed starting from the higher masses. It is compared with the 99% confidence interval for the DMS-CS between two Gaussian random variables with mean 0 and variances equal to the asymptotic variance of the ON and OFF signals (gray dash).

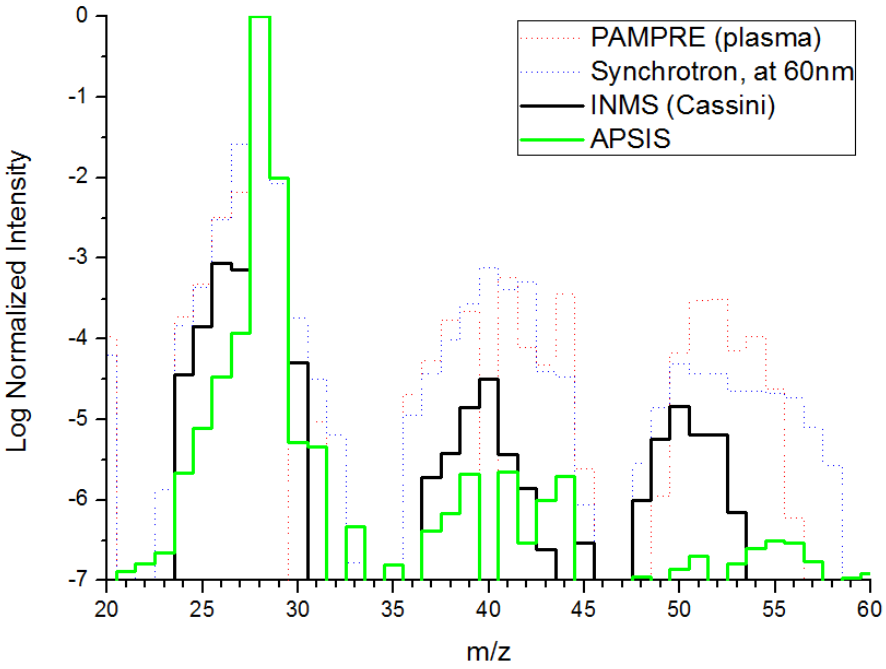

Figure 4.12: Mass spectra of neutral species in (a) the PAMPRE plasma discharge study (Carrasco et al., 2012) (black dot), (b) a synchrotron experiment at 60 nm reported in (Imanaka and Smith, 2010) (grey dot), (c) Titan atmosphere measured by the INMS (Waite et al., 2007) (black solid), and (d) the APSIS experiment at 10 sccm (grey solid). The intensities at m/z=28 and 29, corresponding to N_2, in (a) and (d) are artificially added for convenience in comparison.

4.4 Discussion

We compared on Fig. 4.12 the neutral mass spectrum obtained at 10 sccm with the APSIS experiment with other neutral compositions observed in several cases of interest for Titan atmospheric study: (a) the neutral mass spectrum obtained with the PAMPRE plasma discharge (Carrasco et al., 2012); (b) the neutral mass spectrum obtained with a synchrotron radiation experiment with 60 nm photons (Imanaka and Smith, 2010); and (c) a measurement of the INMS mass spectrometer onboard Cassini (Waite et al., 2007). We have chosen the m/z 20 - 60 range to focus on the significant productions observed with the APSIS experiment, corresponding to the C2, C3 and C4 compounds. In the experimental simulations, the peaks at m/z 40 and 44 are often disturbed by a contribution of argon and carbon dioxide respectively due to residual air signature in the system. The productions at these masses should therefore not be further considered.

A general decrease of the intensities with the size of the detected species is well observed in all spectra, but with differing orders of magnitude, reported in Tab. 4.4. The product mixing ratios in the 60 nm synchrotron irradiation (Imanaka and Smith, 2010) and in the PAMPRE plasma discharge (Carrasco et al., 2012) are one order of magnitude higher than in Titan INMS spectra and about two orders of magnitude higher than in the APSIS experiment.

Mass spectra	C2	C3	C4
PAMPRE, plasma	10^{-3}	10^{-4}	$10^{-5} - 10^{-4}$
Synchrotron, 60 nm	10^{-3}	10^{-4}	10^{-5}
INMS	10^{-4}	$10^{-6} - 10^{-5}$	$10^{-6} - 10^{-5}$
APSIS	10^{-5}	10^{-6}	10^{-7}

Table 4.4: Order of magnitude of the neutral product mixing ratios. Observed in Titan atmosphere (INMS), in a synchrotron experiment at 60 nm (Imanaka and Smith, 2010), in the plasma PAMPRE experiment (Carrasco et al., 2012) and in APSIS.

The higher productions in PAMPRE and in the reactor of Imanaka & Smith may result from their higher energy deposition. In APSIS, the production is lower than in Titan atmosphere despite a higher photon influx (Fig. 4.1). This could be due to a much shorter residence time of the gas: a few hundred seconds in the APSIS reactor (Tab. 4.1) compared to $10^7 - 10^8$ s in Titan's stratosphere (see Chapter 5 and Lebonnois et al. (2001)).

More important is the distribution among the products, in particular the ratio between the intensities at *m/z* 26 and 27, corresponding on a first approach to the mixing ratios of C_2H_2 and HCN. Both the synchrotron radiation study at 60 nm and the PAMPRE plasma experiments measure a significantly higher intensity at *m/z* 27, in opposition to the INMS and the APSIS mass spectra.

Other nitrogen-bearing species, CH_3CN *m/z* 41, and C_2N_2 *m/z* 52, are detected in Titan and in the APSIS and PAMPRE reactors, but not significantly in the synchrotron experiment of Imanaka and Smith (only an upper limit for CH_3CN is provided by their MS deconvolution analysis) (Imanaka and Smith, 2010). CH_3CN and C_2N_2 are both produced by reactions involving atomic nitrogen as a reactant: $N\left(^2D\right) + C_2H_4 \longrightarrow CH_3CN + H$ and $CHCN + N \longrightarrow C_2N_2 + H$ respectively.

Nitrogen atoms are also efficiently adsorbed on the reactor walls. Therefore, we can suspect in the case of Imanaka and Smith that a lower pressure decreases the bimolecular reaction rate to benefit atomic nitrogen adsorption on the walls (M. Smith, personal communication).

Overall, in spite of systematic lower productions rates, the APSIS reactor provides a new complementary tool to simulate Titan atmospheric reactivity. In the future, the low production efficiency could be improved by either decreasing the pressure in the reactor or prolonging the residence time of the reactive gas.

4.5 Conclusion

A new reactor, named APSIS (Atmospheric Photochemistry SImulated by Synchrotron), has been designed to simulate planetary atmospheric photochemistry processes. We report here a study focusing on Titan's upper atmosphere. We used a nitrogen-methane gas flow irradiated by a continuous 60-350 nm VUV beam provided by the DISCO line at SOLEIL synchrotron radiation facility. The neutral photochemical products were monitored by mass spectrometry, showing a time-scale of about 15 min, and a measurable production of species with two up to four (probably five) heavy atoms. The C2 hydrocarbons are by far the major products, but nitrogen bearing species such as HCN, CH_3CN and C_2N_2 were also detected, in agreement with Cassini's INMS observations at Titan.

We compared the mass spectra with those obtained by a plasma experiment (Carrasco et al., 2012) and with another synchrotron based experiment (Imanaka and Smith, 2010), and with the

in situ measurements of the INMS mass spectrometer instrument onboard Cassini probing the neutral content of Titan's upper atmosphere. In spite of lower photochemical production efficiency and different environmental conditions, the APSIS reactor seems to simulate Titan's neutral composition rather well. Nevertheless, its production efficiency should be improved in the future by increasing the residence time of the gas in the reactor.

The pressure in the reactor is higher than in Titan upper atmosphere. The main differences expected on the chemistry compared to Titan are developed in a review paper (Cable et al., 2012): influence of termolecular reactions, more efficient quenching of excited states... Nevertheless, working at higher pressure is mandatory for adapting the mean free path of the reactants to the reactor scale. Seeing that none of the simulation experiments previously discussed convincingly reproduces the neutral compounds in Titan atmosphere at both levels of species identity and relative amounts, we present a modeling study in the next chapter, to help interpret these experiments and to improve their performance.

Overall, the feasibility of the novel APSIS experiment, for atmospheric photochemistry simulation, has been demonstrated in this study, showing the great interest of this platform for further investigation of planetary atmospheres.

Chapter 5

Photochemical modeling of the APSIS experiments

Contents

The existing experimental results of APSIS (see Chapter 4) are not able to give us detailed insights into the formation pathways of the photochemical products. In order to understand this mechanism better, we developed a model of the APSIS experiments, starting from tools already used for the atmospheric photochemistry of Titan (see Chapters 2 and 3).

This model is a fully coupled one, integrating simultaneously photolysis, neutral chemistry and ion chemistry. Both neutral and ionic photolysis pathways, whose branching ratios are expressed by our new probabilistic representation (see Section 2.2.4), are taken into account in the model.

The spectrum of the DISCO beam, in which 30 % of the photons are able to ionize the major reactants (N_2 and CH_4), hints at the importance of ion chemistry. However, we have *a priori* no knowledge about *the key ionic reactions* in the chemical scheme in the conditions of APSIS. Having known very few important reactions in the chemistry of the APSIS experiments, we have to start with a reaction scheme as complete as possible, to avoid getting misleading results from an arbitrarily simplified chemical scheme, although a simplified scheme is much less expensive in calculation time.

As previously discussed, there are many reactions whose kinetic parameters (cross-sections and branching ratios in photolytic processes, preexponential factors and activation energies in thermal reactions *etc.*) are measured with large uncertainty or even estimated (most rate constant uncertainty factors vary from 2 to 10). Thus, it is necessary to include the uncertainties on input parameters and results (*i.e.* species concentrations) in the model of the APSIS reactor. In this case, a statistical distribution of concentration is much more informative than a nominal value only.

An important advantage of modeling laboratory simulations is that we avoid the large uncertainties on some parameters due to the extrapolation to low temperature. Sander et al. (2006) proposed to estimate the uncertainty factor of a rate constant at temperature T, $F(T)$, by the following formula

$$F(T) = F(300\,\mathrm{K}) \exp\left|g\left(\frac{1}{T} - \frac{1}{300\,\mathrm{K}}\right)\right| \tag{5.1}$$

where g is an "uncertainty-extrapolation" coefficient. Since measurements are usually conducted at room temperature (300 K), the uncertainties on the extrapolated rate constants increase exponentially as temperature decreases to that of Titan's atmosphere (∼100-150 K). In the model of a laboratory setup at room temperature, this problem disappears: we do not need to extrapolate the rate constants. The uncertainties on the rate constants are considerably reduced.

However, it is quite expensive to perform statistics on the results of repeated runs of the model with uncertain parameter samples generated by Monte Carlo method (*e.g.* 500 runs, each run costs at least one day for a preliminary 2D model).

On the other hand, because the MS sampling through the capillary at various positions results in similar spectra with only slight pressure change in the APSIS experiments (see Fig. 4.3), we assume, for simplicity, a uniform distribution of gas in the reactor, *i.e.* a 1-cell model (see Fig. 5.1). This transport simplification cancels much of the heaviness of calculation, enabling to take into account the complete reaction scheme. The stationary state of the model becomes reachable in moderate calculation time and the statistics on the uncertain results is realizable.

5.1 Model description

In the 1-cell model, we assume no transport in the reactor and a uniform distribution of all species. However, we try our best to incorporate most information while working at low dimensionality: the gas inflow and outflow are still taken into account; the radiative transfer is considered through the Beer-Lambert-type photoabsorption, but in the assumption of the uniform gas (the residual photon flux, resulting in the absorbed photon number, is obtained according to the Beer-Lambert law).

5.1.1 Total balance and transport

We express explicitly the advection relevant to the gas inflow and outflow in the present model.

We observe that the pressure in the reactor hardly varies during the experiments and has only a slight decrease in the direction of the gas transport, according to the *in situ* MS results (see Chapter 4), indicating a nearly uniform motion of the gas in the reactor. We assume a constant gas advective velocity v_{ad} (in m.s^{-1}) in the reactor for the modeling of the experiments. Assuming the ideal gas law, v_{ad} is calculated from the reactive gas inflow rate q_{re} (in sccm in the experiments, converted into mol.s^{-1} in the model, given the temperature T at 300 K) and the reactive gas partial pressure P_{re} (in mbar in the experiments, converted into Pa in the model) in the reactor by

$$v_{ad} = \frac{RTq_{re}}{P_{re}A}, \tag{5.2}$$

where the reactor's cross-section A is also converted into m^2 to keep *all quantities in the model in SI units* (the same below).

The carrier gas inflow rate q_{ca} can be obtained as the counterpart of the reactive gas in their contribution to the total pressure P, by the following formula

$$q_{ca} = \frac{(P - P_{re})\, Av_{ad}}{RT}. \tag{5.3}$$

We assume that at the exit of the reactor, the gas is pumped out also at v_{ad}, so as to ensure, in absence of reactions, the mass balance anywhere in the reactor, including at the entrance and the exit. Hence, the residence time of the reactive gas t_{res} is

$$t_{res} = \frac{L}{v_{ad}} \tag{5.4}$$

where L is the reactor length (in m).

However, in the presence of reactions, the concentration variation due to the transport and the reactions should be considered simultaneously. Thus, the differential of concentration for the ith species, c_i (in mol.m^{-3}), can be written as

$$\frac{\mathrm{d}c_i}{\mathrm{d}t} = Q_i + R_i \tag{5.5}$$

where t is time, Q_i and R_i are the concentration variation (in mol.m^{-3}.s^{-1}) due to transport and reactions, respectively.

Considering the single cell in the model, the term Q_i can be written as

$$Q_i = \frac{\Phi_{i,in} - \Phi_{i,out}}{L} \tag{5.6}$$

where $\Phi_{i,in}$ and $\Phi_{i,out}$ are respectively the influx and the outflux of the ith species. As discussed

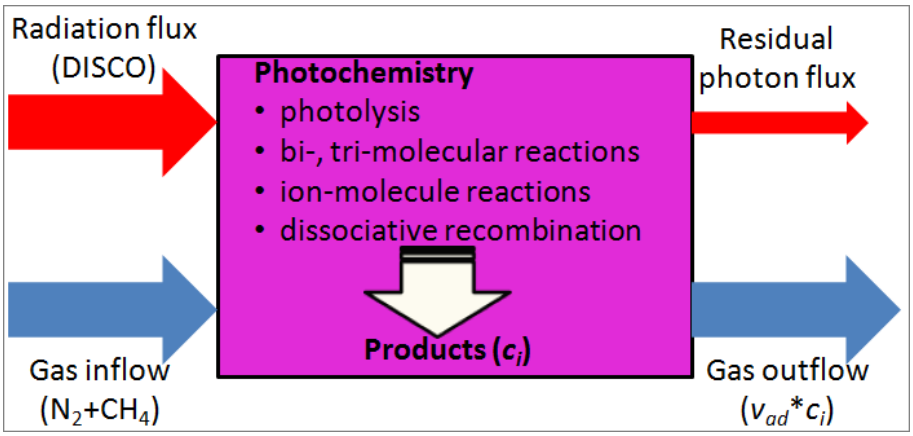

Figure 5.1: Scheme of the 1-cell model.

about the advection above, $\Phi_{i,in}$ and $\Phi_{i,out}$ are, in detail,

$$\Phi_{\mathrm{N_2},in} = \frac{0.9 q_{re}}{A} \tag{5.7}$$

$$\Phi_{\mathrm{CH_4},in} = \frac{0.1 q_{re}}{A} \tag{5.8}$$

$$\Phi_{\mathrm{He},in} = \frac{q_{ca}}{A} \tag{5.9}$$

$$\Phi_{i,in} = 0 \qquad \forall i \notin \{\mathrm{N_2},\ \mathrm{CH_4},\ \mathrm{He}\} \tag{5.10}$$

and

$$\Phi_{i,out} = c_i v_{ad} \tag{5.11}$$

respectively.

5.1.2 The reaction scheme

R_i in Eq. 5.5 measures the algebraic sum of the rate of all reactions involving the ith species.

The chemical scheme incorporates the neutral chemistry, *i.e.* photodissociation, bimolecular thermal reaction and trimolecular thermal recombination, from Hébrard (2006); Hébrard et al. (2009) complete neutral model, with adaptations for the photolysis branching ratios as described earlier (see Section 2.2.4). In addition, thanks to the complete ionic chemistry database established by Plessis et al. (2010), all known reactions of photoionization, ion-molecule reaction and dissociative recombination involving C, H and N atoms are added in the reaction list while reactions involving O atoms are excluded, since dioxygen is just a trace gas in the reactor and does not play a significant role in the photochemistry in APSIS according to the GC-MS results (see Fig. 4.8). Electronic impact in Plessis et al. (2010) is also excluded from the present model, since the photoelectrons (the only electron source in the APSIS reactor) have hardly sufficient energy to ionize the medium.

In total, there are 244 species (125 neutrals and 119 ions) reacting with each other through 1708 reactions in the present chemical scheme (Tab. 5.1).

There is also a scheme commonly used for dissociative recombination in the models, called "H-loss" scheme, in which we only consider the fragmentation pattern with a loss of a single H atom, *i.e.*

$$\mathrm{MH^+} + e^- \longrightarrow \mathrm{M} + \mathrm{H} \tag{5.12}$$

Reaction type	Number of reactions
Photolysis	33
Bimolecular reactions	415
Trimolecular reactions	82
Dissociative recombination (Full / H-loss)	574 / 114
Ion-molecule reactions	604

Table 5.1: Number of reactions of each type in the present models.

for all MH^+ ions (Plessis et al., 2012). We also study the effect of an "H-loss" scheme, composed of 114 reactions, in the present model, for a comparison with the full dissociative recombination scheme.

The rate equations of the included reaction types are listed below:

- photolysis:

$$v_{ij}^{ph} = J_{ij} c_i \tag{5.13}$$

where v_{ij}^{ph} and J_{ij} are respectively the rate (in mol.m^{-3}.s^{-1}) and the rate constant (in s^{-1}, for its calculation see Section 5.1.3) of the jth channel of the photolysis of the ith involved species.

- neutral bimolecular and trimolecular reactions:

$$v_i^{bi} = k_i^{bi} c_{i,1} c_{i,2} \tag{5.14}$$

$$v_i^{tri} = k_i^{tri} c_{i,1} c_{i,2} \tag{5.15}$$

where v_i^{bi} and k_i^{tri} (in m^3.mol^{-1}.s^{-1}) are respectively the rate and the rate constant of the ith neutral bimolecular reaction, v_i^{tri} and k_i^{tri} (in m^3.mol^{-1}.s^{-1}) are those of the ith neutral trimolecular recombination, and $c_{i,1}$ and $c_{i,2}$ are the concentrations of the two reactants. Note that a third molecule involved in trimolecular recombination always acts as an excess energy receptor, but not a real reactant. k_i^{bi} and k_i^{tri} are respectively calculated by the Kooij formula (modified Arrhenius equation) and the Lindemann-Hinshelwood equation, *i.e.*

$$k_i^{bi} = A_i \left(\frac{T}{300\,\mathrm{K}} \right)^n e^{-\frac{E_{a_i}}{RT}} \tag{5.16}$$

and

$$k_i^{tri} = \frac{k_{0_i} k_{\infty_i} c_M}{k_{0_i} c_M + k_{\infty_i}} \tag{5.17}$$

where A_i, n and E_{a_i} are respectively the preexponential factor (in m^3.mol^{-1}.s^{-1}), a unitless power and the activation energy (in J.mol^{-1}) of the ith neutral bimolecular reaction, k_{0_i} (in m^6.mol^{-2}.s^{-1}) and k_{∞_i} (in m^3.mol^{-1}.s^{-1}) are respectively the rate constants at low-pressure and high-pressure limits of the ith neutral trimolecular recombination, and c_M represents the total gas concentration in the reactor (in mol.m^{-3}, deduced from the total pressure P). k_{0_i} and k_{∞_i} are also obtained by the Kooij formula with the pre-exponential factors and activation energies provided in the databases.

- ion-molecule reactions and dissociative recombination:

$$v_{ij}^{im} = k_i^{im} b_{ij}^{im} c_{i,ion} c_{i,neu} \tag{5.18}$$

$$v_{ij}^{dr} = k_i^{dr} b_{ij}^{dr} c_{i,ion} c_{el} \tag{5.19}$$

where k_i^{im}, b_{ij}^{im} and v_{ij}^{im} are respectively the total rate constant (in $\mathrm{m^3.mol^{-1}.s^{-1}}$), the branching ratio of the the jth channel and the rate of the jth channel of the ith ion-molecule reaction, and k_i^{dr} (in $\mathrm{m^3.mol^{-1}.s^{-1}}$), b_{ij}^{dr} and v_{ij}^{dr} are those of the ith dissociative recombination. $c_{i,ion}$ and $c_{i,neu}$ are respectively the concentrations of the ion and the molecule involved in the ith ion-molecule reaction or dissociative recombination. c_{el} represents the total electron density (in $\mathrm{mol.m^{-3}}$, equal to the total ion concentration under the assumption of electro-neutrality of the reactor). It is assumed that k_i^{im} are not sensitive to temperature, thus, we refer directly to the database (Plessis et al., 2010) for its value. k_i^{dr} has the following temperature dependence

$$k_i^{dr} = k_{i,0}^{dr} \left(\frac{T_e}{300\,\mathrm{K}} \right)^{-n} \tag{5.20}$$

where $k_{i,0}^{dr}$ and n are the total rate constant of the ith dissociative recombination measured at 300 K and a unitless power, respectively. T_e is the electronic temperature. We assume $T_e = T$ in this study, in view of the pressure of a few mbar in the reactor, high enough to thermalize the photoelectrons before their dissociative recombination (we also checked that even in the cases at low pressure (see Sections 5.3.2 and 5.4.3), whose real T_e is often much higher (T_e=750 K in the test case), the results are similar).

Associative recombination is also a known reaction type (Troe, 2005). It forms ion-molecule adducts with a reactivity to some extent (McLain et al., 2009). However, according to the NIST database, this type of reactions are generally not enough exergonic ($|\Delta_r G^o| < 10\,\mathrm{kJ.mol^{-1}}$) to be considered independently of their precursors. We can still use a fast equilibrium approximation to treat them: they are regarded as intermediates of the reactions of their precursors and ignored in the present model.

5.1.3 Radiative transfer and photolysis rate constant

In the standard formulation of Beer-Lambert absorption, we have

$$I(x,\lambda) = I_0(\lambda)\, e^{-\sum_i \tau_i(x,\lambda)} \tag{5.21}$$

where x is the position or the optical path from the entrance ($x = 0$), $I(x,\lambda)$ and $I_0(\lambda)$ are respectively the photon fluxes at the wavelength λ (in $\mathrm{mol.m^{-3}.s^{-1}}$) at the position x and the entrance. $\tau_i(x,\lambda)$ is the optical depth of the ith absorber at wavelength λ and position x. It depends on the ith absorber's concentration $c_i(x)$ in the covered optical path and photoabsorption cross-section at wavelength λ, $\sigma_i(\lambda)$ (in $\mathrm{m^2.mol^{-1}}$), which is expressed as

$$\tau_i(x,\lambda) = \sigma_i(\lambda) \int_0^x c_i(x)\,\mathrm{d}x. \tag{5.22}$$

The photolysis rate constant of the jth channel of the ith absorber at the position x, $J_{ij}(x)$, is given by

$$J_{ij}(x) = \int_{\lambda} I(x,\lambda)\,\sigma_i(\lambda)\,b_{ij}(\lambda)\,\mathrm{d}\lambda \tag{5.23}$$

where $b_{ij}(\lambda)$ is the branching ratio at wavelength λ of this channel.

However, there is only one large cell in the present model. $J_{ij}(x)$ at the cell center, $J_{ij}(\bar{x})$, commonly chosen as $J_{ij}(x)$ of the whole cell in atmospheric modeling studies (Hébrard et al., 2007), is not appropriate for the present model. Here, we calculate the average of $J_{ij}(x)$ along the optical path, *i.e.* the reactor length L,

$$\overline{J_{ij}(x)} = \frac{\int_0^L J_{ij}(x)\,\mathrm{d}x}{L}. \tag{5.24}$$

Based on the assumption of gas uniformity, one can easily derive

$$\overline{J_{ij}(x)} = \int_{\lambda} I_0(\lambda)\,\sigma_i(\lambda)\,b_{ij}(\lambda)\,\frac{1-e^{-L\sum_i (c_i\sigma_i(\lambda))}}{L\sum_i (c_i\sigma_i(\lambda))}\mathrm{d}\lambda \tag{5.25}$$

where the wavelength is also discretized with a resolution, $\Delta\lambda$, of 1 nm, adapted to the spectral resolution in the database of Hébrard et al. (2006). The additional photolysis data used in this study, the SWRI database (Huebner and Link, 2011), are interpolated using Gauss-Legendre quadrature to fit the present wavelength discretization.

5.1.4 Integration method

In addition to the stationary state, the time-evolution of the model is also of interest, because it provides a comparison with the evolution results in the experiments (see Figs. 4.5, 4.6 and 4.7 and Tab. 4.3). Therefore, we perform an integration of Eq. 5.5 over time rather than find the stationary state of the whole system by a faster method.

The implicit-explicit Runge-Kutta-Chebyshev (IRKC) method (Shampine et al., 2006), capable of integrating systems of partial differential equations (PDEs), is applied to the present model. It handles the equations by both an explicit part $F_E(t,y)$ and an implicit part $F_I(t,y)$, *i.e.*

$$y'(t) = F_E(t,y) + F_I(t,y) \tag{5.26}$$

For a transport-reaction model, it is suggested that F_E and F_I respectively decribe the parts of a cell's differential which are dependent (*e.g.* diffusion and photolysis) and independent (*e.g.* thermal reactions) on other cells. The latter, F_I, is usually regarded as a system of ordinary differential equations (ODEs) and can be very stiff. In consideration of the high complexity and the large difference between the time-scales of ionic and neutral reactions, the reaction scheme of the present model may also be very stiff. The IRKC method is able to cope with the problem of stiffness in F_I (Verwer and Sommeijer, 2004).

The present model has no internal transport. In theory, the whole model can be considered as a set of ODEs and solved in F_I or by other ODE solvers. However, the photolysis is treated in

Case	Radiation	Pressure (Pa)	Temperature (K)	Residence time (s)	Modification of reaction scheme	Uncertain parameters
1	DISCO	700	300	284.2	no	all
1a	DISCO	700	300	284.2	no	photolysis
1b	DISCO	700	300	284.2	no	bi-, trimolec.
1c	DISCO	700	300	284.2	no	DR
2	DISCO	700	300	284.2	only neutral*	all
3	DISCO	700	300	284.2	H-loss DR**	all
4	60 nm (DISCO flux)	700	300	284.2	no	all
5	82 nm (DISCO flux)	700	300	284.2	no	all
6	Solar (DISCO flux)	700	300	284.2	no	all
7	DISCO	7×10^{-4}	300	284.2	no	all
8	DISCO	700	150	284.2	no	all
9	Solar (flux at Titan)	7×10^{-4}	150	2.842×10^{6}	no	all
10	60 nm (flux: 10^{16}ph.s^{-1})	6.6	300	113.7	no	all
11a	Solar (flux at Titan)	7×10^{-4}	150	2.842×10^{6}	only neutral	all
11b	Solar (flux at Titan)	7×10^{-4}	150	2.842×10^{6}	H-loss DR	all
12a	60 nm (flux: 10^{16}ph.s^{-1})	6.6	300	113.7	only neutral	all
12b	60 nm (flux: 10^{16}ph.s^{-1})	6.6	300	113.7	H-loss DR	all

Table 5.2: Summary of the 1-cell model variants in this study. *only neutral: only neutral reactions in the chemical scheme; **H-loss DR: only H-loss pathways for dissociative recombination.

F_E, as in real transport-reaction models, because of the problem of its Jacobian evaluation. The Jacobian is crucial for many ODE integration methods as well as the implicit function of IRKC method, F_I. As we still treat the radiative transfer explicitly, very complex evaluation of Jacobian elements concerning the photolysis makes it impractical to regard the photolysis rate equations as ODEs.

Besides, IRKC provides a simple way to account for diffusion. For further studies in higher dimensionality (1D or 2D), IRKC would be more powerful according to the system's transport-reaction nature: the part of thermal reactions, independent on other cells, could be treated implicitly and separately in each cell, so that it could be repeatedly implemented by the program. The features above lead to small storage requirements and good calculation performance.

Tests were performed to verify the convergence and the stability of the stationary state of the present model integrated by IRKC method.

5.2 Results of the reference APSIS model (Case 1)

The reference case of the APSIS model corresponds to the experiments at 7 sccm (see Chapter 4), which was the best one available when we began to develop the model. The conditions of the reference case are: a pressure of 7 mbar (700 Pa), room temperature (300 K) and a gas inflow of 7

sccm, resulting in a gas residence time of 284.2 s (see Tab. 5.2).

We integrate this model until the stationary state (after 1000 s, close to the time constant of the peak at m/z 52, the longest time constant measured in the APSIS experiments (see Chapter 4)). A Monte Carlo sample of 500 runs of the model is performed. The samples of all kinetic parameters and the concentrations of all species are stored for further treatment.

5.2.1 Relative abundance of the species

The distribution of the mole fractions at the stationary state (normalized with respect to N_2) is presented in Fig. 5.2. Starting from the C2 block, the concentrations of stable neutrals decrease, in general, with their molar mass, as expected (Fig. 5.3). Without taking the uncertainties into account, the main C2 species, *i.e.* C_2H_2, C_2H_4, C_2H_6 and HCN, have mole fractions around 10^{-5}, and the main C3 (C_3H_6, C_3H_8, *etc.*), C4 (C_2H_3CN, C_4H_8, *etc.*) mole fractions are close to 10^{-6} and 10^{-7}, respectively. In the C7 and C8 blocks, several species still have a mole fraction between 10^{-10} and 10^{-15}, *e.g.* C_7H_4, C_7H_6 and C_8H_2. Note that there are also stable products in the C0 and C1 blocks, *i.e.* H_2 and NH_3, respectively.

The decrease of the ion concentration with their molar mass is less evident. Most of the major ions (from C1 to C10) have mole fraction between 10^{-15} and 10^{-10}. However, several ions of relatively large stability, *i.e.* NH_4^+, $HCNH^+$, $CH_2NH_2^+$ *etc.*, are more abundant and determine the ion/electron density in the model.

Comparison to experimental results

The CH_4 consumption percentages in the experiments and in the model are respectively 0.30±0.06% and 0.07±0.01%. They are not in perfect agreement. Nevertheless, in view of the model's simplicity, a factor of ∼4 between them is still tolerable. The simplified description of advection and radiative transfer may result in a bias of the effective gas residence time and of the methane consumption.

The stationary concentrations of the products in the present 1-cell model are also globally in good agreement with the MS measurements in the APSIS experiments (Fig. 5.3), except some C2 concentrations, probably due to large measurement uncertainties of the intensities on the N_2's peak shoulders. Note that this good agreement is also based on the large uncertainty of the model prediction. Thus, the re-evaluation of very uncertain kinetic parameters is always needed.

The mole fractions of most products detected in the cryogenic trap experiment (see Chapter 4) are significantly large in the model. Some species were not detected in the APSIS experiments, *e.g.* NH_3 and CH_2NH, whose parent MS peaks are completely hidden by the signals of OH^+ and $^{14}N^{15}N^+$. But their formation is confirmed in the PAMPRE reactor in similar conditions (Carrasco et al., 2012), and thus likely in the APSIS experiments as well. Those are actually shown to be produced by the model. Besides, the model predicts the formation of other species with a concentration below the detection limit of the MS measurements, *e.g.* most C5 and C6 species, especially benzene.

5.2.2 Uncertainty on the species concentrations

The relative uncertainties on the stationary neutral and ion mole fractions are presented in Fig. 5.4. As in Hébrard et al. (2007); Peng et al. (2010), we observe in this study that the uncertainty factors increase with molecular mass, which may be roughly interpreted as the accumulation of

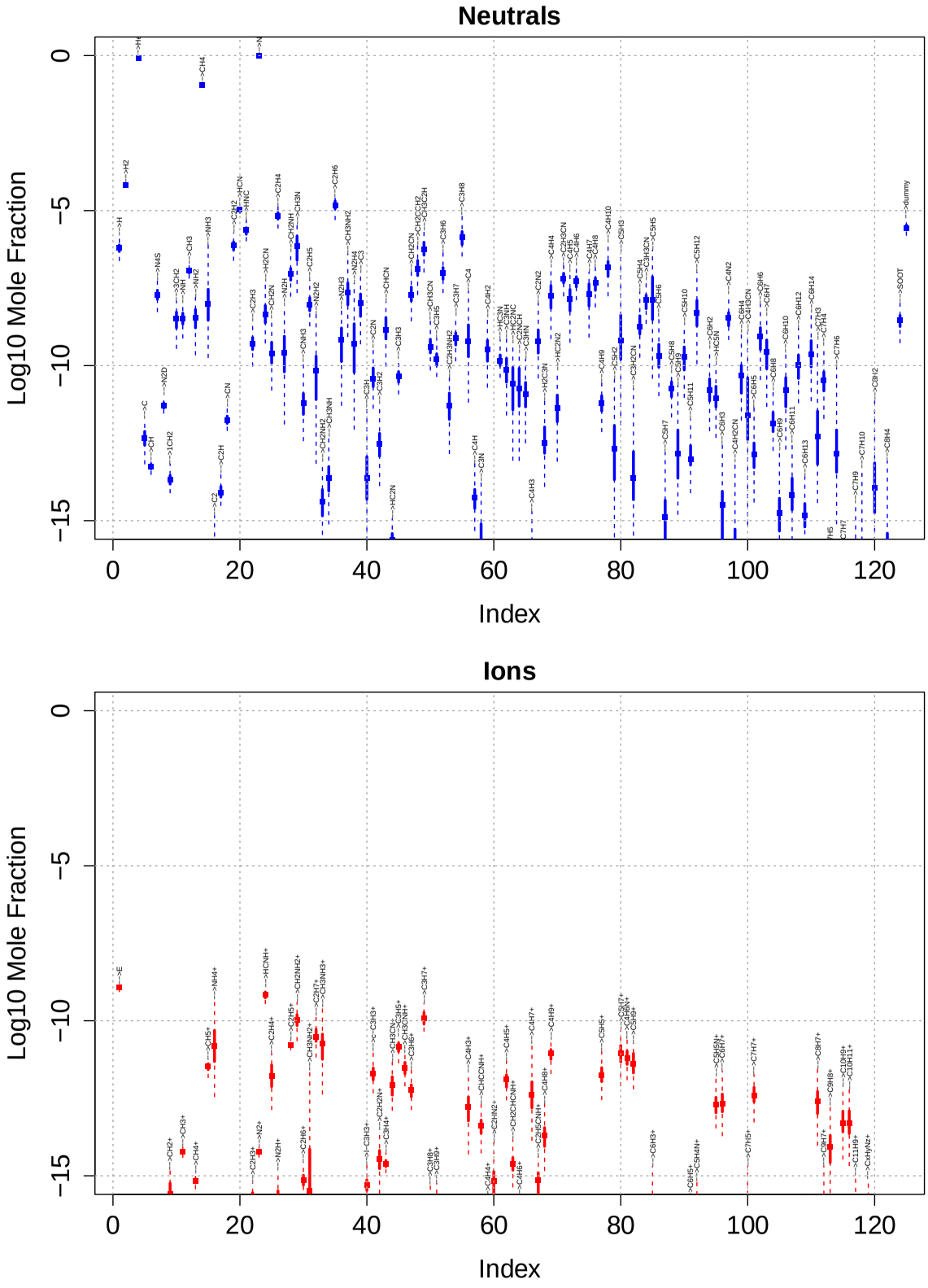

Figure 5.2: Boxplot of mole fractions (normalized with respect to N_2) of the neutrals (blue, upper) and the ions (red, lower) at the stationary state for the 500 runs of the 1-cell model with all uncertain parameters. Solid and dashed error bars cover respectively 50% and 95% confidence intervals.

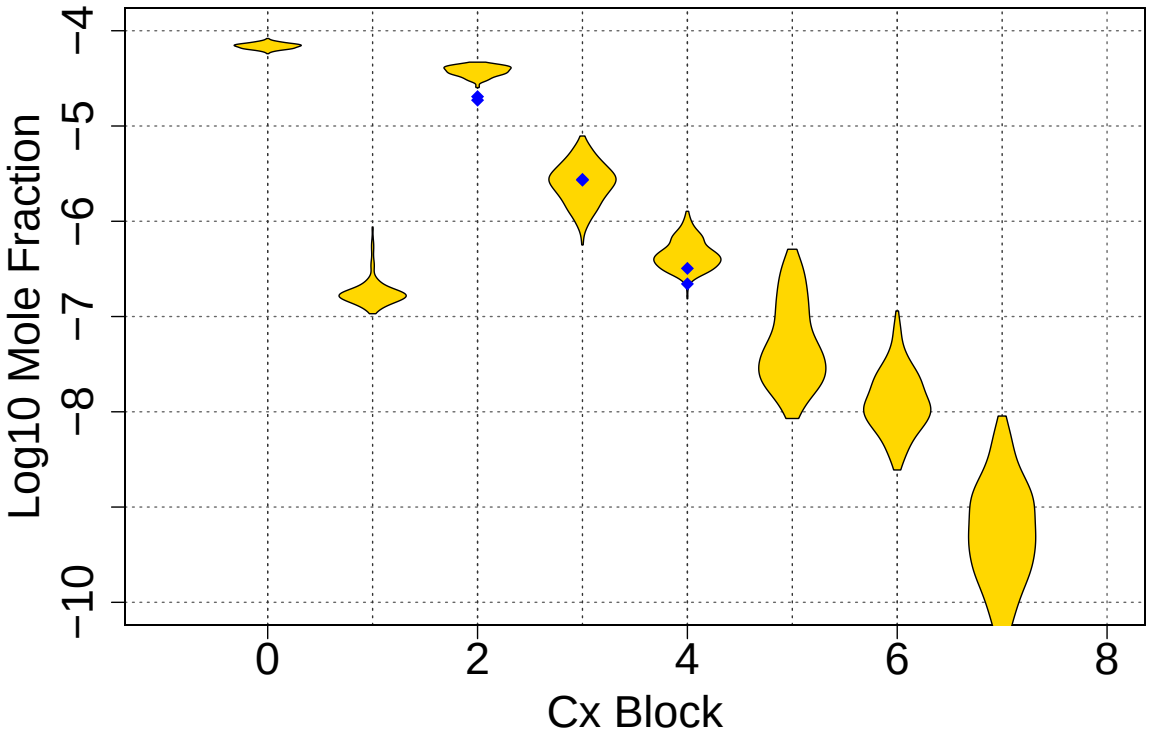

Figure 5.3: Violin plots of the mole fractions of the blocks (species with the same heavy atom (C or N) number) in the APSIS reference model. In each block, the distribution of the modeling results is expressed by a violin plot, whose widths at different mole fraction values show the corresponding probability density. Two sets of significant experimental results (C2-C4 blocks) are added (blue points). The experimental mole fractions in the C2-C4 blocks are respectively obtained from the experimental intensities divided by their corresponding approximate relative ionization cross-sections to N_2 (3, 4 and 5 for C2, C3 and C4 blocks, respectively, estimated according to Section 2.5). The mole fractions of N_2 and CH_4, not products, are excluded.

uncertainties on the kinetic parameters of reactions that molecular growth involves (except for some particular cases, *e.g.* those discussed in Peng et al. (2010)). In Fig. 5.4, the ion concentrations are generally more precise than those of neutrals of comparable molar mass, since measurements for ionic processes are usually conducted with lower uncertainties.

Sensitivity to reaction types

To analyze the dependence of the relative uncertainty of species concentrations on the reaction types, we calculate the ratios between the concentrations relative variances in the cases where only one *reaction type* is uncertain and those in the reference case with all uncertain reaction types (Case 1): photolysis (Case 1a), bi- and trimolecular reactions (neutral and ionic) (Case 1b), or dissociative recombination (Case 1c) (see Fig. 5.5).

If there were no correlation or interaction between *the reaction types* (not between specific reactions), the variances of the species concentrations in Case 1 would simply be the sum of those in Cases 1a, 1b and 1c, and thus, we would be able to identify the sensitivity of all reaction types directly.

The dominant contribution of bi- and trimolecular reactions to the concentration uncertainties in Case 1 can be identified, as well as the marginal contribution of photolysis and dissociative

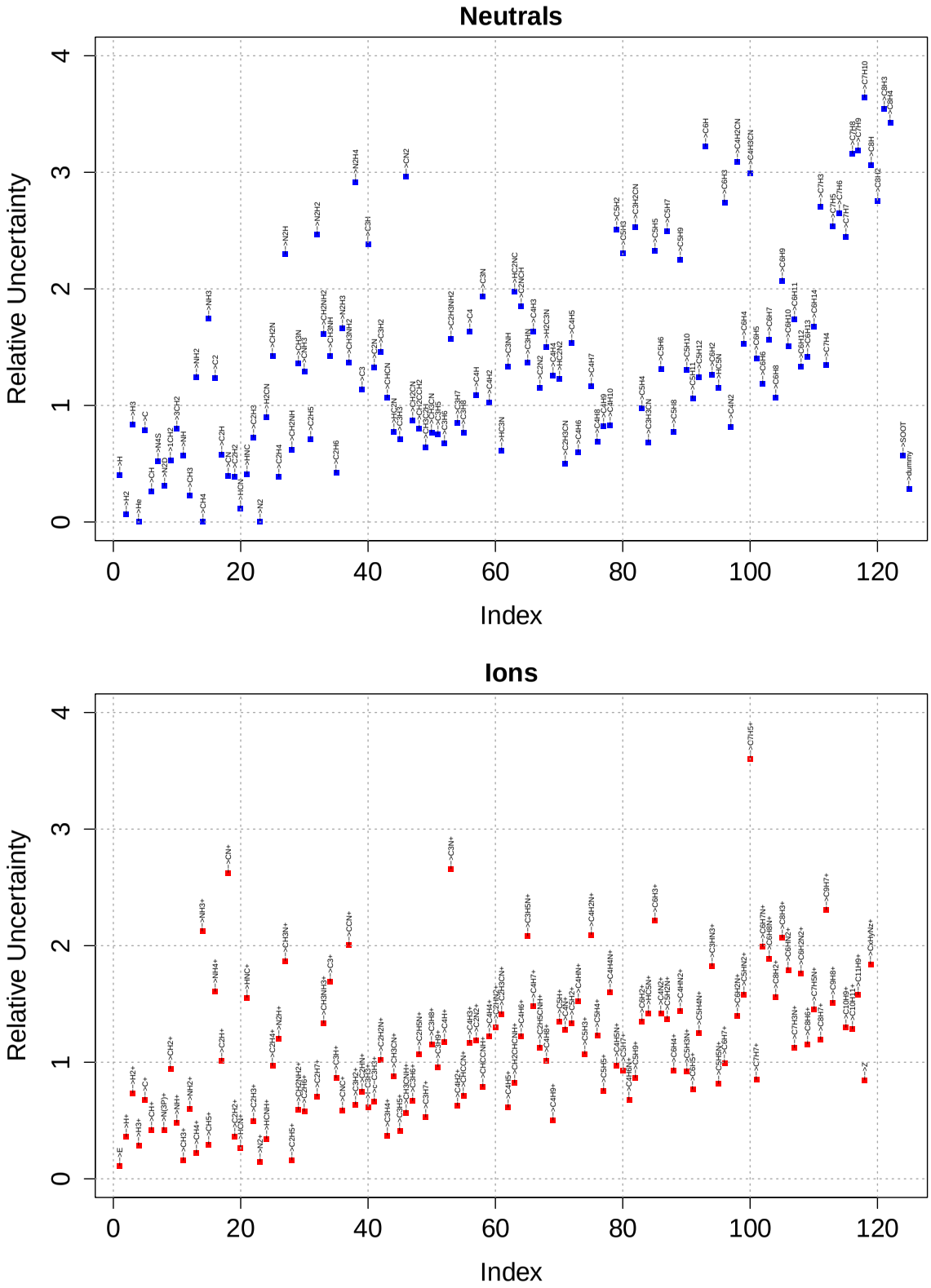

Figure 5.4: Relative uncertainties of the neutral (blue, upper) and ion (red, lower) concentrations at the stationary state of the 1-cell model with all uncertain parameters.

recombination to the concentration uncertainties, except for a minor part of the species, most of which are directly formed or consumed by these 2 reaction types (*e.g.* HNC, CH_3N and $CH_3NH_3^+$).

In the species concentration uncertainty budget, bi- and trimolecular reactions are dominant, due to the preponderant number of reaction of this type (∼1100/1700). Though representing a significant part of the reactions (∼550/1700), dissociative recombination, whose cross-sections are generally precisely measured and branching ratios are constrained to sum to 1, does not introduce much uncertainty. Therefore, it is to be noted that the highly uncertain representation of photolysis of methane and other photoabsorbers (see Section 2.2.4) does not increase output uncertainties substantially, though the photolysis have been demonstrated to be generally important at the level of individual reaction, since there are only 10 methane photolysis channels and 33 photolytic reactions in the present scheme.

5.2.3 Importance of the coupled ion-neutral chemical scheme

The ion chemistry has been found to play an important role in Titan's upper atmosphere, by analysis of the Cassini observation data or modeling (Wilson and Atreya, 2004; Waite et al., 2005; Vuitton et al., 2006, 2007; Yelle et al., 2010). Recently, Plessis et al. (2010, 2012) showed that the dissociative recombination significantly contributes to the neutral production. This neutral production is substantially decreased in general, if we apply the commonly used "H-loss" dissociative scheme.

However, the modeling studies mentioned above is based on either a rather reduced reaction scheme (Wilson and Atreya, 2004; Vuitton et al., 2007), or an indirectly coupled model (Plessis et al., 2010, 2012) (through iterations between a neutral model giving stationary neutral concentrations and an ion model giving stationary neutral production by the ion chemistry).

In this study, the photochemical model includes a reaction scheme as complete as possible and its neutral and ion parts are directly coupled. Thus, we can thoroughly study the effects of the ion chemistry and the H-loss dissociative recombination pathways on the products of the present model, by comparing the reference case with 2 cases (Cases 2 and 3 in Tab. 5.2) where the chemical schemes are subsets of the reference case.

Impact of ion chemistry on molecular growth

The mole fraction ratios between the model with a neutral chemical scheme (Case 2) and the reference model (Case 1), as well as the associated uncertainties, are presented in Fig. 5.6. We observe a spectacular difference between the stationary concentrations of the two cases. The C2 and several C3 species in Case 2 are produced by an amount comparable to Case 1. However, at higher masses, the species concentrations fall as molar mass increases, till 10^{-15} of those in Case 1. The neutral reactions are obviously not as efficient as the ionic reactions to achieve the growth of heavy species. This highlights the importance of the ion chemistry and its coupling with neutral chemistry in the reaction scheme, in agreement with Waite et al. (2005); Vuitton et al. (2006, 2007); Plessis et al. (2012).

Comparison to the H-loss model for dissociative recombination

In Fig. 5.7, the deviation of the stationary concentrations of the model with only H-loss pathways for dissociative recombination (Case 3) from those of the reference model is also notable.

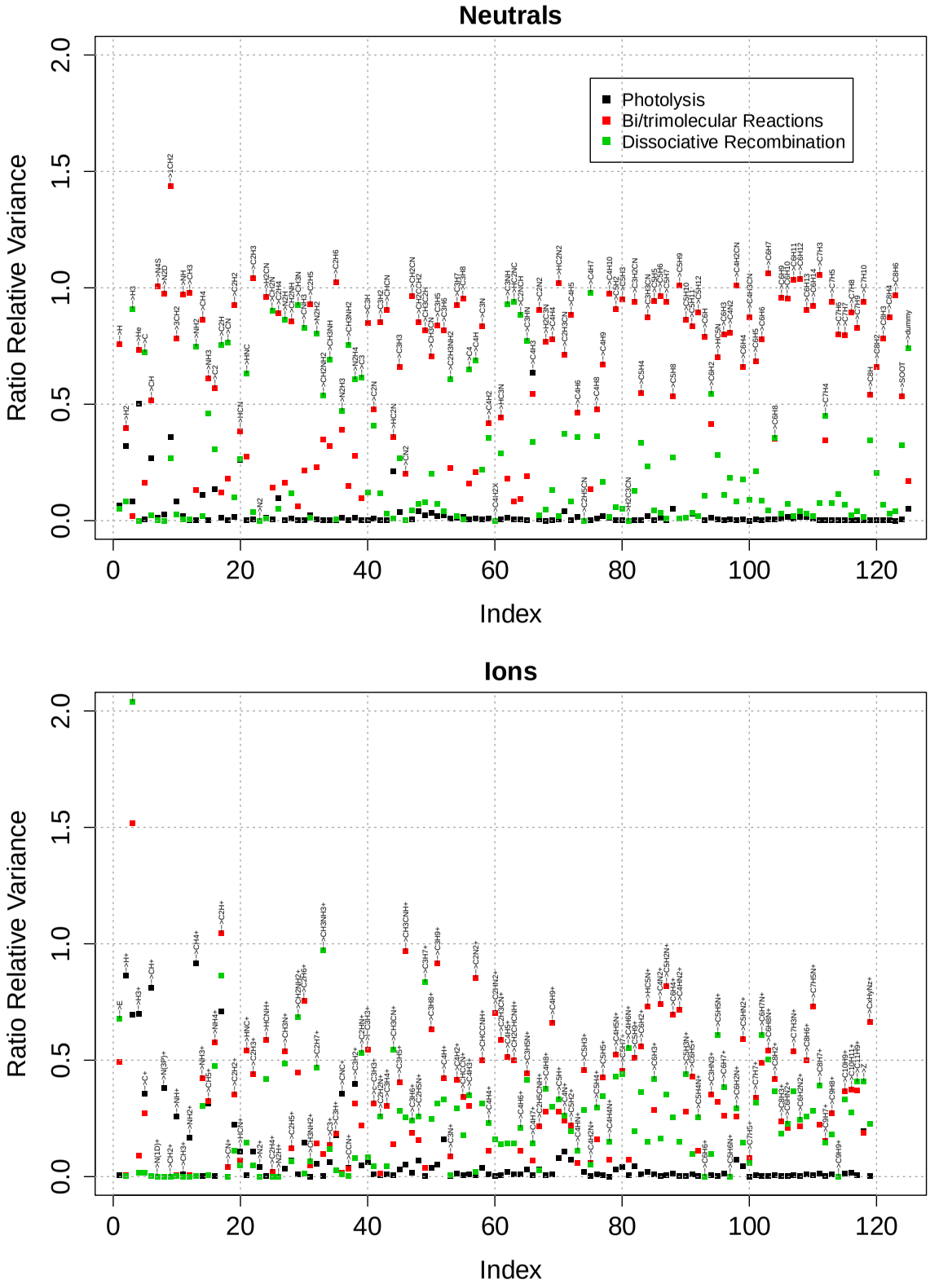

Figure 5.5: Ratios of relative variances of stationary concentrations in the 1-cell model with uncertain photolysis (Case 1a, black), bi- and trimolecular reactions (Case 1b, red), and dissociative recombination (Case 1c, green) to those with all uncertain reaction types.

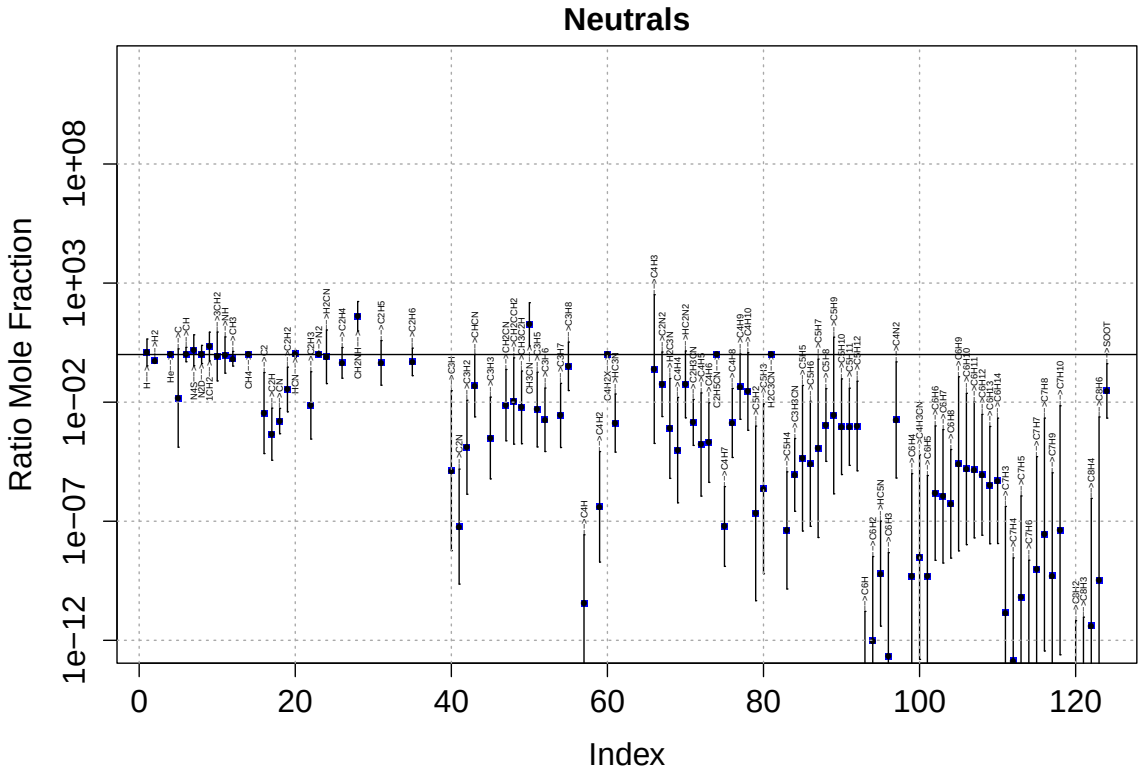

Figure 5.6: Ratios of stationary concentrations in Case 2 (neutral chemical scheme) to those in the reference model (Case 1). Ratios' mean values and uncertainties (95% confidence interval) are respectively denoted by squares and error bars.

Similarly to those in Case 2, the neutral concentrations in Case 3 remarkably decrease with molar mass from the values close to those in Case 1 to 10^{-10} of those in Case 1. Nevertheless, in each Cx block, the more unsaturated the species are, the more depleted. The most saturated species in each block are not significantly affected. Besides, several small species largely formed through dissociative recombination other than H-loss pathways, *i.e.* NH_3, N_2H_2 *etc.*, have concentration ratios between Case 3 and Case 1 distinctly lower than adjacent species in Fig. 5.7. There is also a generally decreasing tendency with molar mass among the ion concentration ratios, from 1 to 10^{-6}, less significant than the neutral concentration ratios.

Although, up to now, we have not found out why a complete dissociative recombination scheme has such strong influence on the species concentrations (discussed later, see Section 5.2.4.2), the complete dissociative recombination scheme is an important asset of the present model. This is in agreement with the conclusions of Plessis et al. (2012). The stationary concentrations in Case 3 are direct proofs of the importance of the complete dissociative recombination scheme, inferred by Plessis et al. (2012) through production rate calculations.

5.2.4 Identification of molecular growth pathways

A few studies were conducted for finding the *key reactions* of reaction networks in planetary atmospheres by computing the correlation coefficients between rate constants and species concentrations (Dobrijevic et al., 2010; Hébrard et al., 2009; Peng et al., 2010; Wakelam et al., 2010). Dobrijevic et al. (2011) suggested performing sensitivity analysis between rate constants and species concentrations in a low dimension model to build a reduced reaction scheme for 2D/3D model. In this

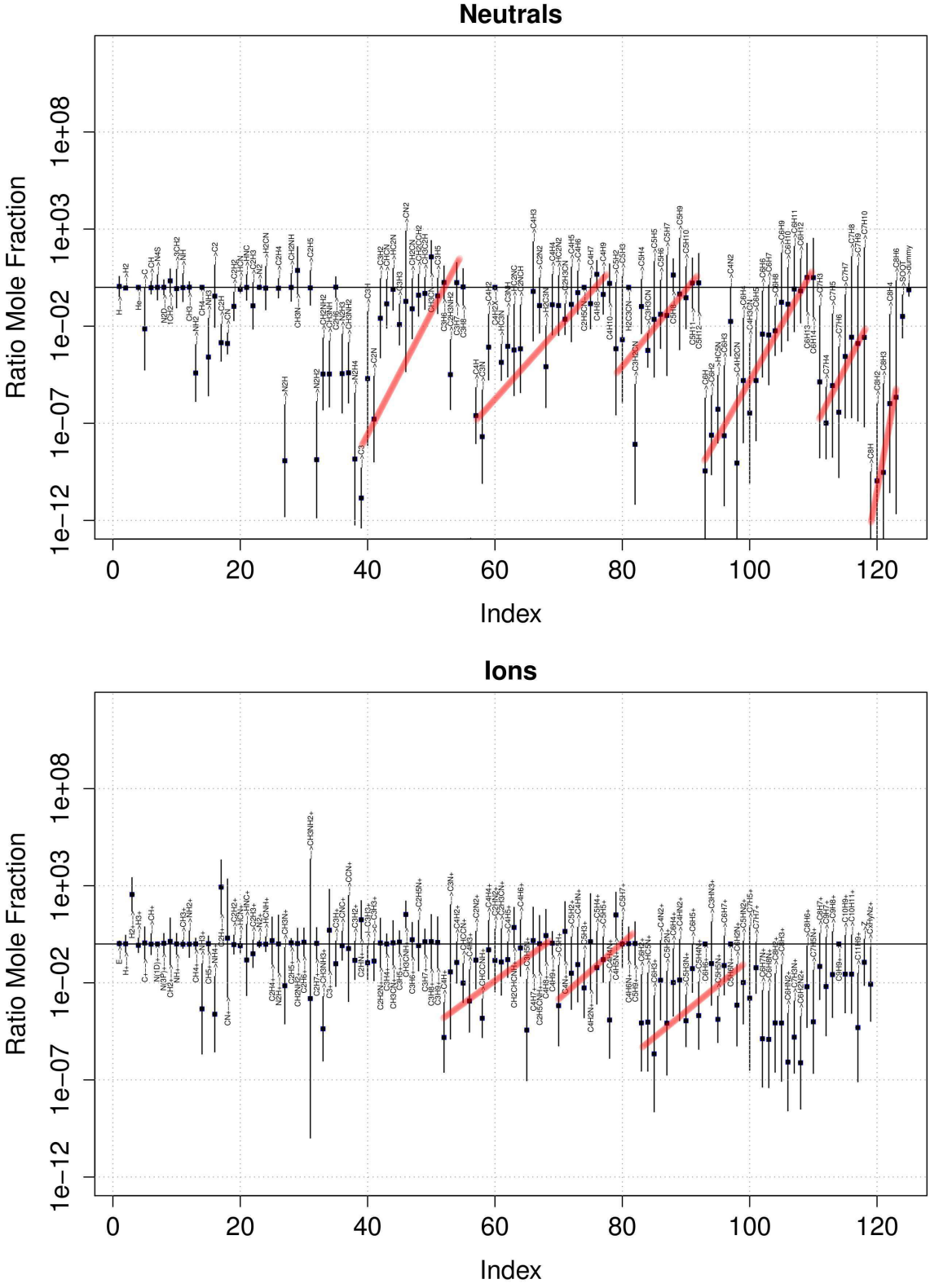

Figure 5.7: Ratios of stationary concentrations of neutrals (top) and ions (bottom) in Case 3 (only H-loss pathways for dissociative recombination) to those in the reference model (Case 1). Ratios' mean values and uncertainties (95% confidence interval) are respectively denoted by squares and error bars. The discrimination between unsaturated and saturated species in each block is highlighted by red bars.

study, we perform a similar sensitivity analysis, in the hope of building a representative reduced chemical scheme for further use, as well as finding the reactions foremost requiring a reevaluation to improve the precision of the model prediction.

5.2.4.1 Correlations between mole fractions and rate constants

The correlation matrix has been calculated from the Monte Carlo samples (see Section 2.4) for Case 1. The histogram of correlation coefficients is shown in Fig. 5.8. We observe that very few concentrations are significantly correlated with rate constants (*i.e.* absolute value of correlation coefficient greater than a threshold of 0.2, according to Hébrard et al. (2009); Peng et al. (2010). This is in contrast with the sensitivity analysis of the methane photolysis branching ratios, where the absolute value of correlation coefficients are often larger than 0.5 (see Fig. 3.6). Note that the sensitivity analysis corresponding to Fig. 3.6 is a *local* one: other parameters were all fixed at their nominal values so that the effects of the methane branching ratios are enhanced. In the case where all parameters are uncertain (see Fig. 3.7), these effects are completely "submerged" by the uncertainties of other parameters.

In the APSIS model, the situation is similar: there are ∼1700 reactions in the chemical scheme, even much more than in the case corresponding to Fig. 3.7. Moreover, molecular growth pathways and dissociative recombination, forming and breaking heavy species, respectively, form many loops in the reaction network. This leads to a dispersion of the influence of the parameters in a loop to the whole loop. As a result, the influence of each reaction on a given species is likely to be quite "diluted" by the large number of reactions.

If we lower the absolute value of the threshold of *significant* correlation coefficients, too many artificial key reactions emerge. Our tests show that the limited size of the samples (500 sets) leads to a standard deviation of rank correlation coefficients as large as ∼0.04 and some correlation coefficients even biased by ∼0.1. The "signal-to-noise ratios" of individual correlation coefficients are low enough to prevent us from counting the number of the species significantly influenced by each reaction for the *key reaction* search. This precludes the possibility of reaction scheme reduction by sensitivity analysis using correlation coefficients for the present model.

Nevertheless, we can still roughly estimate a reaction's global influence, *i.e.* its influence on all species. Ignoring the interactions between the rate constants, the square of the correlation coefficient between a concentration and a rate constant can be a linear estimate of their dependence (see Section 2.4). Hence, the sum of the squares of the correlation coefficients of all concentrations to a certain rate constant can be an estimate of this reaction's global influence. We define the score S_j of the jth reaction as

$$S_j = \sum_{i \in \{\text{species}\}} r_{ij}^2 \tag{5.27}$$

where r_{ij} is the rank correlation coefficient between the ith species and the rate constant of the jth reaction. Assuming the negligible correlations between correlation coefficients and uncertainties on correlation coefficients less than 0.1, *i.e.* $u_{r_{ij}} \leq 0.1$, we can estimate the variance of a score u_{S_j} by

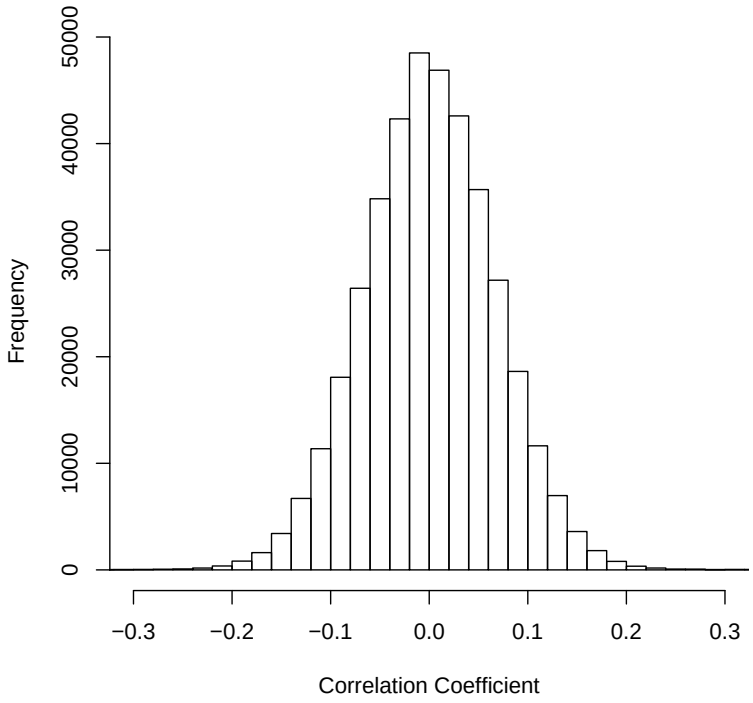

Figure 5.8: Histogram of the rank correlation coefficients between the rate constants and the species concentrations.

combination of variance

$$u_{S_j}^2 = \sum_{i\in\{\text{species}\}} \left(\frac{\partial S_j}{\partial r_{ij}}\right)^2 u_{r_{ij}}^2; \qquad j \in \{\text{reactions}\} \tag{5.28}$$

$$\leq \sum_{i\in\{\text{species}\}} (2r_{ij})^2\, 0.1^2 \tag{5.29}$$

$$= 0.04 S_j \tag{5.30}$$

Thus, the relative uncertainty of the score satisfies

$$\frac{u_{S_j}}{S_j} \leq \frac{0.2}{\sqrt{S_j}}; \qquad j \in \{\text{reactions}\} \tag{5.31}$$

We observe that the maximum of the relative uncertainty of the score is inversely proportional to its square root. The scores of the most influential reactions are simultaneously the largest and the least uncertain, which facilitates the key reaction search.

The reactions with scores larger than 3 are listed in Tab. 5.3. The score threshold of 3 (with a maximum of relative uncertainty of ∼12%) has been chosen to highlight a reasonable number (∼20) of influential reactions.

In agreement with Hébrard et al. (2009); Peng et al. (2010), the photolysis processes are found important, but only globally, no longer specifically for certain species. A photolytic reaction is generally more influential than a reaction of any other type. However, the photolysis is far from being a dominantly important reaction type, according to its score comparable to other reaction types. Among the photolytic reactions in Tab. 5.3, most of them produce ions, and the neutral

channels of the methane photolysis with large uncertainty do not have much global impact.

Despite the rather sizable uncertainty on its rate constant, $H + CH \rightarrow C + H_2$, the most influential reaction in the model of Titan's upper atmosphere found by Hébrard et al. (2009), is not identified as a key reaction in the present model. $CHCN + CHCN \rightarrow C_4N_2 + H_2$ (KBi5), $N\left(^2D\right) + N_2 \rightarrow N\left(^4S\right) + N_2$ (KBi6), $H + CH_3 \rightarrow CH_4$ (KTri1) and $H + C_2H_4 \rightarrow C_2H_5$ (KTri2) seem to be the most influential thermal neutral reactions. Most of them (KBi6, KTri1 and KTri2) sensitively depend on the pressure, which is much higher in the APSIS reactor than in Titan's ionosphere. This shows the important role of the pressure in the determination of the major molecular growth pathways. As there are only ∼80 trimolecular reactions, but more than 400 bimolecular reactions in the present scheme, their relative presence in Tab. 5.3 demonstrates the influence of the trimolecular reactions in the APSIS experiments. For comparison, in the model of Titan's upper atmosphere (Hébrard et al., 2009), most key reactions are photolysis and bimolecular reactions, and only one trimolecular reaction is found to be influential. This excludes that the large uncertainties of trimolecular reactions make themselves key reactions, since the rate constants and the uncertainties of the trimolecular reactions in the two models are identical. Indeed, trimolecular reactions are influential in the APSIS model for intrinsic reasons of the chemical scheme, likely to be their large rates, notably enhanced by the pressure.

Ionic reactions, *i.e.* photoionizations, dissociative recombinations and ion-molecule reactions, represent a large part of the *key reactions*, confirming the importance of the ion chemistry in the uncertainty budget of the present model. Moreover, most important dissociative recombinations are not simple H-loss reactions, proving also the importance of the full dissociative recombination scheme in the uncertainty budget. The charge transfer reaction $N_2^+ + CH_4 \rightarrow CH_2^+ + H_2 + N_2$ (KIM3), with a moderate uncertainty on its rate constant, is found the most influential in the present model, demonstrating its importance in the primary hydrocarbon ion production, hence the growth through ion chemistry, already highlighted in Imanaka and Smith (2007); Thissen et al. (2009).

5.2.4.2 Correlations between mole fractions

The correlation coefficients between the species mole fractions may also provide information on the mechanism of the molecular growth. If some species have similar behaviors when we perturb the model inputs (during the Monte Carlo uncertainty propagation), their statistical correlations may indicate the similarity of their underlying growth pathways:

- a highly positive correlation between two species often suggests that they are either a reactant and a product or two products of a reaction;
- a highly negative correlation between two species often suggests that they are two reactants of a reaction (a larger concentration of one species leads to a larger consumption of the other);
- for species with similar growth pathways, in general, the weaker correlations they have, the farther they are from each other in the global growth scheme.

In this study, we perform a calculation of the matrix of the correlation coefficients between the stationary mole fractions, and map the correlation coefficient matrix in Fig. 5.9 with the species sorted by increasing molar mass (left-to-right).

Clear block patterns are visible along the diagonal: species with the same heavy atom number often form square blocks of red pixels, representing positive correlation. This hints to similarity

No.	Reaction	Score
KPh1	$N_2+h\nu \rightarrow N\left(^4S\right)+N\left(^2D\right)$	4.38
KPh2	$N_2+h\nu \rightarrow N_2^+ + e^-$	4.10
KPh3	$CH_4+h\nu \rightarrow CH_4^+ + e^-$	3.81
KPh4	$CH_4+h\nu \rightarrow CH^+ + H_2 + H + e^-$	3.67
KPh5	$CH_4+h\nu \rightarrow H^+ + CH_3 + e^-$	3.24
KBi1	$H+C_2H_3 \rightarrow C_2H_2+H_2$	6.88
KBi2	$H+C_2H_5 \rightarrow CH_3+CH_3$	3.50
KBi3	$C_4H_3+CH_4 \rightarrow C_4H_4+CH_3$	4.42
KBi4	$N\left(^4S\right)+CHCN \rightarrow C_2N_2+H$	3.31
KBi5	$\mathbf{CHCN+CHCN \rightarrow C_4N_2+H_2}$	**6.18**
KBi6	$\mathbf{N\left(^2D\right)+N_2 \rightarrow N\left(^4S\right)+N_2}$	**5.01**
KTri1	$\mathbf{H+CH_3 \rightarrow CH_4}$	**6.90**
KTri2	$\mathbf{H+C_2H_4 \rightarrow C_2H_5}$	**6.56**
KDR1	$C_4H_5^+ + e^- \rightarrow C_4H_2+H_2+H$	3.60
KDR2	$\mathbf{CH_2NH_2^+ + e^- \rightarrow {}^1CH_2+NH_2}$	**7.11**
KDR3	$\mathbf{CH_2NH_2^+ + e^- \rightarrow {}^3CH_2+NH_2}$	**7.43**
KDR4	$CH_2NH_2^+ + e^- \rightarrow CN+H_2+H_2$	3.50
KIM1	$CH_2^+ + N\left(^4S\right) \rightarrow CN^+ + H_2$	3.29
KIM2	$C_2H_5^+ + HCN \rightarrow HCNH^+ + C_2H_4$	3.08
KIM3	$\mathbf{N_2^+ + CH_4 \rightarrow CH_2^+ + H_2 + N_2}$	**8.07**
KIM4	$N_2^+ + CH_4 \rightarrow CH_3^+ + H + N_2$	3.35

Table 5.3: Reactions with the sum of the squares of their correlation coefficients to all concentrations (score) larger than 3. The most influential ones (score>5) are in bold.

between their formation mechanism. The off-diagonal red square blocks reveal the relation between the species with different heavy atom number. In these blocks, deep red pixels (highly positive correlation) indicate that the 2 concerned species are linked by a reaction, *i.e.* the addition of small units in the growth, which are likely to be C1 or C2 species. There are also a series of small blocks in the gaps of the large blocks, mainly composed of the relatively saturated neutrals, *i.e.* C_5H_{11}, C_5H_{12}, C_6H_{13}, C_6H_{14}, *etc.* This series of block patterns start from a mixture of relatively saturated C3 neutrals and ions, unlike the major series, starting from C2, or even C1 species.

Westlake et al. (2012) mapped the correlation coefficient matrix between the INMS ion data at different m/z to seek the primary ionic reactions in Titan's ionosphere. They also discovered the block patterns in the matrix and interpreted them as the addition of C1 or C2 units. This highlights the importance of the addition of small units through ion-molecule reactions in Titan's atmospheric chemistry and is in agreement with our discussion above.

To obtain more direct information, the species in the correlation matrix are classified into a hierarchical binary tree by similarity (realized with the *heatmap* function in R (Development Core Team, 2010)). In Fig. 5.10, a prominent square block in red can be observed at the bottom right ($C_5H_4 - C_6H_4^+$, framed in orange) (see Fig. 5.11 and Tab. 5.4), in which C_2H_2 is located. Obviously, it has strong positive correlation with other species in the large square block (according to the color code). All of them are rather unsatured and most (77%) of them are ions. Considering these features, as well as the addition of small units discussed previously, we find a growth pathway for the species in this square block, *i.e.* repeating addition of C_2H_2 through ion-molecule reactions. A typical pathway would be

$$C_2H_2^+ \xrightarrow[-H]{+C_2H_2} C_4H_3^+ \longrightarrow C_6H_5^+ \xrightarrow[-H]{+C_2H_2} C_8H_6^+ \tag{5.32}$$

In the chemical scheme, C_2H_2 can be added to most ions with a sizable rate constant, while elevating the products' degree of unsaturation.

On the other hand, the importance of the ion chemistry does not mean that the contribution of the neutral chemistry is negligible. A neutral growth scheme was highlighted in Peng et al. (2010), *i.e.*

$$C_2H \xrightarrow[-H]{+C_2H_2} C_4H_2 \xrightarrow[-BH]{+B} C_4H \xrightarrow[-H]{+C_2H_2} C_6H_2 \tag{5.33}$$

where B can be various radicals. This pathway may also contribute significantly to the production of unsaturated species, albeit a hydrogen abstraction step is necessary to reactivate the intermediate. Otherwise 2 hydrocarbons of even hydrogen atom number, usually stable species, are not able to react with each other.

There are similar square blocks along the diagonal of the correlation matrix (Fig. 5.10): the ones between C_4H_8 and C_3H_7 (framed in violet) and between CH_3CNH^+ and $C_6H_7N^+$ (framed in dark green) (see Tab. 5.4). The latter block mainly consists of less unsaturated species (compared to those in C_2H_2's block), including C_2H_4. By analogy with the pathway led by C_2H_2, we propose a major growth pathway for this square block, the repeating addition of C_2H_4 through ion-molecule

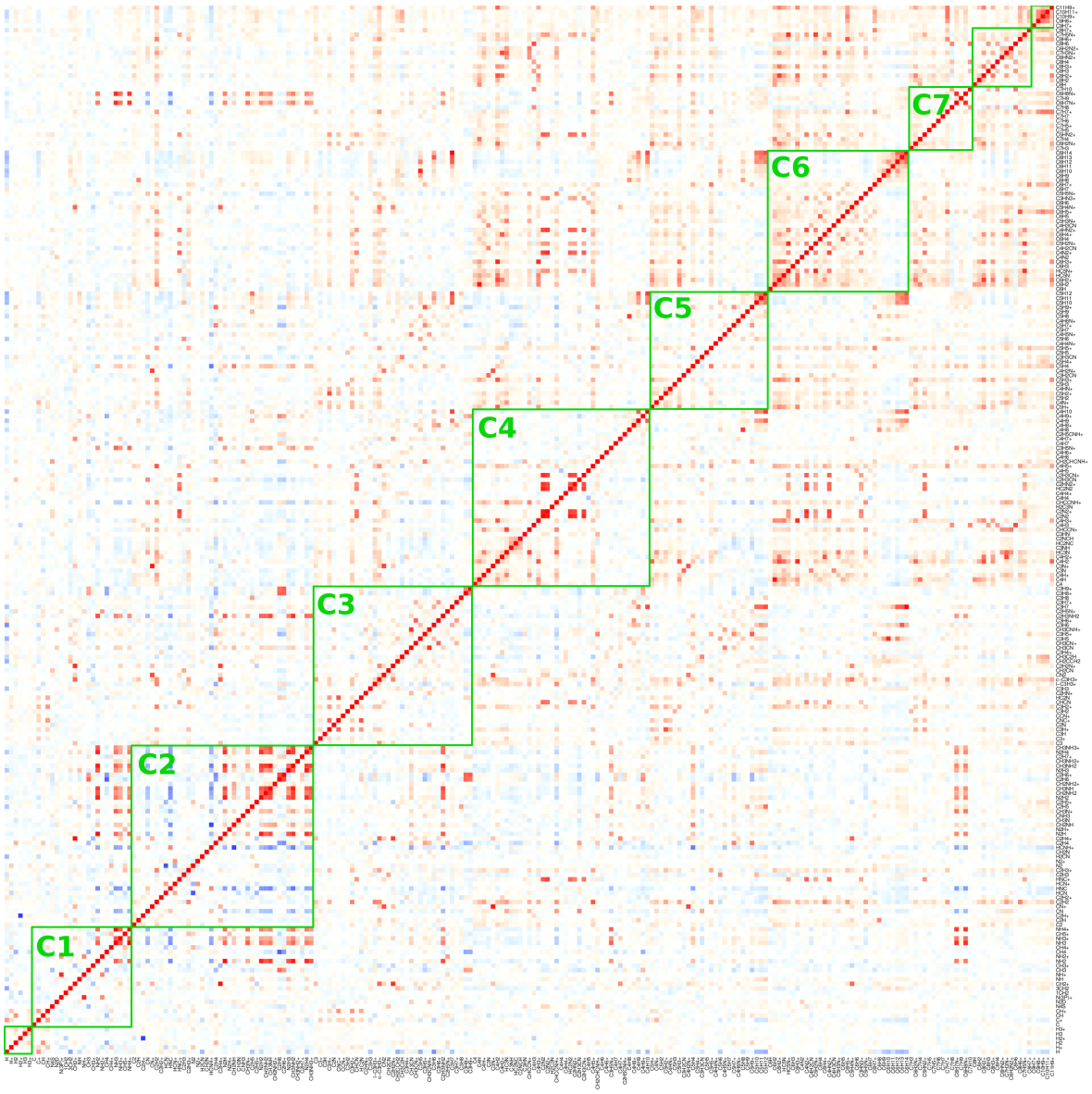

Figure 5.9: Direct plot of the correlation matrix among species concentrations. Species are sorted by increasing molar mass (left-to-right and bottom-to-top). Correlation coefficients from -1 to 1 are denoted by squares whose color gradually changes from blue (-1) to red (1) via white (0). The blocks along the diagonal are enclosed with green frames.

reactions, *e.g.*

$$\mathrm{CH_3^+} \xrightarrow[-\mathrm{H_2}]{+\mathrm{C_2H_4}} \mathrm{C_3H_5^+} \xrightarrow{+\mathrm{C_2H_4}} \mathrm{C_5H_9^+} \tag{5.34}$$

that form species more saturated than those in C_2H_2's block.

However, the importance of this block in hydrocarbon growth is quite limited. The rate constants of neutral growth reactions involving C_2H_4 are significantly smaller than those of the C_2H_2 growth family: for example, the active neutral additions of C_2H_2 and C_2H_4 with the same substrate, C_4H, have the nominal rate constants of 6.13×10^{-8} and 1.84×10^{-9} $\mathrm{cm^3.s^{-1}}$, respectively, at 300 K. This is consistent with the fact that there are few neutral hydrocarbons in C_2H_4's block. Moreover, 83% of the species in this block are N-bearing ones, the growth of most of which is not directly related to the repeating addition of C_2H_4. They are strongly correlated to C_2H_4 due to their nitrogenation by NH_3 or NH_4^+, which are provided by an important series of reactions starting from C_2H_4, *i.e.*

$$\mathrm{C_2H_4} \xrightarrow[-\mathrm{H}]{+\mathrm{N}\left(^2\mathrm{D}\right)} \mathrm{CH_3CN} \xrightarrow[-\mathrm{B}]{+\mathrm{BH^+}} \mathrm{CH_3CNH^+} \xrightarrow[-\mathrm{C_2H}]{+e^-} \mathrm{NH_3} \xrightarrow[-\mathrm{B}]{+\mathrm{BH^+}} \mathrm{NH_4^+} \tag{5.35}$$

where all intermediates are essentially produced by their respective previous steps. This scheme highlights a major nitrogen fixation pathway in the present model.

We cannot propose a typical growth pathway promoted by the other stable C2 hydrocarbon, C_2H_6, like C_2H_4 and C_2H_2, because the growth through ion-molecule reactions of C_2H_6 can only form C3 species, but not heavier ones. The addition of C_2H_6 lowers the product's degree of unsaturation if no dehydrogenation is associated, and large saturated ions are generally too stable to drive C_2H_6's hydrogen to leave. Nevertheless, neutral growth pathways promoted by C_2H_6's corresponding radical, C_2H_5, is possible. The square block between C_4H_8 and C_3H_7 mainly consists of relatively saturated species, including the most saturated hydrocarbons, *e.g.* C_2H_5, C_3H_8, C_5H_{11} and C_6H_{14}. This family might also play an important role in molecular growth, especially for saturated species. The following scheme presents a typical pathway:

$$\mathrm{{}^1CH_2} \xrightarrow[-\mathrm{H}]{+\mathrm{C_2H_5}} \mathrm{C_3H_6} \xrightarrow{+\mathrm{C_2H_5}} \mathrm{C_5H_{11}} \tag{5.36}$$

Note that C_2H_5 has a lower concentration than stable C2 species and lower rate constants for its neutral radical reactions, compared with ion-molecule reactions. Thus, it should not be as efficient in promoting molecular growth as C_2H_2.

In spite of the partition of the correlation matrix, the interaction between the blocks, in other words the 3 families of pathways above, still exists, forming species of a degree of unsaturation between the typical cases and complexifying the growth scheme. However, simply according to the size of the blocks in Fig. 5.10, the prominence of C_2H_2's block is flagrant. Furthermore, in view of the importance of ion chemistry, the addition of C_2H_2 through ion-molecule reactions might be at the center of the growth scheme.

Growth unit	Species in the block
C_2H_4	CH_3CNH^+, CH_3CN, C_2HN^+, $C_4H_5N^+$, C_2H_4, CH_2CHCNH^+, $C_3H_5^+$, $C_5H_7^+$, $C_5H_9^+$, $CH_2NH_2^+$, CH_2NH, N_2H_3, N_2H_2, N_2H_4, N_2H, NH_2, NH_4^+, NH_3, CH_2NH_2, $CH_3NH_3^+$, $C_2H_3NH_2$, CH_3NH, CH_3NH_2, NH_3^+, CH_3N^+, $C_3H_5N^+$, $C_6H_8N^+$, $C_6H_7N^+$
C_2H_5	C_4H_8, C_5H_8, C_6H_8, H_2CN, NH, C_5H_9, C_3H_8, C_2H_5, C_2H_3, C_5H_6, CH_3C_2H, $3\,CH_2$, C_6H_9, C_6H_{10}, C_3H_5, C_6H_{11}, C_3H_3, CH_2CCH_2, C_4H_9, C_4H_{10}, C_5H_{12}, C_3H_6, C_6H_{13}, C_5H_{11}, C_6H_{12}, C_5H_{10}, C_6H_{14}, C_3H_7
C_2H_2	C_5H_4, $C_8H_7^+$, $C_6H_7^+$, $C_9H_8^+$, $C_{10}H_9^+$, $C_{10}H_{11}^+$, $C_4H_2N^+$, CN^+, CN_2, C_3N^+, C_2H, C_3, $C_2H_2N^+$, $C_2H_4^+$, CH_2^+, HC_5N^+, $C_7H_5N^+$, $C_5H_2N^+$, $C_5HN_2^+$, $C_4N_2^+$, $C_4HN_2^+$, $C_3HN_3^+$, $CHCN$, HNC^+, HC_2N_2, $C_2H_3CN^+$, $C_2HN_2^+$, C_2N_2, $C_2N_2^+$, C_3NH, HC_2NC, C_2NCH, $CHCCNH^+$, $l{-}C_3H_3^+$, C_4HN^+, C_3^+, C_4N^+, $C_5H_3N^+$, $C_6HN_2^+$, $C_6H_2N_2^+$, $C_5H_5N^+$, C_4H^+, $CHCCN^+$, HC_3N, $C_2H_3^+$, $C_5H_5^+$, $C_5H_4N^+$, $c{-}C_3H_3^+$, $C_{11}H_9^+$, $C_7H_7^+$, $C_6H_5^+$, $C_8H_6^+$, $C_8H_3^+$, $C_8H_2^+$, $C_6H_2^+$, $C_6H_2N^+$, C_5H^+, $C_5H_3^+$, $C_6H_3^+$, C_4H_2, C_4, $C_4H_3^+$, HC_5N, C_4H, C_6H_2, C_3H^+, $C_5H_2^+$, $C_3H_2^+$, C_2H_2, $C_4H_5^+$, $C_7H_3N^+$, $C_4H_2^+$, $C_6H_4^+$

Table 5.4: List of the species appearing in the three square blocks identified in Fig. 5.10.

Understanding the importance of dissociative recombination. With the aid of the 3 growth families identified above, we are able to explain the impact of the full dissociative recombination scheme. The non H-loss dissociative recombination channels, through most of which small neutrals including C1 and C2 are produced, supply the most influential and unsaturated growth unit C_2H_2, but hardly the relatively saturated one C_2H_5. These channels increase the production rate of C_2H_2 by a factor of $\sim$10, leading to a more efficient growth of unsaturated species. The fact that C_2H_5 is much less formed by dissociative recombination explains the minor impact of this process on the production of saturated species.

The present study completes the discussion of Plessis et al. (2012) about the responsible species for the promotion of the chemistry with full dissociative recombination scheme. Plessis et al. (2012) pointed out that the two antagonistic effects of dissociative recombination: a global chemical lysis of heavy ions and a promotion of the molecular growth due to the production of small reactive species. Here, we can be more specific: dissociative recombination produces small unsaturated species, especially C_2H_2, enhancing the most efficient growth pathways. This illustrates the promoting effects of dissociative recombination discussed by Plessis et al. (2012), and make the promoting effects overtake the chemical lysis effects.

5.3 Model variants with a single physical factor changed

Having highlighted the growth mechanism in the APSIS model, we explore the chemistry of the system in different physical conditions, in order to interpret other observations or experiments. To identify the effect of various physical factors, we design variants of the reference model (Case 1) with a single modified factor (see Tab. 5.2): irradiation spectra (Cases 4, 5 and 6), pressure (Case 7), and temperature (Case 8).

5.3.1 Irradiation spectrum

In Cases 4 and 5, the DISCO spectrum is respectively replaced by monochromatic ones at 60 nm and 82 nm (for comparison to the experiments in Imanaka and Smith (2010)), with the same integrated intensity. The total radiation flux in Imanaka and Smith's experiments is actually very close to that of the DISCO beamline. These models provide direct probes of the influence of our representation of the methane photolysis branching ratios.

In Case 4, the relative production with respect to that in the reference case increases with molar mass (Fig. 5.12). This results from the fact that ion chemistry, more efficient in molecular growth than neutral chemistry, is more involved in Case 4 than in Case 1. The nitrogen photolysis at 60 nm essentially produces N_2^+, which almost quantitatively ionizes methane through the charge transfers

$$N_2^+ + CH_4 \longrightarrow CH_2^+ + H_2 + N_2 \tag{5.37}$$

$$N_2^+ + CH_4 \longrightarrow CH_3^+ + H + N_2 \tag{5.38}$$

and initiates the hydrocarbon ion growth. These charge transfers have been identified as key reactions in Section 5.2.4.1 and their effect in promoting the growth through ion chemistry has also been highlighted in Imanaka and Smith (2007); Thissen et al. (2009).

This rationalization is supported not only by Case 5, but also by Case 6, where the irradiation spectrum is changed for the solar one while the same intensity as the DISCO beam. In both cases, the production is generally less efficient than in Case 1 (Figs. 5.13 and 5.14), as the ionizing part of the radiation is substantially lower than in the DISCO spectrum (see Fig. 4.1). On the other hand, in Case 5, N_2 molecules having absorbed a photon are not ionized but produce nitrogen atoms, generally promoting the formation of N-bearing species, in agreement with the experimental results of Imanaka and Smith (2010).

The uncertainties on the stationary concentrations in Cases 4 and 6 are also found to be little sensitive to the irradiation type (Fig. 5.15). In Section 5.2.2, the contribution of the photolysis to the concentration uncertainties is shown to be marginal. As long as the uncertainty introduced by the photolysis is not increased drastically, their total contribution to the uncertainty cannot be significant. In these two cases, the principal contribution of the photolysis stems from photoionization at 60 nm and photodissociation at Ly-α, respectively. The branching ratios at these two wavelengths are relatively accurately measured (relative uncertainties within 20%). Therefore, the major uncertainty source remains neutral thermal reactions, which are not modified, and the concentration uncertainties are close to those in Case 1.

The concentration uncertainties increase substantially and globally in Case 5, which is quite different from the previous cases. At 82 nm, one is close to the lower extremity of the wavelength range depicted by the representation of the branching ratios of the neutral channels of methane pho-

tolysis (see Section 2.2.4, Fig. 2.2(b)). In this region, far from the wavelengths where measurements exist, all neutral channel branching ratios are strongly uncertain (relative uncertainties ∼50-100%) owing to long-range extrapolation and uniform distribution imposed for lack of knowledge. Since the photolysis is globally important, this large uncertainty, which may be further amplified in the reaction network, contributes significantly to the uncertainty budget of the species concentrations.

Despite the substantial increase of the uncertainties in Case 5, the previously identified promotion of the formation of N-bearing species by the exclusive production of N atoms in N_2 photolysis is significant for many species, such as $N\left(^4S\right)$, HCN, CH_2NH *etc.*

5.3.2 Pressure

In Case 7, the pressure is lowered by a factor 10^6 in order to approach the pressure around 850 km in Titan's upper atmosphere ($\sim 5 \times 10^{-4}$ Pa). At the same time, the cell is elongated by the same factor, to conserve the quantity of gas, hence its optical depth in the cell. Accordingly, the photoabsorption rate of N_2 and CH_4 are identical to the reference case.

Higher mole fractions than in Case 1 are observed in general (see Fig. 5.16). Some species (C_6H, C^+ and CN^+, for instance) are $\sim 10^8$ times more abundant than in Case 1. This increase of the production simply results from lower termination rates of the active species (*i.e.* radicals and ions) due to the lower pressure. As a consequence, we observe also a shift of the product distribution toward lower masses, signifying limited growth.

It is notable that in each Cx block there is a systematic discrimination between saturated and unsaturated species. The mole fraction ratio between Case 7 and Case 1 of a species increases in general with its degree of unsaturation within a block (see the red bars in Fig. 5.16). In the C5 and C6 blocks, it can be more than 10 orders of magnitude. This phenomenon reminds us of the 2 major growth families, *i.e.* those of C_2H_2 and C_2H_5, whose efficiency also increases with the degree of unsaturation of the growth units, exhibit the same discrimination.

Via the growth families, how does the low pressure lead to favor unsaturated products and disadvantage saturated ones? Assuming the composition of the reactive gas unchanged, while lowering the pressure by a factor of 10^6, we lower the rate of all reactions in the growth families in the same manner, *i.e.* by a factor of 10^{12}, except for the radical recombination forming heavy saturated species (*e.g.* the last step in Eq. 5.36), which is usually trimolecular and more sensitive to the pressure (slowed down by a factor of 10^{18}). Trimolecular reactions are important at several mbar (see Section 5.2.4.1) and should contribute significantly to the production of the relatively saturated species. However, this contribution vanishes rapidly as the pressure decreases, resulting in very low mole fractions of the most saturated species, *i.e.* C_5H_{11}, C_6H_{14} *etc.*, and less lowered mole fractions of more unsaturated species, *i.e.* C_5H_7, C_6H_{10} *etc.*,. The most unsaturated species, *i.e.* C_5H_3, C_6H_2 *etc.*, are hardly affected. Similar trends are observed among the ions. This can be explained, since heavy neutrals can be globally correlated to their corresponding ion by (de)protonation, as Waite et al. (2007) proposed (see Fig. 2 of the article).

5.3.3 Temperature

In Case 8, the temperature is lowered down to 150 K, close to that in Titan's ionosphere. Few stationary concentrations are significantly different from those in the reference case, except those of heavy saturated neutral species. A low temperature is obviously not as effective to slow down

the growth as a low pressure in Case 7, because only neutral reaction rate constants decrease with temperature. There are only marginal differences between the two temperatures (according to the data of the photolysis cross-sections of major absorbers at room temperature and ~150 K recommended by E. Hébrard in a personal communication). The ionic reactions, the most important undertakers of the growth, are not either slower at 150 K.

However, there is a discrimination between the species of various degree of unsaturation in heavy species blocks (see Fig. 5.17). As in Case 7, among the growth families, only the one driven by C_2H_5, remarkably slowed down by the low temperature, is responsible for the discrimination in Case 8. Cases 3 and 6 provide examples of the opposite behavior (see Figs. 5.7 and 5.14): in the former case, H-loss pathways of dissociative recombination produce less unsaturated species; in the latter case, photons of solar spectrum produce less ions. Both of these facts favor the saturated species and disfavor the unsaturated ones in each block.

5.4 Applications of the model to different setups

Having investigated the effect of individual factors on the model, we apply it to three concrete cases: APSIS experiments, Imanaka and Smith's reactor (Imanaka and Smith, 2007) and Titan's ionosphere, comparing the simulated MS of the modeling results with experimental MS and the INMS data of the Cassini orbiter. Simulated MS for the three cases are generated using stationary concentrations as detailed in Section 2.5.

5.4.1 APSIS experiments

In the model for the APSIS experiments (Case 1), radicals and ions only account for about one third of the total mass. Thus, the simulated MS, ignoring radicals for the lack of fragmentation data, is directly comparable to the MS measured in the experiments at 7 sccm (see Fig. 5.18) for qualitative and semi-quantitative purposes.

Except for the C2 block, whose experimental values are rather uncertain owing to the large overlap with the N_2 signal, the major bands in the experimental spectrum are well covered by the 95% confidence intervals of the simulated MS (the red shaded area in Fig. 5.18). However, the mean of the simulated spectrum is not in satisfactory agreement with the experimental spectrum: it underestimates the production of saturated C3 and C4 species and overestimates that of unsaturated C4 species. In previous sections, the preponderance of unsaturated species in each block was often mentioned. However, it is not visible in the experimental spectrum.

To find out the main cause(s) of this discrepancy, we proceed by elimination:

- **Incompleteness of the reaction scheme**: an exhaustive search has been performed for the construction of the reaction scheme. Up to now, most C3-producing reactions have been included in the model, while saturated C3 species are still not satisfactorily reproduced in the model. Moreover, it is weakly probable that missing reactions, randomly taken for each reaction type, could result in a systematic underestimation of saturated species.

- **Oversimplification of the reactor's geometry**: we prove this effect with a model without irradiation but with a gas inflow whose composition is identical to that of the gas outflow in the reference case. The gas inflow models the non-irradiated or weakly irradiated part in the reactor where reactive species other than N_2 and CH_4 are supplied by transport/diffusion.

The stationary state of this test case is little shifted from the reference case, demonstrating, at least, that the basic growth scheme could hardly change (this problem could be directly addressed by a 2D model).

- **Chemistry taking place in the capillary between the reactor and the mass spectrometer**: radicals and ions, of about one third of total mass, pumped into the capillary cannot qualitatively change the gas composition before reaching the mass spectrometer. This is shown by another test case, where we let the reactive gas in the stationary state of the reference case react until equilibrium in an isolated box without irradiation. In this case, radicals and ions have infinitely long time to combine with each other and be recombined with electrons, respectively, no matter whether heterogeneously catalyzed by the stainless steel capillary or not. In these conditions, saturated species concentrations are increased by at most ∼40%, still far from the observed difference between the experimental and simulated spectra.

Considering the small increase of saturated species concentration resulting from radical recombination in the last test case, we argue that higher radical recombination rates would lead to a better reproduction of saturated species. How could they be actually higher than in our model? It is unlikely due to homogeneous trimolecular reactions, since, again, although very poorly known in general, their rate constants could hardly be underestimated *systematically*. It is also unlikely due to the growth conducted by negative ions (Zabka et al., 2012), not included in the present model yet, since this type of growth essentially involves unsaturated species. Therefore, we may only ascribe it to heterogeneous catalysis, not included in the model either, most probably on the reactor's stainless steel wall. Thissen et al. (2009) discussed a similar problem, *i.e.* surface effects on ion production, in their laboratory simulation experiment of Titan's atmosphere.

Gorodetsky et al. (2005) measured a CH_3 recombination coefficient of 0.0003 on stainless steel at 300 K. According to this value, the reaction rate of CH_3 recombination on stainless steel is in the order of magnitude of $10^{-2} \sim 10^{-1}$ of that of the homogeneous one. They determined also the temperature dependency of the rate constant, usually more reliable than its absolute value. They showed that recombination is accelerated about 10 times as temperature increases by 10 K. This high sensitivity may make the recombination rate highly uncertain, since the temperature during the experiments is not strictly constant. In addition, the large uncertainty usually associated with measurements of heterogeneous reaction rates and the existence of various radical recombinations on the reactor's wall should also be considered. The large uncertainties prevent us from making a significant comparison of the contributions of the homogeneous and the heterogeneous radical recombinations. In another word, there is a significant probability that the heterogeneous recombinations have a comparable, or even larger contribution than the homogeneous ones.

Due to lack of data, it is difficult to model heterogeneous recombination explicitly. To globally account for the heterogeneous recombination whose rate is close to, or even higher than that of homogeneous recombination, we simply multiply the homogeneous trimolecular rate constants by a factor of 3 or 10 (cyan and dark green solid lines in Fig. 5.18, respectively). In the case of a factor 3, the unsaturated parts of the C3 and C4 bands decrease slightly and their saturated parts increase significantly, by a factor around 3, leading to a satisfactory agreement of the C3 and C4 bands between the experimental and simulated spectra. When trimolecular rate constants become 10 times larger, the simulated MS keeps on evolving in the same direction, resulting in an

overestimation of the saturated part.

Obviously, a faster recombination produces more saturated species, at the expense of unsaturated neutrals, and hence unsaturated ions. Unsaturated species play a major role in the growth without "heterogeneous recombination" included in the model, and their preponderance over saturated ones, not observed in the experiments, can be well compensated in the model by "heterogeneous recombination" that consumes unsaturated species and produces saturated ones. This is a strong indication of the contribution of the heterogeneous reactions in the laboratory simulation setups of atmospheric chemistry, such as the APSIS reactor. An option to reduce these wall effects would be to use a reactor made of Pyrex instead of stainless-steel (Oinuma et al., 2010). However, this is forbidden in the SOLEIL synchrotron radiation facility for safety reasons.

5.4.2 Imanaka and Smith's reactor

Case 10 models Imanaka and Smith's experiment at 60 nm (Imanaka and Smith, 2010)]. We do not model their experiment at 82.5 nm, in which *in situ* MS, necessary for our comparison, was not measured. Their *in situ* MS and a simulated MS of Case 10 are compared in Fig. 5.19. The experimental spectrum is basically out of the 95% confidence interval of the simulated MS. The model overestimates the unsaturated production and underestimates the saturated production systematically. Especially, the intensity of saturated species is lower than 1/1000 of the experimental intensity. It is important to find out the reasons of this disagreement, which may invalidate the present model.

The mass spectrometer in Imanaka and Smith's experiments was used at too high pressure to retain the linearity of its MS signals (see discussion in Chapter 4). This argument cannot explain the overestimation and the severe underestimation coexisting in a single band, because the non-linearity of MS signals exhibits in a relatively uniform way in a band.

Furthermore, it is notable that the stable species considered in the simulated spectrum only accounts for a minor part of total mass in the case of Imanaka and Smith's reactor ($\sim 10\%$). The radicals and ions, accounting for most of the total mass and ignored in the simulated spectrum, are certainly an important source of disagreement, no matter whether the MS signals are linear. However, the factor 1000 between the saturated parts of measured and simulated MS bands is still not explained. Assuming that the chemistry in Case 10 is basically correct, the saturated part may have a concentration (not an intensity in the simulated MS) comparable to the unsaturated part in the same block only if large radical and ions ignored in the simulated MS are (nearly) saturated, which is evidently not true. Even in the homogeneous model of the APSIS experiments (Case 1), at a remarkably higher pressure disfavoring the growth of unsaturated species, they are still dominant in the blocks of heavy species. Therefore, the assumption of a correct chemistry in Case 10 is not true, *i.e.* the homogeneous model of Case 10 is not adequate to reveal the chemistry occurring during Imanaka and Smith's experiments.

As in Case 1's variants in Section 5.4.1, pseudo-heterogeneous recombination could be introduced by enhancing the trimolecular rate constants. In view of lower pressure and larger internal surface-to-volume ratio of Imanaka and Smith's reactor than the APSIS reactor, resulting in a larger relative contribution of heterogeneous chemistry, we test 3 cases with 10, 30 and 100 times faster trimolecular rate constants, respectively. The simulated spectra of these cases are shown in Fig. 5.19. Like this kind of treatment for Case 1, the unsaturated part of MS bands is slightly lowered and the saturated part is significantly increased. As trimolecular rate constants are amplified, the unsaturated part

of the C3-C5 bands of the simulated MS gradually approaches the experimental results and their saturated part reaches and overtakes the measured values.

Though still not satisfactory, for instance in the unsaturated part of the C4-C6 band, always overestimated, possibly due to the lack of reactions in the scheme, the agreement between the simulated spectra of the case with 30 times faster recombination rates constants and the experimental one is notably improved, especially for the saturated part. This may illustrate the very important effect of heterogeneous chemistry, probably even stronger than in the APSIS reactor, because of the lower pressure in Imanaka and Smith's experience and the more favorable (more tube-like) geometry of their reactor. The production of tholins in their experiments, is also an indication of the heterogeneous chemistry, since the growth of the size of solid products (tholins) should be a heterogeneous process.

5.4.3 Titan's ionosphere

Although the present model is oversimplified for Titan atmosphere, it is still possible to choose suitable values for physical conditions: temperature (150 K), pressure (as Case 7, but without helium), optical depth (as Case 7), radiation type (solar spectrum) and intensity (lower than the terrestrial value by the factor of square of the ratio between Titan-Sun and Earth-Sun distances), *etc.* The main difference of physical conditions between Titan atmosphere and the present 1-cell model is the effective gas residence time corresponding to complex transport processes at Titan (De La Haye, 2005; Yelle et al., 2008; Strobel, 2009). According to our tests, the production in the blocks varies relatively uniformly with the residence time. Thus, we can adjust the effective residence time to fit INMS data as well as possible, without scrambling the relative production of each block. An effective residence time of 2.8×10^6 s gives a globally good total production. It is 10^4 and $\sim$10 times larger than that in Case 1 and the transport time constant at 850 km in Titan's atmosphere (De La Haye, 2005), respectively.

In Fig. 5.20, a simulated MS for Case 9 is compared to the INMS neutral spectrum of T19 flyby between 950 and 1000 km, published in Waite et al. (2007). The agreement between the observations and the simulated spectrum for Titan is better than for APSIS experiments (Case 1), especially because of a good reproduction of the preponderance of unsaturated species in each block. This results from the fact that the conditions favoring the growth of unsaturated species, *i.e.* low pressure and low temperature, are well met in Titan's ionosphere. The preponderance of unsaturated species at Titan indirectly supports that the reactor's metallic wall plays an important role in the production of saturated species in the laboratory simulation experiments, simply because in Titan's atmosphere, there is no such an efficient "wall" that promotes heterogeneous chemistry.

The reproduction of the fact that C6 block's concentration is larger than C5 block's also validates the present reaction scheme in general terms. Though underestimated, C_6H_6 (mainly at m/z 78) is shown to be an important heavy product in Case 9, owing to its high degree of unsaturation and thanks to the physical conditions for its growth, *i.e.* low pressure and low temperature. On the other side, the overestimation of C5 species and C_4N_2 (at m/z 76) reveals a lack of reactions in the present "complete" scheme.

Ion chemistry (Vuitton et al., 2007; Imanaka and Smith, 2007) and full dissociative recombination scheme (Plessis et al., 2012) were shown to be important to the molecular growth in Titan's atmosphere. Their impacts are also investigated by modeling in the present study, like for the APSIS experiments. The chemical scheme includes respectively only neutral reactions in Case 11a

and only H-loss reactions for dissociative recombination in Case 11b. Mole fractions of important species and simulated MS in the 2 cases as well as Case 9 are shown in Tab. 5.5 and Fig. 5.20, respectively.

It is notable that, except for the intensities at m/z 55 and 56, there is no qualitative difference between simulated MS of these cases, for the following reasons:

- Ion chemistry is relatively less important in Titan's atmosphere than in the APSIS reactor (see Tab. 5.5 and discussions in Section 5.5.1).
- The shape of neutral MS bands is essentially determined by the most abundant species of each block, usually also the least sensitive one(s) to the modification of the chemical scheme.

The similarity of simulated MS of Cases 9, 11a and 11b illustrates the impossibility of clarifying if ion chemistry or dissociative recombination other than H-loss pathways are important for minor species, for instance NH_3, stated by Yelle et al. (2010), just by comparison of experimental and simulated neutral MS. Nevertheless, we can still demonstrate that the ion chemistry and the dissociative recombination other than H-loss pathways are important in the production of NH_3, comparing its mole fraction in Cases 9, 11a and 11b (see Tab. 5.5): NH_3 is not formed in Case 11a, because it is exclusively produced by the ion-molecule reactions starting from N^+. NH_3's mole fractions in Case 11b is lower than in Case 9 by $\sim$4 orders of magnitude, because it interchanges with N-bearing ions through the former's ion-molecule reactions and the latter's dissociative recombination. In an H-loss dissociative recombination scheme, N-bearing ions have less pathways to form small species, such as NH_3.

5.5 Discussion

5.5.1 Impact of ion chemistry and dissociative recombination

In addition to being compared with measurements, modeling results in the cases for the APSIS experiments, Imanaka and Smith's experiments and Titan's atmosphere are compared with each other. In Section 5.2.1, we have demonstrated that ion chemistry and full dissociative recombination scheme are important in the conditions of the APSIS experiments. It is interesting to know whether it is also true in other conditions, for instance the typical cases in the present study, Titan or of Imanaka and Smith's experiments. To achieve this, we list the concentrations of several species reported in Waite et al. (2007); Vuitton et al. (2009b), in the cases of Titan and Imanaka and Smith's experiments modeled with the complete reaction scheme (Cases 9 and 10, respectively), the neutral scheme (Cases 11a and 12a, respectively) and the H-loss dissociative recombination scheme (Cases 11b and 12b, respectively), as well as the counterpart of the APSIS experiments (Cases 1, 2 and 3), in Tab. 5.5.

In the conditions of Imanaka and Smith's experiments, the concentrations of the purely neutral model (Case 12a) are drastically different from those of the model with the complete scheme (Case 10), for example even those of 2 major C2 products C_2H_2 and C_2H_4 are lower in Case 12a than in Case 10 by about 10 orders of magnitude. This great difference can be interpreted by the fact that the irradiation of Imanaka and Smith's experiments, at 60 nm, is so ionizing ($\sim$ 97% branching ratio of ion-producing photolytic pathways of N_2 and 100% branching ratio of those of CH_4), that the chemistry of the model is no longer active at all if ions are excluded.

Table 5.5: Comparison of common logarithms of mole fraction of certain species (selected according to Waite et al. (2007); Vuitton et al. (2009b)) in the cases with complete reaction scheme for APSIS (Case 1), Titan (Case 9) and Imanaka and Smith's reactor (Case 10) to the corresponding cases with neutral scheme (Case 2, Case 11a and Case 12a, respectively) and H-loss scheme for dissociative recombination (Cases 3, 11b and 12b, respectively). Uncertainties are shown in parentheses. Species not formed in certain cases are noted by dashes.

	APSIS			**Titan**			**Imanaka and Smith's reactor**		
	Case 1 (Full)	**Case 2 (Neutral)**	**Case 3 (H-loss)**	**Case 9 (Full)**	**Case 11a (Neutral)**	**Case 11b (H-loss)**	**Case 10 (Full)**	**Case 12a (Neutral)**	**Case 12b (H-loss)**
C_2H_2	-6.13 (17)	-7.60 (44)	-7.11 (32)	-3.67 (11)	-3.65 (11)	-3.67 (11)	-3.58 (12)	-14.2 (8)	-4.01 (33)
C_2H_4	-5.18 (17)	-5.53 (28)	-5.23 (18)	-3.48 (10)	-3.48 (10)	-3.48 (10)	-3.69 (16)	-12.2 (8)	-3.03 (17)
C_2H_6	-4.84 (18)	-5.15 (22)	-4.84 (19)	-3.56 (18)	-3.56 (19)	-3.56 (18)	-4.76 (137)	-10.0 (6)	-3.81 (83)
CH_3C_2H	-6.24 (28)	-8.46 (71)	-6.55 (30)	-4.93 (34)	-4.84 (32)	-4.90 (33)	-2.70 (24)	-19.2 (15)	-2.51 (24)
CH_2CCH_2	-6.86 (35)	-8.81 (84)	-7.27 (41)	-5.72 (45)	-5.71 (46)	-5.71 (45)	-4.87 (42)	-21.8 (17)	-5.05 (43)
C_4H_2	-9.53 (45)	-15.9 (11)	-12.6 (7)	-5.79 (36)	-5.64 (37)	-5.77 (36)	-5.64 (35)	-27.6 (31)	-7.16 (68)
C_2N_2	-9.22 (50)	-10.5 (5)	-10.2 (5)	-9.08 (77)	-9.11 (78)	-9.13 (77)	-6.57 (82)	-14.4 (9)	-7.07 (72)
C_6H_6	-9.12 (51)	-14.9 (13)	-11.5 (10)	-7.04 (83)	-7.65 (139)	-7.63 (138)	-4.69 (52)	-34.2 (25)	-5.92 (78)
C_3H_6	-7.03 (29)	-9.77 (60)	-6.78 (30)	-7.67 (54)	-7.70 (55)	-7.66 (54)	-6.07 (45)	-21.9 (14)	-5.88 (46)
C_7H_8	-20.7 (14)	-28.2 (20)	-23.2 (16)	-24.7 (19)	-25.2 (21)	-25.1 (21)	-15.5 (15)	-	-17.0 (15)
C_8H_2	-13.9 (12)	-30.5 (24)	-23.9 (16)	-8.76 (134)	-9.42 (176)	-9.53 (174)	-6.53 (103)	-	-11.6 (16)
HCN	-4.96 (5)	-4.94 (6)	-5.06 (9)	-4.22 (5)	-4.22 (5)	-4.23 (5)	-4.28 (15)	-3.40 (13)	-3.81 (45)
CH_3CN	-9.36 (33)	-8.10 (31)	-7.80 (25)	-5.14 (39)	-4.86 (27)	-4.86 (27)	-6.51 (27)	-12.9 (9)	-4.37 (31)
C_2H_3CN	-7.18 (22)	-10.0 (4)	-8.83 (33)	-5.73 (18)	-6.15 (21)	-6.07 (19)	-4.29 (35)	-18.5 (10)	-4.19 (27)
HC_3N	-9.81 (27)	-12.7 (5)	-13.7 (4)	-6.26 (28)	-6.38 (28)	-6.61 (28)	-6.52 (37)	-24.3 (20)	-8.20 (68)
HC_5N	-11.0 (5)	-20.2 (10)	-17.3 (7)	-7.39 (60)	-7.67 (65)	-7.84 (66)	-5.41 (51)	-34.4 (27)	-8.80 (90)
NH_3	-7.99 (76)	-	-11.6 (6)	-7.37 (56)	-	-11.5 (4)	-6.14 (86)	-	-6.84 (80)
CH_2NH	-7.05 (27)	-5.44 (15)	-7.06 (23)	-5.45 (35)	-5.16 (33)	-5.38 (32)	-6.07 (25)	-3.23 (16)	-5.93 (22)
$C_2H_3NH_2$	-11.4 (7)	-	-15.9 (6)	-9.50 (67)	-	-12.8 (7)	-8.08 (71)	-	-11.4 (10)
CH_3NH_2	-7.75 (59)	-	-12.1 (5)	-6.98 (52)	-	-10.3 (5)	-7.03 (64)	-	-8.63 (86)
CH_5^+	-11.5 (1)	-	-11.5 (1)	-10.9 (1)	-	-10.9 (1)	-6.85 (19)	-	-7.27 (21)
$C_2H_5^+$	-10.8 (1)	-	-10.7 (1)	-9.91 (6)	-	-9.94 (7)	-6.78 (9)	-	-6.91 (22)
$HCNH^+$	-9.19 (15)	-	-9.20 (11)	-9.40 (30)	-	-9.61 (26)	-6.94 (12)	-	-6.89 (20)
$l-C_3H_3^+$	-15.3 (3)	-	-16.3 (3)	-12.8 (2)	-	-12.8 (2)	-8.97 (17)	-	-9.89 (35)
$c-C_3H_3^+$	-11.7 (3)	-	-12.6 (4)	-9.66 (16)	-	-9.68 (17)	-8.07 (19)	-	-8.63 (32)
$C_4H_3^+$	-12.8 (5)	-	-15.8 (6)	-10.9 (4)	-	-11.1 (4)	-9.22 (40)	-	-10.4 (7)
$C_4H_5^+$	-11.9 (3)	-	-12.7 (4)	-9.69 (28)	-	-9.68 (23)	-8.49 (25)	-	-9.13 (46)
$C_6H_5^+$	-16.5 (3)	-	-17.8 (5)	-12.7 (2)	-	-12.8 (2)	-9.58 (21)	-	-10.2 (3)
$C_6H_7^+$	-12.7 (4)	-	-13.8 (6)	-10.0 (3)	-	-10.1 (3)	-8.81 (30)	-	-9.40 (43)
$C_7H_7^+$	-12.4 (4)	-	-13.6 (5)	-9.45 (23)	-	-9.48 (29)	-8.60 (22)	-	-9.19 (39)

In the conditions of Titan's atmosphere, the concentrations of the purely neutral model (Case 11a) are close to those of the model with the complete scheme (Case 9). For instance, the differences of the common logarithms of the C2 (C_2H_2, C_2H_4 and C_2H_6) concentrations between Cases 9 and 11a are tiny. And the difference of those of C_6H_6 is around 0.6, whilst the associated uncertainties are even larger, making the difference little significant. This is an evidence of the impossibility of distinguishing the effect of neutral and ion chemistries by a comparison of experimental and simulated neutral MS (see Fig. 5.20). The neutral MS diagnosis is therefore little sensitive to the ion chemistry description. Note that the "little" difference discussed above in the scale of order of magnitude only means the total production and the part going through the neutral chemistry are in the same order of magnitude, but not that the ion chemistry is negligible.

Obviously, neutral and ion chemistries are in competition. The relative activity of the latter with respect to the former may be relevant to the ion radical ratios (the ratios between ion and radical concentrations): $10^{-5} - 10^{-4}$ in the model for the APSIS experiments (Case 1), 10^{-6} for Titan (Case 9), and around 10^{-5} for Imanaka and Smith's experiments (Case 10). Imanaka and Smith's reactor, where most primary radicals are generated by ion chemistry, but not by photolysis, may be an exception to this relation. In Titan's atmosphere, low pressure and low temperature decrease drastically the rate constants of trimolecular recombination, resulting in a lower ion radical ratio. However, lower contribution of the ion chemistry, through which the growth of unsaturated species is quite efficient, does not disfavor it, since the radical pathways for the growth of unsaturated species become more important and compensate the decrease of the ionic contribution.

In the models for Titan, as for the neutral scheme (Case 11a), the global effect of H-loss scheme for dissociative recombination (Case 11b) on most species is weak, for the same reason as in Case 11a. Nevertheless, relatively large effects are observed for several N-bearing species, due to the dominant contribution of dissociative recombination other than H-loss pathways to their production. In the models for Imanaka and Smith's reactor, the effect of H-loss scheme for dissociative recombination (Case 12b) is comparable to that for the APSIS experiments (Case 3). In general, the magnitude of this effect in various cases can also be explained by the ion radical ratios. Nevertheless, Imanaka and Smith's experiments are still of particularity to some extent: the neutral pathway

$$\mathrm{CH_4 + CH} \xrightarrow[-\mathrm{H}]{} \mathrm{C_2H_4} \xrightarrow[-2\mathrm{H/H_2}]{+h\nu} \mathrm{C_2H_2} \tag{5.39}$$

that forms C_2H_2 is always active in the APSIS experiments and Titan's atmosphere, while the production of the central species of molecular growth, C_2H_2, almost completely relies on ion chemistry, especially dissociative recombination, because the photolyses of CH_4 and C_2H_4 produce no CH or C_2H_2, but only ions at 60 nm. That is why the change of the dissociative recombination scheme should have a larger impact on C_2H_2 production, and hence the growth, than expected simply according to the ion radical ratio.

5.6 Conclusion

The APSIS experiments have been studied by a model with a fully coupled chemical scheme, *i.e.* involving all photolysis, bimolecular, trimolecular and ion-molecule reactions and dissociative recombinations with available kinetic data. The methane consumption is acceptable and the production

Case	Radiation	Pressure (Pa)	Temperature (K)	Residence time (s)	Modification of reaction scheme	Main conclusions
1	DISCO	700	300	284.2	-	probable recombinations on the reactor walls
2	DISCO	700	300	284.2	neutral*	large decrease of the production of heavy species
3	DISCO	700	300	284.2	H-loss**	large decrease of the production of unsaturated heavy species
4	60 nm	700	300	284.2	-	more production of heavy saturated species than in Case 1 due to charge transfer
5	82 nm	700	300	284.2	-	larger uncertainties due to the methane photolysis branching ratios, larger N-bearing species production
6	Solar	700	300	284.2	-	less production due to less ionizing photons
7	DISCO	7×10^{-4}	300	284.2	-	growth of unsaturated species favored due to slower trimolecular reactions
8	DISCO	700	150	284.2	-	growth of heavy unsaturated species favored due to slower neutral chemistry
9	Solar	7×10^{-4}	150	2.842×10^{6}	-	production in good agreement with the observations at the level of MS
10	60 nm	6.6	300	113.7	-	poor agreement between simulated and experimental MS probably due to heterogeneous chemistry
11a	Solar	7×10^{-4}	150	2.842×10^{6}	neutral	few significant deviations from Case 9 due to efficient unsaturated neutral growth pathways
11b	Solar	7×10^{-4}	150	2.842×10^{6}	H-loss	*id.*, except for several N-bearing species mainly produced by DR other than H-loss pathways
12a	60 nm	6.6	300	113.7	neutral	chemistry almost completely deactivated since the initiation step is essentially photoionization
12b	60 nm	6.6	300	113.7	H-loss	comparable to Case 3 owing to the cancellation between the impacts of lower ion-radical ratios and C_2H_2 essentially formed through ionic pathways

Table 5.6: Summary of the main conclusions in the cases of the 1-cell model variants in this study. *neutral: only neutral reactions; **H-loss: only H-loss pathways for dissociative recombination.

in Cx blocks is in good agreement with the measurements. The uncertainties on the species stationary concentrations, whose major sources are bimolecular and ion-molecule reactions, generally increase with molar mass.

Ion chemistry and full dissociative recombination scheme have been shown to be important to the model. Without them, the production of heavy species and heavy unsaturated species, respectively, would be drastically lowered.

By sensitivity analysis, few reactions were found to be influential on individual species, preventing us from reducing the chemical scheme. Nevertheless, photolysis and several reactions sensitive to pressure, mostly trimolecular reactions, appear as global *key reactions*. Influential photolysis are consistent with the previous studies (Hébrard et al., 2009; Peng et al., 2010), and influential trimolecular reactions result from the relatively high pressure in the APSIS reactor. Block patterns (see Fig. 5.9) were observed in a species correlation analysis similar to Westlake et al. (2012), indicating the importance of the addition of small (C1 or C2) units in the molecular growth. After a classification of the elements in the block patterns by similarity, 3 growth families, promoted by C_2H_2, C_2H_4 and C_2H_5, respectively, were highlighted: C_2H_2's family promotes the growth of unsaturated species, remarkably with the aid of ion-molecule reactions, while C_2H_5's family, where radical chemistry plays a major role, promotes the growth of saturated species, essentially with a trimolecular termination; C_2H_4's family is less important in molecular growth, but highly important in nitrogen fixation, a major pathway of which starts with the reaction of C_2H_4 with $N\left(^2D\right)$. The prominence of C_2H_2's family among the three was clearly identified, *i.e.* the growth pathways of *unsaturated* species via *ion* chemistry are the most efficient and important.

We also studied the impacts of radiation spectrum, pressure, temperature and gas residence time through variants of the reference model (Case 1) (see Tab. 5.6). The case with a monochromatic irradiation at 60 nm (Case 4) has more production of heavy saturated species than in Case 1, due to the charge transfer of photoionized nitrogen to methane, also highlighted in Imanaka and Smith (2007), while the cases with a monochromatic irradiation at 82 nm (Case 5) or solar spectrum (Case 6) have generally less production, due to much smaller ionizing portion in their radiation. In the cases at low pressure (Case 7) and low temperature (Case 8), trimolecular reactions and neutral reactions are respectively slowed down, leading to the disfavored production of saturated species in each block.

Titan's ionosphere meets simultaneously the conditions favoring the growth of unsaturated species, *i.e.* low pressure and low temperature, leading to a production of unsaturated species, detected in an INMS neutral spectrum (Waite et al., 2007) well reproduced by our modeling results. However, the models for Titan with the neutral scheme or H-loss dissociative recombination pathways do not qualitatively change the simulated MS. Furthermore, Bézard et al. (2013) pointed that INMS neutral data are not adequate to quantitatively determine the species concentrations. Based on the two arguments above, INMS neutral spectra can hardly reflect the effect of ion chemistry on neutral species.

The simulated MS for the APSIS experiments and Imanaka and Smith's experiments (Imanaka and Smith, 2010) are not in good agreement with the experimental ones, especially in the saturated part of each band. The simulated MS systematically underestimate the intensities of the saturated part.

This large discrepancy reveals the inadequacy of the homogeneous model, always favoring the growth of unsaturated species, in describing the formation of saturated species in the experiments.

If the recombination catalyzed by the reactor's walls are taken into account, the simulated MS are significantly improved, which strongly suggests the existence of such effects in the laboratory simulation setups of atmospheric chemistry.

On the other hand, we have well identified the homogenous and heterogeneous chemistries in the reactor. The former essentially involves the growth of unsaturated species and is representative of the chemistry in Titan's upper atmosphere, and the latter promotes the production of saturated species and can be regarded as a bias from Titan's photochemistry. Seeing that the variations of the unsaturated parts in the simulated MS are much smaller than the saturated parts in the test cases with different trimolecular rate constants, one may consider only the experimental results of unsaturated species for a qualitative laboratory simulation study of Titan's photochemistry.

The existence of wall effects also reveals the needs of relevant further studies: simulation experiments at relatively low temperature (*e.g.* at ∼0 °C, leading to wall recombinations ∼100-1000 times slower than at room temperature (Gorodetsky et al., 2005)) or using less catalytic wall materials to reduce these effects, and measurements of the kinetic parameters of involved heterogeneous reactions for their appropriate consideration in the model.

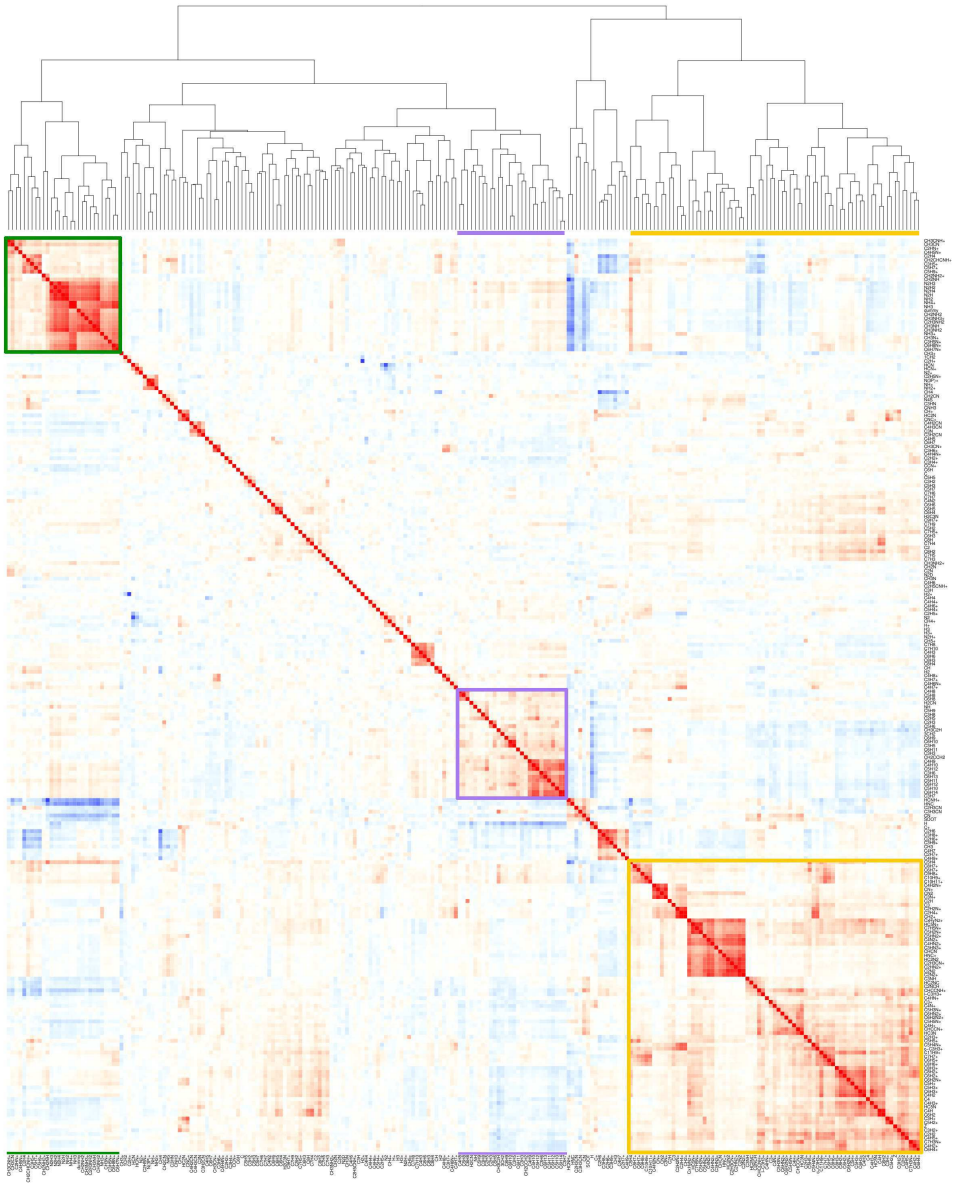

Figure 5.10: Heatmap of the correlation matrix among species concentrations. Correlation coefficients from -1 to 1 are denoted by squares whose color gradually changes from blue (-1) to red (1) via white (0). 3 main square blocks are framed in dark green, violet and orange, respectively (from top left to bottom right).

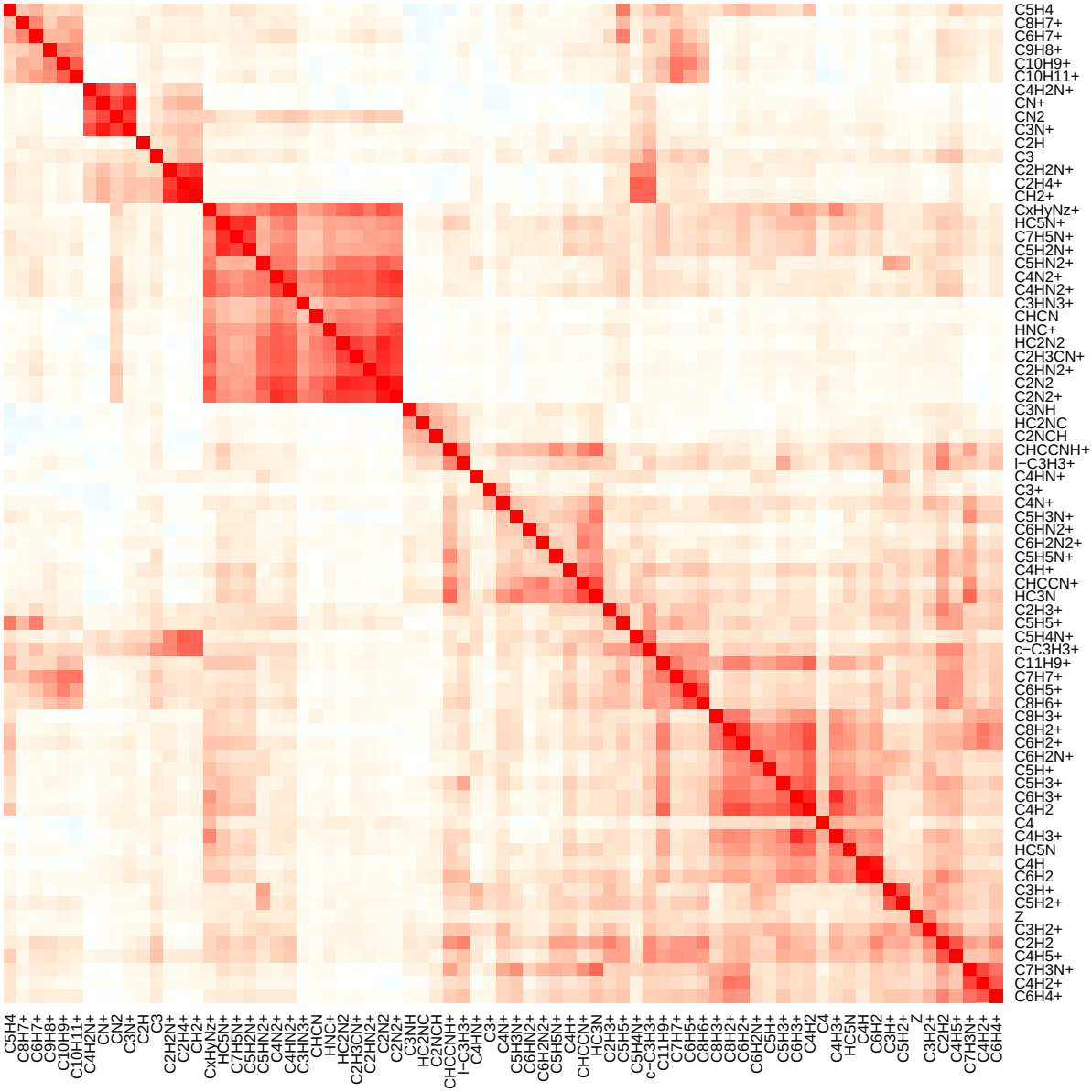

Figure 5.11: Zoom-in of C_2H_2's block in the heatmap of the correlation matrix among species concentrations. Correlation coefficients from -1 to 1 are denoted by squares whose color gradually changes from blue (-1) to red (1) via white (0).

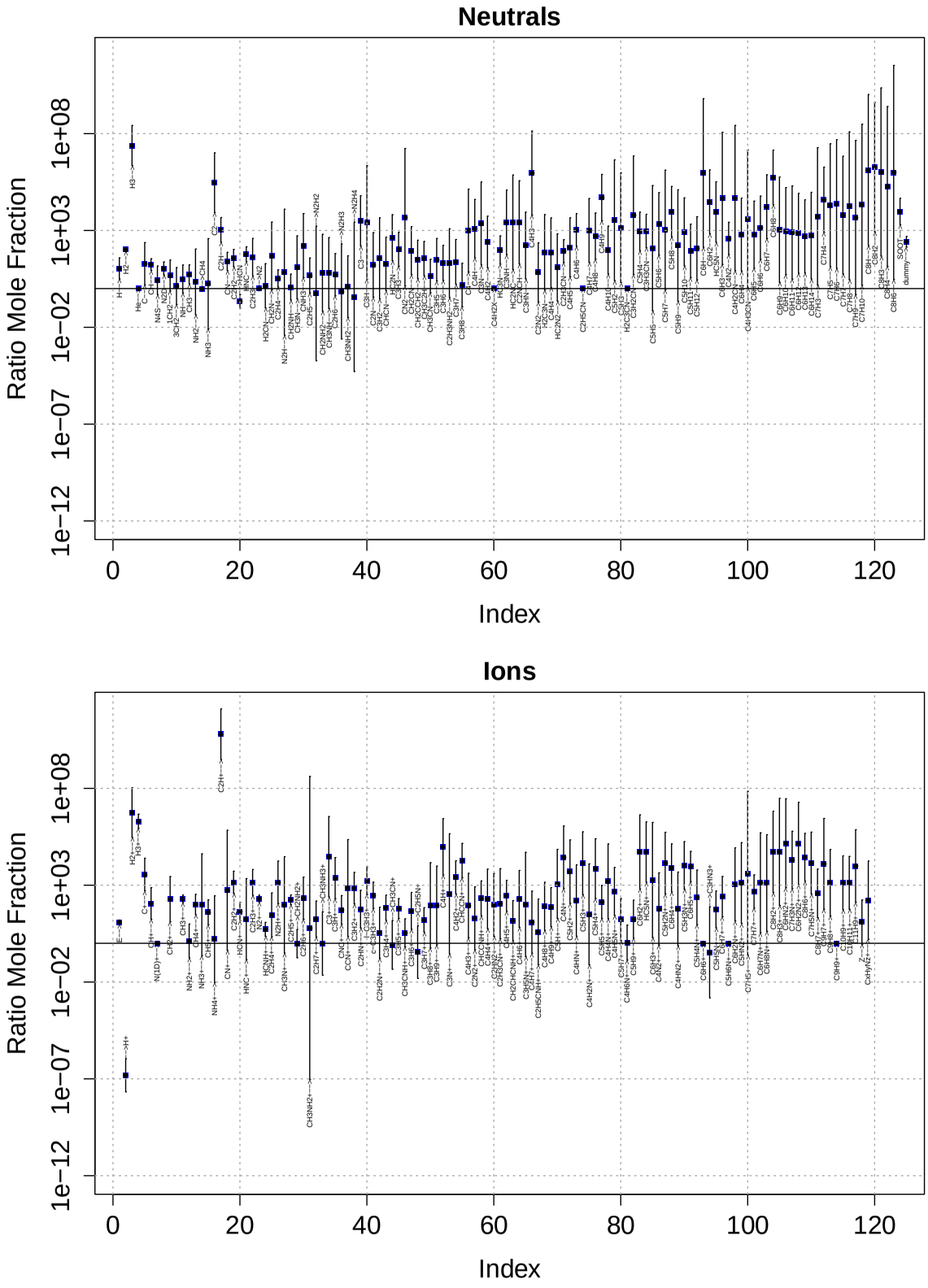

Figure 5.12: Ratios of stationary concentrations of neutrals (top) and ions (bottom) in Case 4 (monochromatic irradiation at 60 nm) to those in the reference model (Case 1). Ratios' mean values and uncertainties (95% confidence interval) are respectively denoted by squares and error bars.

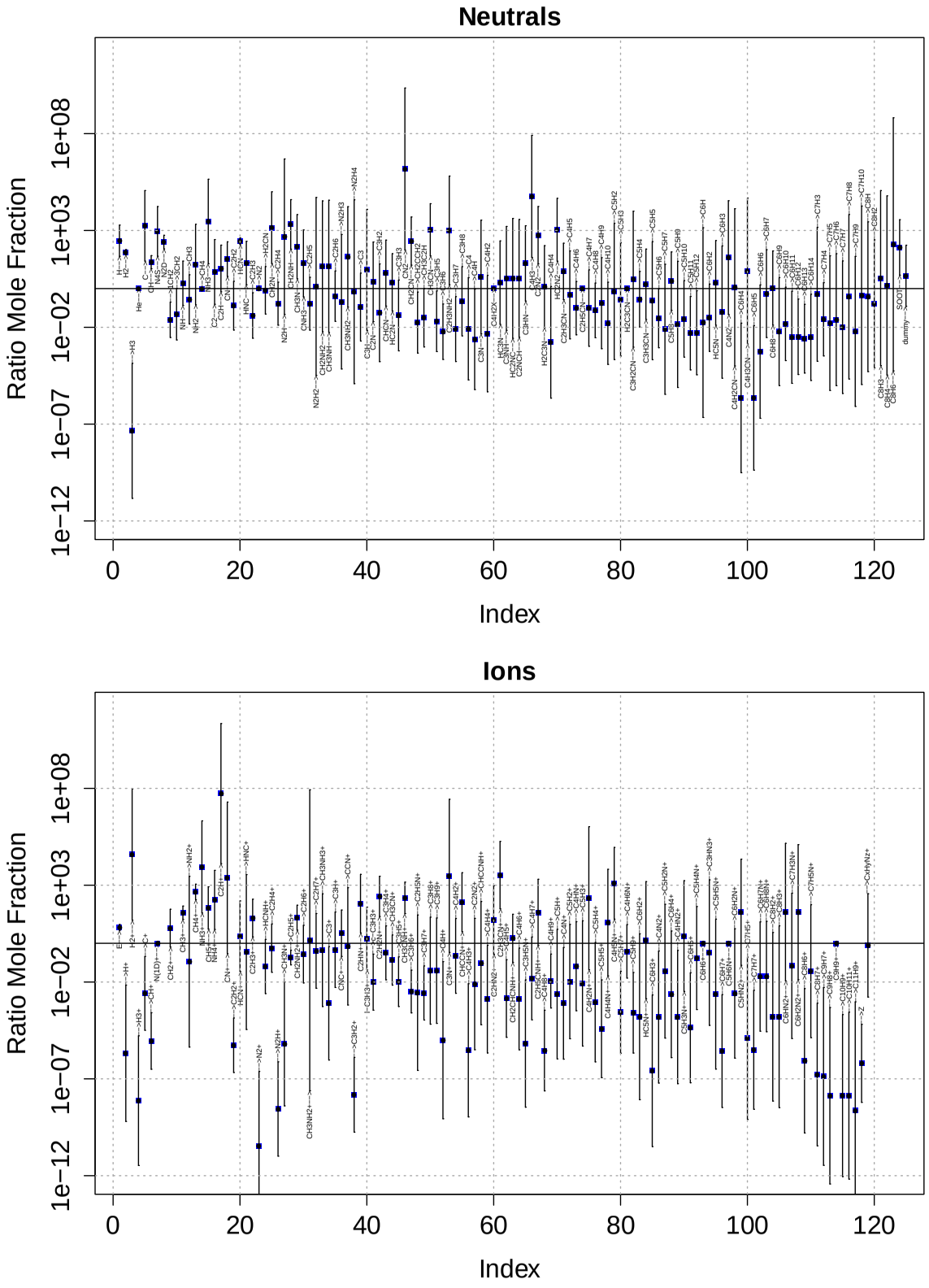

Figure 5.13: Ratios of stationary concentrations of neutrals (top) and ions (bottom) in Case 5 (monochromatic irradiation at 82 nm) to those in the reference model (Case 1). Ratios' mean values and uncertainties (95% confidence interval) are respectively denoted by squares and error bars.

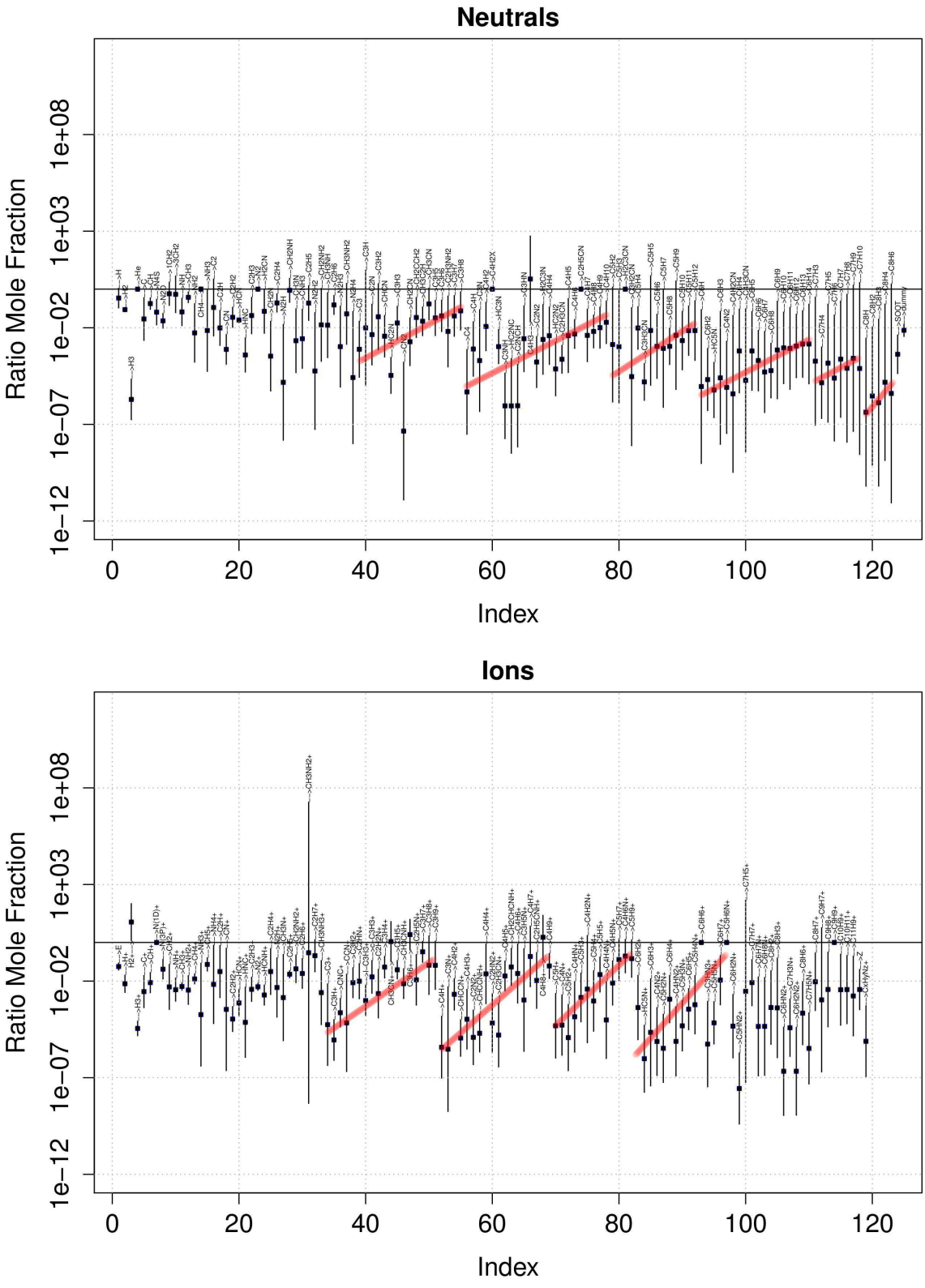

Figure 5.14: Ratios of stationary concentrations of neutrals (top) and ions (bottom) in Case 6 (irradiation with solar spectrum) to those in the reference model (Case 1). Ratios' mean values and uncertainties (95% confidence interval) are respectively denoted by squares and error bars. The discrimination between unsaturated and saturated species in each block is highlighted by red bars.

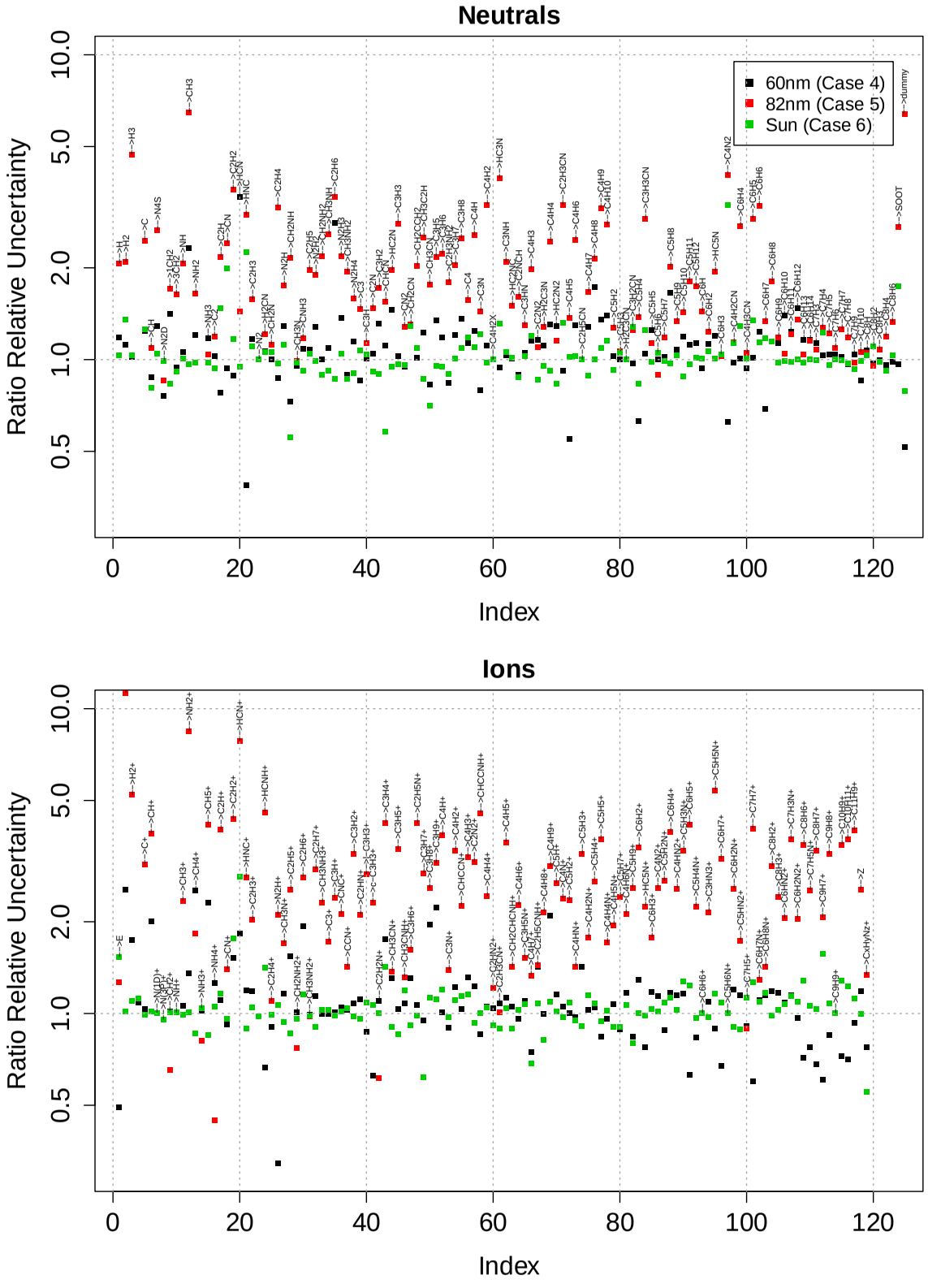

Figure 5.15: Ratios of uncertainties on stationary concentrations of neutrals (top) and ions (bottom) in the 1-cell model variants in this study with radiation spectrum changed for monochromatic radiation at 60 nm (Case 4, black) and 82 nm (Case 5, red) and solar spectrum (Case 6, green) to those in the standard 0D model (Case 1).

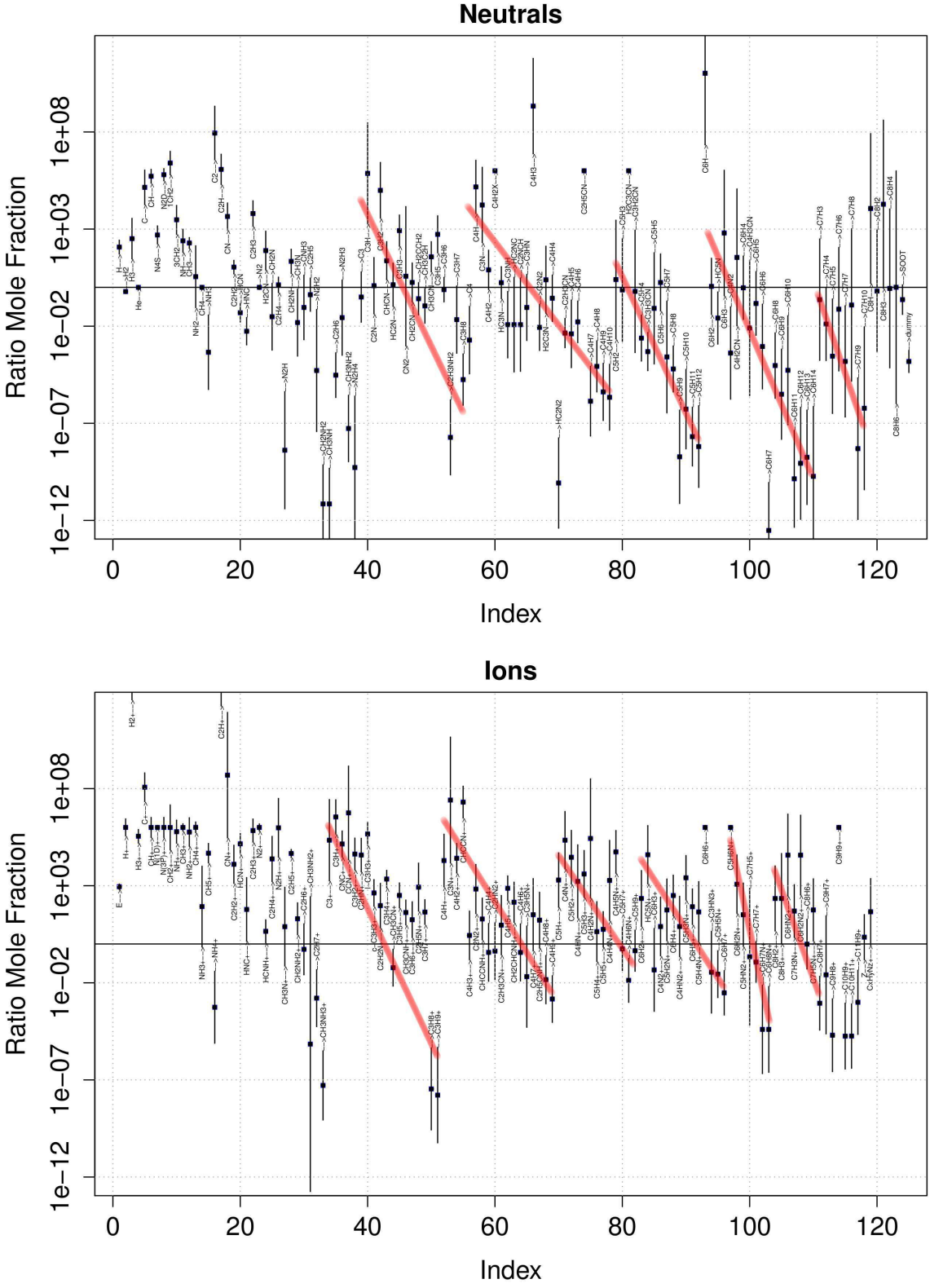

Figure 5.16: Ratios of stationary concentrations of neutrals (top) and ions (bottom) in Case 7 (at 7×10^{-4} Pa, 10^{-6} of the pressure in Case 1) to those in the reference model (Case 1). Ratios' mean values and uncertainties (95% confidence interval) are respectively denoted by squares and error bars. The discrimination between unsaturated and saturated species in each block is highlighted by red bars.

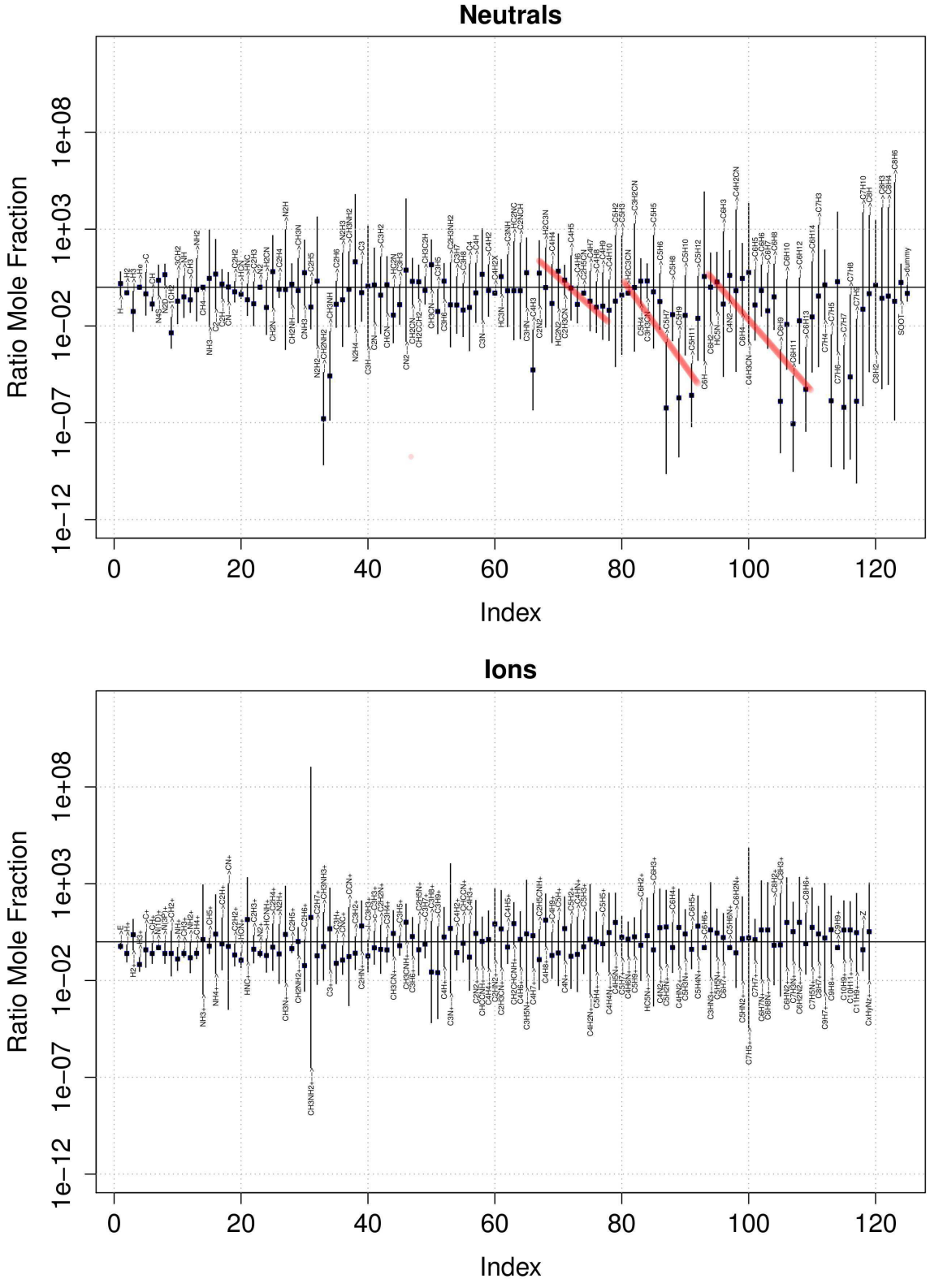

Figure 5.17: Ratios of stationary concentrations of neutrals (top) and ions (bottom) in Case 8 (at 150 K) to those in the reference model (Case 1). Ratios' mean values and uncertainties (95% confidence interval) are respectively denoted by squares and error bars. The discrimination between unsaturated and saturated species in each block is highlighted by red bars.

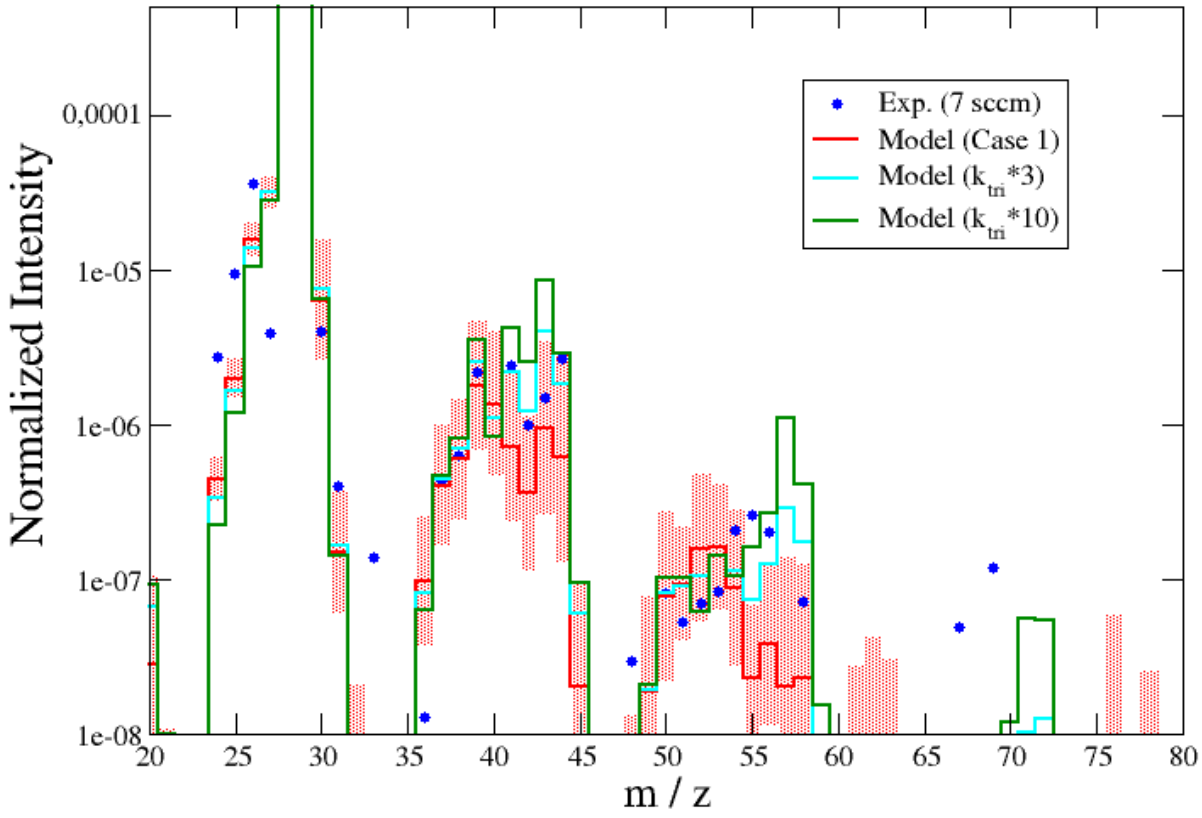

Figure 5.18: Simulated neutral mass spectra (solid lines) of Case 1 (red) and Case 1 with trimolecular rate constants multiplied by a factor of 3 (cyan) and 10 (dark green), compared to *in situ* gas phase MS in an APSIS experiment at 7 sccm (blue points). The MS intensities are normalized with respect to that of N_2. The 95% confidence intervals of simulated spectra of Case 1 are shown by shaded area. Those of cases with modified reactions are not presented for better legibility.

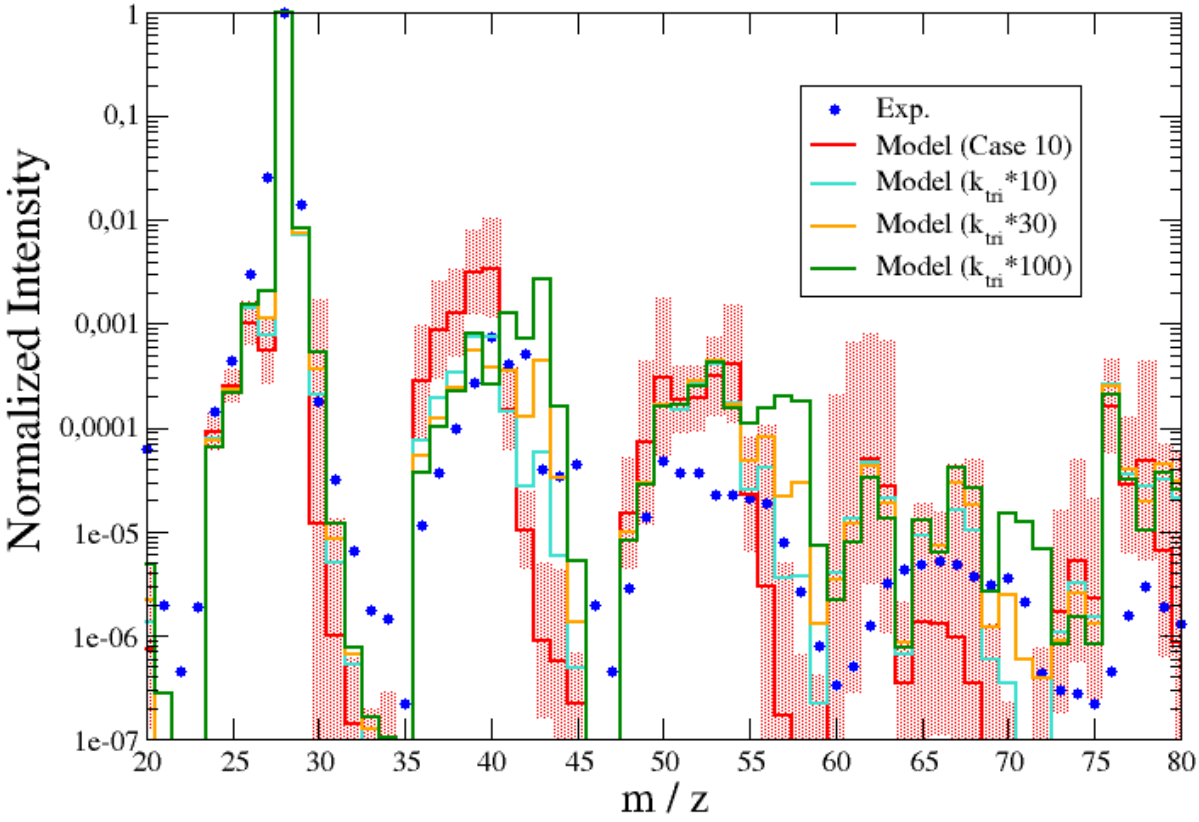

Figure 5.19: Simulated neutral mass spectra (solid lines) of Case 10 (red) and Case 10 with trimolecular rate constants multiplied by a factor of 10 (magenta), 30 (dark green) 100 (orange), compared to *in situ* gas phase MS in Imanaka and Smith (2010) (blue points). The MS intensities are normalized with respect to that of N_2. The 95% confidence intervals of simulated spectra of Case 10 are shown by shaded area. Those of cases with modified reactions are not presented for better legibility.

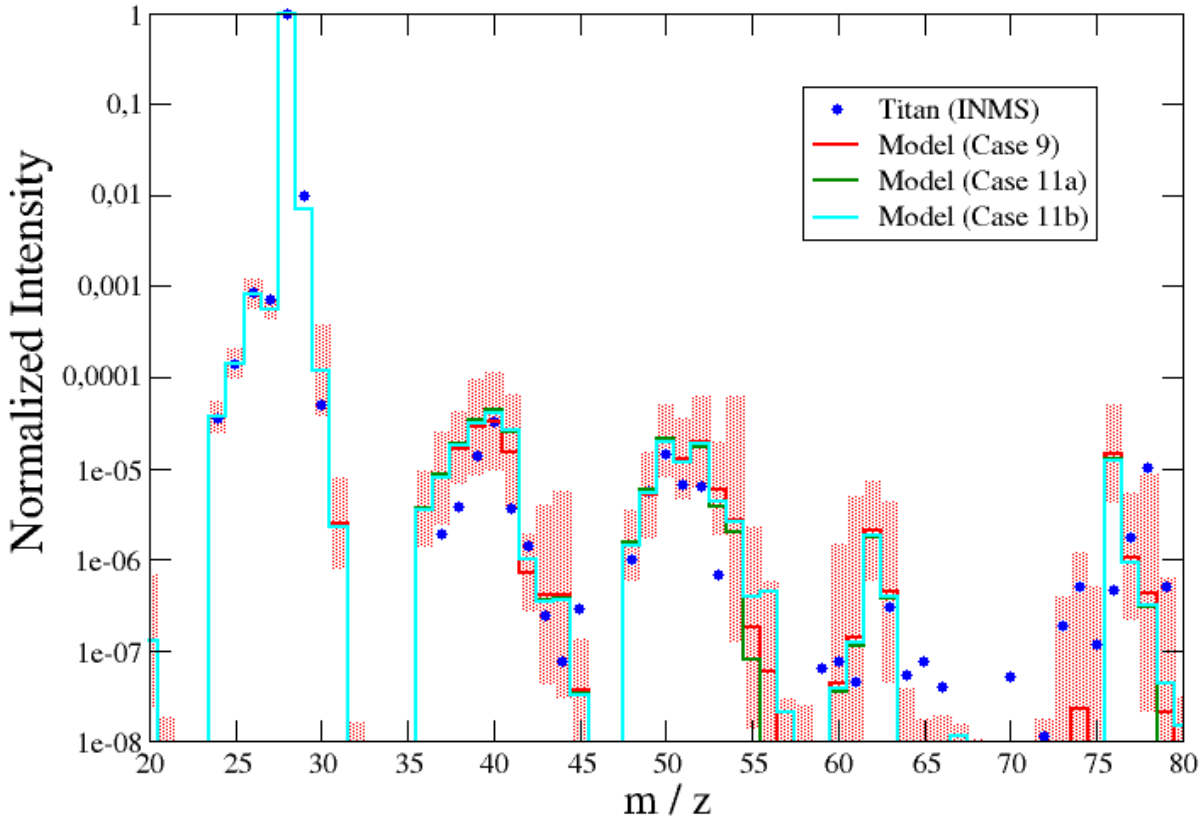

Figure 5.20: Simulated neutral mass spectra (solid lines) of Cases 9 (red), 11a (dark green) and 11b (cyan), compared to INMS neutral MS for Titan Waite et al. (2007) (blue points). The MS intensities are normalized with respect to that of N_2. The 95% confidence intervals of simulated spectra of Case 9 are shown by shaded area. Those of cases with modified reactions are not presented for better legibility.

Chapter 6

Conclusions and perspectives

6.1 Overview and main findings

In the work of this thesis, we performed both experimental and theoretical simulations of Titan's photochemistry.

Experimentally, laboratory simulations were conducted with the new setup, APSIS (Atmospheric Photochemistry SImulated by Synchrotron), windowless coupled with the DISCO VUV beamline at the SOLEIL synchrotron radiation facility. In the APSIS reactor, a gas flow of N_2/CH_4 (90/10) was irradiated by a continuous VUV (60-350 nm) beam. The neutral photochemical products were detected by *in situ* mass spectrometry and *ex situ* GC-MS of a cryogenic experiment.

Products with detectable signals in the mass spectra (MS) are of two up to four (probably five) heavy (C or N) atoms. The production of C2-C4 hydrocarbons are confirmed by GC-MS results. Several nitriles are also detected by GC-MS. Compared to the MS in a plasma experiment (Carrasco et al., 2012) and in an experiment with monochromatic synchrotron radiation (Imanaka and Smith, 2010), and to the neutral spectra of the INMS onboard Cassini (Waite et al., 2007), the APSIS reactor seems to well reproduce Titan's relative neutral production, despite its different environmental conditions and lower production efficiency.

Theoretically, the uncertain photolysis processes, having uncertain cross-sections and branching ratios, were explicitly treated in Titan's photochemical models for the first time. This is based on a separate treatment of cross-sections and branching ratios, and on adequate representations of these two types of parameters, especially branching ratios.

We developed a wavelength-dependent model for the branching ratios of CH_4 in its whole absorption wavelength range. This model inherits the important advantage of the representation of Plessis et al. (2010), *i.e.* the strong ability to use all available information as far as possible, even if the information is very limited. It also preserves the correlations between the branching ratios at different wavelengths.

We considered explicitly the uncertainty on the photolysis cross-sections in a radiative transfer model of Titan's atmosphere, and observed strong altitude variations of the uncertainty on the photolysis rate constants and the presence of *Null Variance Altitudes* (NVAs), *i.e.* specific altitudes where the uncertainty on the photolysis rate constants vanishes. We demonstrated analytically that the NVAs are born by major absorbing species with a barometric, or nearly barometric, distribution, and located at the altitudes of unity optical depth, where the species have maximal photolysis rates.

In addition, we applied the new wavelength-dependent branching ratios representation for CH_4

to a Titan neutral photochemical model. It was shown that the model is mainly sensitive to the CH_2/CH_3 ratio, and that a slight bias is introduced in the model predictions when neglecting the electronic state description of CH_2. Several models used the experimental values of Wang et al. (2000) to describe methane photolysis branching ratios at Ly-α, which lead to an overestimation of the CH_2 chemistry chain and should be updated to those of (Gans et al., 2011). Also, the arbitary scenarii, *i.e.* a "100% CH_3" one and a Ly-α-like one, for branching ratios at non-Ly-α wavelengths, should be avoided.

Based on the neutral model of Hébrard and coworkers (Hébrard, 2006; Hébrard et al., 2007), including bi- and tri-molecular reactions, the model of ion chemistry of S. Plessis (Plessis et al., 2010, 2012), including ion-molecule reactions and dissociative recombination, and our new representation of photolysis parameters, we developed a fully ion-neutral coupled photochemical model for the APSIS experiments. This model enabled us to interpret the results of the APSIS experiments and their comparison with Titan's upper atmosphere (the INMS data) and Imanaka and Smith's experiments, which can also be investigated by photochemical models.

Compared to the measurements, the production in Cx blocks is in good agreement and the methane consumption is acceptable. Ion chemistry and the full dissociative recombination scheme have been demonstrated to be important to the model, confirming the value of our ion-neutral coupled model. As in the previous studies Hébrard et al. (2009); Peng et al. (2010), the photolysis processes were confirmed by sensivity analysis to be globally influential.

After a species correlation analysis, we found the importance of the addition of small (C1 or C2) units in the molecular growth, as Westlake et al. (2012), as well as 3 growth families, promoted by C_2H_2, C_2H_4 and C_2H_5, respectively. Among the three families, the prominence of the C_2H_2 family, in which the growth pathways of *unsaturated* species via *ion* chemistry are the most efficient, was clearly identified.

Through variants of the reference model of the APSIS experiments with a single modified physical factor, we showed that low pressure and low temperature favor the growth of unsaturated species. These conditions are fulfilled in Titan's ionosphere. The INMS neutral spectrum in (Waite et al., 2007), in which there is mainly the signal of unsaturated species, can be well reproduced by our simulated MS.

Compared to the experimental MS of the APSIS experiments and Imanaka and Smith's experiments (Imanaka and Smith, 2010), the simulated MS systematically underestimate the intensities of the saturated part of each band, illustrating the inadequacy of an homogeneous kinetics model. After the consideration of the recombinations catalyzed by the reactor's walls, we improved the simulated MS significantly. This strongly suggests the existence of wall effects in the laboratory simulation setups of atmospheric chemistry. Therefore, we distinguished the homogenous chemistry involving the growth of unsaturated species and representative of that in Titan's upper atmosphere, and the heterogeneous chemistry resulting in the promotion of the production of saturated species, a bias from Titan's photochemistry. For a qualitative laboratory simulation study of Titan's photochemistry, it may be enough to consider only the experimental results of unsaturated species.

6.2 Data needs

Note that our probabilistic representations only reflect all available information properly, and *do not improve* the precision of kinetic parameters, which usually requires new measurements. Thus,

the strong need for re-evaluation of some parameters are not reduced, but correctly manifested in the models.

The methane photolysis branching ratios around 80 nm and between 130 and 140 nm require measurements to reduce their uncertainty due to the interpolation/extrapolation to the extremities of the wavelength range of the neutral photolysis pathways. Their measurements will considerably improve the precision of the model predictions on nitrogen chemistry, mainly initiated by photons in the range of 75-100 nm, and Titan's photochemistry around 600 km, where the photolysis of CH_4 between 130 and 140 nm is dominant (see Fig. 3.3), respectively.

In spite of large global influences of individual photolytic processes, the most numerous among the reaction types, bimolecular (including ion-molecule) and trimolecular reactions, contribute most to the total uncertainty budget of the models, of both Titan and the APSIS experiments. Thus, we still need to keep improving the precision of the rate constants of these reactions, especially the ones appearing as key reactions, as depicted in the Fig. 1 of Wakelam et al. (2010). Since the influence of individual reactions are substantially "diluted" in a very large chemical scheme, many bimolecular and trimolecular reactions of a moderate influence need to be re-evaluated. Considering the large uncertainty on the models of both of Titan and the APSIS experiments, there is still a long way to go to achieve quantitative predictions of the chemistry.

6.3 Perspectives

The effects of transport, especially the diffusion inside the reaction systems, were rarely studied in this work. However, they might also play an important role in the models. Although it was shown through our 1-cell model tests that an APSIS model at a higher dimensionality would not change the basic chemical regime, it is still better to establish a model for the APSIS experiments explicitly accounting for the strongly, weakly and non irradiated regions in the reactor and the transport between them. A preliminary 2D model has been developed for the APSIS experiments (Peng et al., 2011), and the study of the effect of the internal diffusion on the chemistry is in progress. The mass exchange between the gas phase and the reactor walls, on which heterogeneous chemistry occurs, should be included in the model. However, for a severe lack of measurements or even estimations of involved heterogeneous kinetic parameters, a detailed treatment of the wall effects seems to be difficult. Any new data of these parameters are thus welcome.

With the aid of the APSIS model, we highlighted the importance of ion chemistry and identified the wall effects in the APSIS experiments. Therefore, in the further APSIS experiments, we may introduce measurements of ions, a direct experimental study of ion chemistry. To reduce wall effects, we may also conduct the experiments at lower temperature or with a reactor with passivated wall material.

Finally, many tools developed and results obtained during this thesis work have a rather wide usability: (i) the APSIS experiment, whose feasibility has been demonstrated in this study, can be easily transformed into a platform for the investigation of other planetary atmospheres, by modulating the physical conditions; (ii) the Null Variance Altitudes may exist for major absorbers with a barometric or nearly barometric distribution in other atmospheres, not only Titan's; (iii) the novel probabilistic representation of photolysis parameters is obviously not only applicable to the species in this work, but also to all photolysis processes; and (iv) the species correlation analysis, powerful in the identification of the major molecular growth pathways in the APSIS model, can

also be applied to reveal the mechanism of other highly complex chemical systems.

Appendix A

Preliminary 2D model for the APSIS experiments

The APSIS reactor is a parallelepiped with internal dimensions (length × width × height) of 500 mm × l14 mm × 92 mm. The DISCO beam, with a diameter of ∼1 cm, irradiate the gas mixture along the reactor length (see Section 4.1). As a consequence, only a very narrow column in the reactor is irradiated, and only thermal reactions take place in most of the reactor's internal space. Even in the irradiated column, the radiative transfer occurs in a rather heterogeneous way: methane has an optical depth of a few centimeters in the experiments at 7 sccm, and that of nitrogen is even much shorter, while the reactor length is 50 cm. In order to describe these heterogeneous structures in the system of interest, we extended the 1-cell model for the APSIS experiments (see Chapter 5) to a 2-dimensional one and compared the product concentrations at the stationary state.

A.1 Model description

It is much more important to describe properly the narrow irradiated column and the space close to it than the region near the reactor walls. We eliminate a dimension (from the real parallelepiped reactor's 3D to the model's 2D) by altering the reactor's cross-section to a circular form in the model. Consequently, the reactor can be transformed into a cylindrical 2D geometry with a radial coordinate r, perpendicular to the reactor length (called the axial coordinate, x, thereafter). The angular coordinate is omitted thanks to the hypothetical cylindrical symmetry of the system. The radius of the hypothetical circular cross-section is evaluated from the area of the real rectangular cross-section of the reactor. Conventionally, the radial coordinate measures the distance to the center of the cross-section ($r = 0$).

To present the 2D model, we use the same unit system as the 1-cell model, and the same notations when possible.

As in the 1-cell model, the total balance equation (Eq. 5.5) plays a central role, nevertheless, the internal transport should now be taken into account, *i.e.*

$$Q_i = -\boldsymbol{\nabla} \cdot \boldsymbol{\Phi_i} \tag{A.1}$$

The form of this formula in the cylindrical coordinate system is

$$Q_i = -\frac{\partial\left(\boldsymbol{\Phi_i}\cdot\boldsymbol{e_x}\right)}{\partial x} - \left(\frac{\partial}{\partial r}+\frac{1}{r}\right)\left(\boldsymbol{\Phi_i}\cdot\boldsymbol{e_r}\right) \tag{A.2}$$

where vectors are in bold and $\boldsymbol{e_x}$ and $\boldsymbol{e_r}$ are the unit vectors of the axial and the radial directions, respectively.

For simplicity, we neglect electrostatic effects among charged species and bewteen them and the reactor's metallic walls. Accordingly, except at the reactor's entrance and exit, the transport flux of the ith species in the new coordinate system is expressed as a combination of the contributions of diffusion and advection, *i.e.*

$$\begin{aligned}\boldsymbol{\Phi_i} &= -D_i\boldsymbol{\nabla}c_i + c_i\boldsymbol{v_{ad}} &\text{(A.3)}\\ &= \left(-D_i\frac{\partial c_i}{\partial x}+c_i v_{ad}\right)\boldsymbol{e_x} - D_i\frac{\partial c_i}{\partial r}\boldsymbol{e_r} &\text{(A.4)}\end{aligned}$$

where the first term, $-D_i\boldsymbol{\nabla}c_i$, is written according to Fick's first law and D_i is the diffusion coefficient of the ith species (in $\mathrm{m}^2.\mathrm{s}^{-1}$), estimated by the method described in Wilson (2002).

A.1.1 Discretization of the model

Considering the heterogeneous structure of the present photochemical system, we adopt a formulation allowing a non-uniform model discretization. The reactor is divided into k_{max} cells axially and l_{max} cells radially, resulting in $k_{max}+1$ axial interfaces and $l_{max}+1$ radial interfaces, composed of $k_{max}-1$ or $l_{max}-1$ interfaces between the cells and 2 interfaces at the extremities of each coordinate: the reactor's entrance and exit in the axial coordinate and the center of the irradiated column ($r=0$) and the reactor's internal lateral edges in the radial coordinate. The two subscripts, k and l, respectively denote the axial and the radial numbers of a cell (*e.g.* the kth axial and the lth radial cell is denoted as the cell-kl) or an interface.

According to the separation of the transport fluxes in the two coordinates in Eq. A.4, the discretization of the transport part the of the 2D model can be done along the axial and the radial coordinates separately, *i.e.*

$$\Phi_{x,ikl} = -2D_i\frac{c_{ikl}-c_{i(k-1)l}}{\Delta x_{k-1}+\Delta x_k} + \frac{\Delta x_k c_{i(k-1)l}+\Delta x_{k-1}c_{ikl}}{\Delta x_k+\Delta x_{k-1}}v_{ad}, \qquad k=2,3,\cdots,k_{max} \tag{A.5}$$

$$\Phi_{r,ikl} = -2D_i\frac{c_{ikl}-c_{ik(l-1)}}{\Delta r_{l-1}+\Delta r_l}, \qquad l=2,3,\cdots,l_{max} \tag{A.6}$$

where $\Phi_{x,ikl}$ and $\Phi_{r,ikl}$ are respectively the axial and the radial scalar components of the ith species transport flux entering into the cell-kl (accordingly, the outgoing scalar components of this cell are $\Phi_{x,i(k+1)l}$ and $\Phi_{r,ik(l+1)}$). c_{ikl} is the concentration of the ith species at the center of the cell kl. Δx_k and Δr_l are respectively the lengths of the kth axial cell and the lth radial cell. $\frac{\Delta x_k c_{i(k-1)l}+\Delta x_{k-1}c_{ikl}}{\Delta x_k+\Delta x_{k-1}}$ approximates to the concentration of the ith species at the interface through which the axial flux enters into the cell-kl, and $\frac{\Delta x_{k-1}+\Delta x_k}{2}$ and $\frac{\Delta r_{l-1}+\Delta r_l}{2}$ measure the distances between the centers of the axially and radially adjacent cells, respectively.

The boundary conditions of the axial transport are defined in the same manner as in the 1-cell

model, *i.e.* at the entrance

$$\Phi_{\mathrm{N_2},1l} = \frac{0.9q_{re}}{A} \tag{A.7}$$

$$\Phi_{\mathrm{CH_4},1l} = \frac{0.1q_{re}}{A} \tag{A.8}$$

$$\Phi_{\mathrm{He},1l} = \frac{q_{ca}}{A} \tag{A.9}$$

$$\Phi_{i,1l} = 0 \qquad \forall i \notin \{\mathrm{N_2},\ \mathrm{CH_4},\ \mathrm{He}\} \tag{A.10}$$

and at the exit

$$\Phi_{i,k_{max}l} = c_{ik_{max}l} v_{ad} \tag{A.11}$$

The radial transport fluxes at the center and the edge of the reactor's cross-section, *i.e.* the first and the last interfaces along the radial coordinate, are fixed at 0, due to the symmetry around the rotational axis at the center of the cross-section and the reflection of the reactor walls.

Given the transport fluxes, we calculate the ith species concentration variation stemming from the transport at the cell-kl, Q_{ikl}, by combining the fluxes in the two coordinates

$$Q_{ikl} = \frac{\Phi_{ikl} - \Phi_{i(k+1)l}}{\Delta x_k} + \frac{\Phi_{ikl} - \Phi_{ik(l+1)}}{\Delta r_l} - \frac{1}{2}\left(\frac{\Phi_{ikl}}{\sum_{l'=1}^{l-1} \Delta r_{l'}} + \frac{\Phi_{ik(l+1)}}{\sum_{l'=1}^{l} \Delta r_{l'}} \right) \tag{A.12}$$

where $\sum_{l'=1}^{l} \Delta r_{l'}$ substitutes for r in the continuous model (Eq. A.2) at the lth interface along the radial coordinate and $\frac{1}{2}\left(\frac{\Phi_{ikl}}{\sum_{l'=1}^{l-1} \Delta r_{l'}} + \frac{\Phi_{ik(l+1)}}{\sum_{l'=1}^{l} \Delta r_{l'}} \right)$, the average of $\frac{\boldsymbol{\Phi_i} \cdot \boldsymbol{e_r}}{r}$ at the two radial interfaces of the cell-kl, approximates to $\frac{\boldsymbol{\Phi_i} \cdot \boldsymbol{e_r}}{r}$ at its center.

A.1.2 Radiative transfer

The radiative transfer is treated more consistently in the 2D model than the 1-cell model: it is considered to occur only in the first radial column and the photon flux is no longer averaged over the whole reactor cross-section. In the irradiated column, there is no longer only one large cell, but k_{max} cells. Nevertheless, we present a similar formulation for the calculation of photolysis rate constants. $J_{ijk}(x)$ is the rate constant of the jth channel of the photolysis of the ith species for the kth axial cell in the irradiated column. It is represented by the average of the rate constant of the jth channel of the photolysis of the ith species, $J_{ij}(x)$, over the whole cell. This average is noted as $\overline{J_{ijk}(x)}$ and obtained by a generalization of Eq. 5.24, *i.e.*

$$\overline{J_{ijk}(x)} = \frac{\int_{L_k}^{L_{k+1}} J_{ij}(x)\,\mathrm{d}x}{\Delta x_k}. \tag{A.13}$$

where L_k is the distance between the reactor entrance and the kth axial interface, *i.e.*

$$L_k = \begin{cases} 0 & k = 1 \\ \sum_i^{k-1} & k = 2, 3, \cdots, k_{max} \end{cases} \tag{A.14}$$

By analogy with the 1-cell model, L_k and L_{k+1} are respectively the coordinates of the "entrance" and the "exit" of the kth axial cell. With all concentrations given, Eq. A.13 can be expressed as

$$\overline{J_{ijk}(x)} = \int_\lambda I_0(\lambda)\,\sigma_i(\lambda)\,b_{ij}(\lambda)\,\frac{e^{-\tau_k}\left(1 - e^{-\Delta x_k \sum_i (c_{ik}\sigma_i(\lambda))}\right)}{\Delta x_k \sum_i (c_{ik}\sigma_i(\lambda))}\mathrm{d}\lambda \tag{A.15}$$

where τ_k is the optical depth at the kth axial interface and approximately obtained by

$$\tau_k = \begin{cases} 0 & k = 1 \\ \sum_j^{k-1} \sum_i (c_{ik}\sigma_i(\lambda)) & k = 2, 3, \cdots, k_{max} \end{cases} \tag{A.16}$$

This formulation approaches to that in Hébrard (2006) if the total number of cells k_{max} is very large. However, for a preliminary study, in which k_{max} should be limited, this formulation is still more appropriate than that in Hébrard (2006).

A.1.3 Reactions

Owing to the difficulty in reducing the reaction scheme of the APSIS models (see Section 5.2.4.1), the same reaction scheme as for the 1-cell model is applied. We treat the reaction terms of all cells, R_{kl} ($k = 1, 2, \cdots, k_{max}$, $l = 1, 2, \cdots, l_{max}$), separately. In each cell, the reaction term is calculated in the same way as in the 1-cell model.

A.1.4 Integration method

As described in Section 5.1.4, the IRKC method is applied to solve this 2D reaction-transport problem. For each cell, the parts dependent (transport and photolysis) and independent (reactions other than photolysis) on other cells are respectively treated explicitly and implicitly.

A.2 Results and discussions

Due to the large reaction scheme, to avoid the problem of calculation time, the grid of the reactor cannot be very complex. A non-uniform grid may adapt better the heterogenous structure in the reactor. However, with very limited cell number, a highly non-uniform grid is necessary to express the heterogeneous structure significantly better than a uniform one. This type of non-uniform grid causes integration problems of the transport terms. Therefore, for this preliminary study, we adopt a uniform 4 (axial) × 2 (radial) grid ($\Delta x_1 = \cdots = \Delta x_4$ and $\Delta r_1 = \Delta r_2$). The photon flux is averaged on the cross-section of the first radial column. Although the irradiated column in this

model is still larger than the real one, the grid of this model manifests the heterogeneity in the reactor.

We integrate the 2D model in the same conditions as the reference case to the stationary state (after 1000 s), which costs about one day per run. In spite of the simple grid, this integration is still very expensive. Therefore, only 50 Monte Carlo samples of the stationary state are calculated.

In the 2D model, the methane consumption percentage is $0.20 \pm 0.02\%$. Compared to the experimental value, $0.30 \pm 0.06\%$, the methane consumption percentage in the 2D model is remarkably better than that in the 1-cell reference case, $0.07 \pm 0.01\%$. Observing the quasi-uniformity of most stable species in the grid at the stationary state, we present the stationary concentrations of only one cell, *i.e.* the cell-11, in Fig A.1. In the 2D model, the production is slightly higher than in the reference case, consistent with its higher methane consumption. The product composition is very close to that in the reference case, implying the same main growth mechanism. Thus, the difference between the methane consumption in the 2D model and the reference case is likely to stem from the 2D structure.

Several species, such as C_2, C_2H^+ and C_4H^+, are exceptions of the observation that the product composition in the 2D case is very close to that in the reference case. Most of these species are remarkably more produced in the irradiated column, due to the combined effect of multiple involvement of photons in their production and high reactivity in their consumption:

- The formation of these species requires three or more photons, *e.g.*

$$\mathrm{CH_4} \xrightarrow[-\mathrm{H}-\mathrm{H_2}]{+h\nu} \mathrm{CH} \xrightarrow[-\mathrm{H}]{+\mathrm{CH_4}} \mathrm{C_2H_4} \xrightarrow[-2\mathrm{H}/\mathrm{H_2}]{+h\nu} \mathrm{C_2H_2} \xrightarrow[-\mathrm{H}-e^-]{+h\nu} \mathrm{C_2H^+} \ . \tag{A.17}$$

  It is much more enhanced than in a linear way by the intense radiation in the irradiated column.

- These species are highly reactive and can hardly diffuse out of the irradiated column, especially the region close to its entrance, before being consumed.

They are more produced and confined in the most irradiated region, leading to their exceptionally high concentrations. In the non-irradiated region, their concentrations are much lower, even lower than those in the 1-cell model.

In order clarify the effect of this heterogeneous structure, we perform, with the 1-cell model, two tests that roughly simulate the irradiated and the non-irradiated regions in the reactor, respectively:

- for the irradiated region, a test with a photon flux 10 or 100 times higher than in the reference case, which simulates the concentrated radiation;

- for the non-irradiated region, a test without photon flux, but with a molecular inflow whose composition is that of the previous test at the stationary state, which simulates the species formed in the irradiated region and diffusing to the non-irradiated region.

In the first test, methane is approximately 10 or 100 times more consumed than in the reference case, in accordance with the 10 or 100 times higher photon flux, respectively. The methane consumption increases roughly in a linear way with the photon flux. The product composition is close to that of the reference case. Interestingly, the second test gives very similar methane consumption and

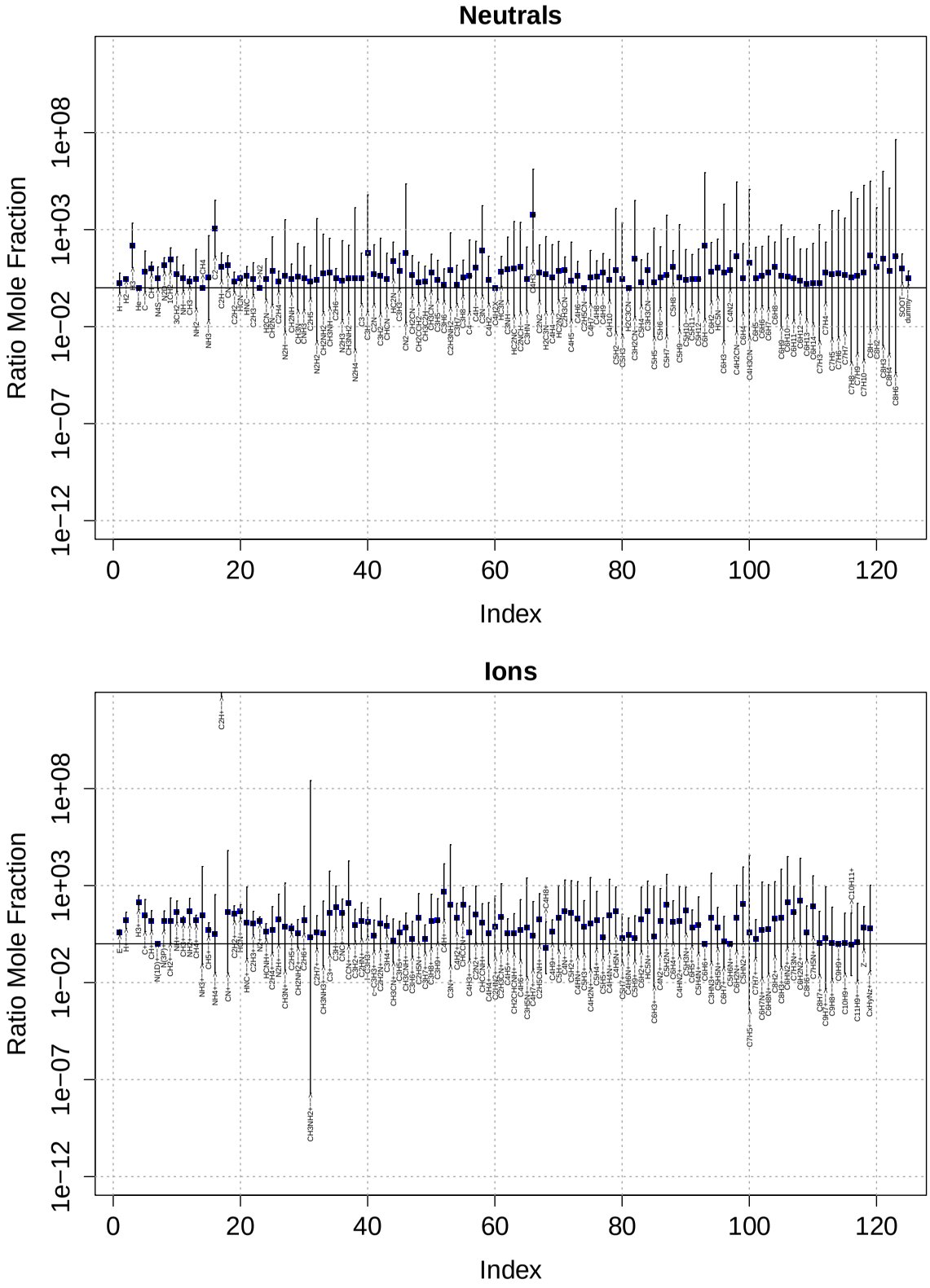

Figure A.1: Ratios of stationary concentrations of neutrals (top) and ions (bottom) in the 2D model to those in the reference model (Case 1). Ratios' mean values and uncertainties (95% confidence interval) are respectively denoted by squares and error bars.

product composition to the first. This indicates that the chemistry in the irradiated column may propagate to the non-irradiated region to a large extent.

According to the observations above, a more concentrated radiation through a narrow column consumes almost the same amount of methane as a radiation with identical photon number per unit time. In other words, almost the same amount of methane is consumed in the reference case and the irradiated column of the 2D model. The chemistry in the non-irradiated region enhances the total methane consumption in the 2D model, but not significantly change the product composition.

Bibliography

Adamkovics, M.; Boering, K. A. (2003). Photochemical formation rates of organic aerosols through time-resolved in situ laboratory measurements. *Journal of Geophysical Research: Planets*, **108**: 11/1–11/14.

Aitchison, J. (1986). *The Statistical Analysis of Compositional Data*. Monographs on Statistics and Applied Probability. Chapman and Hall, London.

Alcouffe, G.; Cavarroc, M.; Cernogora, G.; Ouni, F.; Jolly, A.; Boufendi, L.; Szopa, C. (2010). Capacitively coupled plasma used to simulate titan's atmospheric chemistry. *Plasma Sources Science and Technology*, **19**:015008.

Anicich, V. (1993). Evaluated bimolecular ion-molecule gas phase kinetics of positive ions for use in modelling planetary atmospheres, cometary comae and interstellar clouds. *J. Phys. Chem. Ref. Data*, **22**:1469–1569.

Atreya, S. K. (2007). Titan's organic factory. *Science*, **316**:843–845.

Banaszkiewicz, M.; Lara, L.; Rodrigo, R.; Lopez-Moreno, J.; Molina-Cuberos, G. (2000)a. A coupled model of Titan's atmosphere and ionosphere. *Icarus*, **147**:386–404.

Banaszkiewicz, M.; Lara, L. M.; Rodrigo, R.; Lopez-Moreno, J. J.; Molina-Cuberos, G. J. (2000)b. The upper atmosphere and ionosphere of Titan: A coupled model. *Advances in Space Research*, **26**(10):1547–1550.

Bell, J. M.; Bougher, S. W.; Waite, J. Hunter, J.; Ridley, A. J.; Magee, B. A.; Mandt, K. E.; Westlake, J.; DeJong, A. D.; Bar-Nun, A.; Jacovi, R.; Toth, G.; De La Haye, V. (2010). Simulating the one-dimensional structure of Titan's upper atmosphere: 1. Formulation of the Titan Global Ionosphere-Thermosphere Model and benchmark simulations. *J. Geophys. Res.*, **115**:E12002.

Bézard, B.; Yelle, R.; Nixon, C. *Titan. Interior, Surface, Atmosphere, and Space Environment*, chapter The composition of Titan's atmosphere. Cambridge University Press (2013).

BIPM,; IEC,; IFCC,; ILAC,; ISO,; IUPAC,; IUPAP,; OIML, (2008). Evaluation of measurement data - Guide to the expression of uncertainty in measurement (GUM). Technical Report 100:2008, Joint Committee for Guides in Metrology, JCGM.

BIPM,; IEC,; IFCC,; ILAC,; ISO,; IUPAC,; IUPAP,; OIML, (2008). Evaluation of measurement data - Supplement 1 to the "Guide to the expression of uncertainty in measurement" - Propagation of distributions using a Monte Carlo method. Technical Report 101:2008, Joint Committee for Guides in Metrology, JCGM.

Breth, A.; Dobrozemsky, R.; Kraus, B. (1983)a. Comments on accuracy in mass-spectrometric gas analysis. *Vacuum*, **33**:73–76.

Breth, A.; Dobrozemsky, R.; Schwarzinger, G. (1983)b. Some basic problems in the deconvolution of gas-analytical mass spectra. *International Journal of Mass Spectrometry and Ion Physics*, **48**: 3–6.

Brown, R.; Lebreton, J.-P.; Waite, H. (2009). *Titan from Cassini-Huygens*. Springer.

Brownsword, R. A.; Hillenkamp, M.; Laurent, T.; Vatsa, R. K.; Volpp, H. R.; Wolfrum, J. (1997). Quantum yield for H atom formation in the methane dissociation after photoexcitation at the Lyman α (121.6 nm) wavelength. *Chemical Physics Letters*, **266**(1-2):259–266.

Cable, M. L.; Hoerst, S. M.; Hodyss, R.; Beauchamp, P. M.; Smith, M. A.; Willis, P. A. (2012). Titan Tholins: Simulating Titan Organic Chemistry in the Cassini-Huygens Era. *Chem. Rev.*, **112**:1882–1909.

Carrasco, N.; Pernot, P. (2007). Modeling of branching ratio uncertainty in chemical networks by Dirichlet distributions. *Journal of Physical Chemistry A*, **11(18)**:3507–3512.

Carrasco, N.; Dutuit, O.; Thissen, R.; Banaszkiewicz, M.; Pernot, P. (2007)a. Uncertainty analysis of bimolecular reactions in Titan ionosphere chemistry model. *Planetary and Space Science*, **55**: 141–157.

Carrasco, N.; Hébrard, E.; Banaszkiewicz, M.; Dobrijevic, M.; Pernot, P. (2007)b. Influence of neutral transport on ion chemistry uncertainties in Titan ionosphere. *Icarus*, **192**:519–526.

Carrasco, N.; Alcaraz, C.; Dutuit, O.; Plessis, S.; Thissen, R.; Vuitton, V.; Yelle, R.; Pernot, P. (2008)a. Sensitvity of a Titan ionospheric model to the ion-molecule reaction parameters. *Planetary and Space Science*, **55**:1644–1657.

Carrasco, N.; Plessis, S.; Dobrijevic, M.; Pernot, P. (2008)b. Toward a reduction of the bimolecular reaction model for Titan's ionosphere. *International Journal of Chemical Kinetics*, **40**:699–709.

Carrasco, N.; Schmitz-Afonso, I.; Bonnet, J. Y.; Quirico, E.; Thissen, R.; Dutuit, O.; Bagag, A.; Laprévote, O.; Buch, A.; Giulani, A.; Adandé, G.; Ouni, F.; Hadamcik, E.; Szopa, C.; Cernogora, G. (2009). Chemical characterization of Titan's tholins: Solubility, morphology and molecular structure revisited. *The Journal of Physical Chemistry A*, **113**:11195–11203.

Carrasco, N.; Gautier, T.; Essebbar, E.; Pernot, P.; Cernogora, G. (2012). Volatile products controlling Titan's tholins production. *Icarus*, **219**:230–240.

Chan, W.; Cooper, G.; Sodhi, R.; Brion, C. (1993). Absolute optical oscillator strengths for discrete and continuum photoabsorption of molecular nitrogen (11-200 eV). *Chemical Physics*, **170**:81–97.

Chen, F. Z.; Wu, C. Y. R. (2004). Temperature-dependent photoabsorption cross sections in the VUV-UV region. I. Methane and ethane. *Journal of Quantitative Spectroscopy and Radiative Transfer*, **85**:195–209.

Clark, K. C. (1952). Ionospheric absorption by N_2 and O_2 of certain extreme ultraviolet solar wavelengths. *Phys. Rev.*, **87**:271–276.

Connor, R. J.; Mosimann, J. E. (1969). Concepts of Independence for Proportions with a Generalization of the Dirichlet Distribution. *Journal of the American Statistical Association*, **64**(325): 194–206.

Cook, G. R.; Metzger, P. H. (1964). Photoionization and absorption cross sections of N_2 and O_2 in the 600 to 1000 A region. *The Journal of Chemical Physics*, **41**:321–336.

Coustenis, A. *et al.* (2007). The composition of Titan's stratosphere from Cassini/CIRS mid-infrared spectra. *Icarus*, **189**(1):35 – 62.

Cravens, T.; Robertson, I.; Jr, J. W.; Kasprzak, W.; Keller, C.; Ledvina, S.; Niemann, H.; Luhmann, J.; McNutt, R.; Ip, W.; Haye, V. D. L.; Mueller-Wodarg, I.; Wahlung, J.; Anicich, V.; Vuitton, V. (2006). Composition of Titan's ionosphere. *Geophys. Res. Lett.*, **33**:L07312.

Cui, J.; Yelle, R.; Vuitton, V.; Jr., J. W.; Kasprzak, W.; Gell, D.; Niemann, H.; Mueller-Wodarg, I.; Borggren, N.; Fletcher, G.; Patrick, E.; Raaen, E.; Magee, B. (2009). Analysis of Titan's neutral upper atmosphere from Cassini Ion Neutral Mass Spectrometer measurements. *Icarus*, **200**(2):581–615.

De La Haye, V.; Waite, J.; Cravens, T.; Robertson, I.; Lebonnois, S. (2008). Coupled ion and neutral rotating model of Titan's upper atmosphere. *Icarus*, **197**:110–136.

De La Haye, V. (2005). *Corona Formation and Heating Efficiencies in Titan's Upper Atmosphere: Construction of a coupled Ion, Neutral and Thermal Structure Model To Interpret the First INMS Cassini Data.* PhD thesis, The University of Michigan.

Development Core Team, R. R: A language and environment for statistical computing. R Foundation for Statistical Computing, Vienna, Austria. online (2010).

Dobrijevic, M.; Dutour, I. (2006). A random graphs model for the study of chemical complexity in planetary atmospheres. *Planetary and Space Science*, **54**:287 – 295.

Dobrijevic, M.; Parisot, J. (1998). Effect of chemical kinetic uncertainties on hydrocarbon production in the stratosphere of Neptune. *Planetary and Space Science*, **46**:491–505.

Dobrijevic, M.; Ollivier, J.; Billebaud, F.; Brillet, J.; Parisot, J. (2003). Effect of chemical kinetic uncertainties on photochemical modeling results: Application to Saturn's atmosphere. *A & A*, **398**:335–344.

Dobrijevic, M.; Carrasco, N.; Hébrard, E.; Pernot, P. (2008). Epistemic bimodality and kinetic hypersensitivity in photochemical models of Titan's atmosphere. *Planetary and Space Science*, **56**:1630–1643.

Dobrijevic, M.; Hébrard, E.; Plessis, S.; Carrasco, N.; Bruno-Claeys, M.; Pernot, P. (2010). Comparison of methods for the determination of key reactions in chemical systems: Application to Titan's atmosphere. *Adv. Space Res.*, **45**:77–91.

Dobrijevic, M.; Cavalié, T.; Billebaud, F. (2011). A methodology to construct a reduced chemical scheme for 2D-3D photochemical models: Application to Saturn. *Icarus*, **214**:275–285.

Ehrenfreund, P.; Rasmussen, S.; Cleaves, Jamesand Chen, L. (2006). Experimentally tracing the key steps in the origin of life: The aromatic world. *Astrobiology*, pages 490–520.

Evans, M.; Hastings, N.; Peacock, B. (2000). *Statistical Distributions*. Wiley-Interscience, 3rd edition.

Fang, K.-T.; Yang, Z.-H. (2000). On uniform design of experiments with restricted mixtures and generation of uniform distribution on some domains. *Statistics & Probability Letters*, **46**:113 – 120.

Frenklach, M. (2002). Reaction mechanism of soot formation in flames. *Physical Chemistry Chemical Physics*, **4**(11):2028–2037.

Gans, B.; Boye-Peronne, S.; Broquier, M.; Delsaut, M.; Douin, S.; Fellows, C.; Halvick, P.; Loison, J.-C.; Lucchese, R.; Gauyacq, D. (2011). Photolysis of methane revisited at 121.6 nm and at 118.2 nm: quantum yields of the primary products, measured by mass spectrometry. *Phys. Chem. Chem. Phys.*, **13**:8140–8152.

Gans, B.; Peng, Z.; Carrasco, N.; Gauyacq, D.; Lebonnois, S.; Pernot, P. (2013). Impact of a new wavelength-dependent representation of methane photolysis branching ratios on the modeling of Titan's atmospheric photochemistry. *Icarus*, **223**:330 – 343.

Gautier, T.; Carrasco, N.; Buch, A.; Szopa, C.; Sciamma-O'Brien, E.; Cernogora, G. (2011). Nitrile gas chemistry in Titan atmosphere. *Icarus*, **213**:625–635.

Giuliani, A.; Jamme, F.; Rouam, V.; Wien, F.; Giorgetta, J.-L.; Lagarde, B.; Chubar, O.; Bac, S.; Yao, I.; Rey, S.; Herbeaux, C.; Marlats, J.-L.; Zerbib, D.; Polack, F.; Refregiers, M. (2009). DISCO: a low-energy multipurpose beamline at synchrotron SOLEIL. *Journal of Synchrotron Radiation*, **16**:835–841.

Giuliani, A. *et al.* (2011). A differential pumping system to deliver windowless VUV photons at atmospheric pressure. *Journal of Synchrotron Radiation*, **18**:546–549.

Gorodetsky, A.; Zalavutdinov, R.; Zakharov, A.; Vnukov, S.; Varshavskaya, I.; Makhankov, A.; Mazul, I.; Federici, G. (2005). Increased recombination of CH_3 radicals on stainless steel. *Journal of Nuclear Materials*, **337-339**:892 – 896.

Gregory, P. (2005). *Bayesian Logical Data Analysis for the Physical Sciences*. Cambridge University Press.

Hébrard, E.; Dobrijevic, M.; Bénilan, Y.; Raulin, F. (2006). Photochemical kinetics uncertainties in modeling Titan's atmosphere: A review. *Journal of Photochemistry and Photobiology A: Chemistry*, **7**:211–230.

Hébrard, E.; Dobrijevic, M.; Bénilan, Y.; Raulin, F. (2007). Photochemical kinetics uncertainties in modeling Titan's atmosphere: First consequences. *Planetary and Space Science*, **55**:1470–1489.

Hébrard, E.; Dobrijevic, M.; Pernot, P.; Carrasco, N.; Bergeat, A.; Hickson, K. M.; Canosa, A.; Le Picard, S. D.; Sims, I. R. (2009). How measurements of rate coefficients at low temperature increase the predictivity of photochemical models of Titan's atmosphere. *The Journal of Physical Chemistry A*, **113**:11227–11237.

Hébrard, E. (2006). *Incertitudes photochimiques dans les modèles de l'atmosphère de Titan : revue et conséquences.* PhD thesis, Université Paris VII - Denis Diderot.

Helton, J.; Johnson, J.; Sallaberry, C.; Storlie, C. (2006). Survey of sampling-based methods for uncertainty and sensitivity analysis. *Reliability Engineering and System Safety*, **91**:1175–1209.

Huber, K. P.; Stark, G.; Ito, K. (1993). Rotational structure in the Hopfield series of N_2. *The Journal of Chemical Physics*, **98**:4471–4477.

Huebner, W.; Link, W. (2011). Photo cross-sections and rate coefficients (http://amop.space.swri.edu/).

Huffman, R. E.; Tanaka, Y.; Larrabee, J. C. (1963). Absorption coefficients of nitrogen in the 1000-580 A wavelength region. *The Journal of Chemical Physics*, **39**:910–925.

Huffman, R. E. (1969). Absorption cross-sections of atmospheric gases for use in aeronomy. *Canadian Journal of Chemistry*, **47**:1823–1834.

Imanaka, H.; Smith, M. (2007). Role of photoionization in the formation of complex organic molecules in Titan's upper atmosphere. *Geophysical Research Letters*, **34**:L02204.

Imanaka, H.; Smith, M. (2008). Formation of nitrogenated organic aerosols by EUV irradiation of a simulated Titan atmosphere. *Bulletin of the American Astronomical Society*, **40**:421.

Imanaka, H.; Smith, M. A. (2010). Formation of nitrogenated organic aerosols in the Titan upper atmosphere. *Proceedings of the National Academy of Sciences*, **107**:12423–12428.

Jaramillo-Botero, A.; An, Q.; Cheng, M.-J.; Goddard, W. A.; Beegle, L. W.; Hodyss, R. (2012). Hypervelocity Impact Effect of Molecules from Enceladus' Plume and Titan's Upper Atmosphere on NASA's Cassini Spectrometer from Reactive Dynamics Simulation. *Phys. Rev. Lett.*, **109**: 213201.

Keller, N.; Anicich, V.; Cravens, T. (1998). Model of Titan's ionosphere with detailed hydrocarbon ion chemistry. *Planetary and Space Science*, **46**:1157.

Kostov, V.; Velinov, P. (2001). Sunrise and sunset effects on solar heating in the jovian thermosphere and ionosphere. *Advances in Space Research*, **27**:1889 – 1893.

Krasnopolsky, V. (2009). A photochemical model of Titan's atmosphere and ionosphere. *Icarus*, **201**:226–256.

Kuiper, G. P. (1944). Titan: a Satellite with an Atmosphere. *Astrophysical Journal*, **100**:378–383.

Lara, L.; Lellouch, E.; Lopez-Moreno, J.; Rodrigo, R. (1996). Vertical distribution of Titan's atmospheric neutral constituents. *J. Geophys. Res.*, **101**:23261–23283.

Lara, L. M.; Banaszkiewicz, M.; Rodrigo, R.; Lopez-Moreno, J. J. (2002). The CH_4 density in the upper atmosphere of Titan. *Icarus*, **158**:191–198.

Larson, H. P. (1980). Infrared spectroscopic observations of the outer planets, their satellites, and the asteroids. *ANNUAL REVIEW OF ASTRONOMY AND ASTROPHYSICS*, **18**:43–75.

Lavvas, P.; Coustenis, A.; Vardavas, I. (2008)a. Coupling photochemistry with haze formation in Titan's atmosphere, Part I: Model description. *Planetary and Space Science*, **56**:27 – 66.

Lavvas, P.; Coustenis, A.; Vardavas, I. (2008)b. Coupling photochemistry with haze formation in Titan's atmosphere, Part II: Results and validation with Cassini/Huygens data. *Planetary and Space Science*, **56**:67–99.

Lavvas, P.; Galand, M.; Yelle, R.; Heays, A.; Lewis, B.; Lewis, G.; Coates, A. (2011). Energy deposition and primary chemical products in Titan's upper atmosphere. *Icarus*, **213**:233 – 251.

Lebonnois, S.; Toublanc, D.; Hourdin, F.; Rannou, P. (2001). Seasonal variations of Titan's atmospheric composition. *Icarus*, **152**:384–406.

Lebonnois, S.; Bakes, E.; McKay, C. (2003). Atomic and molecular hydrogen budget in Titan's atmosphere. *Icarus*, **161**:474–485.

Lebonnois, S.; Burgalat, J.; Rannou, P.; Charnay, B. (2012). Titan global climate model: A new 3-dimensional version of the IPSL Titan GCM. *Icarus*, **218**(1):707–722.

Lebonnois, S. (2005). Benzene and aerosol production in Titan and Jupiter's atmospheres: a sensitivity study. *Planetary and Space Science*, **53**:486–497.

Lee, L. C.; Chiang, C. C. (1983). Fluorescence yield from photo-dissociation of CH_4 at 1060-1420 *Å*. *Journal of Chemical Physics*, **78**:688–691.

Lingwall, J.; Christensen, W.; Reese, C. (2008). Dirichlet based bayesian multivariate receptor modeling. *Environmetrics*, **19**:618–629.

Lipatov, A.; Jr., E. S.; Hartle, R.; Cooper, J.; Simpson, D. (2012). Saturn's magnetosphere interaction with Titan for {T9} encounter: 3D hybrid modeling and comparison with {CAPS} observations. *Planetary and Space Science*, **61**(1):66–78.

Listgarten, J.; Emili, A. (2005). Statistical and computational methods for comparative proteomic profiling using liquid chromatography-tandem mass spectrometry. *Molecular & Cellular Proteomics*, **4**:419–434.

Magee, B. A.; Waite, J. H.; Mandt, K. E.; Westlake, J.; Bell, J.; Gell, D. A. (2009). INMS derived composition of Titan's upper atmosphere: Analysis methods and model comparison. *Planetary and Space Science*, **57**:1895–1916.

Mandt, K. E. *et al.* (2012)a. Ion densities and composition of Titan's upper atmosphere derived from the Cassini Ion Neutral Mass Spectrometer: Analysis methods and comparison of measured ion densities to photochemical model simulations. *Journal of Geophysical Research: Planets*, **117**: 2156–2202.

Mandt, K. E.; Waite, J. H.; Teolis, B.; Magee, B. A.; Bell, J.; Westlake, J. H.; Nixon, C. A.; Mousis, O.; Lunine, J. I. (2012)b. The 12C/13C Ratio on Titan from Cassini INMS Measurements and Implications for the Evolution of Methane. *The Astrophysical Journal*, **749**:160.

Mao, F.; Leck, J. (1987). The quadrupole mass spectrometer in practical operation. *Vacuum*, **37**: 669–675.

McLain, J.; Molek, C.; Jr., D. O.; Adams, N. (2009). Flowing afterglow studies of the electron recombination of protonated cyanides $(R\mathrm{CN})\mathrm{H}^+$ and their proton-bound dimer ions $(R\mathrm{CN})_2\mathrm{H}^+$ where R is H, CH_3, and $\mathrm{CH}_3\mathrm{CH}_2$. *International Journal of Mass Spectrometry*, **282**:85 – 90.

Mebel, A. M.; Lin, S. H.; Chang, C. H. (1997). Theoretical study of vibronic spectra and photodissociation pathways of methane. *Journal of Chemical Physics*, **106**:2612–2620.

Miller, S. L.; Urey, H. C. (1959). Organic Compound Synthesis on the Primitive Earth: Several questions about the origin of life have been answered, but much remains to be studied. *Science*, **130**(3370):245–251.

Mordaunt, D. H.; Lambert, I. R.; Morley, G. P.; Ashfold, M. N. R.; Dixon, R. N.; Western, C. M.; Schnieder, L.; Welge, K. H. (1993). Primary product channels in the photodissociation of methane at 121.6 nm. *Journal of Chemical Physics*, **98**:2054–2065.

Niemann, H. B. *et al.* (2005). The abundances of constituents of Titan's atmosphere from the GCMS instrument on the Huygens probe. *Nature*, **438**(7069):779–784.

Null, B. (2008). The Nested Dirichlet distribution: properties and applications. Working paper, Department of Management Science and Engineering, Stanford University.

Oinuma, G.; Inanaga, Y.; Tanimura, Y.; Kuzumoto, M.; Tabata, Y.; Watanabe, K. (2010). A comparative study of the surface recombination of nitrogen atoms on various materials at atmospheric pressure. *Journal of Physics D: Applied Physics*, **43**:255202.

Peng, Z.; Dobrijevic, M.; Hebrard, E.; Carrasco, N.; Pernot, P. (2010). Photochemical modeling of Titan atmosphere at the "10 percent uncertainty horizon". *Faraday Discuss.*, **147**:137–153.

Peng, Z.; Carrasco, N.; Pernot, P. (2011). Modeling of atmospheric photochemitry simulated by synchrotron setup. In *EPSC Abstracts*, volume 6, page 780. EPSC.

Peng, Z.; Cailliez, F.; Dobrijevic, M.; Pernot, P. (2012). Null Variance Altitudes for the photolysis rate constants of species with barometric distribution: Illustration on Titan upper atmosphere modeling. *Icarus*, **218**:950–955.

Peng, Z.; Gautier, T.; Carrasco, N.; Pernot, P.; Giuliani, A.; Mahjoub, A.; Correia, J.-J.; Buch, A.; Bénilan, Y.; Szopa, C.; Cernogora, G. (2013). Titan's atmosphere simulation experiment using continuum UV-VUV synchrotron radiation. *Journal of Geophysical Research: Planets*, **118**:778–788.

Plessis, S.; Carrasco, N.; Pernot, P. (2010). Knowledge-based probabilistic representations of branching ratios in chemical networks: the case of dissociative recombinations. *J. Chem. Phys.*, **133**:134110.

Plessis, S.; Carrasco, N.; Dobrijevic, M.; Pernot, P. (2012). Production of neutral species in Titan's ionosphere through dissociative recombination of ions. *Icarus*, **219**:254 – 266.

Puccio, M. A.; Miller, J. H. (2010). Detection of trace hydrocarbons in flames using direct sampling mass spectrometry coupled with multilinear regression analysis. *Analytical Chemistry*, **82**:5160–5168.

Rebbert, R. E.; Ausloos, P. (1972/73). Photolysis of methane: quantum yield of C(^1D) and CH. *Journal of Photochemistry*, **1**:171–176.

Romani, P. N. (1996). Recent rate constant and product measurements of the reactions C_2H_3 + H_2 and C_2H_3 + H importance for photochemical modeling of hydrocarbons on Jupiter. *Icarus*, **122**: 233 – 241.

Romanzin, C.; Gazeau, M.-C.; Benilan, Y.; Hebrard, E.; Jolly, A.; Raulin, F.; Boye-Peronne, S.; Douin, S.; Gauyacq, D. (2005). Methane photochemistry: A brief review in the frame of a new experimental program of Titan's atmosphere simulations. *Advances in Space Research*, **36**: 258–267.

Romanzin, C.; Bénilan, Y.; Jolly, A.; Gazeau, M.-C. (2008). Photolytic behaviour of methane at Lyman-α and 248 nm: Studies in the frame of a simulation program of Titan's atmosphere (S.E.T.U.P.). *Advances in Space Research*, **42**:2036–2044.

Sagan, C.; Khare, B. N. (1979). Tholins: organic chemistry of interstellar grains and gas. *Nature*, **277**:102–7.

Sagan, C.; Thompson, W. R.; Khare, B. N. (1992). A laboratory for prebiological organic chemistry. *Accounts Chem. Res.*, **25**:286–292.

Saltelli, A.; Chan, K.; Scott, E. M. (2000). *Sensitivity Analysis*. Wiley, Chichester.

Saltelli, A.; Tarantola, S.; Campolongo, F.; Ratto, M. (2004). *Sensitivity Analysis in Practice*. Wiley.

Saltelli, A.; Ratto, M.; Tarantola, S.; Campolongo, F. (2005). Sensitivity analysis for chemical models. *Chem. Rev.*, **105**:2811–2827.

Samson, J.; Cairns, R. (1964). Absorption and photoionization cross sections of N_2 and O_2 at intense solar emission lines. *J. Geophys. Res.*, **69**:4583–4590.

Sander, S. P.; Ravishankara, A. R.; Golden, D. M.; Kolb, C. E.; Kurylo, M. J.; Molina, M. J.; Moortgat, G. K.; Finlayson-Pitts, B. J.; H., W. P.; Huie, R. E. (2006). Chemical kinetics and photochemical data for use in atmospheric studies. Evaluation number 15. *JPL Publication*, **06-2**: 1–522.

Schaufelberger, A.; Wurz, P.; Lammer, H.; Kulikov, Y. (2012). Is hydrodynamic escape from Titan possible? *Planetary and Space Science*, **61**:79–84.

Sciamma-O'Brien, E.; Carrasco, N.; Szopa, C.; Buch, A.; Cernogora, G. (2010). Titan's atmosphere: an optimal gas mixture for aerosol production? *Icarus*, **209**:704–714.

Shampine, L. F.; Sommeijer, B. P.; Verwer, J. G. (2006). IRKC: an IMEX solver for stiff diffusion-reaction PDEs. *J. Comput. Appl. Math.*, **196**:485–497.

Smith, N. S.; Raulin, F. (1999). Modeling of methane photolysis in the reducing atmospheres of the outer solar system. *J. Geophys. Res.*, **104**:1873–1876.

Sobol, I. (1990). Sensitivity analysis for non-linear mathematical models. *Modelling and Computational Experiment*, **1**:407–414.

Solá, J. C. (1908). Observations des satellites principaux de Jupiter et de Titan. *Astronomische Nachrichten*, **179**(18):289–290.

Strobel, D. F. (2009). Titan's hydrodynamically escaping atmosphere: Escape rates and the structure of the exobase region. *Icarus*, **202**:632 – 641.

Szopa, C.; Cernogora, G.; Boufendi, L.; Correia, J.; Coll, P. (2006)a. PAMPRE: a dusty plasma experiment for Titan's tholins production and study. *Planetary and Space Science*, **54**(4):394–404.

Szopa, C.; Freguglia, G.; Sternberg, R.; Nguyen, M.; Coll, P.; Raulin, F.; Pietrogrande, C.; Niemann, H. (2006)b. Performances under representative pressure and temperature conditions of the gas chromatography-mass spectrometry space experiment to investigate Titan's atmospheric composition. *J. Chromatogr. A*, **1131**:215–226.

Thejaswini, H. C.; Majumdar, A.; Maung Tun, T.; Hippler, R. (2011). Plasma chemical reactions in C2H2/N2, C2H4/N2, and C2H6/N2 gas mixtures of a laboratory dielectric barrier discharge. *Advances in Space Research*, **48**:857–861.

Thissen, R.; Vuitton, V.; Lavvas, P.; Lemaire, J.; Dehon, C.; Dutuit, O.; Smith, M. A.; Turchini, S.; Catone, D.; Yelle, R. V.; Pernot, P.; Somogyi, A.; Coreno, M. (2009). Laboratory Studies of Molecular Growth in the Titan Ionosphere. *J. Phys. Chem. A*, **113**:11211–11220.

Thompson, A.; Stewart, R. (1991). Effect of chemical kinetics uncertainties on calculated constituents in a tropospheric photochemical model. *J. Geophys. Res.*, **96**:13089–13108.

Tian, G.-L.; Tang, M.-L.; Yuen, K.; Ng, K. (2010). Further properties and new applications of the Nested Dirichlet distribution. *Computational Statistics & Data Analysis*, **54**:394–405.

Tilford, C. R. (1994). Process monitoring with residual gas analysers (RGAs): limiting factors. *Surface and Coatings Technology*, **68/69**:708–712.

Toublanc, D.; Parisot, J. P.; Brillet, J.; Gautier, D.; Raulin, F.; McKay, C. P. (1995). Photochemical modeling of Titan's atmosphere. *Icarus*, **113**:2–26.

Trainer, M. G.; Pavlov, A. A.; Jimenez, J. L.; McKay, C. P.; Worsnop, D. R.; Toon, O. B.; Tolbert, M. A. (2004). Chemical composition of Titan's haze: are PAHs present? *Geophysical Research Letters*, **31**:L17S08/1–L17S08/4.

Tran, B. N.; Ferris, J. P.; Chera, J. J. (2003). The photochemical formation of a titan haze analog. structural analysis by x-ray photoelectron and infrared spectroscopy. *Icarus*, **162**(1):114–124.

Troe, J. (2005). Temperature and pressure dependence of ion-molecule association and dissociation reactions: the $N_2^+ + N_2$ (+ M) $\Leftrightarrow N_4^+$ (+ M) reaction. *Phys. Chem. Chem. Phys.*, **7**:1560–1567.

Van Harrevelt, R. (2006). Photodissociation of methane: Exploring potential energy surfaces. *Journal of Chemical Physics*, **125**:124302.

Verwer, J.; Sommeijer, B. (2004). An Implicit-Explicit Runge–Kutta–Chebyshev Scheme for Diffusion-Reaction Equations. *SIAM Journal on Scientific Computing*, **25**(5):1824–1835.

Vuitton, V.; Yelle, R.; Anicich, V. (2006). The nitrogen chemistry of Titan's upper atmosphere revealed. *The Astrophysical Journal*, **647**:L175–L178.

Vuitton, V.; Yelle, R.; McEwan, M. (2007). Ion chemistry and N-containing molecules in Titan's upper atmosphere. *Icarus*, **191**:722–742.

Vuitton, V.; Yelle, R. V.; Cui, J. (2008). Formation and distribution of benzene on Titan. *J. Geophys. Res.*, **113**:E05007–.

Vuitton, V.; Lavvas, P.; Yelle, R.; Galand, M.; Wellbrock, A.; Lewis, G.; Coates, A.; Wahlund, J.-E. (2009)a. Negative ion chemistry in Titan's upper atmosphere. *Planetary and Space Science*, **57**:1558 – 1572.

Vuitton, V.; Yelle, R.; Lavvas, P. (2009)b. Composition and chemistry of Titan's thermosphere and ionosphere. *Philosophical Transactions of the Royal Society A: Mathematical, Physical and Engineering Sciences*, **367**:729–741.

Waite, J. *et al.* (2004). The Cassini Ion and Neutral Mass Spectrometer (INMS) Investigation. *Space Science Reviews*, **114**(1):113–231.

Waite, J. *et al.* (2005). Ion Neutral Mass Spectrometer Results from the First Flyby of Titan. *Science*, **308**:982–986.

Waite, J.; Young, D.; Cravens, T.; Coates, A.; Crary, F.; Magee, B.; Westlake, J. (2007). The process of tholin formation in Titan's upper atmosphere. *Science*, **316**:870–875.

Wakelam, V.; Smith, I. W. M.; Herbst, E.; Troe, J.; Geppert, W.; Linnartz, H.; Öberg, K.; Roueff, E.; Agundez, M.; Pernot, P.; Cuppen, H. M.; Loison, J.-C.; Talbi, D. (2010). Reaction Networks For Interstellar Chemical Modelling: Improvements and Challenges. *Space Science Reviews*, **156**:13–72.

Wang, J. H.; Liu, K. P.; Min, Z. Y.; Su, H. M.; Bersohn, R.; Preses, J.; Larese, J. Z. (2000). Vacuum ultraviolet photochemistry of CH_4 and isotopomers. II. Product channel fields and absorption spectra. *Journal of Chemical Physics*, **113**:4146–4152.

Westlake, J. H.; Waite, J. H., J.; Mandt, K. E.; Carrasco, N.; Bell, J. M.; Magee, B. A.; Wahlund, J.-E. (2012). Titan's ionospheric composition and structure: Photochemical modeling of Cassini INMS data. *J. Geophys. Res.*, **117**:E01003.

Wilson, E. H.; Atreya, S. K. (2000). Sensitivity studies of methane photolysis and its impact on hydrocarbon chemistry in the atmosphere of Titan. *J. Geophys. Res.*, **105**:20263–20273.

Wilson, E. H.; Atreya, S. K. (2003). Chemical sources of haze formation in Titan's atmosphere. *Planetary and Space Science*, **51**:1017–1033.

Wilson, E. H.; Atreya, S. K. (2004). Current state of modeling the photochemistry of Titan's mutually dependent atmosphere and ionosphere. *Journal of Geophysical Research*, **109**:E06002.

Wilson, E. H. (2002). *Investigations into the photochemistry of the current and primordial atmosphere of Titan*. PhD thesis, University of Michigan.

Wong, T.-T. (1998). Generalized Dirichlet distribution in Bayesian analysis. *Applied Mathematics and Computation*, **97**:165–181.

Wong, T.-T. (2010). Parameter estimation for generalized Dirichlet distributions from the sample estimates of the first and the second moments of random variables. *Computational Statistics & Data Analysis*, **54**:1756 – 1765.

Yelle, R. V.; Cui, J.; Mueller-Wodarg, I. C. F. (2008). Methane escape from Titan's atmosphere. *Journal of Geophysical Research: Planets*, **113**:E10003.

Yelle, R. V.; Vuitton, V.; Lavvas, P.; Klippenstein, S. J.; Smith, M. A.; Hörst, S. M.; Cui, J. (2010). Formation of NH_3 and CH_2NH in Titan's upper atmosphere. *Faraday Discuss.*, **147**: 31–49.

Yung, Y. L.; Allen, M.; Pinto, J. P. (1984). Photochemistry of the atmosphere of Titan - Comparison between model and observations. *Astrophy. J. Suppl. Ser.*, **55**(3):465–506.

Yung, Y. L. (1987). An update of nitrile photochemistry on Titan. *Icarus*, **72**(2):468–472.

Zabka, J.; Romanzin, C.; Alcaraz, C.; Polasek, M. (2012). Anion chemistry on Titan: a possible route to large N-bearing hydrocarbons. *Icarus*, **219**:161–167.

Zhang, Y.; Yuan, K.; Yu, S.; Yang, X. (2010). Highly rotationally excited CH_3 from methane photodissociation through conical intersection pathways. *Journal of Physical Chemistry Letters*, **1**:475–479.